Université catholique de Louvain

Ph.D. thesis

Modelling propagation impairments of Earth-Space links using Numerical Weather Prediction tools

by
Laurent Quibus

Thesis submitted in partial fulfillment of the requirements for the degree of
Docteur en sciences de l'ingénieur et technologie

Composition of the jury

Prof. Danielle Vanhoenacker-Janvier – *Supervisor*	UCLouvain, BE
Prof. Christophe Craeye – *President*	UCLouvain, BE
Prof. Claude Oestges – *Secretary*	UCLouvain, BE
Dr. Laurent Delobbe	IRM, BE
Dr. Rafiq Hamdi	IRM, BE
Dr. Laurent Féral	U. Toulouse III, FR

Louvain-la-Neuve
2020

Acknowledgments

The content of this work was partially supported by the F.R.S.–FNRS under grant FRFC T.1049.15 (NEWPORT), and by the European Space Agency under the contract ESA4000113886/15/NL/LVH.

First, I wish to express profuse thanks to Danielle Vanhoenacker-Janvier, the supervisor of this thesis at UCLouvain. I thank her for accepting me as her PhD student, back in 2015, with the opportunities to work on the NEWPORT project and on the ASALASCA ESA contract. I thank her for her support during the four years and a half that followed, including the chance to participate in other activities, to attend scientific meetings (EuCAP, ASAPE, ...), and thereof to interact with many scientists in radio-propagation or connected fields. I hardly could have hoped for more understanding, availability, and patience when discussing the progress of the present work and all this entails.

I would like to thank the other supervisors of NEWPORT: Rafiq Hamdi and Laurent Delobbe with the Royal Meteorological Institute of Belgium. They both shared their knowledge, regarding Numerical Weather Predictions and weather radars respectively, with great kindness and a communicative passion. I am thankful they accepted to join the thesis committee. My thanks extend warmly to the other researchers who worked on NEWPORT: Rozemien De Troch for providing data from the ALARO model and for undertaking its comparison with the WRF surface fields, and Maryna Lukach for processing Wideumont's radar data into rain attenuation and for analysing the results.

I am very grateful to the other members of the jury for offering some of their time and expertise to evaluate the present work. My thanks go to Claude Oestges, with UCLouvain, for joining the thesis committee and for insisting for a stronger quantitative assessment of the propagation results. My thanks also go to Christophe Craeye, with UCLouvain too, for accepting to preside over the jury. Additional thanks are reserved for Laurent Féral, with the Université of Toulouse III - Paul Sabatier (FR), who kindly answered the invitation to the jury as an external expert on propagation and its use for NWPs.

This thesis would not have been possible without the prior development of a NWP-based simulator of propagation impairments in the wake of the ESA/ESTEC EODDL contract. I wish to acknowledge especially the contributions of ONERA (FR) and thank Nicolas Jeannin and Laurent Castanet for providing their source code. I also thank Carlos Pereira, formerly with UCLouvain, for his precious help in getting started with WRF.

I owe many thanks to Antonio Martellucci with ESA/ESTEC (NL) for his involvement and leadership regarding ESA propagation activities, most relevantly here the ASALASCA contract and the ASAPE group. I also thank particularly Spiros Ventouras, with STFC/RAL (UK), for his efforts and his feedback as coordinator of the ASALASCA researchers, whom I thank too.

I have multiple reasons to express my gratitude towards Carlo Riva and Lorenzo Luini, with PoLiMi (IT). First, I thank them and ASI (IT) for the

opportunity to test NWP-derived nonrainy attenuation against beacon and radiometric data from the Spino d'Adda station. Second, I thank them for the work on beacon data calibration following Prof. Luini's visit at UCLouvain.

Regarding these activities on beacon data calibration, and about their method with GNSS data, I wish to thank Gustavo Siles, with the Universidad Privada Boliviana (BO), and José Manuel Riera, with the Universidad Politécnica de Madrid (ES). I also thank Prof. Riera and Domingo Pimienta del Valle, with UPM as well, for sharing radiometric statistics from Madrid.

I thank Félix Cuervo, with Joanneum Research (AT), for his work in comparing NWP-derived attenuations to beacon and radiometric data in Graz. Also at JR, I thank Joel Flávio for his feedback on the propagation impairments simulator. I also thank Michael Schoenhuber and Michael Schmidt.

I thank Ondrej Fiser and Viktor Pek, with the Institute of Atmospheric Physics and the University of Pardubice (CZ), and Martin Grabner, with the Czech Metrology Institute (CZ), for the tests on beacon signal processing done at the occasion of Prof. Fiser's short term scientific mission in UCLouvain.

For her extensive work on the nonrainy attenuation during her stay at UCLouvain, and afterwards in India, I also thank Gargi Rakshit, with the University of Calcutta (IN), and I thank her advisor Animesh Maitra.

I thank Eric Pottiaux and Véronique Dehant, with the Royal Observatory of Belgium, for their help in obtaining and processing GNSS data.

I am also highly thankful to Martin Rytir, with the Norwegian Defence Research Establishment (NO), and Terje Tjelta, with Telenor (NO), for the opportunity to work with low-elevation scintillation measurements from Isjord radio. And, for their contribution on this topic during their master's thesis, I thank Cyriac de Villenfagne de Vogelsanck and Joachim Kervyn de Meerendre.

Additionally, I thank Pierre-Yves Gousenbourger and Laurent Jacques, with UCLouvain, for some suggestions regarding interpolation techniques.

There is still plenty of my gratitude left for my colleagues at UCLouvain. I thank Alberto Graziani, for his ideas and involvement in ESA activities about beacon signal processing, radiometry, GNSS, and more. I thank Dmitry Kovalev, for his time spent on the Alphasat station, for sharing this thesis' template, for being so helpful and tolerating my presence in an office the longest. I thank Alessandro Vergani and Mojtaba Razavian for their work and collaboration on beacon data processing, ITU-R models, and NWPs. I thank Pasha Bekhrad for his efforts with NWPs for adaptive optics. I am appreciative for nice interactions with many others: Cleopatra, Jean, Babak, Denis, Thomas, Thomas, Ha, Ferran, Sergei, Evgenii, Igor, Modeste, Julian, Vasilii, Loïc, Bilel, Husnain, Christopher, Martin, Dimitri, Simon, Maxime, Farzad, ...

For their roles in managing the ICTEAM/ELEN computing resources put at work for this thesis, I happily thank Brigitte Dupont and François Hubin.

I was glad to receive great administrative help from UCLouvain. I thank especially Marie-Christine Vandingenen, Christel Derzelle, and Isabelle Dargent.

I wish to also thank the instructors, assistants, technicians, and students of the "Projet 2" for making my teaching duty a new adventure every year.

Finally, I thank my parents, my grandparents, family and friends, for providing perhaps the most important kind of support, if not the kindest even.

Abstract

Communication channels between the Earth and satellites are in the on-going process to be scaled up to higher and higher carrier frequencies above 20 GHz. The change is driven forward as an increasing number of services fill up the spectral bands allocated at lower frequencies, and as using higher frequencies also results in larger bandwidths, antenna gains and directivity. However, challenges to high frequency transmissions are posed by the stronger impairments of the signal as it propagates through the troposphere. In particular, the power of the signal is attenuated due to the presence of oxygen, water vapour, clouds, rain, and turbulence. The attenuation affects the signal-to-noise ratio (SNR) by up to tens of dB so that Fade Mitigation Techniques (FMTs) become needed.

Ideally, the design of FMTs should be based on direct measurements of the attenuation. Earth-space propagation experimental campaigns offer this reference thanks to spaceborne beacons emitting continuously at selected frequencies. These experiments are however costly, limited to a few receiving stations in a certain region, and lasting typically only a few years. The stations also require additional equipments such as radiometers in order to obtain the total attenuation and not just the contribution from rain events and amplitude scintillation. There is therefore an interest for models capable to derive the attenuation components from alternative measurements, so as to supplement the beacon data or fill the gaps in their coverage. Numerical Weather Predictions (NWPs) are important candidates as they aim to re-create, or even forecast, the state of the atmosphere (pressure, temperature, water, ...) starting with the assimilation of various measurements collected globally. This thesis principal objective is hence the investigation of the performances of a NWP-based simulator of the attenuation within the context of propagation experiments.

The thesis opens by introducing further the problems in Earth-space propagation, FMTs, propagation impairments, propagation experiments, and NWPs. A short review of the propagation experiments shows their current limits in frequency (1 to 3, $\sim$ 20 GHz and $<$ 50 GHz), coverage (mostly temperate), duration (usually $\sim 1-5$ years), number of stations (from 1 to rarely $\sim$ 20), and orbits (overwhelmingly geosynchronous orbits (GSO)). A short review of the previous usage of NWPs demonstrates the rarity of results simulated over the long-term ($>$ 1 year), with high resolutions ($<$ 5 km horizontally, $<$ 1 h), or for non-GSO links. It also points out the existence of two methods for the rain attenuation (rain volumetric content or rain rate), and of two methods for the cloud attenuation (NWP parametrisation or Salonen/Mattioli).

The thesis continues on the description of the propagation models, NWP models, interpolations or conversion of coordinates, and error metrics involved in the simulation of the attenuation from NWP data and its comparison with other reference datasets (beacon, radiometer, and weather radar). The theoretical foundations of the work introduce few novelties, with many of the propagation models following the recommendations from the International Telecom-

munication Union-Radiocommunication (ITU-R), and with the implementation of the simulator close to the existing solutions in the literature, especially the work of Jeannin *et al.*. This thesis aims however to test competing approaches, including the two alternatives for rain and cloud attenuations, or different NWP parametrisations. Some practical innovations are presented such as adaptive NWP time steps, and a post-processing without non-linear interpolations. Other originalities concern the estimation of the radiometric accuracy, or the computation non-GSO statistics either directly or from GSO statistics. The novelty is stronger for the validation of the performances in two phases.

In the first validation phase, long-term simulations (5 years) are performed for GSO and non-GSO links (19.701, 26, 39.402 and 75 GHz, Alphasat and METOP) at Louvain-la-Neuve (BE), at resolutions of 4 km and 5 min, with the Weather Research and Forecasting (WRF) model. These simulations are compared to equivalent ones using the ALARO model (4 km and 1 h), to weather radar data for rain (5 min), and to the ITU-R references. Among the results, the correlations in attenuation (at 30° in elevation) between WRF and ALARO are ~ 0.91 for oxygen, ~ 0.78 for water vapour, but only ~ 0.11 for clouds, and even lower for rain. The agreements in complementary cumulative distribution functions (CCDFs) are acceptable for the gases. For the clouds, there is an underestimation by the NWPs (by $\sim$ half) with respect to the ITU-R, though the Salonen/Mattioli models overestimate the ITU-R at high probabilities. Clouds also display a marked instantaneous dependence in azimuth and elevation, but a weak inter-annual variability. Rain attenuation has a strong inter-annual variability, but starts to stabilise after 5 years. The NWPs underestimate the ITU-R CCDFs for rain, though with the WRF rain rate it is by only ~ 1 dB and almost matching the radar results. In the case of non-GSO CCDFs, different attenuations are predicted from non-GSO time series than from a combination of GSO CCDFs, which suggests a design based on the latter is suboptimal.

In the second validation phase, the nonrainy attenuation (gases and cloud) is assessed thanks to four months of Alphasat beacon and radiometric data at Spino d'Adda (IT). Correlations and root-mean square errors between WRF (Tiedtke) and the radiometer are: 0.88 and 0.11 dB at 19.701 GHz, 0.59 and 0.26 dB at 39.402 GHz. The errors are comparable to the limits in radiometric (< 0.1 dB) and beacon processing (~ 0.2 to 0.5 dB) accuracies. The simulator could then act as a radiometer replacement within a propagation experiment.

After the validation, the thesis presents other applications of NWP-derived propagation impairments. Simulated Alphasat gaseous and cloud attenuation CCDFs during one year are shown for nine European ground stations. Other non-GSO CCDFs with the METOP satellites are shown for Graz (AT). The observations made from all those CCDFs are in line with the results obtained during the validation. Finally, an attempt to relate strong scintillation conditions with NWP data is described for a low elevation link in Isfjord (NO).

At the end, the performances are seen to be: good for the gases, sufficient as a radiometer's substitute for the clouds, acceptable statistically over multiple years for rain, only qualitative but promising for scintillation, and suggesting the ITU-R scaling from GSO to non-GSO CCDFs is suboptimal. Many perspectives remain open, e.g. at even higher radio-, or optical, frequencies.

Contents

List of publications

Articles in scientific journals

- M. Lukach, **L. Quibus**, D. Vanhoenacker-Janvier, L. Delobbe. "Rain attenuation statistics at Ka-band estimated from weather radar observations in Belgium," *Int. J. Satell. Commun. Networking*, vol. 36, no. 6, pp. 528-541, 2018.
- **L. Quibus**, L. Luni, C. Riva, D. Vanhoenacker-Janvier. "Use and Accuracy of Numerical Weather Predictions to Support EM Wave Propagation Experiments," *IEEE TAP*, vol. 67, no. 8, pp. 5544-5554, 2019.
- S. Ventouras, A. Martellucci, R. Reeves, E. Rumi, F. Perez-Fontan, F. Machado, V. Pastoriza, A. Rocha, S. Mota, F. Jorge, A.D. Panagopoulos, A.Z. Papafragkakis, C.I. Kourogiorgas, O. Fiser, V. Pek, P. Pesice, M. Grabner, A. Vilhar, A. Kelmendi, A. Hrovat, D. Vanhoenacker-Janvier, **L. Quibus**, G. Goussetis, A. Costouri, J. Nessel. "Assessment of spatial and temporal properties of Ka/Q band earth-space radio channel across Europe using ALPHASAT Aldo Paraboni payload," *Int. J. Satell. Commun. Networking*, vol. 37, no. 5, pp. 477-501, 2019.

Articles in conferences' proceedings

- D. Vanhoenacker-Janvier, **L. Quibus**, M. Rytir, T. Tjelta. "Measurement and modelling of tropospheric scintillation in Ka/Q band," *11th Eur. Conf. Antennas Propag. (EuCAP)*, Paris, FR, 19-24 Mar. 2017.
- S. Ventouras, R. Reeves, E. Rumi, F. Perez-Fontan, F. Machado, V. Pastoriza, A. Rocha, S. Mota, F. Jorge, A.D. Panagopoulos, A.Z. Papafragkakis, C.I. Kourogiorgas, O. Fiser, V. Pek, P. Pesice, M. Grabner, A. Vilhar, A. Kelmendi, A. Hrovat, D. Vanhoenacker-Janvier, A. Graziani, **L. Quibus**, G. Goussetis. "Large scale assessment of Ka/Q band atmospheric channel across Europe with ALPHASAT TDP5: The augmented network," *11th Eur. Conf. Antennas Propag. (EuCAP)*, Paris, FR, 19-24 Mar. 2017.
- **L. Quibus**, L. Luini, C. Riva, D. Vanhoenacker-Janvier. "Numerical Weather Prediction Models for the Estimate of Clear-Sky Attenuation Level in Alphasat Beacon Measurement," *12th Eur. Conf. Antennas Propag. (EuCAP)*, London, UK, 9-13 Apr. 2018.
- L. Luini, C. Riva, **L. Quibus**, D. Vanhoenacker-Janvier, G.A. Siles, J.M. Riera. "Water Vapor Retrieval to Support Electromagnetic Wave Propagation Experiments: Results from Different Techniques," *13th Eur. Conf. Antennas Propag. (EuCAP)*, Kraków, PL, 31 Mar.-5 Apr. 2019.

- M. Razavian, **L. Quibus**, D. Vanhoenacker-Janvier. "Using Numerical Weather Predictions to Compare the LEO Attenuation Statistics Computed from Fixed-Elevation Statistics and from LEO time series," *Ka and Broadband Communications Conf.*, Sorrento, IT, 30 Sep.-2 Oct. 2019.

Abstracts in conferences' proceedings

- M. Lukach, **L. Quibus**, D. Vanhoenacker-Janvier, L. Delobbe. "Rain attenuation statistics at Ka-band estimated from weather radar observations in Belgium," *10th Eur. Conf. Radar in Meteorology and Hydrology (ERAD)*, Ede, NE, 1-6 Jul. 2018.
- G. Rakshit, **L. Quibus**, D. Vanhoenacker-Janvier, A. Maitra. "Using meteorological data for clear sky and cloud attenuation in Belgium and India," *URSI AP-RASC*, New Delhi, IN, 9-15 Mar. 2019.

Articles in workshops' proceedings

- R. Lasagni Manghi, G. Maschwitz, P. Tortora, T. Rose, A. Martellucci, J. de Vicente, J. Villavilla, M. Mercolino, A. Graziani, H. Czekala, E. Orlandi, D. Vanhoenacker-Janvier, **L. Quibus**. "Tropospheric Delay Calibration System (TDCS): design and performances of a new generation of micro-wave radiometers for ESA deep space ground stations," *8th ESA Int. Workshop Tracking, Telemetry and Command Systems for Space (TTC)*, Darmstadt, DE, 24-27 Sep. 2019.
- A. Ardito, R. Abellò, A. Aroumont, M. Baldi, F. Barbaglio, F. Chiaraluce, G. Comoretto, S. Finnocchiaro, A. Graziani, P. Maguire, S. Marti, N. Maturo, M. Mercolino, **L. Quibus**, D. Vanhoenacker-Janvier. "Offline Correlator for Antenna Array Over Long Baselines," *8th ESA Int. Workshop Tracking, Telemetry and Command Systems for Space (TTC)*, Darmstadt, DE, 24-27 Sep. 2019.

Abstract in workshops' proceedings

- M. Razavian, **L. Quibus**, Danielle Vanhoenacker-Janvier. "Roadmap to model LEO links attenuation by integrating Numerical Weather Predictions, ST-MultiEXCELL, and traffic radar data," *28th URSI Benelux Forum*, Brussels, BE, 3 Dec. 2019.

List of acronyms

ACM	Advanced Coding and Modulation
ACTS	Advanced Communication Technology Satellite
AER	Azimuth-Elevation-Range
ALADIN	Aire Limitée Adaptation dynamique Développement International
ALARO	ALADIN-AROME
APSK	Amplitude and Phase-Shift Keying
AROME	Application of Research to Operations at Mesoscale
ARPEGE	Action de Recherche Petite Echelle Grande Echelle
ARW	Advanced Research WRF
ASALASCA	Large Scale Assessement of Ka/Q band atmospheric channel using the Alphasat TDP5 propagation beacon
ASAPE	Alphasat Aldo Paraboni propagation Experimenters
ASI	Agenzia Spaziale Italiana
ATS	Applications Technology Satellite
DVB	Digital Video Broadcasting
CCDF	Complementary Cumulative Distribution Function
CFL	Courant–Friedrichs–Lewy
CNRM	Centre National de Recherches Météorologiques
CTS	Communication Technology Satellite
ECEF	Earth Centered Earth Fixed
ECMWF	European Centre for Medium Range Weather Forecasts
EGM	Earth Gravitational Model
ENU	East-North-Up
EODDL	Earth Orbit Data Download
ETS	Engineering Test Satellite
ERA5	ECMWF 5th re-analysis
ERA-15	ECMWF 15 years re-analysis
ERA-40	ECMWF 40 years re-analysis
ERA-Interim	ECMWF interim re-analysis
ESA	European Space Agency
FFI	Forsvarets forskninginstitutt (Norwegian Defence Research Establishment)
FMT	Fade Mitigation Technique
F.R.S.-FNRS	Fonds de la Recherche Scientifique - Fonds National de la Recherche Scientifique
GEO	Geosynchronous Equatorial Orbit or Geostationary Orbit
GFS	Global Forecast System
GLONASS	Global Navigation Satellite System
GMST	Greenwich Mean Sidereal Time
GNSS	Global Navigation Satellite System
GPS	Global Positioning System

GSO	Geosynchronous Orbit
IFS	Integrated Forecast System
INCA	Integrated Nowcasting Comprehensive Analysis
ISCCP	International Satellite Cloud Climatology Project
ITU	International Telecommunication Union
ITU-R	ITU Radiocommunication sector
IWV	Integrated Water Vapour
LCC	Lambert Conformal Conic
LEO	Low Earth Orbit
LLA	Latitude Longitude Altitude
MAE	Mean Absolute Error
ME	Mean Error
MEO	Medium Earth Orbit
METOP	Meteorological Operational Satellite
METOP-SG	Meteorological Operational Satellite - Second Generation
MM5	5th generation Mesoscale Model
MWR	Microwave Radiometer
NCAR	National Center for Atmospheric Research
NEWPORT	Numerical Weather Prediction models and Weather radar for the Prediction of LEO-earth Radiowave Transmissions
NWP	Numerical Weather Prediction
ONERA	Office National d'Etudes et de Recherches Aérospatiales
OTS	Orbital Test Satellite
PBL	Planetary Boundary Layer
PDE	Partial Differential Equation
PEARP	Prévision d'Ensemble ARPEGE
PEF	Pseudo Earth Fixed
PoLiMi	Politecnico di Milano
PSD	Power Spectral Density
PSK	Phase-Shift Keying
QoS	Quality of Service
RAOBS	Radio-soundings observations
RMIB	Royal Meteorological Institute of Belgium
RMSE	Root Mean Square Error
ROCSAT	Republic of China Satellite
RRTM	Rapid Radiative Transfer Model
SG	Study Group
SGP4	Simplified General Perturbations 4
SNR	Signal-to-Noise Ratio
TDP	Technology Demonstration Payload
TEME	True Equator Mean Equinox
TLEs	Two Line Elements
UM	(UK Met Office) Unified Model
WGS	World Geodetic System
WPS	WRF Pre-processing System
WRF	Weather Research and Forecasting

Chapter 1

Introduction

At the beginning of the 21st century, there are few engineering trends more prominent than the rapid development of information and communication technologies. More precisely, there appears to be a nigh-on unquenchable thirst for the communication of more and more data, higher volumes and at higher rates. One way to transfer data is through the Earth atmosphere, and sometimes this is the sole option. Satellite communications operate thus via links between stations at the surface of the Earth and Earth orbiting satellites. Those Earth-space links are realised by electromagnetic waves with a nearly line-of-sight propagation. There are downsides such as an intrinsic loss of power as the waves spread over large distances, or the latency associated with these distances. But the Earth-space configuration offers important advantages in coverage and/or as a complement to the ground networks (e.g. optical fibers). Also, in the specific case of Earth observation or similar services, the data collected by the satellites on-board instruments must be sent down for processing at the surface.

As the demand for satellite communications increases, the usual part of the electromagnetic spectrum reserved for them, in the bands from C (e.g. 4/6 GHz) to Ku (e.g. 12/14 GHz) [1], becomes crowded with users. To still be able to allocate spectral space for all applications, and not risk interferences, a move to higher frequencies (> 20 GHz) is clearly desirable. Higher frequencies increase the bandwidth, the antenna gain and directivity [2], however they present their own challenges affecting the design of the communication systems. One of these issues are the overall stronger impairments to the propagation of the waves in the atmosphere. Importantly, the waves are more strongly attenuated, i.e. they lose more power, an effect which is largely dominated by rain when it occurs. For the communicated symbols to be interpreted correctly, it is necessary to maintain a sufficiently high signal-to-noise ratio (SNR). But, during strong fades, it becomes prohibitively expensive or infeasible to do so by a constant margin of the amplifier at the transmitter. A series of Fade Mitigation Techniques (FMTs) have been proposed, and some of them are [3]:

- power control, the dynamic adaptation of the transmitted power.
- site diversity, the dynamic redirection of the communication on a ground terminal not (or less) affected by the fade.
- satellite diversity, the dynamic rerouting to another satellite visible in a part of the sky less affected by the fade.
- frequency diversity, the dynamic fallback on another (lower) frequency band less affected by the fade.

- Advanced Coding and Modulations (ACMs), the dynamic modification of the scheme for data encoding to correspond to the SNR conditions, with more robust and error-tolerant encodings selected in case of a fade. The coding rate, i.e. the proportion of useful (non-redundant) bits over the total number of bits, is adapted to predetermined values over a frame, i.e. a message of a given length. But first, a switch in modulation of the signal, usually Phase-Shift Keying (PSK) or Amplitude and Phase-Shift Keying (APSK), determines the number of encoded bits per transmitted symbol. Together they modify the spectral efficiency (in bits/s/Hz). ACMs are an integral part of the Digital Video Broadcasting (DVB) standards [4].

In consequence, to design telecommunication systems with a high throughput and Quality of Service (QoS), there is a strong interest for ways to model the Earth-space propagation impairments and their dynamics beforehand.

This thesis explores the usage of Numerical Weather Predictions (NWPs) for the sake of modelling the propagation impairments on Earth-space radio-links at and above 20 GHz. To explain the utility of NWPs for this purpose, the remainder of this introduction continues with a list of the main Earth-space propagation impairments (see Sec. 1.1), and it contextualises the characterisation efforts conducted on them (see Sec. 1.2). The concept behind NWPs is presented succinctly (see Sec. 1.3). Then, a review of their usage for propagation modelling helps picture where the present work stands with respect to the state-of-the-art (see Sec. 1.4). The introduction ends with an outline of the document (see Sec. 1.5).

1.1 Earth-space propagation impairments

The principal effect of the atmosphere on an Earth-space link is the attenuation of the received power. The main contributors to this phenomenon are [5, 6]:

- the attenuation due to gases, mostly from oxygen and water vapour.
- the attenuation due to clouds, mostly from liquid water droplets.
- the attenuation due to hydrometeors, mostly from raindrops.
- the amplitude scintillation, a fast positive or negative variation of the received power, due to the turbulent motion of the air across the path.

In addition there are impairments affecting other characteristics of the signal such as the angle of arrival (refraction and multipath), phase (phase scintillation), coherence (dispersion and antenna gain degradation), polarisation (depolarisation by rain drops or ice crystals), or signal-to-noise ratio (thermal noise). The weather conditions on the, generally, outdoor ground antenna may also be of concern (wet antenna effect, vibrations of the antenna due to the wind).

As the fundamental origins of the impairments are reasonably well identified and understood, it appears that an accurate knowledge of the atmospheric conditions over time would be ideal for their modelling.

Satellite	f [GHz]	Launch	Long.	Region	Ref.
ATS 5	15.3, 31.65	1969	105°W	NA	[7]
CTS	11.7, 27	1976	116°W	NA	[8]
COMSTAR 1	19.04, 28.56	1976	128°W	NA	[8, 9]
COMSTAR 2	19.04, 28.56	1976	95°W	NA	[8, 9]
COMSTAR 3	19.04, 28.56	1978	87°W	NA	[8, 9]
ETS 2	11.5, 34.5	1977	130°E	JP	[10, 11]
SIRIO-A	11.6, 17.8	1977	15°W	NA, EU	[12]
OTS 2	11, 14	1978	10°E	EU	[13]
Olympus 1	12, 20, 30	1989	19°W	NA, EU	[14]
ITALSAT 1	18.7, 39.6, 49.5	1991	13°E	EU	[15]
ITALSAT 2	18.7, 39.6, 49.5	1996	13°E	EU	[15, 16]
ACTS	20.2, 27.5	1993	100°W	NA	[17]
UFO 9	20.7	1998	23°W	NA, EU	[18]
ROCSAT-1	19.5	1999	/	TW	[19]
Hotbird 6	19.7	2002	13°E	EU	[20, 21]
FedSat	20.1, 29.9	2002	/	AU	[22]
Anik F2	20.2	2004	111°W	NA	[20, 23]
Syracuse 3A	20.2	2005	47°E	MY	[24]
Astra 4A	19.3	2007	5°E	NO	[25]
Astra 3B	20.2	2010	23°E	FR	[21]
Ka-Sat	19.68	2010	9°E	EU	[25, 26]
Amazonas 3	20.2	2013	61°W	GF	[27]
Alphasat	19.7, 39.4	2013	25°E	EU	[28]
GSAT-14	20.2, 30.5	2014	74°E	IN	[29]
INMARSAT-5 F2	20.68	2015	55°W	NO	[25]
Thor 7	20.2	2015	1°E	NO	[26]

Table 1.1 – Examples of satellites used for propagation measurements at the frequencies f, including launch year, longitude specified for geosynchronous (GSO) orbits, region where measurements were collected (as continent or country codes), and some important references regarding those measurements

1.2 Earth-space propagation measurements

At the forefront of the task to model propagation impairments, there are the propagation experimental campaigns meant to serve as references. Typically, a small payload consisting of a beacon emitting an extremely narrowband signal at one frequency is sent onboard of an Earth-orbiting satellite. A network of ground stations may then receive the signal and extract the impairments.

Examples of satellites used for Earth-space propagation studies are given in Tab. 1.1. The most recent propagation measurements cover frequencies above Ku, approximatively in the bands 20-50 GHz. Aiming for even higher frequencies is therefore a goal for the future. The number of years of measurements, and the number of ground stations involved in the experiment, vary greatly between each campaign, with some of them shortened by a failure of the satellite. Another observation is that most of the measurements were obtained at mid-

latitudes, in North America, Europe or Japan, however new works are starting to increasingly consider other locations and climates, e.g. tropical regions in India and Malaysia, or the northernmost parts of Norway. Still there is an interest for a wider coverage as services develop rapidly all over the world. But the most remarkable fact is that almost all the experiments were conducted with geosynchronous (GSO) orbits. There is a quasi absence of published results for non-GSO satellites, with the exceptions of a few publications from ROCSAT-1 in Taiwan and the FedSat campaign in Australia [22].

There are still many challenges ahead and questions that propagation studies need to answer. Some of theses progresses are in march with, for example, a planned campaign with a Low Earth Orbit (LEO) cubesat carrying a W-band ($> 75\,\mathrm{GHz}$) beacon [30]. Nevertheless, the ultimate objective of Earth-space propagation experiments is to lead to an accurate model of the impairments on any Earth-space radio-link. Partly based on propagation measurements, a series of practical models are recommended by the International Telecommunication Union-Radiocommunication (ITU-R) [5]. It highlights the sort of alternative data involved in the modelling, and some of these data are NWPs.

1.3 Numerical Weather Predictions (NWPs)

Numerical Weather Predictions (NWPs) are simulations of the Earth atmosphere (global models), or part of it (regional models). The physical basis of NWPs is a set of partial differential equations (PDEs) describing the movement and thermodynamic state (pressure, temperature, humidity) of the moist air. Horizontally to the Earth surface, the resolution range from tens of kilometers for larger domains to sometimes below one kilometer for smaller ones. Vertically in altitude, there are usually tens of pressure-based levels, sometimes more than a hundred, which are separated by tens of meters near the ground and then by more than one kilometer higher-up. The practical constraints on the dimensions of the simulation domains mean that a lot of phenomenons cannot always be directly resolved by the PDEs, such as cloud, rain, turbulence, solar radiations, surface friction, soil layers, ... NWPs are therefore supplemented by parametrisations providing tendencies to the PDEs to account for e.g. the changes of state of water species, evaporation, condensation, freezing, accretion, precipitation, ... Temporally, the stability of the numerical integration of the PDEs imposes a minimal size of the timestep Δt_{NWP} from a few minutes down to a few seconds. However, largely due to the constraints in data storage, it is very rare for the results of an operational NWP model to be stored more often than with an output period T_{NWP} of one hour. Though it is in theory trivial to choose T_{NWP} as low as Δt_{NWP}, in conventional practice this means a model must be (re-)run with that specific purpose in mind.

Evidently, NWPs require initial and boundary conditions for their PDEs. The state of the atmosphere and its surface must be first reconstituted from available observations during a data assimilation process. The NWP model may then simply run from a point in time, providing a forecast, or be further adjusted variationally to observations, providing an analysis. The data assimilation usually operates at the global scale, and the results from the global

models can then serve as the starting point for regional models at a higher horizontal resolution. This procedure can add further nested regional domains downscaling the atmosphere to the desired resolution for some areas of interest.

The output of a NWP run typically include the following (or equivalent):

- pressure p [Pa], temperature T [K], humidity mixing ratio q_{vap} [kg/kg],
- cloud liquid water mixing ratio $q_{cloud,l}$ [kg/kg],
- rain mixing ratio q_{rain} [kg/kg], and/or ground rain rate R_{rain} [mm/h],
- eastward, northward, and vertical wind speeds u, v, and w [m/s].

These quantities enter readily into the models of some Earth-space propagation impairments, and more particularly the attenuation.

In comparison with individual observation datasets providing similar information, the strengths of NWPs are their universality and versatility. NWPs offer a worldwide view of the atmosphere, with an adjusted resolution anywhere needed. Of course, there are limitations to be expected in the accuracy of NWPs, such as poorer results due to fewer assimilated observations near a given location, or due to parametrisations ill-suited for certain climates. It is also well-known, by the layman as by the meteorologist, that weather forecasts are not to be trusted blindly and that they become progressively useless as they get too far ahead from the observations. The main reason for this famous issue is that, though the NWP PDEs are presumed to be deterministic, they are also very sensitive to the initial conditions, which cannot be known perfectly.

It must be noted however that a topic of increasing interest in NWP is the realisation of ensemble NWP runs. By running a NWP model several times with slightly perturbed initial conditions, one gets an ensemble (i.e. set) of results offering a probabilistic view of the atmospheric conditions, with mean trends, and probability to find a given feature in the ensemble. Another possibility to create an ensemble is to run a model with different physical parametrisations.

Taking their limitations into account, data from both NWPs analyses and forecasts have been incorporated into propagation models for various purposes.

1.4 Review of NWPs usage in propagation

An example of the usage of NWPs in propagation is found in the recommendation ITU-R P.835-6 on standard atmospheres [31]. A global map of average atmospheric profiles (pressure, temperature, humidity) at a resolution of 1.5° is extracted from the European Centre for Medium Range Weather Forecasts (ECMWF)'s ERA-15 dataset. For the modelling of e.g. the gaseous attenuation, it serves as a more comprehensive alternative to a mean annual global reference atmosphere, or to average profiles from long-term radio-soundings measurements for a limited number of stations.

Other usages of NWPs are found in the ITU-R recommendations and other related models, and from them a statistical view of certain propagation impairments is possible. This type of approach is well accepted and will continue

to benefit from the impressive improvements in the temporal and spatial resolutions of the global NWP models. This is especially true for the ECMWF models. However, more can be done with regional models, by reducing the resolutions even further, to the point where most propagation impairments could be modelled at the level of time series and/or statistically with enough samples (small output period T_{NWP}) to reach low probabilities of exceedance.

Hodges *et al.* [32–34] first proposed a NWP-based simulator of Earth-space propagation impairments time series using the UK Met Office Unified Model (UM) (12 km) and the 5$^{\text{th}}$ generation Mesoscale Model (MM5) (varying from 50 to 2 km, output as often as every 4 min). Their procedure produces time series of gases, cloud and rain attenuations, as well as scintillation variance, all of which are then further processed into first and second order statistics of the attenuation (fade and fade slope). Some of the reported results were very encouraging for the concept, with e.g. errors $< 6\%$ with respect to the ITU-R statistics from 3 months of data at 50 GHz for Bath (UK) [33], and examples of qualitatively well resolved events at 20.7 GHz for UFO-9 in Sparsholt (UK) [33, 34] and at 39.6 GHz for ITALSAT in Spino d'Adda (IT) [34]. The Earth-space links of interest remained however limited to GEO satellites at that time.

In the framework of an ESA contract, involving ONERA (FR), UCLouvain (BE), PoLiMi (IT), and Thales Alenia Space (IT), Jeannin and co-authors [35–38] developed another similar simulator capable to generate propagation impairments time series for LEO satellites as well. The simulator is built around the Weather Research and Forecasting (WRF) model, which can be considered as the successor of MM5. The physical basis for the conversion of the NWP data into simulated propagation impairments show some other innovations in comparison to the work of Hodges *et al.* Tab. 1.2 presents the main differences between the two simulators. Most notably, the method of Hodges *et al.* does not use directly the model output for the cloud and rain liquid water content in volume, but instead they are estimated from the atmospheric profiles and the ground rain rate respectively. Hodges *et al.* also use only surface properties to model the scintillation variance, whereas Jeannin *et al.* estimate it from the whole atmospheric profiles. Consequently, the approach by Hodges *et al.* remains closer to the ITU-R models, while the approach by Jeannin *et al.* attempts to make use of all the information provided by NWPs in volume. The WRF resolutions used with the method of Jeannin *et al.* are typically 2 km horizontally and 5 min in time [39]. Examples of results include a comparison of the total attenuation at 18.7 GHz from ITALSAT measurements at Spino d'Adda in 1996, for which an error < 5 dB is found at each reference probability level, in spite of a poor correlation ~ 0.2 of the time series [36]. Some later results with improved rain dropsize distribution [39] show even better statistical agreements with experimental data, an error < 2 dB, at 20.2 GHz for ASTRA-3B site diversity links in the South of France, for a one-year period mostly in 2014. Applications of the NWP-based propagation impairments simulator to FMTs are given in [40] for earth observation data downlink sizing with ACMs and in [41, 42] for smart gateways switching. Similar stategies for FMTs are considered over 2 years in the South of France from ensemble NWP runs [43, 44], using the Prévision d'Ensemble ARPEGE (PEARP) model (0.5°, 3 h), with an

	Jeannin *et al.*		Hodges *et al.*	
Effect	Model	Input	Model	Input
Gases	ITU-R P.676 [45]	p, T, q_{vap}	ITU-R P.676 [45]	p, T, q_{vap}
Cloud	ITU-R P.840 [46]	p, T, $q_{cloud,l}$	Salonen-Uppala [47], Rayleigh scattering	p, T, q_{vap}
Rain	Marshall-Palmer [48], Mie scattering [49]	p, T, q_{rain}	Leitao-Watson [50]	T, R_{rain}
Turbulence	Ishimaru [51]	p, T, q_{vap}	van de Kamp [52]	p, T, q_{vap}

Table 1.2 – Comparison of Hodges *et al.* and Jeannin *et al.* methods to retrieve propagation impairments time series from NWP data

ensemble of 35 members constructed using different parametrisations, and with a super-ensemble of 70 members created based on two different starting times.

There are other recent works simulating propagation impairments with NWPs. Cuervo *et al.* [53] studied the attenuation due to gases, cloud, and rain using the same principles as Hodges *et al.*. They used NWP data from the ECMWF (13 km, 1 h), ALARO (4.8 km, 1 h), and surface parameters from the Integrated Nowcasting Comprehensive Analysis (INCA) (1 km, 15 min) forecast models over six months in 2016. For the rain attenuation, Alphasat 39.402 GHz measurements in Graz are compared with simulations based on INCA and show a correlation ~ 0.53, but it is much lower than the correlation ~ 0.86 obtained by using the measurements assimilated into the NWPs instead. For the gaseous attenuation, tropospheric delay measurements in Madrid are compared with ECMWF-based simulations and high correlations and low errors, e.g. root mean square error of 0.04 dB at 39.402 GHz, are found.

Grythe *et al.* [54] used the AROME-MetCoOp model (2.5 km, 1 h) to forecast the Ka-Sat 19.68 GHz rain attenuation over three summer months in 2015 for Eggemoen, Nittedal, and Kjeller (NO). The prediction method is essentially the same as Hodges *et al.*, though both the rain rate on the ground and on pressure levels are tested. The hit rate stays within 65-75 % and the false alarm rate is around 25 %, except for Eggemoen where it reaches up to 50 %. The standard deviations are between 1 and 1.7 dB. Their results emphasize varying performances between the sites, but their authors consider them encouraging for the usage of NWP-based propagation forecasts.

Kourogiorgas *et al.* [55] compared 39.402 GHz Alphasat data from Chilton and Chilbolton (UK) to time series derived from the ECMWF operational forecast (10 km, 1 h) and ensemble prediction system with 50 members. The published results are limited to examples of a few days in 2017 and aim to explore the validity of NWP for medium- to long-term (hours, days) propagation impairments forecasts, in opposition to machine learning algorithms used for very short-term (seconds, minutes) forecasts.

Some very recent results by Marziani *et al.* [56] also concern NWP-based excess attenuation forecast, with a special interest in scintillation.

There are yet some other notable results indirectly related to the use of NWPs for propagation. For example, Memmo *et al.* [57] found good agreements between the integrated water vapour estimates obtained by the MM5 model (3 km, 1 h), microwave radiometer, GPS, and radiosonde measurements. These estimates are all potentially useful with distinct advantages and drawbacks for the purpose of calibrating propagation beacon measurements.

Many efforts were also dedicated to the simulation of Earth-space links for Deep-Space missions. Davarian *et al.* [58] designed a NWP-based link management system for the Mars Reconnaissance Orbiter. A large body of work by Biscarini and co-authors [59–69] consider the problems of optimal data transfer for missions such as BepiColombo, using NWP data generated with either MM5 or WRF into a radiative transfer model, and including validations with radiosondes, radiometers, sun-tracking radiometers. For example in [62] MM5 data (6 km, 1 h) are produced for the station in Cebreros (ES).

In summary, the following aspects remain as insufficiently studied in the state-of-the-art at the beginning and during the elaboration of this thesis:

1. few results involve long periods of one to multiple years.
2. few results combine both high horizontal and temporal resolutions.
3. the published works take one specific approach out of two to model the rain attenuation, and a similar situation occurs for the cloud attenuation.
4. most results are limited to GSO links.
5. the modelling of scintillation has not been validated extensively and it is questionable if the NWP resolutions and parametrisations are sufficient.
6. the capability of NWPs to forecast propagation impairments, and therefore to intervene dynamically into link management strategies and FMTs, remain by large at the proof of concept level.

1.5 Outline of the thesis and its contributions

The thesis has essentially two parts: one part devoted to the theory and the methods from Chap. 2 to Chap. 4, and one part presenting the results of their applications from Chap. 5 to Chap. 7. The outline of the thesis is as follows:

- Chap. 2 presents the foundations of the propagation of electromagnetic waves through the atmosphere. The exposition is limited to the models and algorithms most relevant for usage with NWP data and their comparison with measurements.
- Chap. 3 gives a broader overview of NWP models, in terms of simulation grids and solvers, parametrisation options, input and output data.
- Chap. 4 serves as a bridge between Chap. 2 and Chap. 3. It details the transformations, change of coordinates and interpolations, that must be applied to go from NWP grids to propagation grids. It then explains

the further dimensional reductions going from impairments known as 4D matrices to 1D time series or statistical distributions.

- Chap. 5 shows results from the NEWPORT F.R.S-FNRS. project and is meant as a validity check for NWP-derived attenuation components. There is a comparison at 19.701, 26, 39.402 and 75 GHz between the results from two NWP models, WRF and ALARO, run over similar domains around Louvain-la-Neuve (BE), and also a comparison with radar-derived rain attenuation at 20 GHz. The NWP comparison currently spawns 5 years, while the radar reference provided by the RMIB lasts 10 years. Both GEO and LEO configurations are investigated.

- Chap. 6 proposes another type of validation focused on the NWP-derived nonrainy attenuation components, with the goal to use them to complement measurements of the other impairments. Four months of Alphasat (19.701 and 39.402 GHz) propagation beacon and radiometric measurements at Spino d'Adda (IT) form the reference dataset for a comparison.

- Chap. 7 gathers examples of applications of the NWP-based methods:

  - Sec. 7.1 presents results produced for the ASALASCA ESA contract. Under the same principle as in Chap. 6, NWP-derived nonrainy attenuation is obtained over one year for 10 stations in Europe to support Alphasat experimenters with no radiometric equipment. It puts the methodology into perspective at a larger scale, though the comparison is not based on measurements but only on the ITU-R references statistics for the gases and clouds.
  - Sec. 7.2 shows further simulations of LEO links at 19.701, 39.402 and 75 GHz for Graz (AT), of note in its quality of Alphasat receiving station and participant in a future W band propagation experiment.
  - Sec. 7.3 is a brief illustration on the question of amplitude scintillation, by looking at some NWP-derived profiles of the refractive index structure constant and Ka-Sat (19.68 GHz) low-elevation scintillation measurements at Isfjord radio (NO).

- Chap. 8 concludes with a summary of the work and reflects on what has been accomplished, what has been learned, what are the potential future uses for the studied methods based on the observed results, and also what would be particularly worth investigating further.

Chapter 2

Electromagnetic properties of the atmosphere

This chapter goes through the electromagnetic bases behind the modelling of the propagation impairments encountered by Earth-space links when they cross the atmosphere. The scope is limited to effects relevant to radio-frequencies at and above K band, and to the models and algorithms useful with NWP data. In a first time, it is explained why, assuming a plane wave propagation, the atmospheric complex refractive index must be described (see Sec. 2.1) as a function of the atmospheric constituents. Secondly, the principal contributors to the imaginary part of the refractive index, corresponding to the losses or attenuation, are detailed: the atmospheric gases (see Sec. 2.2), the clouds and rain (see Sec. 2.3). Thirdly, the phenomenon of scintillation, fade or enhancement of the signal due to the turbulent air movement, is also introduced (see Sec. 2.4). Finally, it is discussed how a variety of measurements relate to the atmospheric propagation impairments, and how those measurements may be compared with simulations, or may benefit from them: propagation beacons (see Sec. 2.5), microwave radiometers (see Sec. 2.6), and others (see Sec. 2.7).

2.1 Atmospheric refractive index

The atmosphere as a medium for the propagation of electromagnetic waves interacts with them principally as a function of their frequencies on the one hand, and as a function of its thermodynamic state (pressure and temperature) and the presence of water species (humidity, hydrometeors) on the other hand. For Earth-space links, considering the large distances between the transmitter and the receiver, the signal is a plane wave and must be modelled accordingly.

2.1.1 Plane wave propagation through the atmosphere

A plane electromagnetic wave propagating in the direction z at the time t is described by its electric field $\mathbf{E}$ in the plane (x, y) perpendicular to z, with a variation with respect to electric field at the source $\mathbf{E}_0$ such that

$$\begin{aligned} \mathbf{E} &= \mathbf{E}_0 \exp\left(-j(kz - 2\pi f t)\right) \\ &= \mathbf{E}_0 \exp\left(-j\left(\frac{2\pi f}{c_0} n z - 2\pi f t\right)\right) \end{aligned} \tag{2.1}$$

where the wavenumber k is replaced by the frequency f and the refractive index n, and with $c_0 = 299\,792\,458\,\mathrm{m\,s^{-1}}$ the speed of light in vacuum.

In generality, the refractive index is a complex number such as

$$n(f) = n_0 + n'(f) - jn''(f) \tag{2.2}$$

with n_0 the frequency independent (non-dispersive) real component, n' the dispersive real component, and n'' the dispersive imaginary component. Using (2.2), (2.1) is rewritten as follows

$$\mathbf{E} = \mathbf{E}_0 \exp\left(-j\left(\frac{2\pi f}{c_0}(n_0 + n'(f))z - 2\pi f t\right)\right) \exp\left(\left(-\frac{2\pi f}{c_0} n''(f) z\right)\right) \tag{2.3}$$

where it is apparent that to get $\mathbf{E}$ the field at the source $\mathbf{E}_0$ is being multiplied by a complex exponential but also by a decreasing real one (if $n'' > 0$).

2.1.2 Atmospheric refractivity

Because the air has a refractive index $n \approx 1$, it is useful to introduce the refractivity N [ppm] [70] such as

$$n = 1 + N \times 10^{-6} \tag{2.4}$$

and then, as in (2.2),

$$N(f) = N_0 + N'(f) - jN''(f) \tag{2.5}$$

with terms corresponding to the equivalent refractive index components.

For microwaves, the non-dispersive term N_0 for moist air is [70]

$$\begin{aligned} N_0 &= 77.6\frac{p_{dry}}{T} + 72\frac{p_{vap}}{T} + 3.75 \times 10^5 \frac{p_{vap}}{T^2} \\ &= 77.6\frac{p}{T} - 5.6\frac{p_{vap}}{T} + 3.75 \times 10^5 \frac{p_{vap}}{T^2} \\ &\approx \frac{77.6}{T}\left(p + 4810\frac{p_{vap}}{T}\right) \end{aligned} \tag{2.6}$$

where T [K] is the temperature and

$$p = p_{dry} + p_{vap} \tag{2.7}$$

with p [hPa] the pressure, p_{dry} [hPa] the dry air pressure, and p_{vap} [hPa] the water vapour partial pressure. The format of (2.6) derives from Debye theory, whereas the values of the coefficients were obtained by considering the typical composition of the atmosphere and experimental results [71]. The contribution of the air to $N'(f)$ is essentially zero, and generally $N_0 >> N'(f)$, i.e. the real part of the air refractivity is, in good approximation, frequency independent. Note that the latter does not remain true at optical frequencies however.

The imaginary part of the dispersive term $N''(f)$ comes from the absorption and/or scattering by the various atmospheric constituents. It is the cause of the main impairment studied in electromagnetic propagation and in the present thesis: the atmospheric attenuation.

2.1.3 Atmospheric attenuation

Considering the propagation of a plane wave as in (2.3), the relative power loss A [dB] (> 0), i.e. the attenuation, over the distance z is given by

$$\begin{aligned} A(f) &= -10\log_{10}\left(\frac{|\mathbf{E}|}{|\mathbf{E}_0|}\right)^2 \\ &= -20\log_{10}\left(\exp\left(-\frac{2\pi f}{c_0}n''(f)z\right)\right) \\ &= \frac{20}{\ln 10}\frac{2\pi}{c_0}fn''(f)z \\ &= \frac{20}{\ln 10}\frac{2\pi}{c_0}f(\text{GHz})\times 10^9 N''(f)\times 10^{-6}z(\text{km})\times 10^3 \\ &\approx 0.182f(\text{GHz})N''(f)z(\text{km}) \end{aligned} \tag{2.8}$$

and from it the specific attenuation γ [dB km^{-1}] is defined as

$$A(f) = \gamma(f)z(\text{km}) \tag{2.9}$$

hence

$$\gamma(f) = 0.182f(\text{GHz})N''(f). \tag{2.10}$$

In practice $N''(f)$, and so $\gamma(f)$, vary along the propagation path of the wave and instead of (2.9) one has rather

$$A(f) = \int_0^S \gamma(f,s)ds \tag{2.11}$$

where s [km] is the slant path coordinate and S [km] the length of the path.

Because, depending on the atmospheric conditions, there are different effects contributing to $N''(f)$, there are also different sources of $\gamma(f)$. In the modelling, it is generally assumed that the contributions are independent and additive. The sum of the individual attenuation components is the total attenuation A_{tot}.

2.2 Attenuation due to atmospheric gases

A first part of the atmospheric attenuation is the one due to the atmospheric gases themselves. This contribution is driven principally by the absorption modes of the molecules present in the air. As for the real refractivity in (2.6), there is a contribution from the dry air, mostly from oxygen, and a contribution from the water vapour. These contributions stay comparatively smaller than those from water in liquid phase, but unlike the latter they are always present. This situation makes gaseous absorption worth studying, also when considering the general increase of attenuation with frequency in (2.10), or the presence of strong absorption peaks in some bands.

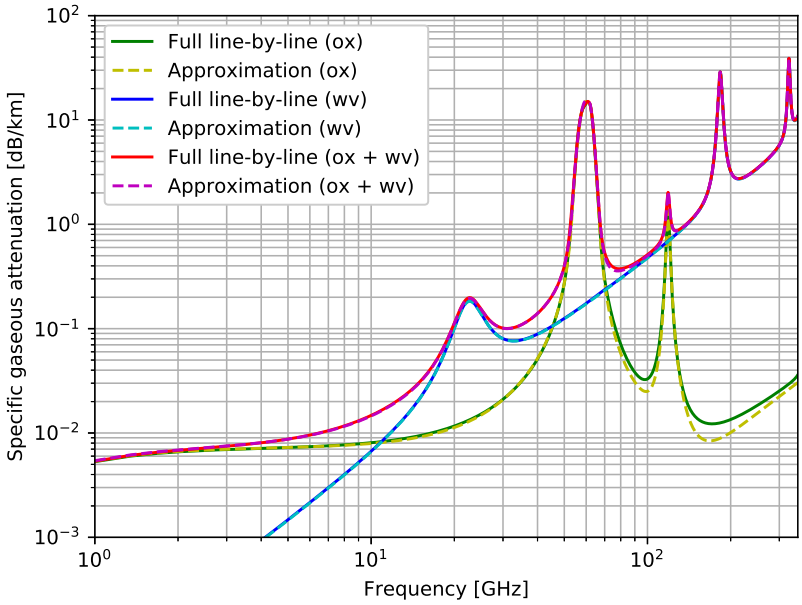

Figure 2.1 – Specific gaseous attenuation between 1 GHz and 350 GHz for $T = 15\,°\text{C}$, $p = 1013.15\,\text{hPa}$ and $\rho_{vap} = 7.5\,\text{g/m}^3$ (based on [45])

2.2.1 Oxygen and water vapour absorption spectra

The modelling of gaseous attenuation takes the form of a summation over all the absorption lines relevant to the radio-waves. An implementation of this approach is suggested in the recommendation ITU-R P.676-11 [45] (see Sec. 2.2.2). Performing that computation gets rather expensive however, and some of the lines or factors of the model may be omitted at a generally inconsequential loss of accuracy. Previously, another approximative method was proposed by the recommendation ITU-R P.676-10 [72] (see Sec. 2.2.3). This algorithm is presented here because it is the one in use for the results of this thesis. The acceleration with respect to the full method is appreciable and roughly ~ 10.

As is observed from Fig. 2.1, these two methods described hereinafter produce nearly identical gaseous absorption spectra, with the only noticeable differences found for oxygen above 100 GHz, which are anyway easily dwarfed by the water vapour contribution at this frequency.

When looking at the frequencies of interest for this work, there are two other particularly remarkable features in Fig. 2.1:

- a water vapour absorption peak centred at 22.2 GHz,
- an oxygen absorption peak around 60 GHz.

2.2.2 Specific gaseous attenuation line-by-line method

According to [45], and largely based on [73] the specific attenuation due to the atmospheric gases γ_{gases} is the sum of the specific attenuation due to oxygen (i.e. dry air) γ_{ox} and the specific attenuation due to water vapour γ_{wv} as in

$$\gamma_{gases} = \gamma_{ox} + \gamma_{wv} = 0.182 f \left(N''_{ox}(f) + N''_{wv}(f) \right) \tag{2.12}$$

where the refractivity components N''_{ox} and N''_{wv} are given by

$$N''_{ox}(f) = \sum_i S_{ox,i} F_{ox,i}(f) + N''_D(f) \tag{2.13}$$

$$N''_{wv}(f) = \sum_i S_{wv,i} F_{wv,i}(f) \tag{2.14}$$

which are summation expressions involving the strengths of the absorption lines $S_{ox,i}$ and $S_{wv,i}$, their shape factors $F_{ox,i}$ and $F_{wv,i}$, and the Debye contribution N''_D of the non-resonant oxygen spectrum which is also made to include the pressure-induced nitrogen absorption (relevant only above 100 GHz).

The frequencies $f_{ox,i}$ and $f_{wv,i}$ for each line of index i, and the modelling coefficients $a_{j,i}$ and $b_{j,i}$ for $j \in \{1, \ldots, 6\}$ used below, are given by Tab. 2.1 on p. 19 and Tab. 2.2 on p. 20 for oxygen and water vapour respectively.

The strengths of the absorption lines have the forms

$$S_{ox,i} = a_{1,i} \times 10^{-7} p_{dry} \theta_T^3 \exp(a_{2,i}(1 - \theta_T)) \tag{2.15}$$

$$S_{wv,i} = b_{1,i} \times 10^{-1} p_{vap} \theta_T^{3.5} \exp(b_{2,i}(1 - \theta_T)) \tag{2.16}$$

with the dry pressure p_{dry} [hPa], the water vapour pressure p_{vap} [hPa], the function $\theta_T = 300/T$ of the temperature T [K].

The shape factors of the absorption lines are modified Van Vleck-Weisskopf functions [73, 74] such as

$$F_{ox,i}(f) = \frac{f}{f_{ox,i}} \left(\frac{\Delta f_{ox,i} - \delta_{ox,i}(f_{ox,i} - f)}{(f_{ox,i} - f)^2 + \Delta f_{ox,i}^2} + \frac{\Delta f_{ox,i} - \delta_{ox,i}(f_{ox,i} + f)}{(f_{ox,i} + f)^2 + \Delta f_{ox,i}^2} \right) \tag{2.17}$$

$$F_{wv,i}(f) = \frac{f}{f_{wv,i}} \left(\frac{\Delta f_{wv,i}}{(f_{wv,i} - f)^2 + \Delta f_{wv,i}^2} + \frac{\Delta f_{wv,i}}{(f_{wv,i} + f)^2 + \Delta f_{wv,i}^2} \right) \tag{2.18}$$

where $\Delta f_{ox,i}$ and $\Delta f_{wv,i}$ are obtained at first from the expressions

$$\tilde{\Delta} f_{ox,i} = a_{3,i} \times 10^{-4} \left(p_{dry} \theta_T^{(0.8 - a_{4,i})} + 1.1 p_{vap} \theta_T \right) \tag{2.19}$$

$$\tilde{\Delta} f_{wv,i} = b_{3,i} \times 10^{-4} \left(p_{dry} \theta_T^{b_{4,i}} + b_{5,i} p_{vap} \theta_T^{b_{6,i}} \right) \tag{2.20}$$

which are then modified to include the Zeeman splitting of oxygen lines and the Doppler broadening of water vapour lines

$$\Delta f_{ox,i} = \sqrt{\tilde{\Delta} f_{ox,i}^2 + 2.25 \times 10^{-6}} \tag{2.21}$$

$$\Delta f_{wv,i} = 0.535\tilde{\Delta} f_{wv,i} + \sqrt{0.217\tilde{\Delta} f_{wv,i}^2 + \frac{2.1316 \times 10^{-12} f_{wv,i}^2}{\theta_T}} \tag{2.22}$$

and where finally $\delta_{ox,i}$ are correction factors for the interference in oxygen lines

$$\delta_{ox,i} = (a_{5,i} + a_{6,i}\theta_T) \times 10^{-4} p \theta_T^{0.8} \tag{2.23}$$

the latter which were introduced by Rosenkranz [73].

The Debye contribution for dry air is

$$N_D''(f) = f p_{dry} \theta_T^2 \left(\frac{6.14 \times 10^{-5}}{d_D \left(1 + (f/d_D)^2\right)} + \frac{1.4 \times 10^{-12} p_{dry} \theta_T^{1.5}}{1 + 1.9 \times 10^{-5} f^{1.5}} \right) \tag{2.24}$$

$$d_D = 5.6 \times 10^{-4} p \theta_T^{0.8} \tag{2.25}$$

with d_D the relaxation frequency.

The full procedure above, ITU-R P.676-11 Annex 1, is valid for the whole atmosphere and up to 1000 GHz. The ITU-R P.676-11 Annex 2 suggests some simplifications which are acceptable below 10 km and up to 350 GHz [45]:

- to limit the summation in (2.14) to the water vapour absorption lines marked by an asterisk in Tab. 2.2.
- to assume $\Delta f_{ox,i} = \tilde{\Delta} f_{ox,i}$ and $\Delta f_{wv,i} = \tilde{\Delta} f_{wv,i}$, i.e. to neglect the Zeeman splitting and Doppler broadening and disregard (2.21) and (2.22).

2.2.3 Specific gaseous attenuation approximation

An older approximation of the line-by-line gaseous attenuation model exists in ITU-R P.676-10 [72]. As was stated, this is the method chosen for the computations of gaseous attenuation presented in this thesis. The model has a lot of parameters but uses fewer functions fitting the absorption peaks.

The quantities $r_p = p/1013$ and $r_t = 288/(t + 273)$ are introduced, from p [hPa] the total pressure and t [°C] the temperature.

For oxygen and for $f \leq 54$ GHz

$$\gamma_{ox} = \left(\frac{7.2 r_t^{2.8}}{f^2 + 0.34 r_p^2 r_t^{1.6}} + \frac{0.62 \xi_3}{(54 - f)^{1.16\xi_1} + 0.83\xi_2} \right) f^2 r_p^2 \times 10^{-3}, \tag{2.26}$$

for $54\,\text{GHz} < f \leq 60\,\text{GHz}$

$$\gamma_{ox} = \exp\left(\frac{\ln \gamma_{54}}{24}(f - 58)(f - 60) - \frac{\gamma_{58}}{8}(f - 54)(f - 60) + \right. \\ \left. + \frac{\ln \gamma_{60}}{12}(f - 54)(f - 58) \right), \tag{2.27}$$

for $60\,\text{GHz} < f \leq 62\,\text{GHz}$

$$\gamma_{ox} = \gamma_{60} + (\gamma_{62} - \gamma_{60}) \frac{f - 60}{2}, \tag{2.28}$$

for $62\,\mathrm{GHz} < f \leq 66\,\mathrm{GHz}$

$$\gamma_{ox} = \exp\left(\frac{\ln\gamma_{62}}{8}(f-64)(f-66) - \frac{\gamma_{64}}{4}(f-62)(f-66) + \right. \\ \left. + \frac{\ln\gamma_{66}}{8}(f-62)(f-64)\right), \tag{2.29}$$

for $66\,\mathrm{GHz} < f \leq 120\,\mathrm{GHz}$

$$\gamma_{ox} = \left(3.02\times10^{-4}r_t^{3.5} + \frac{0.283r_t^{3.8}}{(f-118.75)^2+2.91r_p^2r_t^{1.6}} + \right. \\ \left. + \frac{0.502\xi_6(1-0.0163\xi_7(f-66))}{(f-66)^{1.4346\xi_4}+1.15\xi_5}\right) f^2r_p^2\times10^{-3}, \tag{2.30}$$

for $120\,\mathrm{GHz} < f \leq 350\,\mathrm{GHz}$

$$\gamma_{ox} = \left(\frac{3.02\times10^{-4}}{1+1.9\times10^{-5}f^{1.5}} + \right. \\ \left. + \frac{0.283r_t^{0.3}}{(f-118.75)^2+2.91r_p^2r_t^{1.6}}\right) f^2r_p^2r_t^{3.5}\times10^{-3} + \delta, \tag{2.31}$$

with the following quantities being defined

$$\varphi(r_p, r_t, a, b, c, d) = r_p^a r_t^b \exp(c(1-r_p+d(1-r_t)) \tag{2.32}$$

$$\xi_1 = \varphi(r_p, r_t, 0.0717, -1.8132, 0.0156, -1.6515) \tag{2.33}$$

$$\xi_2 = \varphi(r_p, r_t, 0.5146, -4.6368, -0.1921, -5.7416) \tag{2.34}$$

$$\xi_3 = \varphi(r_p, r_t, 0.3414, -6.5851, 0.2130, -8.5854) \tag{2.35}$$

$$\xi_4 = \varphi(r_p, r_t, -0.0112, 0.0092, -0.1033, -0.0009) \tag{2.36}$$

$$\xi_5 = \varphi(r_p, r_t, 0.2705, -2.7192, -0.3016, -4.1033) \tag{2.37}$$

$$\xi_6 = \varphi(r_p, r_t, 0.2445, -5.9191, 0.0422, -8.0719) \tag{2.38}$$

$$\xi_7 = \varphi(r_p, r_t, -0.1833, 6.5589, -0.2402, 6.131) \tag{2.39}$$

$$\gamma_{54} = 2.192\varphi(r_p, r_t, 1.8286, -1.9487, 0.4051, -2.8509) \tag{2.40}$$

$$\gamma_{58} = 12.59\varphi(r_p, r_t, 1.0045, 3.5610, 0.1588, 1.2834) \tag{2.41}$$

$$\gamma_{60} = 15.0\varphi(r_p, r_t, 0.9003, 4.1335, 0.0427, 1.6088) \tag{2.42}$$

$$\gamma_{62} = 14.28\varphi(r_p, r_t, 0.9886, 3.4176, 0.1827, 1.3429) \tag{2.43}$$

$$\gamma_{64} = 6.819\varphi(r_p, r_t, 1.4320, 0.6258, 0.3177, -0.5914) \tag{2.44}$$

$$\gamma_{66} = 1.908\varphi(r_p, r_t, 2.0717, -4.1404, 0.4910, -4.8718) \tag{2.45}$$

$$\delta = -0.00306\varphi(r_p, r_t, 3.211, -14.94, 1.583, -16.37). \tag{2.46}$$

For water vapour

$$\begin{aligned}\gamma_{wv} = \Bigg(& \frac{3.98\eta_1 \exp(2.23(1-r_t))}{(f-22.235)^2+9.42\eta_1^2} g(f,22) + \frac{11.96\eta_1 \exp(0.7(1-r_t))}{(f-183.31)^2+11.14\eta_1^2} + \\ & + \frac{0.081\eta_1 \exp(6.44(1-r_t))}{(f-321.226)^2+6.29\eta_1^2} + \frac{3.66\eta_1 \exp(1.6(1-r_t))}{(f-325.153)^2+9.22\eta_1^2} + \\ & + \frac{25.37\eta_1 \exp(1.09(1-r_t))}{(f-390)^2} + \frac{17.4\eta_1 \exp(1.46(1-r_t))}{(f-448)^2} + \\ & + \frac{844.6\eta_1 \exp(0.17(1-r_t))}{(f-557)^2} g(f,557) + \\ & + \frac{290\eta_1 \exp(0.41(1-r_t))}{(f-752)^2} g(f,752) + \\ & + \frac{8.3328\times 10^{-4}\eta_2 \exp(0.99(1-r_t))}{(f-1780)^2} g(f,1780) \Bigg) f^2 r_t^{2.5} \rho \times 10^{-4}\end{aligned} \tag{2.47}$$

with the following quantities being defined

$$\eta_1 = 0.966 r_p r_t^{0.68} + 0.006\rho_{vap} \tag{2.48}$$

$$\eta_2 = 0.735 r_p r_t^{0.5} + 0.0353 r_t^4 \rho_{vap} \tag{2.49}$$

$$g(f, f_i) = 1 + \left(\frac{f - f_i}{f + f_i} \right)^2 \tag{2.50}$$

using the water vapour density ρ_{vap} [$\mathrm{g\,m^{-3}}$] instead of p_{vap} (see (3.37)).

2.2.4 Gaseous attenuation reference statistics

Using either the procedures in Sec. 2.2.2 or 2.2.3, the specific attenuation due to gases may be obtained at one point where (T, p, p_{vap}) (or equivalent) is known. The gaseous attenuation then comes from (2.11) by integrating along the path. To assess the quality of the gaseous attenuation obtained in this fashion from a certain dataset (in this work NWPs), it will be useful to have a reference at least at the statistical level. The ITU-R reference model for the gaseous attenuation CCDF is very briefly summarized here:

- a mean annual value for the oxygen attenuation is given by P.676-11 Annex 2 §2.2 [45] for the equivalent oxygen attenuation height model (and the approximative model described here at the end of Sec. 2.2.2, using P.1510-1 Annex 1 §1 [75] for the ERA-Interim mean surface temperature, and using the ERA15 mean profiles in P.835-6 Annex 3 §1 [31] to retrieve a mean surface pressure and a mean surface water vapour density,
- the water vapour attenuation CCDF (99 % to 0.1 %) is obtained from P.676-11 Annex 2 §2.3 [45] (and the approximative model described here at the end of Sec. 2.2.2), using P.836-6 Annex 2 §1 [76] for the integrated water vapour content maps,
- the gaseous attenuation CCDF (99 % to 0.1 %) is the sum of the above-mentioned mean oxygen attenuation and water vapour attenuation CCDF.

$f_{i,ox}$ [GHz]	$a_{1,i}$	$a_{2,i}$	$a_{3,i}$	$a_{4,i}$	$a_{5,i}$	$a_{6,i}$
50.474214	0.975	9.651	6.690	0	2.566	6.850
50.987745	2.529	8.653	7.170	0	2.246	6.800
51.503360	6.193	7.709	7.640	0	1.947	6.729
52.021429	14.320	6.819	8.110	0	1.667	6.640
52.542418	31.240	5.983	8.580	0	1.388	6.526
53.066934	64.290	5.201	9.060	0	1.349	6.206
53.595775	124.600	4.474	9.550	0	2.227	5.085
54.130025	227.300	3.800	9.960	0	3.170	3.750
54.671180	389.700	3.182	10.370	0	3.558	2.654
55.221384	627.100	2.618	10.890	0	2.560	2.952
55.783815	945.300	2.109	11.340	0	–1.172	6.135
56.264774	543.400	0.014	17.030	0	3.525	–0.978
56.363399	1331.800	1.654	11.890	0	–2.378	6.547
56.968211	1746.600	1.255	12.230	0	–3.545	6.451
57.612486	2120.100	0.910	12.620	0	–5.416	6.056
58.323877	2363.700	0.621	12.950	0	–1.932	0.436
58.446588	1442.100	0.083	14.910	0	6.768	–1.273
59.164204	2379.900	0.387	13.530	0	–6.561	2.309
59.590983	2090.700	0.207	14.080	0	6.957	–0.776
60.306056	2103.400	0.207	14.150	0	–6.395	0.699
60.434778	2438.000	0.386	13.390	0	6.342	–2.825
61.150562	2479.500	0.621	12.920	0	1.014	–0.584
61.800158	2275.900	0.910	12.630	0	5.014	–6.619
62.411220	1915.400	1.255	12.170	0	3.029	–6.759
62.486253	1503.000	0.083	15.130	0	–4.499	0.844
62.997984	1490.200	1.654	11.740	0	1.856	–6.675
63.568526	1078.000	2.108	11.340	0	0.658	–6.139
64.127775	728.700	2.617	10.880	0	–3.036	–2.895
64.678910	461.300	3.181	10.380	0	–3.968	–2.590
65.224078	274.000	3.800	9.960	0	–3.528	–3.680
65.764779	153.000	4.473	9.550	0	–2.548	–5.002
66.302096	80.400	5.200	9.060	0	–1.660	–6.091
66.836834	39.800	5.982	8.580	0	–1.680	–6.393
67.369601	18.560	6.818	8.110	0	–1.956	–6.475
67.900868	8.172	7.708	7.640	0	–2.216	–6.545
68.431006	3.397	8.652	7.170	0	–2.492	–6.600
68.960312	1.334	9.650	6.690	0	–2.773	–6.650
118.750334	940.300	0.010	16.640	0	–0.439	0.079
368.498246	67.400	0.048	16.400	0	0.000	0.000
424.763020	637.700	0.044	16.400	0	0.000	0.000
487.249273	237.400	0.049	16.000	0	0.000	0.000
715.392902	98.100	0.145	16.000	0	0.000	0.000
773.839490	572.300	0.141	16.200	0	0.000	0.000
834.145546	183.100	0.145	14.700	0	0.000	0.000

Table 2.1 – Oxygen absorption lines parameters

$f_{i,wv}$ [GHz]	$b_{1,i}$	$b_{2,i}$	$b_{3,i}$	$b_{4,i}$	$b_{5,i}$	$b_{6,i}$
*22.235080	0.1079	2.144	26.38	0.76	5.087	1.00
67.803960	0.0011	8.732	28.58	0.69	4.930	0.82
119.995940	0.0007	8.353	29.48	0.70	4.780	0.79
*183.310087	2.273	0.668	29.06	0.77	5.022	0.85
*321.225630	0.0470	6.179	24.04	0.67	4.398	0.54
*325.152888	1.514	1.541	28.23	0.64	4.893	0.74
336.227764	0.0010	9.825	26.93	0.69	4.740	0.61
*380.197353	11.67	1.048	28.11	0.54	5.063	0.89
390.134508	0.0045	7.347	21.52	0.63	4.810	0.55
437.346667	0.0632	5.048	18.45	0.60	4.230	0.48
439.150807	0.9098	3.595	20.07	0.63	4.483	0.52
443.018343	0.1920	5.048	15.55	0.60	5.083	0.50
*448.001085	10.41	1.405	25.64	0.66	5.028	0.67
470.888999	0.3254	3.597	21.34	0.66	4.506	0.65
474.689092	1.260	2.379	23.20	0.65	4.804	0.64
488.490108	0.2529	2.852	25.86	0.69	5.201	0.72
503.568532	0.0372	6.731	16.12	0.61	3.980	0.43
504.482692	0.0124	6.731	16.12	0.61	4.010	0.45
547.676440	0.9785	0.158	26.00	0.70	4.500	1.00
552.020960	0.1840	0.158	26.00	0.70	4.500	1.00
*556.935985	497.0	0.159	30.86	0.69	4.552	1.00
620.700807	5.015	2.391	24.38	0.71	4.856	0.68
645.766085	0.0067	8.633	18.00	0.60	4.000	0.50
658.005280	0.2732	7.816	32.10	0.69	4.140	1.00
*752.033113	243.4	0.396	30.86	0.68	4.352	0.84
841.051732	0.0134	8.177	15.90	0.33	5.760	0.45
859.965698	0.1325	8.055	30.60	0.68	4.090	0.84
899.303175	0.0547	7.914	29.85	0.68	4.530	0.90
902.611085	0.0386	8.429	28.65	0.70	5.100	0.95
906.205957	0.1836	5.110	24.08	0.70	4.700	0.53
916.171582	8.400	1.441	26.73	0.70	5.150	0.78
923.112692	0.0079	10.293	29.00	0.70	5.000	0.80
970.315022	9.009	1.919	25.50	0.64	4.940	0.67
987.926764	134.6	0.257	29.85	0.68	4.550	0.90
*1780.000000	17506	0.952	196.3	2.00	24.15	5.00

Table 2.2 – Water vapour absorption lines parameters (main lines with *)

2.3 Attenuation due to clouds or rain

Other important contributors to the attenuation are the liquid water species. There are on the one hand the small suspended water droplets present in clouds of fog, and on the other hand the larger precipitating rain drops. Clouds occur fairly often (typically a few 10 % of the time) and lasts sometimes entire days or more, while rain is usually rarer (typically a few % of the time) and is more localized in time over a couple of hours or less. Both can cause much larger

attenuations than the gases, especially rain. The origin of their attenuation is indeed not limited to absorption as it includes the scattering of the incoming waves by the drops depending on their sizes relative to the wavelength.

To model the attenuation by liquid water, this section first goes through:

- models for the refractive index of liquid water (see Sec. 2.3.1),
- models for the dropsize distributions of cloud and rain (see Sec. 2.3.2),
- Mie theory for the scattering by spherical drops (see Sec. 2.3.3),
- Rayleigh simplification to Mie theory (see Sec. 2.3.4) applying to clouds.

Then the section presents the subsequent computations of the specific attenuation for clouds (see Sec. 2.3.5, 2.3.6 and 2.3.7) and for rain (see Sec. 2.3.8 and 2.3.9). Finally the ITU-R distribution is also reviewed (see Sec. 2.3.10).

2.3.1 Refractive index of liquid water

The modelling of the interaction between a plane wave and a water drop requires the knowledge of the refractive index inside the drop, i.e. the refractive index m of liquid water. It is equivalent to specify the relative permittivity ϵ_r instead, as one has $m = \sqrt{\epsilon_r}$ (assuming the relative permeability μ_r is unity).

Two models for ϵ_r are in use in this thesis. The first one, "ITU-R", is found in the recommendation ITU-R P.840-7 [46] for clouds and was given by Liebe et al. in [77]. It is valid up to 1000 GHz. The second one, "Ray", was proposed by Ray in [78]. It is valid up to infrared radiations. Fig. 2.2 shows the two models at 298 K between 1 GHz and 200 GHz. The differences between the models in this frequency range are negligible. In this work, the ITU-R model is used for cloud and the Ray model for rain, mostly because of earlier implementations.

Similarly to (2.2), the liquid water permittivity is complex such that

$$\epsilon_r(f) = \epsilon'_r(f) - j\epsilon''_r(f). \tag{2.51}$$

The ITU-R model for ϵ_r is a double-Debye model of the form

$$\epsilon_r(f) = \epsilon_{s2} + \frac{\epsilon_{s0} - \epsilon_{s1}}{1 + j\,(f/f_p)} + \frac{\epsilon_{s1} - \epsilon_{s2}}{1 + j\,(f/f_s)} \tag{2.52}$$

hence

$$\epsilon'_r(f) = \epsilon_{s2} + \frac{\epsilon_{s0} - \epsilon_{s1}}{1 + (f/f_p)^2} + \frac{\epsilon_{s1} - \epsilon_{s2}}{1 + (f/f_s)^2} \tag{2.53}$$

$$\epsilon''_r(f) = \frac{f}{f_p}\frac{\epsilon_{s0} - \epsilon_{s1}}{1 + (f/f_p)^2} + \frac{f}{f_s}\frac{\epsilon_{s1} - \epsilon_{s2}}{1 + (f/f_s)^2} \tag{2.54}$$

with the permittivity terms ϵ_{s0}, ϵ_{s1}, and ϵ_{s2} given by

$$\epsilon_{s0} = 77.66 + 103.3(\theta_T - 1) \tag{2.55}$$

$$\epsilon_{s1} = 0.0671\epsilon_{s0} \tag{2.56}$$

$$\epsilon_{s2} = 3.52 \tag{2.57}$$

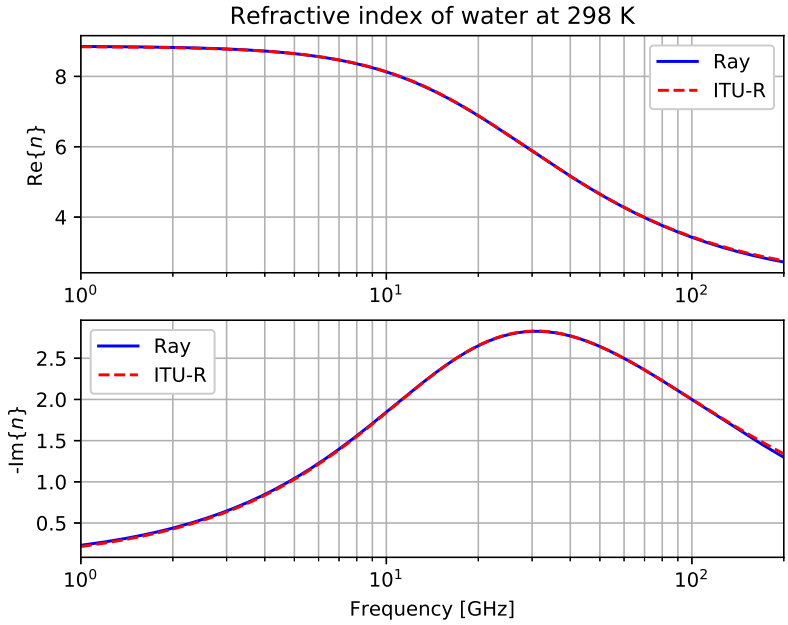

Figure 2.2 – Refractive index of water at 298 K in between 1 GHz and 200 GHz with either the Ray or the ITU-R model

with the relaxation frequencies f_p [GHz] and f_s [GHz] given by

$$f_p = 20.20 - 146(\theta_T - 1) + 316(\theta_T - 1)^2 \tag{2.58}$$

$$f_s = 39.8 f_p \tag{2.59}$$

where the parameters are the frequency f [GHz] and the function $\theta_T = 300/T$ of the temperature T [K].

The basis of the Ray model for ϵ_r is a Cole-Cole model, with a frequency independent conductivity term $\sigma = 12.5664 \times 10^8$ S, of the form

$$\epsilon_r(f) = \epsilon_\infty + \frac{\epsilon_s - \epsilon_\infty}{1 + \left(j\,(f/f_s)\right)^\beta} - j\frac{\sigma}{2\pi f} \times 10^{-9} \tag{2.60}$$

hence

$$\epsilon'_r(f) = \epsilon_\infty + \frac{(\epsilon_s - \epsilon_\infty)\left(1 + (f/f_s)^\beta \cos\left(\frac{\pi}{2}\beta\right)\right)}{1 + 2(f/f_s)^\beta \cos\left(\frac{\pi}{2}\beta\right) + (f/f_s)^{2\beta}} \tag{2.61}$$

$$\epsilon''_r(f) = \frac{(\epsilon_s - \epsilon_\infty)(f/f_s)^\beta \sin\left(\frac{\pi}{2}\beta\right)}{1 + 2(f/f_s)^\beta \cos\left(\frac{\pi}{2}\beta\right) + (f/f_s)^{2\beta}} + \frac{\sigma}{2\pi f} \times 10^{-9} \tag{2.62}$$

with the permittivity terms ϵ_s and ϵ_∞ given by

$$\begin{aligned}\epsilon_s = 78.54\big(1.0 - 4.579 \times 10^{-3}(t - 25.0) + 1.19 \times 10^{-5}(t - 25.0)^2 \\ -2.8 \times 10^{-8}(t - 25.0)^3\big)\end{aligned} \tag{2.63}$$

$$\epsilon_\infty = 5.2717 + 0.0216474t - 0.00131198t^2 \tag{2.64}$$

with the exponent β given by

$$\beta = 0.9390735 + 16.8129/(t + 273) \tag{2.65}$$

with the relaxation frequency f_s [GHz] given by

$$f_s = \frac{c_0}{3.3836 \times 10^3} \exp\left(-2513.98/(t + 273)\right) \tag{2.66}$$

where the parameters are the frequency f [GHz] and the temperature t [°C].

2.3.2 Cloud and rain dropsize distributions

The dropsize distribution of the water species must also enters the modelling of the interaction of their containing medium with an incoming plane wave.

In the case of clouds, their exact distributions may vary significantly from one cloud to another, with bigger differences between stratiform and convective clouds. Here the discussion is limited to the observation that cloud droplets have typically diameters of a few micrometers only ($< 50\,\mu$m) [77, 79]. As will be shown in Sec. 2.3.4, this information is sufficient and the detailed knowledge of the distribution is not essential from the propagation point of view.

For rain, the dropsize distribution N_d [$\mathrm{m^{-3}\,m^{-1}}$], or number of drops per unit volume, is often assumed to be a gamma distribution written as [37]

$$N_d(D_d) = N_{d,0} D_d^\mu \exp\left(-\Lambda_d D_d\right) \tag{2.67}$$

for D_d [m] the diameter of the drop, μ the shape factor and Λ_d [$\mathrm{m^{-1}}$] the slope of the distribution. A widely accepted average distribution is the Marshall-Palmer distribution [48] which has $N_{d,0} = 8 \times 10^6\,\mathrm{m^{-3}\,m^{-1}}$ and $\mu = 0$, and was developed for the mid-latitudes. The slope Λ_d is not assumed to be universal and has to be related to the rain conditions. For this, one can use e.g. the mass of rain water per unit volume M_{rain} [$\mathrm{kg\,m^{-3}}$] which is obtained as

$$M_{rain} = \rho_w \frac{\pi}{6} \int_0^\infty N_d(D_d) D_d^3 dD_d \tag{2.68}$$

with $\rho_w = 1000\,\mathrm{kg\,m^{-3}}$ the density of water. Then, after integration,

$$\Lambda_d = \left(\frac{\pi}{6} \frac{\rho_w}{M_{rain}} N_{d,0} \Gamma(\mu + 4)\right)^{\frac{1}{\mu+4}}. \tag{2.69}$$

Fig. 2.3 shows Marshall-Palmer distributions for different values of M_{rain}.

Note that N_d can also be related to the rain rate R_{rain} [$\mathrm{mm\,h^{-1}}$]

$$R_{rain} = \rho_w \frac{\pi}{6} \int_0^\infty N_d(D_d) D_d^3 v_d(D_d) dD_d \times 3600\,\mathrm{s\,h^{-1}} \tag{2.70}$$

knowing $v_d(D_d)$ [$\mathrm{m\,s^{-1}}$] the terminal velocity of the drop of diameter D_d.

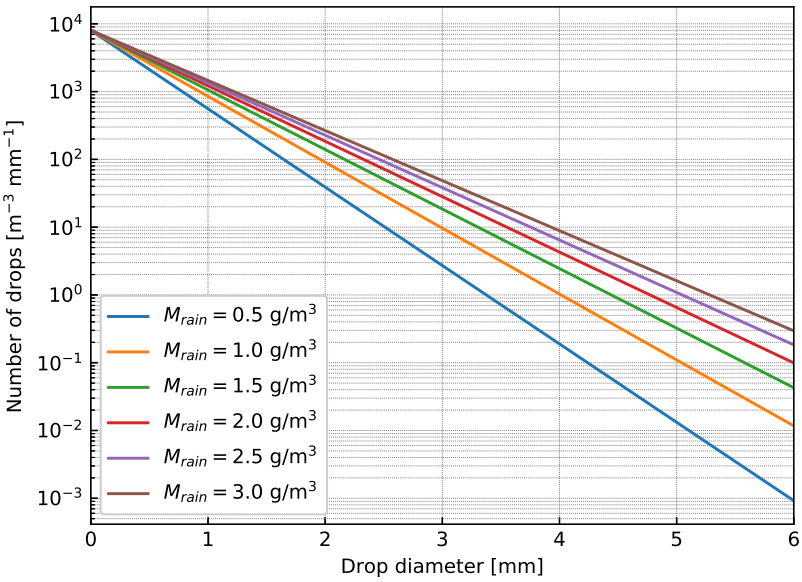

Figure 2.3 – Marshall-Palmer rain dropsize distribution in function of the mass of rain water per unit volume M_{rain}

2.3.3 Mie scattering

The Mie theory of scattering proposes a formalism to compute the exctinction of an incident wave caused by spherical drops dispersed in the medium. From [35, 37, 49, 80], the specific attenuation γ_{ext} [dB km^{-1}] is

$$\gamma_{ext} = \left(\frac{20}{\ln 10} \times 10^3\right) \times \frac{1}{2} \int_0^\infty \sigma_{ext}(D_d) N_d(D_d) dD_d \tag{2.71}$$

with as before N_d [m^{-3} m^{-1}] the dropsize distribution for drops of diameter D_d [m], and σ_{ext} [m] the equivalent extinction cross-section of those same drops. Following [49], σ_{ext} is found as

$$\sigma_{ext} = \frac{\lambda^2}{2\pi} \sum_{\nu=1}^{\infty} (2\nu + 1) \mathrm{Re}\{a_\nu + b_\nu\} \tag{2.72}$$

for the wavelength λ [m] and involving the coefficients a_ν and b_ν such that

$$a_\nu = \frac{\psi'_\nu(y)\psi_\nu(x) - m\psi_\nu(y)\psi'_\nu(x)}{\psi'_\nu(y)\zeta_\nu(x) - m\psi_\nu(y)\zeta'_\nu(x)} \tag{2.73}$$

$$b_\nu = \frac{m\psi'_\nu(y)\psi_\nu(x) - \psi_\nu(y)\psi'_\nu(x)}{m\psi'_\nu(y)\zeta_\nu(x) - \psi_\nu(y)\zeta'_\nu(x)} \tag{2.74}$$

where m is the refractive index of liquid water, where the variables $x = kr_d$, $y = mkr_d = mx$ are defined in function of the wavenumber k and the drop radius r_d, and where the Ricatti-Bessel functions ψ_ν, χ_ν, and ζ_ν, are

$$\psi_\nu(z) = z j_\nu(z) \tag{2.75}$$

$$\chi_\nu(z) = -z y_\nu(z) \tag{2.76}$$

$$\zeta_\nu(z) = z h_\nu^{(2)} = \psi_\nu(z) + j\chi_\nu(z) \tag{2.77}$$

in function of the better known spherical Bessel functions j_ν and y_ν of the first and second kind, and of the spherical Hankel function $h_\nu^{(2)}$ of the second kind.

It appears rather clearly that computing γ_{ext} from (2.71) must be computationally expensive, due to the integrand requiring all these special functions. Some simplifications should therefore be undertaken whenever possible.

2.3.4 Rayleigh scattering

In Sec. 2.3.2, the cloud droplet diameters were stated to be of the order of a few micrometers. What are the consequences for the terms in (2.72)? Fig. 2.4 (a) shows typical ($f = 40\,\text{GHz}$, $T = 298\,\text{K}$) curves for the terms of the summation in (2.72) as a function of r_d. For $r_d < 10^{-5}$m it is apparent that the term for $\nu = 1$ is largely dominant. Moreover, Fig. 2.4 (b) shows that, in those same conditions, a_1 is much larger than b_1. Hence (2.72) is simplified as

$$\sigma_{ext} \approx \frac{3\lambda^2}{2\pi}\text{Re}\{a_1\} = \frac{6}{x^2}\text{Re}\{a_1\} \times \pi r_d^2 \tag{2.78}$$

and this expression can be simplified further by working more deeply on a_1.

In order to simplify (2.73), it is useful to study the Ricatti-Bessel functions by using the Rayleigh formulas for the spherical Bessel functions

$$j_\nu(z) = \left(-\frac{d}{dz}\right)^\nu \left[\frac{\sin(z)}{z}\right] \tag{2.79}$$

$$y_\nu(z) = -\left(-\frac{d}{dz}\right)^\nu \left[\frac{\cos(z)}{z}\right]. \tag{2.80}$$

Then, if $z \to 0$, it can be found that

$$\psi_1(z) \approx \frac{1}{3}z^2 \qquad \psi_1'(z) \approx \frac{2}{3}z \tag{2.81}$$

$$\chi_1(z) \approx \frac{1}{z} \qquad \chi_1'(z) \approx -\frac{1}{z^2} \tag{2.82}$$

and indeed the variable x in (2.73) is very small for microwaves as $r_d \ll \lambda$ (e.g. $\lambda = 7.5\,\text{mm}$ at $40\,\text{GHz}$), and this remains true for the variable y as for liquid water $|m| \lesssim 10$ (see Fig. 2.2).

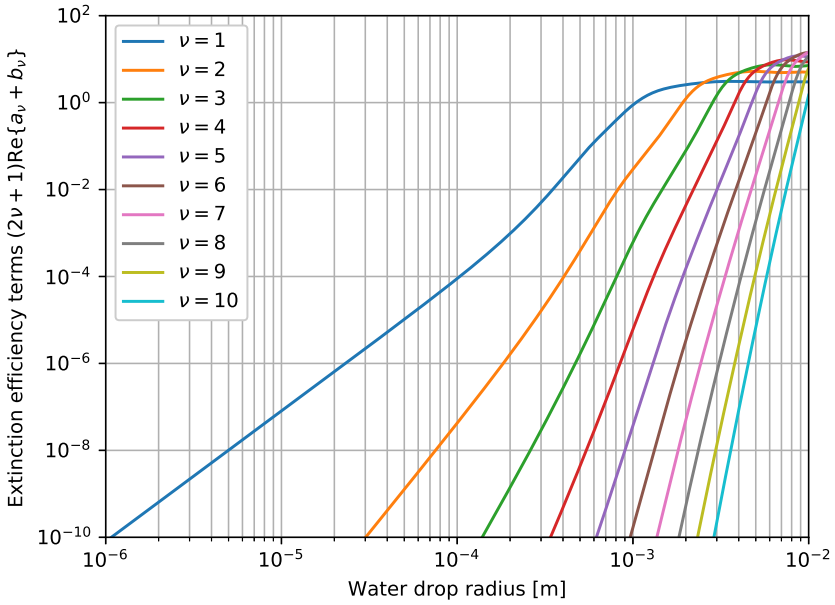

(a) Extinction efficiency terms

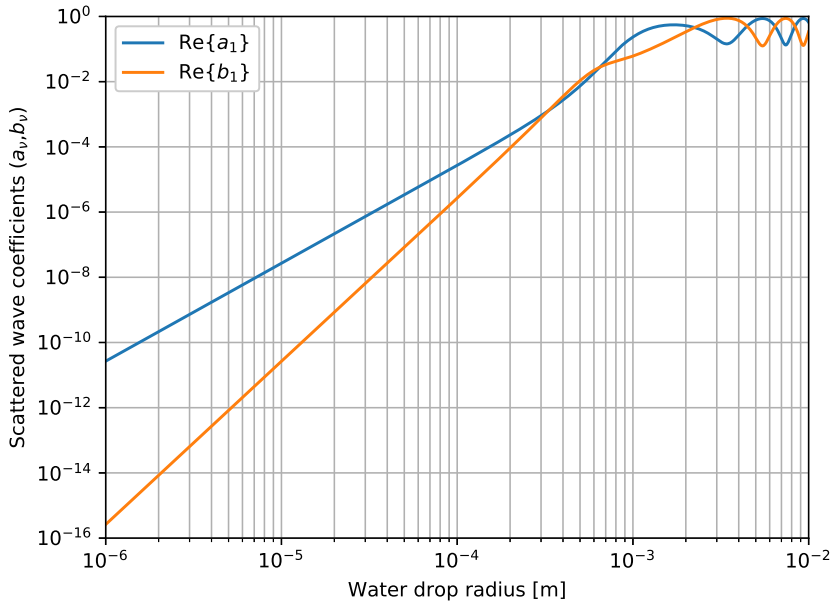

(b) Scattered wave coefficients a_1 and b_1

Figure 2.4 – Evolution of some Mie scattering parameters as a function of the radius of the water drop at 298 K and 40 GHz

For easier manipulations, (2.73) is rewritten as

$$a_\nu = \frac{1}{1 + j\dfrac{\psi'_\nu(y)\chi_\nu(x) - m\psi_\nu(y)\chi'_\nu(x)}{\psi'_\nu(y)\psi_\nu(x) - m\psi_\nu(y)\psi'_\nu(x)}} \tag{2.83}$$

then from (2.81) and (2.82)

$$\begin{aligned} a_1 \approx & \frac{1}{1 - j\dfrac{\frac{2}{3}mx\frac{1}{x} - m\frac{1}{3}(mx)^2\left(-\frac{1}{x^2}\right)}{\frac{2}{3}mx\frac{1}{3}x^2 - m\frac{1}{3}(mx)^2\frac{2}{3}x}} \\ = & \frac{1}{1 + j\dfrac{3}{2x^3}\dfrac{m^2+2}{m^2-1}} \approx j\frac{2x^3}{3}\frac{m^2-1}{m^2+2} \end{aligned} \tag{2.84}$$

where the assumption that $x \ll 1$ is re-used in the last step. Finally, a_1 is expanded to obtain its real part

$$\begin{aligned} a_1 = & j\frac{2x^3}{3}\frac{\epsilon_r - 1}{\epsilon_r + 2} = j\frac{2x^3}{3}\frac{(\epsilon'_r - 1) - j\epsilon''_r}{(\epsilon'_r + 2) - j\epsilon''_r} = \frac{2x^3}{3}\frac{\epsilon''_r + j(\epsilon'_r - 1)}{(\epsilon'_r + 2) - j\epsilon''_r} \\ = & \frac{2x^3}{3}\frac{\epsilon''_r((\epsilon'_r + 2) - (\epsilon'_r - 1)) + j(\epsilon''^2_r + (\epsilon'_r - 1)(\epsilon'_r + 2))}{(\epsilon'_r + 2)^2 + \epsilon''^2_r} \\ = & \frac{2x^3}{3}\frac{3\epsilon''_r + j(\epsilon''^2_r + (\epsilon'_r - 1)(\epsilon'_r + 2))}{(\epsilon'_r + 2)^2 + \epsilon''^2_r} \end{aligned} \tag{2.85}$$

and after some re-arrangements in (2.78)

$$\sigma_{ext} \approx 24\pi^2\frac{r_d^3}{\lambda}\frac{\epsilon''_r}{(\epsilon'_r + 2)^2 + \epsilon''^2_r} = 24\pi^2\frac{r_d^3}{\lambda}\frac{1}{\epsilon''_r\left(\left(\frac{\epsilon'_r+2}{\epsilon''_r}\right)^2 + 1\right)}. \tag{2.86}$$

Now, because the extinction cross section depends only on the drop dimension in r_d^3, the integral in (2.71) is proportional to the third moment of the dropsize distribution, i.e. to the mass of drops per unit volume as in (2.68). Hence if the latter is known, it is not necessary to know the details of the distribution.

2.3.5 Specific cloud attenuation using Rayleigh scattering

In the recommendation ITU-R P.840-7 [46], and in [77], the specific cloud attenuation is specified via a contribution to the imaginary refractivity as in

$$N''_{cloud,l} = \frac{9}{2}\frac{M_{cloud,l}}{\rho_w}\frac{\epsilon''_r}{(\epsilon'_r + 2)^2 + \epsilon''^2_r} \times 10^6 \tag{2.87}$$

with $M_{cloud,l}$ [kg m^{-3}] the mass of cloud liquid water per unit volume, ρ_w [kg m^{-3}] the liquid water density, and ϵ_r the liquid water permittivity from (2.52). Then, the specific attenuation due to clouds γ_{cloud} [dB km^{-1}] is given by (2.10). The validity of this result is found by injecting (2.86) in (2.71).

Measurements of $M_{cloud,l}$ are uncommon, though it is a typical output of NWPs. Algorithms were developed to estimate $M_{cloud,l}$ from more common quantities. The next two sections presents such models, similarly to [81].

2.3.6 Salonen cloud liquid water content detection model

The Salonen model [47], modified by [82, 83], receives as input vertical profiles of the pressure p, temperature T, and relative humidity RH (see (3.38)), and provides as output, profiles of the liquid water content $M_{cloud,l}$. Cloudy conditions are identified when $RH > RH_c$, with

$$RH_c = 1 - \alpha\sigma(1-\sigma)\left(1+\beta(\sigma-0.5)\right), \tag{2.88}$$

$\alpha = 1$, $\beta = \sqrt{3}$, and $\sigma = p/p_s$ where p_s is the ground pressure. Then, the total water content M_{cloud} at the altitude h in the cloud is calculated as

$$M_{cloud} = \begin{cases} w_0 \left(\frac{h-h_b}{h_r}\right)^a (1+cT) & T \geq 0\,^\circ\mathrm{C} \\ w_0 \left(\frac{h-h_b}{h_r}\right)^a \exp(cT) & T < 0\,^\circ\mathrm{C} \end{cases} \tag{2.89}$$

with $w_0 = 0.17\,\mathrm{g\,m^{-3}}$, $a = 1$, $c = 0.04\,^\circ\mathrm{C}^{-1}$, $h_r = 1.5\,\mathrm{km}$, and where h_b is the cloud base. Finally,

$$M_{cloud,l} = M_{cloud} f_{cloud,l} \tag{2.90}$$

$$f_{cloud,l} = \begin{cases} 1 & T \geq 0\,^\circ\mathrm{C} \\ 1 + T/20 & -20 \leq T < 0\,^\circ\mathrm{C} \\ 0 & T < -20\,^\circ\mathrm{C} \end{cases} \tag{2.91}$$

where $f_{cloud,l}$ is the liquid water fraction.

2.3.7 Mattioli cloud liquid water content detection model

The Mattioli model [84] aims to improve the Salonen model. First, the critical relative humidity in (2.88) now has $\alpha = 0.59$ and $\beta = 1.37$. Second, M_{cloud} is

$$M_{cloud} = cz^a(1 - z^{a+1})^b \tag{2.92}$$

introducing a dependency on the cloud thickness ΔH with

$$c = \begin{cases} 0.8RH & \Delta H < 0.1\,\mathrm{km} \\ 1.46RH\Delta H & 0.1\,\mathrm{km} \leq \Delta H < 0.6\,\mathrm{km} \\ 0.74RH & \Delta H > 0.6\,\mathrm{km} \end{cases}, \tag{2.93}$$

$z = (h - h_b)/\Delta H$, $a = z/1.5$, and $b = 1.5 + z/1.5$. Third, $f_{cloud,l}$ is

$$f_{cloud,l} = \begin{cases} 1 & T \geq 0\,^\circ\mathrm{C} \\ 1 - (T/35)^2 & -35 \leq T < 0\,^\circ\mathrm{C} \\ 0 & T < -35\,^\circ\mathrm{C} \end{cases} \tag{2.94}$$

whereas $M_{cloud,l}$ is still calculated as in (2.90).

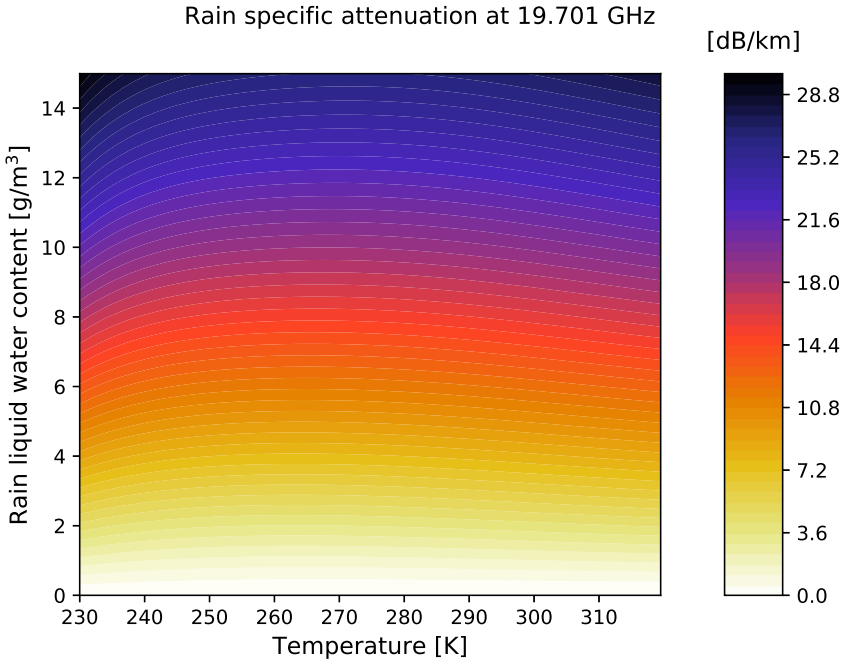

(a) 19.701 GHz

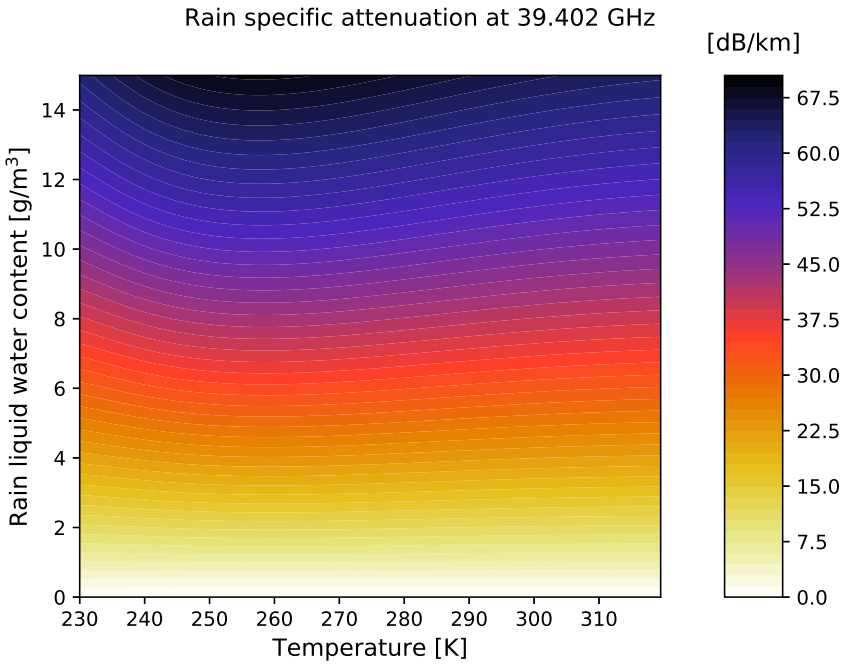

(b) 39.402 GHz

Figure 2.5 – Rain specific attenuation look-up tables using Mie scattering with Marshall-Palmer rain dropsize distribution

2.3.8 Specific rain attenuation using Mie scattering

In the case of rain, the proposed model is the Mie specific attenuation (2.71), with the Marshall-Palmer distribution in (2.67) parametrized by M_{rain} [kg m^{-3}] using (2.69), and the extinction cross section (2.72) as a function of f and T using the Ray permittivity model in (2.60).

However, for numerical reasons, it is still necessary to select a value $D_{d,max}$ to bound the integral in (2.71), and to limit the number of terms used for the sum in (2.72). The strategy is the one found within [37]. Firstly, $D_{d,max} = 4\,\text{mm}$. This choice is well supported by Fig. 2.3 where the number of drops from the Marshall-Palmer distribution is seen to become negligible after a dropsize $\sim D_{d,max}$. The number of terms ν_{max} follows the heuristic of Jeannin *et al.*

$$\nu_{max} = \text{round}\left(2 + x_{max} + 4x_{max}^{1/3}\right) \tag{2.95}$$

with $x_{max} = kD_{d,max}/2$. Fig. 2.4 (a) illustrates the contributions of the terms in ν at 40 GHz, and based on them (2.72) is expected to converge quite well for ~ 5 terms, though $\nu_{max} = 8$ is this case. Hence (2.95) is rather safe.

In the end, γ_{rain}, is a function of (T, M_{rain}) at a given frequency f. Instead of performing the full Mie scattering computations every time, the approach proposed in [37] is to pre-compute the results for arrays in (T, M_{rain}), e.g. a grid with $T \in [230, 320]$ K with a resolution of 0.5 K and $M_{rain} \in [0, 15]$ g m^{-3} with a resolution of 0.01 g m^{-3}. Then, γ_{rain} is recovered approximatively at any (T, M_{rain}) with a bilinear interpolation. Fig. 2.5 gives examples of the grids with this look-up table approach.

2.3.9 Specific rain attenuation from the rain rate

The recommendation ITU-R P.838-3 [85] contains another model for the specific attenuation due to rain. It is based on the rain rate. As is shown by (2.70), the rain rate R_{rain} [mm h^{-1}] is also related to an integral of the dropsize distribution and could be substituted to M_{rain} in scattering computations.

The model for γ_{rain} [dB km^{-1}] is a power law such that

$$\gamma_{rain} = k_R R_{rain}^{\alpha_R} \tag{2.96}$$

with two parameters k_R and α_R. This model takes into account the non-sphericity of the rain drops and introduces a dependency on the polarisation direction. For the polarisation $P \in \{H, V\}$, where H stands for horizontal and V for vertical, the power law terms are

$$\log_{10} k_R^P = \sum_{j=1}^{4} a_{j,k}^P \exp\left(-\left(\frac{\log_{10} f - b_{j,k}^P}{c_{j,k}^P}\right)^2\right) + m_k^P \log_{10} f + c_k^P \tag{2.97}$$

$$\alpha_R^P = \sum_{j=1}^{5} a_{j,\alpha}^P \exp\left(-\left(\frac{\log_{10} f - b_{j,\alpha}^P}{c_{j,\alpha}^P}\right)^2\right) + m_\alpha^P \log_{10} f + c_\alpha^P \tag{2.98}$$

for which all the necessary coefficients are given in Tab. 2.3 for k_R^H, Tab. 2.4 for k_R^V, Tab. 2.5 for α_R^H, and Tab. 2.6 for α_R^V.

The power law terms for each polarisation are also shown in Fig. 2.6. Between 10 and 100 GHz, it is observed that $\alpha_R^V < \alpha_R^H$, while $k_R^V \approx k_R^H$. Therefore, the vertical polarisation is generally more favourable for Earth-space communications as it causes a lower value of γ_{rain} for the same value of R_{rain}. The differences between horizontal and vertical polarisations are however not very strong, and it can be understood why assuming spherical rain drops is already a good approximation.

j	$a_{j,k}^H$	$b_{j,k}^H$	$c_{j,k}^H$	m_k^H	c_k^H
1	-5.33980	-0.10008	1.13098		
2	-0.35351	1.26970	0.45400	-0.18961	0.71147
3	-0.23789	0.86036	0.15354		
4	-0.94158	0.64552	0.16817		

Table 2.3 – Coefficients to compute the power law term k_R^H

j	$a_{j,k}^V$	$b_{j,k}^V$	$c_{j,k}^V$	m_k^V	c_k^V
1	-3.80595	0.56934	0.81061		
2	-3.44965	-0.22911	0.51059	-0.16398	0.63297
3	-0.39902	0.73042	0.11899		
4	0.50167	1.07319	0.27195		

Table 2.4 – Coefficients to compute the power law term k_R^V

j	$a_{j,\alpha}^H$	$b_{j,\alpha}^H$	$c_{j,\alpha}^H$	m_α^H	c_α^H
1	-0.14318	1.82442	-0.55197		
2	0.29591	0.77564	0.19822		
3	0.32177	0.63773	0.13164	0.67849	-1.95537
4	-5.37610	-0.96230	1.47828		
5	16.1721	-3.29980	3.43990		

Table 2.5 – Coefficients to compute the power law term α_R^H

j	$a_{j,\alpha}^V$	$b_{j,\alpha}^V$	$c_{j,\alpha}^V$	m_α^V	c_α^V
1	-0.07771	2.33840	-0.76284		
2	0.56727	0.95545	0.54039		
3	-0.20238	1.14520	0.26809	-0.053739	0.83433
4	-48.2991	0.791669	0.116226		
5	48.5833	0.791459	0.116479		

Table 2.6 – Coefficients to compute the power law term α_R^V

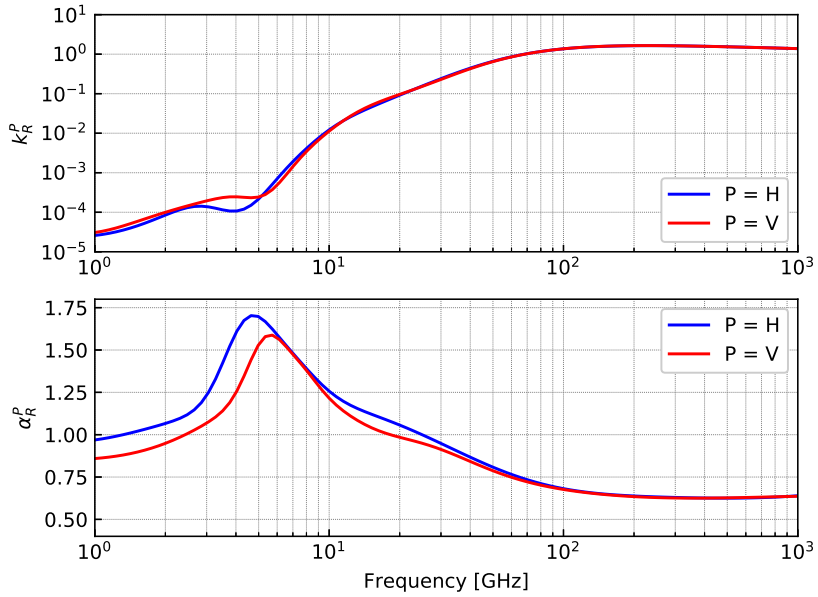

Figure 2.6 – Specific rain attenuation power law terms k_R^H, k_R^V, α_R^H and α_R^V in the frequency range from 1 to 1000 GHz

From the power law terms at each polarisation, the power law terms k_R and α_R corresponding to any given Earth-space link configuration are obtained as

$$k_R = \frac{k_R^H + k_R^V + (k_R^H - k_R^V)\cos^2\theta\cos(2\tau)}{2} \tag{2.99}$$

$$\alpha_R = \frac{k_R^H\alpha_R^H + k_R^V\alpha_R^V + (k_R^H\alpha_R^H - k_R^V\alpha_R^V)\cos^2\theta\cos(2\tau)}{2k_R} \tag{2.100}$$

where θ is the link elevation angle and τ is the polarisation tilt angle relative to the horizontal. A tilt angle of $\tau = 45°$ corresponds also to a circular polarisation, which is often the preferred choice for LEO links. If the polarisation is linear but τ is not known, $\tau = 45°$ offers a good compromise as well.

Note that the model presented in this section is independent of the temperature, even though the one in Sec. 2.3.8 takes it into account. Fig. 2.5 suggests it is probably not a big issue, except perhaps for a very high rain content.

In order to apply (2.96) to (2.11), R_{rain} must in principle be known everywhere along the propagation path. Because the rain rate is most widely available as surface measurements, a possibility is to assume that the ground value of R_{rain} remains constant in altitude up to a certain level. In rough approximation, the rain height can be assumed to be the 0 °C isotherm. This is not strictly correct, as liquid rain drops can exist above the freezing height. So, if no further correction to the rain height is performed (e.g. based on [86]) the slant path rain attenuation is likely to be underestimated with this method.

2.3.10 Cloud and rain attenuation reference statistics

Using the procedure in Sec. 2.3.5, the specific attenuation due to clouds may be obtained from (T, $M_{cloud,l}$) at a given point. Similarly, using the procedure in Sec. 2.3.8 or 2.3.9, the specific attenuation due to rain may be obtained from (T, M_{rain}) or (R_{rain}). And the slant path attenuations are found with (2.11). As was remarked in Sec. 2.2.4 for the gases, a statistical reference may prove useful and there are also ITU-R models for the cloud and rain attenuation CCDFs:

- the cloud attenuation CCDF (99 % to 0.1 %) is from P.840-7 Annex 1 §3.1 using the reduced integrated cloud liquid water content maps (and the specific attenuation model described here in Sec. 2.3.5),
- the rain attenuation CCDF (5 % to 0.001 %) is from P.618-13 Annex 1 §2.2.1.1, using P.837-7 [87] Annex 1 for the 0.01 % rainfall rate, P.839-4 [86] for the rain height, and the specific attenuation model described here in Sec. 2.3.9. Note that the model is validated only up to 55 GHz.

If we exclude amplitude scintillation (see Sec. 2.4), the "total" attenuation ITU-R CCDF (50 % to 0.001 %) is also obtained from P.618-13 Annex 1 §2.5:

- the contribution of the gaseous attenuation CCDF from Sec. 2.2.4 is modified such that $A_{gases}(P < 1\%) = A_{gases}(P = 1\%)$,
- the contribution of the cloud attenuation CCDF from this section is also modified such that $A_{cloud}(P < 1\%) = A_{cloud}(P = 1\%)$,
- it is assumed that $A_{rain}(P > 5\%) = 0\,\mathrm{dB}$,
- one has $A_{tot}(P) = A_{gases}(P) + A_{cloud}(P) + A_{rain}(P)$.

2.4 Amplitude scintillation

In this section, the general principles of amplitude scintillation are shortly presented without much proof of details. It is a rather mathematically complex topic which is not investigated in depth within the results of this thesis. Nevertheless, it is an important part of the Earth-space links dynamics and is well worth mentioning. Some useful further references are [51, 88–91].

2.4.1 Refractive index and log-amplitude fluctuations

At the center of the scintillation phenomenon, there are the fluctuations of the air refractive index n caused by the turbulent movement of air masses. In this situation, n may take a form like

$$n = \langle n \rangle + \delta n \tag{2.101}$$

with δn denoting the fluctuations of n around its mean $\langle n \rangle$. Without entering into any detail, it is easily understood that the electric field $\mathbf{E}$ will too

experience similar fluctuations. In [51], a proper treatment of the line-of-sight propagation of a plane wave through a random medium is given. The log-amplitude fluctuation χ [dB] is introduced and is loosely equivalent to

$$\chi \simeq 20 \log_{10} \left(\frac{|\mathbf{E}|}{\langle |\mathbf{E}| \rangle} \right) \tag{2.102}$$

which, looking at (2.8), qualifies as a part of the atmospheric attenuation.

In the rest of this section, the main models regarding χ are explored.

2.4.2 Turbulence and refractive index structure constant

The atmospheric turbulence is a process driven by the fluctuations of the air velocity. At a large scale, the phenomenon is largely anisotropic until the kinetic energy is transferred to turbulent eddies of smaller size. Those turbulent eddies are characterized by two scales: the outer scale L_0 ($\sim 1 - 100\,\mathrm{m}$), and the inner scale l_0 ($\sim 1 - 10\,\mathrm{mm}$). For eddies of size l, the turbulent regimes are:

- $l > L_0$, the input range when energy enters the turbulent process from the larger turbulent structures in the atmosphere.
- $L_0 > l > l_0$, the inertial sub-range where there is the formation of a cascade of eddies progressively transferring almost all their kinetic energy, with negligible dissipation, to eddies of smaller and smaller sizes.
- $l < l_0$, the dissipation range when turbulent eddies becomes too small and are dissipated into heat.

Based on the turbulent theory of Kolmogorov, the fluctuation of the refractive index n is related to the structure constant C_n^2 [$\mathrm{m}^{-2/3}$] such that

$$C_n^2(r) = \frac{\left\langle (n(r + \delta r) - n(r))^2 \right\rangle}{|\delta r|^{2/3}} \tag{2.103}$$

for δr [m] within the inertial subrange from the position r [m], i.e. $L_0 > \delta r > l_0$. The C_n^2 is, much like the other aspects of this theory, not simple to measure or to model. From (2.6) for the refractivity of air, the C_n^2 is expected to depends on the variations of temperature and humidity at microwave frequencies.

Some models of the microwave C_n^2 using atmospheric profiles have been developed by [92, 93] and applied to amplitude scintillation in [94, 95].

2.4.3 Log-amplitude scintillation variance and cut-off

There are models relating the log-amplitude variance σ_χ^2 [dB^2] to the C_n^2 along the propagation path [51, 88]. Their validity depends on the direction of the Earth-space link. Indeed, turbulent eddies close (uplink) or far (downlink) from the emitter affect the wave front differently [96]. Unlike the attenuation, the amplitude scintillation is not a reciprocal property of the link. Here only downlinks are considered. If L_t [m] is the extent of the slant path through turbulence, the models differ also depending on how the dimension of the Fresnel first zone $\sqrt{\lambda L_t}$ compares to the outer scale of turbulence L_0.

For $\sqrt{\lambda L_t} < L_0$, one has [97]

$$\sigma_\chi^2 = 42.48 k^{7/6} \int_0^{L_t} C_n^2(r) r^{5/6} dr \tag{2.104}$$

which, if C_n^2 is constant, reduces to

$$\sigma_\chi^2 = 23.39 k^{7/6} C_n^2 L_t^{11/6}. \tag{2.105}$$

For $\sqrt{\lambda L_t} > L_0$, one has instead [98]

$$\sigma_\chi^2 = 29.5 k^2 L_0^{5/3} \int_0^{L_t} C_n^2(r) dr \tag{2.106}$$

which, if C_n^2 is constant, reduces to

$$\sigma_\chi^2 = 29.5 k^2 C_n^2 L_0^{5/3} L_t. \tag{2.107}$$

The formulas for σ_χ^2 are actually found by integrating the power spectral density (PSD) $W_\chi(\omega)$ [$\mathrm{dB\,Hz^{-1}}$], which takes the general asymptotic form

$$W_\chi(\omega) = \begin{cases} W_\chi^0 & \omega < \omega_c \\ W_\chi^0 \left(\frac{\omega}{\omega_c}\right)^{-8/3} & \omega > \omega_c \end{cases} \tag{2.108}$$

where ω_c [$\mathrm{rad\,s^{-1}}$] is the cut-off frequency marking the transition between the constant W_χ^0 at low frequencies and the -8/3 slope at high frequencies. The cut-off frequency ω_c is linked to the transverse speed v_t [m/s] of the eddies with respect to the direction of propagation.

For $\sqrt{\lambda L_t} < L_0$, one has

$$\omega_c = 1.43 v_t \sqrt{\frac{k}{L_t}} \tag{2.109}$$

and

$$W_\chi^0 = \frac{3.954}{\omega_c} \sigma_\chi^2. \tag{2.110}$$

For $\sqrt{\lambda L_t} > L_0$, one has

$$\omega_c = \frac{v_t}{L_0} \tag{2.111}$$

and

$$W_\chi^0 = \frac{5.61}{\omega_c} \sigma_\chi^2. \tag{2.112}$$

It appears in (2.106) and (2.111) that, when $\sqrt{\lambda L_t} > L_0$, σ_χ^2 and ω_c depends on the outer scale L_0. As L_0 is typically not well known, it makes it difficult to link σ_χ^2 to the atmospheric properties. The case $\sqrt{\lambda L_t} > L_0$ is encountered mainly at low elevations for downlinks. Indeed, if the height of the turbulence layer is h_t, then $L_t \simeq h_t / \sin(\theta)$ for an elevation angle θ. And, for example at 20 GHz, if $L_0 \sim 10\,\mathrm{m}$ and $h_t \sim 1\,\mathrm{km}$ then $\theta \lesssim 8.6°$ to satisfy $\sqrt{\lambda L_t} > L_0$.

The previous models of σ_χ^2 deal with clear air scintillation, however it is known that scintillation displays a different behaviour during rainy conditions. The Matricciani model [99] permits to redefine σ_χ^2 as $\sigma_{r\chi}^2$ in rain such that

$$\sigma_{r\chi}^2 = \begin{cases} \sigma_\chi^2 A_{rain}^{10/12} & \text{if } A_{rain} > 1\,\text{dB} \\ \sigma_\chi^2 & \text{otherwise} \end{cases} \tag{2.113}$$

where A_{rain} [dB] is the rain attenuation.

Furthermore, the scintillation variance is also affected by the dimensions of the receiving antenna, as on a larger aperture antenna the turbulence-induced fluctuations in the wave front are averaged out. The recommendation ITU-R P.618-13 §2.4.1 [5] proposes an example of such an antenna averaging factor, and similar expressions are also found e.g. in [96].

Finally, assuming the PSD $W_\chi(\omega)$ is reconstructed from σ_χ^2 and ω_c, a time-varying filter may then be built from it and used to synthesize amplitude scintillation time series starting from a gaussian white noise. This strategy is described in [38].

2.5 Propagation beacon and excess attenuation

Now that the main Earth-space propagation impairments have been presented, this sections explores what their direct measurements entail, similarly to [81]. Part of the attenuation can indeed be recovered by measuring the signals received on the ground from single frequency spaceborne propagation beacons.

2.5.1 Beacon signal power and total attenuation

The power P_r [W] received from the satellite beacon at the ground station is usually expressed with respect to a reference power P_0 [W] as the received power level L_r such that

$$L_r = 10\log_{10}\left(\frac{P_r}{P_0}\right) \tag{2.114}$$

and, oftentimes $P_0 = 1\,\text{mW}$ so that L_r is expressed in dBm. The value of L_r depends on the whole system and is not a universal metric of the atmospheric attenuation. This metric would be the total attenuation A_{tot} [dB] given here in terms of powers by

$$A_{tot} = -10\log_{10}\left(\frac{P_r}{P_{na}}\right) \tag{2.115}$$

where P_{na} [W] is the received power in hypothetical conditions of absence of the atmosphere. In practice, however, P_{na} cannot be known with high accuracy [100, 101], as it also depends on several system parameters that might vary in time. Only some of the attenuation components are usually extracted from a propagation beacon signal with good accuracy: the rain attenuation and the log-amplitude scintillation. The next section explains the reasons why.

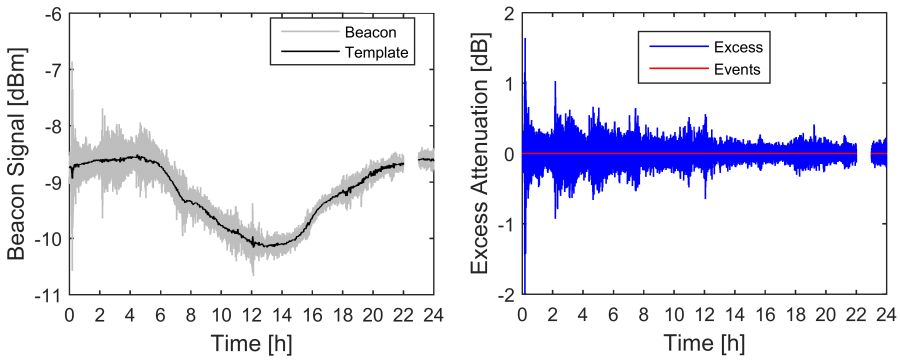

(a) 2015-07-10, clear-sky conditions

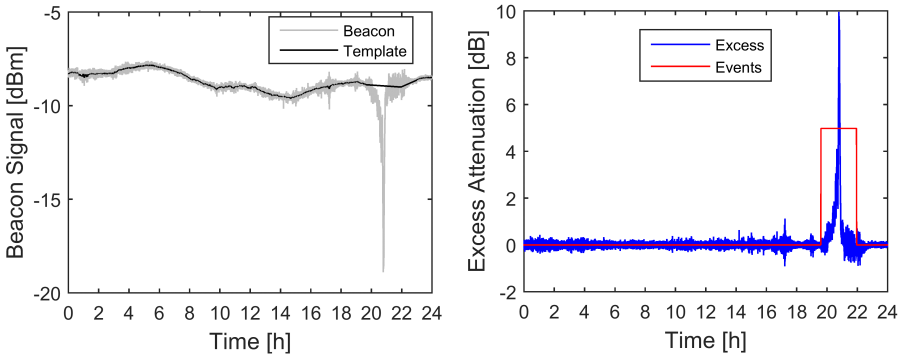

(b) 2015-05-02, rain event

Figure 2.7 – Example of rain event identification, template construction, and excess attenuation extraction from the Alphasat 19.701 GHz at Spino d'Adda

2.5.2 Identification of precipitation events and extraction of the excess attenuation from the measured signal

Figs 2.7 (a) and (b) show examples of the measured co-polar beacon signals (on the left) and the result of their processing (on the right) for the link between Alphasat and Spino d'Adda (IT) at 19.701 GHz. Fig. 2.7 (a) shows the 10th July 2015, a day with clear-sky conditions. Fig. 2.7 (b) shows the 2nd May 2015, a day with a strong rain event.

In the left part of Fig. 2.7 (a), the beacon signal (in grey) has the general trend to vary between around −8.5 dBm near midnight and around −10 dBm near noon. On top of this trend, there appears to be a random fluctuation of the signal which varies in intensity over time. The general trend is mainly due to the satellite motion, whereas the fluctuations are characteristic of scintillation. What is called the template (in black) is this trend found by filtering the scintillation out of the signal. Then, in the right part of the figure, the filtered out scintillation constitutes what is called the excess attenuation (in blue).

In the left part of Fig. 2.7 (b), a trend and fluctuations, as those observed for the clear-sky day, are also visible. The most striking feature of the beacon signal (in grey) is however the marked negative peak in the evening. This peak is caused by a rain event. To be able to build a smooth template (in black) from the signal, it is necessary to accurately flag the rain event and remove it from the signal, e.g. by a linear interpolation between the start and end of the event. The right part of the figure shows how the limits of the event were defined (in red). It also shows the resulting excess attenuation (in blue) found by subtracting the beacon signal from the template. This time, the excess attenuation contains contributions from both the log-amplitude scintillation and the rain attenuation.

More generally, the processing of the beacon signal implies the construction of a template where, during rain events, L_r is replaced by a linear interpolation and the scintillation is filtered out. The rain events can be flagged either by visual inspection or by means of some semi-automatic methods. The scintillation can be removed by a low-pass filter which exploits its known spectral properties [99, 102]. In other words, this template is the level L_{nr} of the power P_{nr} that would have been measured without rain and turbulence. By subtracting the beacon signal from the template, we obtain the excess attenuation A_{exc} [dB]

$$A_{exc} = L_{nr} - L_r = -10 \log_{10} \left(\frac{P_r}{P_{nr}} \right) \tag{2.116}$$

a metric including only the effects of rain and turbulence. The relation between A_{exc} and A_{tot} is, from (2.115) and (2.116),

$$A_{tot} = A_{exc} + A_{nr} \tag{2.117}$$

$$A_{nr} = -10 \log_{10} \left(\frac{P_{nr}}{P_{na}} \right) \tag{2.118}$$

where the nonrainy attenuation A_{nr} [dB] appears as a quantity that must be estimated independently from the beacon signal in order to obtain the total attenuation. From what has been seen before in this chapter, the components of the nonrainy attenuation are due to the gases and to the clouds.

It must be noted that, because the presence of clouds and rain are correlated, because the identification or rain events is not always straightforward, or simply because there are discrepancies in the processing/filtering methods, what is included in practice in the excess attenuation is susceptible to variation between an experiment and another. The accuracy of the excess attenuation from propagation beacon experiment has been estimated to be $\sim 0.2 - 0.5\,\text{dB}$ in the range $20 - 50\,\text{GHz}$ [16].

2.6 Radiometers and brightness temperature

Another type of apparatus which relates to the atmospheric attenuation is the ground-based microwave radiometer. It is a passive device measuring the thermal noise of the atmosphere for a certain number of frequencies. This section explains, similarly to [81], how the nonrainy attenuation may be estimated from radiometric measurements.

2.6.1 Brightness temperature and attenuation

Assuming that the atmosphere acts as a black-body at the frequency f, a radiometer measures the brightness temperature T_b [K] which is defined as [73]

$$T_b(f) = T_c\Gamma(f,\infty) + T_{mr}(f)(1-\Gamma(f,\infty)) \tag{2.119}$$

where $T_c = 2.7\,\mathrm{K}$ is the cosmic background temperature, T_{mr} [K] is the mean radiative temperature given by

$$T_{mr}(f) = \frac{\int_0^\infty T(s)\gamma(f,s)\Gamma(f,s)ds}{\int_0^\infty \gamma(f,s)\Gamma(f,s)ds}, \tag{2.120}$$

with T the temperature, γ the specific attenuation, and where

$$\Gamma(f,s) = \exp\left(-\frac{\ln 10}{10}\int_0^s \gamma(f,s')ds'\right) \tag{2.121}$$

is the transmission factor. From (2.11) and (2.121) it is clear that $\Gamma(f,\infty) = 10^{-0.1A(f)}$ and, as a consequence from (2.119),

$$A(f) = 10\log_{10}\left(\frac{T_{mr}(f)-T_c}{T_{mr}(f)-T_b(f)}\right) \tag{2.122}$$

i.e. measurements of T_b can be used to retrieve the tropospheric attenuation. This simplified view of the radiative transfer is only possible by assuming a scatter-free atmosphere and that the attenuation is due to the atmospheric absorption only. Radiometric measurements are then not suitable to recover the rain attenuation, but contain information about the gases and the clouds.

From radiometric measurements at a list of frequencies f_i, the main interest here would be to reconstruct the nonrainy attenuation at any frequency f_j. Estimates of T_{mr}, not an easily measured quantity, must then also be provided.

2.6.2 Calibration of the radiometric attenuation retrieval

A procedure to retrieve $A_{nr}(f_j)$, from measurements of $T_b(f_i)$ at multiple frequencies $f_i \neq f_j$, is detailed in [100, 101, 103]. The approach needs multiple years of radio-soundings (see Sec. 2.7.3) profiles of p, T and RH collected in a site close to where the radiometer is installed. Firstly, the Salonen model (see Sec. 2.3.6) is used to estimate the liquid water content $M_{cloud,l}$. Secondly, for each vertical profile, the following quantities are computed:

- for f_j and each f_i, the specific attenuations due to oxygen γ_{ox} and water vapour γ_{wv} (e.g. as in Sec. 2.2.2 or 2.2.3), due to clouds γ_{cloud} (e.g. as in Sec. 2.3.5), then summing them to get the specific nonrainy attenuation γ_{nr},
- for f_j and each f_i, the zenithal nonrainy attenuation A_{nr}, by integrating γ_{nr} along the whole vertical profile as in (2.11),
- for each f_i, the mean radiative temperature T_{mr}, from T and γ in (2.120),

The conversion from zenithal attenuations to attenuations along a slant path at a given elevation is achieved using the cosecant law, which assumes a stratified atmosphere. T_{mr} varies little over time or elevation and can be approximated by its monthly means $\bar{T}_{mr}(f_i)$ with an acceptable error [101]. It enables the estimation of $A_{nr}(f_i)$ from $T_b(f_i)$ using (2.122).

The problem of $f_j \neq f_i$ is then solved by combining linearly multiple radiometric channels [101]

$$A_{nr}(f_j) \approx a_0(f_j) + \sum_i a_i(f_j) A_{nr}(f_i) \tag{2.123}$$

where a_0 and each a_i are obtained by linear regression.

At least two radiometric channels, one centred around 20 GHz close to the water vapour absorption peak seen in Fig. 2.1, and one nearer to 30 GHz are often used to estimate $A_{nr}(f_j)$ with a sufficient discrimination between water vapour and clouds. More frequencies f_j are useful for the purpose of higher accuracy. A procedure to estimate the accuracy of the radiometric attenuation is given in the next section.

2.6.3 Accuracy of the radiometric attenuation

Taking from [104], the following procedure was formulated to estimate the accuracy of the attenuation obtained by combining the measurements of a certain number of radiometric channels. The methodology turned out to be almost the same as in [105], but differs as it extends to (2.123) for multiple frequencies and as it considers an average instead of a worst case scenario.

The accuracy of the measured radiometric attenuation is the standard deviation of the error ϵ_{nr} (dB) defined as

$$\epsilon_{nr}(f) \triangleq A_{nr}^{MWR}(f) - A_{nr}^{*}(f) \tag{2.124}$$

where A_{nr}^{MWR} (dB) and A_{nr}^{*} (dB) are respectively the measured and the true radiometric attenuations given by

$$A_{nr}^{MWR}(f) = 10 \log_{10} \left(\frac{\bar{T}_{mr}(f) - T_c}{\bar{T}_{mr}(f) - T_b(f)} \right) \tag{2.125}$$

$$A_{nr}^{*}(f) = 10 \log_{10} \left(\frac{T_{mr}^{*}(f) - T_c}{T_{mr}^{*}(f) - T_b^{*}(f)} \right) \tag{2.126}$$

with the true temperatures also denoted by an asterisk. It is more convenient to replace the true temperatures T_b^* and T_{mr}^* in (2.126) by defining the errors in temperature ζ and ξ as

$$\zeta(f) \triangleq T_b(f) - T_b^{*}(f) \tag{2.127}$$

$$\xi(f) \triangleq \bar{T}_{mr}(f) - T_{mr}^{*}(f) \tag{2.128}$$

whose standard deviations can be estimated respectively from the instrumental characteristics of the radiometer, and from the error caused by taking the

monthly mean $\bar{T}_{mr}$. The error is then a random function $\epsilon_{nr}(T_b, \zeta, \xi)$ and by linearisation around a point $(\bar{T}_b, 0, 0)$ its variance becomes

$$\sigma^2_{\epsilon_{nr}}(f) \approx \left(\frac{\partial \epsilon_{nr}}{\partial \zeta}(f)\right)^2 \sigma^2_\zeta + \left(\frac{\partial \epsilon_{nr}}{\partial \xi}(f)\right)^2 \sigma^2_\xi \tag{2.129}$$

$$\frac{\partial \epsilon_{nr}}{\partial \zeta}(f) = \frac{10}{\ln 10} \frac{1}{\bar{T}_{mr}(f) - \bar{T}_b(f)} \tag{2.130}$$

$$\frac{\partial \epsilon_{nr}}{\partial \xi}(f) = \frac{10}{\ln 10} \left(\frac{1}{\bar{T}_{mr}(f) - T_c} - \frac{1}{\bar{T}_{mr}(f) - \bar{T}_b(f)}\right) \tag{2.131}$$

where it has been assumed that the errors $\zeta(f)$ and $\xi(f)$ are independent.

If the attenuation must be retrieved from (2.123), then

$$\sigma^2_{\epsilon_{nr}}(f_j) \approx \sum_i a_i^2(f_j)\sigma^2_{\epsilon_{nr}}(f_i) + \sum_{k \neq l} a_k(f_j)a_l(f_j)\sigma_{\epsilon_{nr}}(f_k)\sigma_{\epsilon_{nr}}(f_l)r_{kl} \tag{2.132}$$

where the correlations between the errors at different frequencies r_{kl} are assumed to be nonnegative, i.e. $r_{kl} \in [0, 1]$.

A direct implementation of the methods presented here and in the previous section is found later, tied to the presentation of some results, in Sec. 6.1.2.

2.7 Other measurements or ancillary data

In addition to the measurements performed with propagation beacons and with microwave radiometers, traditionally the main devices for the characterisation of the tropospheric propagation, there are many other type of datasets which are related to the attenuation components or the atmospheric quantities entering into their modelling. This last section of this chapter reviews in a few words some of the most important ones and those most relevant for this thesis.

2.7.1 Weather radars

The main objective of radars, named for "radio detection and ranging", is to measure the position and velocity of remote objects by emitting radio-waves in their direction and measuring the reflected signal. Weather radars are particularly interested in the detection of hydrometeors, and they are commonly pulse-Doppler radars, with one antenna for both emission and detection [106]. The choice of the radar frequency and polarisation must account for:

- the size of the targets. For rain drops Rayleigh scattering is applicable for frequencies of a few GHz.
- the desired range. At higher frequencies the attenuation becomes a concern. Dual-polarisation radars alleviate the issue by providing means to correct for the attenuation.
- the size of the antenna. Higher frequencies require smaller antennas which tend to reduce the cost of building/operating/maintaining the system.

The primary output of the weather radar is the reflectivity Z [$\mathrm{mm^6 m^{-3}}$], usually given in logarithm form as

$$\mathrm{dB}_Z = 10 \log_{10}(Z), \tag{2.133}$$

and a function of the sixth moment of the rain dropsize distribution as

$$Z = \int_0^\infty N_d(D_d) D_d^6 dD_d \times 10^{18} \tag{2.134}$$

with as before D_d in [m]. This means radar measurements are linked to the other moments if the form of the dropsize distribution is known (see Sec. 2.3.2). Indeed, the reflectivity Z and the rain rate R_{rain} [$\mathrm{mm\,h^{-1}}$] are related by

$$Z = a R_{rain}^b \tag{2.135}$$

with the typical parameters $a = 200$, $b = 1.6$ for mid-latitudes and stratiform precipitations [107]. Note that these values of the parameters a and b are improved empirically from the original findings of Marshall and Palmer of $\Lambda_d = 4.1 \times 10^3 R_{rain}^{-0.21}$ $\mathrm{m^{-1}}$ [48] which with (2.134) lead to the values $a = 296$ and $b = 1.47$ for consistency with the Marshall-Palmer distribution [108]. Note also that combining the Marshall-Palmer distribution with the raindrop terminal velocity formula $v_d(D_d) = 386.6 D_d^{0.67} \mathrm{m\,s^{-1}}$ of Atlas and Ulbrich [109] leads to $a = 238$ and $b = 1.5$ using (2.134) and (2.70).

Finally note that the reflectivity is also affected by hail and high dB_Z values could predict incorrectly high rain rates if not handled appropriately [110].

2.7.2 Rain gauges and disdrometers

As explained at the end of Sec. 2.3.9, the value of the rain rate at the ground is a good substitute if no information in volume is available.

Rain gauges are widespread equipments to measure the ground rain rate. There are diverse systems with their own practical issues, but the general idea is to measure, e.g. by weighting, how fast a container is filled by the rain.

Disdrometers have a more sophisticated working principle than rain gauges. The effect of individual drops are better accounted for as they cross a beam or fall on a plate. Hence disdrometers also provide the dropsize distribution.

2.7.3 Radiosoundings and synoptic observations

The modelling of the atmospheric propagation is of course not limited to rain. Acting as references for the thermodynamic state (pressure, temperature, water vapour, wind velocities, ...) of the atmosphere, there two type of measurements typically carried out near meteorological offices, airports or military bases.

Radiosoundings observations (RAOBs) work with balloons launched from the ground and rising upwards until they pop from the lack of pressure. The ballons carry the sensors and the measurements are communicated down periodically. They provides vertical profiles of the atmosphere up to a couple of times per day, and with usual resolutions in the tens of meters.

Synoptic observations (SYNOPs) encompass all sort of standardized surface weather observations from barometer, thermometer (2 m temperature), anemometer (10 m winds), ... Some qualitative or semi-qualitative descriptions of the weather as seen from the location are also often available. The latter type of measurements includes e.g. the cloud cover in oktats (eighths of the sky), with information about the type of clouds (stratiform, convective) at different altitudes (low, medium, high), or the presence of overcast, fog, mist, haze, drizzle, showers, thunderstorms, snow, ...

2.7.4 GNSS delays

The Global Navigation Satellite Systems (GNSS) comprise the American Global Positioning System (GPS), the Russian Global Navigation Satellite System (GLONASS), the European Galileo, and the Chinese BeiDou. With those systems, a couple dozen of satellites are visible from any location on Earth. A combination of the propagation delays measured from some of them offers an accurate way to retrieve the integrated water vapour content, which in turns is sufficient for an accurate modelling of the gaseous attenuation [111, 112].

2.7.5 Others

It is clear that there are many more measurement systems, ground-based or spaceborne, with potential ties to the atmospheric propagation. Some examples are the Earth observation satellites' radiances, data from planes or buoys, tower masts, sun-tracking radiometers, high frequency cloud radars, ceilometers, or other specialized apparatus like scintillometers.

Though they are not themselves measurements, NWPs are particularly useful simulated data based on the assimilation of a lot of measurements. The main principles behind them and their utility relatively to the simulation of propagation impairments is the topic of the next chapter.

2.8 Concluding remarks

This chapter went through the following content and for the following reasons:

- in Sec. 2.1, the atmospheric refractivity N. The imaginary part N'' leads to the concepts of specific attenuation γ in (2.10) and attenuation A in (2.11) via the integration of γ along the path. The attenuation is the primary propagation impairment of concern for this thesis and its definition enters in the models in use from Chap. 5 to 7. The real part N_0 is also shown in (2.6) as a function of (T, p, p_{vap}): refraction on Earth-space paths is neglected throughout the thesis, though the refractive index intervenes in its structure constant given in (2.103), which serves as a basis for the identification of scintillation conditions later in Sec. 7.3.

- in Sec. 2.2, the contribution of the atmospheric gases (essentially oxygen and water vapour) to the attenuation through molecular absorption. Two methods to compute γ_{gases} from (T, p, p_{vap}) are reviewed in Sec. 2.2.2

(line-by-line) and 2.2.3 (approximation). The methods are shown to be practically equivalent in Fig. 2.1. Hence, and as it is faster to compute, the approximation is used with NWP data in Sec. 5.2.4, 6.2, or 7.1.3.

- in Sec. 2.3, the contribution of clouds and rain to the attenuation caused by absorption and scattering by water drop(let)s. Two models in (f, T) for the refractivity of water (ITU-R and Ray) are introduced in Sec. 2.3.1 and shown to be nearly equivalent in Fig. 2.2. The dropsize distribution N_d is introduced in Sec. 2.3.2, with the Marshall-Palmer distribution for rain in (2.67) and in Fig. 2.3, and assuming that the knowledge of the exact distribution is unnecessary for clouds. From Mie scattering in Sec? 2.3.3, the specific attenuation γ_{ext} of extinction by drops in (2.71) uses N_d. However with the Rayleigh scattering approximation in Sec. 2.3.4, only the third moment of N_d is shown to be needed, as seen with Fig. 2.4. Hence γ_{cloud} is given by (2.10) and (2.87) as function of (T, $M_{cloud,l}$). The Salonen and Mattioli models, as options to obtain $M_{cloud,l}$ from (T, p, RH), are described in Sec. 2.3.6 and 2.3.7. The cloud models are applied in Sec. 5.2.5, 6.2, and 7.1.4. For γ_{rain}, values of (T, M_{rain}) are needed and a look-up table approach is suggested as in Fig. 2.5. Another approach with the rain rate is given in Sec. 2.3.9 by the power law (2.96) whose coefficients are in Fig. 2.6. The rain models are applied in Sec. 5.2.6, depending on the data that is available.

- in Sec. 2.2.4 and 2.3.10, the ITU-R CCDF models for gases, clouds, rain, and total attenuation. They serve as a reference in Sec. 5.2, 7.1 and 7.2.

- in Sec. 2.4, the amplitude scintillation χ given by (2.102). As stated earlier, (2.6) and (2.103) are applied in Sec. 7.3. The other concepts, such as the scintillation variance σ_χ in (2.104) or (2.106), and the scintillation spectrum W_χ in (2.108), are only presented here for context.

- in Sec. 2.5, the extraction of the excess attenuation from beacon data. The excess attenuation A_{exc} is obtained as in (2.116) and as illustrated in Fig. 2.7. The relation with the total attenuation A_{tot} in (2.117) shows the need for a separate estimate of the nonrainy attenuation A_{nr} (gases and clouds) as in (2.118). This situation is relevant to the validation in Chap. 6 and found for a large number of ground stations in Sec. 7.1.

- in Sec. 2.6, the extraction of the nonrainy attenuation from a radiometer's brightness temperatures. In the absence of scatterers, the brightness temperature T_b in (2.119) has an equivalent attenuation as in (2.122). A calibration method leads to (2.123) to estimate the attenuation at any desired frequency. The accuracy of this estimate is obtained in (2.132). These methods are applied in Chap. 6, particularly in Sec. 6.1.2.

- in Sec. 2.7, a brief review of other useful measurements. Importantly, weather radar data are used in Chap. 5. Radiosoundings data are involved in the calibration of the radiometric data of Chap. 6, whereas rain gauges and synoptic observations data help Chap. 6 discussion, and whereas GNSS data are also cited here as a point of comparison.

Chapter 3

Numerical Weather Predictions

The chapter is conceived as a practical introduction to understand the use of NWPs within this thesis. Firstly, a broad overview of NWPs is given (see Sec. 3.1), along with basic information about relevant NWP models, and the origin of the partial differential equations at the center of the models. Then, words are spent on the general strategy to discretise and solve the problem, on the necessary initial and boundary conditions and where to get them, and on the additional parametrisations to model subgrid physical processes (see Sec. 3.2). Finally, the typical output of a NWP model, useful for propagation modelling, is described (see Sec. 3.3), with an emphasis on the thermodynamic conversions necessary to obtain the quantities found in Chap. 2.

3.1 Overview of Numerical Weather Predictions

The first section of this chapter lays out a rapid overview about Numerical Weather Predictions (NWPs), with some more details not already in Sec. 1.3.

3.1.1 General principles of NWP

The role of NWPs is, as their name indicates, to predict the weather through numerical means (i.e. computer simulations). What is understood by prediction can be either a true prediction of how the weather will be from a few hours to days in the future, i.e. a forecast, or an analysis to reconstruct as faithfully as possible past states of the atmosphere. Numerically, NWPs are a very involved process, as the weather includes many subprocesses at different temporal and spatial scales. Correspondingly there are different scales at which NWPs operate and the existence of both global or regional models.

3.1.2 Global NWP models

Global NWP models consider, also as their name indicates, the system composed by the entire Earth atmosphere and surface. As running a global model requires to collect and assimilate data for the entire world, very few organisations are capable of such a feat. The best known global models available to the public are run by the European Centre for Medium Range Weather Forecasts (ECMWF), with the Integrated Forecast System (IFS), and the National Center for Atmospheric Research (NCAR), with the Global Forecast System

(GFS). As will be discussed further in Sec. 3.2.6, data from global models are of great interest as initialisation and boundary conditions for anyone wishing to run NWPs at a regional level.

3.1.3 Regional NWP models

Regional NWP models, also called limited area models, are models which are indeed limited to a certain area of the globe. The modelling strategy in terms of simulation grids is significantly different from global models, first and foremost as regional domains do not benefit from the closed system and periodic boundary conditions obtained by considering the entire Earth. These boundary conditions must then be specified externally, and the most natural sources of data for this task are the global NWP models themselves.

Note that the distinction between forecast and analysis is a bit more nuanced for a regional model. Even in the absence of data assimilation and variational analysis, a regional model is not necessarily a real forecast. Indeed, if the model is driven by boundary conditions from a global analysis, it has then access to future information from its starting time. Using this approach the performances of the regional model are expected to be better than with boundary conditions from a global forecast. In a situation where a forecast is actually needed, i.e. no global analyses are available, then the sole option is indeed to fix the boundaries with a global forecast.

In this work, certain NWP models will be of use. The Weather Research and Forecasting (WRF) software by NCAR [113], and more specifically the Advance Research WRF (ARW) solver [114], is the primarily model exploited for the simulations of propagation impairments. This NWP model is freely available and hence a popular research tool. Some other NWP models used in propagation research were mentioned in Sec. 1.4. In this thesis, the only other regional NWP models in use will be the Belgian ALARO model [115] (see Chap. 5) and the Norwegian AROME-Arctic model [116] (see Sec. 7.3).

3.1.4 Primitive equations

At the origin of the NWP modelling, there are a set of Partial Differential Equations (PDEs) to describe the movement of the moist air. These equations are called the primitive equations [117] and are essentially an appropriate rendition of these principles well known in physics as in fluid mechanics:

- conservation of mass (a.k.a. continuity),
- conservation of momentum,
- conservation of energy.

In the case of the non-hydrostatic solver WRF-ARW, the set of PDEs takes a form known as Euler equations. The description of how these equations are formulated and implemented in practice is given in the note in [113]. Some parts of the next section will be based on the content of that note.

But first, in order to illustrate the primitive equations in more generality, here are the (cartesian) conservation equations of continuum mechanics

$$\frac{\partial \rho}{\partial t} + \nabla \cdot (\rho \mathbf{v}) = F_\rho \tag{3.1}$$

$$\frac{\partial \rho \mathbf{v}}{\partial t} + \nabla \cdot (\rho \mathbf{v}\mathbf{v}) - \nabla \cdot \boldsymbol{\sigma} - \rho \mathbf{g} = F_\mathbf{v} \tag{3.2}$$

$$\frac{\partial \rho u_e}{\partial t} + \nabla \cdot (\rho u_e \mathbf{v}) - \boldsymbol{\sigma} : \mathbf{d} = F_{u_e} \tag{3.3}$$

which introduces the following variables:

- ρ [kg/m^3] the density of the continuum/fluid (here: the air),
- $\mathbf{v}$ [m/s] the velocity vector,
- u_e [J/kg] the internal energy per unit mass,
- $\boldsymbol{\sigma}$ [N/m^2 = Pa] the stress tensor,
- $\mathbf{d}$ [s^{-1}] the strain rate tensor,
- $\mathbf{g}$ [m/s^2] the body forces per unit mass (i.e. gravity),
- F_ρ [kg m^{-3} s^{-1}] a source/forcing rate of mass per unit volume,
- $F_\mathbf{v}$ [kg m^{-3} s^{-1}] a source/forcing rate of momentum per unit volume,
- F_{u_e} the [J m^{-3} s^{-1}] a source/forcing rate of energy per unit volume.

Generally it is assumed in (3.21) that there is no creation of mass, so that $F_\rho = 0$. The conservation of momentum equation (3.2) is only valid in an inertial frame of reference so that the term $F_\mathbf{v}$ includes a contribution from a non-inertial frame of reference (for the Earth rotating at constant angular speed, it is the Coriolis effect). Another contribution of note to $F_\mathbf{v}$ is the turbulent motion. For the conservation of energy equation (3.3), the term F_{u_e} includes notably contributions from radiative transfer, phase transitions, turbulence, ...

The strain rate tensor $\mathbf{d}$ is defined as

$$\mathbf{d} = \frac{1}{2}(\nabla \mathbf{v} + \nabla \mathbf{v}^T) \tag{3.4}$$

while, for a newtonian fluid, the stress tensor $\boldsymbol{\sigma}$ is obtained as

$$\boldsymbol{\sigma} = -p\boldsymbol{\delta} + \boldsymbol{\tau} \tag{3.5}$$

with p [Pa] the pressure, $\boldsymbol{\delta}$ [/] the Kronecker delta tensor (i.e. identity matrix in the context), and $\boldsymbol{\tau}$ [Pa] the deviatoric or viscous stress tensor. If one assumes $\boldsymbol{\tau} \neq 0$, one obtains the more general Navier-Stokes equations. If one assumes $\boldsymbol{\tau} = 0$, that is the viscosity of the fluid is also null (inviscid flow), then one obtains the Euler equations.

The Euler equations for momentum and energy are

$$\frac{\partial \rho \mathbf{v}}{\partial t} + \nabla \cdot (\rho \mathbf{v}\mathbf{v}) + \nabla p - \rho \mathbf{g} = F_{\mathbf{v}} \tag{3.6}$$

$$\frac{\partial \rho u_e}{\partial t} + \nabla \cdot (\rho u_e \mathbf{v}) + p \nabla \cdot \mathbf{v} = F_{u_e}. \tag{3.7}$$

In order to make the link between the thermodynamic variables present in the primitive equations, considering the air as an ideal gas allows to write

$$p = \rho R_{air} T \tag{3.8}$$

which is the ideal gas law as equation of state, making the temperature T [K] appear, and with $R_{air} = 287.058\,\mathrm{J\,K^{-1}\,kg^{-1}}$ the ideal gas constant for dry air. With $R = 8.314\,\mathrm{J\,K^{-1}\,mol^{-1}}$ the universal gas constant, this corresponds to a molar mass of 28.96 g/mol for dry air of average composition (approximately 78 % N_2, 21 % O_2, and 1 % Ar). For an ideal gas, the following also holds

$$u_e = c_v T \tag{3.9}$$

$$c_p = c_v + R_{air} \tag{3.10}$$

where c_v [$\mathrm{J\,K^{-1}\,kg^{-1}}$] and c_p [$\mathrm{J\,K^{-1}\,kg^{-1}}$] are the specific heat capacities of dry air at constant volume (isochoric) and constant pressure (isobaric) respectively. At $T = 0\,^{\circ}\mathrm{C}$ and $p = 1\,\mathrm{atm}$, $c_p = 29.07\,\mathrm{J\,K^{-1}\,mol^{-1}} = 1003.7\,\mathrm{J\,K^{-1}\,kg^{-1}}$. The practical interest of these formulas here is to show that by combining them with the conservation of energy equation (3.3) it is possible to write prognostic equations for pressure and temperature.

Starting from (3.3), and then using (3.8) and (3.9) to replace ρ and u_e, one immediately obtains

$$\frac{c_v}{R_{air}} \left\{ \frac{\partial p}{\partial t} + \nabla \cdot (p \mathbf{v}) \right\} + p \nabla \cdot \mathbf{v} = F_{u_e}. \tag{3.11}$$

where only the pressure p and velocity $\mathbf{v}$ intervene. A more compact version of (3.11) is found with the material derivative defined as

$$\frac{D}{Dt} = \frac{\partial}{\partial t} + \mathbf{v} \cdot \nabla \tag{3.12}$$

by developing $\nabla \cdot (p\mathbf{v}) = (\nabla p) \cdot \mathbf{v} + p \nabla \cdot \mathbf{v}$ and by using (3.10) so that

$$\frac{Dp}{Dt} + \frac{c_p}{c_v} p \nabla \cdot \mathbf{v} = F_{u_e} \frac{R_{air}}{c_v} \tag{3.13}$$

which is a cartesian form found e.g. in [118].

To express the conservation of energy in terms of temperature, it is convenient to first rewrite the conservation of energy (3.7) in terms of material derivative by expending the terms (ρu_e) and $(\rho u_e \mathbf{v})$, and then by simplifying the results with the conservation of mass equation (3.21) assuming $F_\rho = 0$. Then

$$\frac{Du_e}{Dt} + \frac{p}{\rho} \nabla \cdot \mathbf{v} = \frac{F_{u_e}}{\rho} \tag{3.14}$$

and by using again the conservation of mass written as

$$\frac{1}{\rho}\nabla \cdot \mathbf{v} = -\frac{1}{\rho^2}\frac{D\rho}{Dt} = \frac{D\alpha}{Dt} \tag{3.15}$$

with $\alpha = \rho^{-1}$ the inverse density it becomes, including also (3.9),

$$c_v \frac{DT}{Dt} + p\frac{D\alpha}{Dt} = \frac{F_{u_e}}{\rho} \tag{3.16}$$

or, from (3.8) and (3.10),

$$c_p \frac{DT}{Dt} - \alpha\frac{Dp}{Dt} = \frac{F_{u_e}}{\rho} \tag{3.17}$$

which is also a cartesian form found e.g. in [118]. From (3.17) it is notable that in adiabatic conditions ($F_{u_e} = 0$) the relation between T and p leads to

$$\frac{T_0}{T} = \left(\frac{p_0}{p}\right)^{\frac{R_{air}}{c_p}} \tag{3.18}$$

where T_0 and p_0 are two reference values. For $p_0 = 10^5$ Pa, one then introduces the potential temperature θ [K] such that $\theta \triangleq T_0$ as in (3.18). Hence (3.17 ultimately simplifies to

$$\frac{D\theta}{Dt} = \frac{F_{u_e}}{\rho c_p}\frac{\theta}{T} \triangleq F_\theta \tag{3.19}$$

which means an equation involving only θ and a forcing term F_θ is obtained.

Since the equations discussed so far were all in connection to the dry air, it is necessary to introduce water vapour into them to model a realistic atmosphere. The density of air can be decomposed as

$$\rho = \rho_{dry} + \rho_{vap} \tag{3.20}$$

with ρ_{dry} [kg/m^3] the density of dry air and ρ_{vap} [kg/m^3] the density of water vapour. It means, for a start, that the conservation of mass (3.21) can be split by linearity and that for water vapour one finds

$$\frac{\partial \rho_{vap}}{\partial t} + \nabla \cdot (\rho_{vap}\mathbf{v}) = F_{\rho_{vap}} \tag{3.21}$$

where unlike for dry air, $F_{\rho_{vap}} \neq 0$ due to phase changes in water. The ideal gas law applied to dry air and water vapour are

$$p_{dry} = \rho_{dry} R_{air} T \tag{3.22}$$

$$p_{air} = \rho_{vap} R_{water} T \tag{3.23}$$

where $R_{water} = 461.52\,\mathrm{J\,K^{-1}\,kg^{-1}}$. It is customary to rewrite them as

$$p = \rho_{dry} R_{dry} T_v \tag{3.24}$$

$$T_v = T\left(1 + \frac{R_{water}}{R_{air}}\frac{\rho_{vap}}{\rho_{dry}}\right) = T\left(1 + \frac{R_{water}}{R_{air}} q_{vap}\right) \tag{3.25}$$

by introducing the virtual temperature T_v [K], and the water vapour mass mixing ratio q_{vap} [kg/kg]. The consequences on the other conservation equations are not presented in this text, see e.g. [119] for a treatment of the problem.

3.2 Simulation grid, coordinates and solvers

This section presents the necessary know-how about running a NWP model properly, more particularly WRF-ARW with input data from ECMWF.

3.2.1 Vertical coordinates

Most NWP models use a pressure-based coordinate in the vertical direction from the ground. Instead of fixed pressure levels, the coordinate is generally designed to be terrain-following near the ground and tends towards fixed pressure only near the top of the atmosphere.

In WRF-ARW version 3.7.1, the vertical coordinates are called η coordinates and are defined as [113]

$$\eta(p_h, p_{hs}) = \frac{p_h - p_{ht}}{p_{hs} - p_{ht}} \tag{3.26}$$

where p_h [Pa] is the hydrostatic pressure, p_{hs} [Pa] is the hydrostatic pressure at the surface, and p_{ht} [Pa] is the hydrostatic pressure at the top of the atmosphere. The concept is illustrated in the Fig. 3.1. As can be seen, $\eta(p_{hs}, p_{hs}) = 1$ at the surface, and $\eta(p_{ht}, p_{hs}) = 0$ at the top. The details of the consequence of this definition on the PDEs are not relevant to the level of this document and can be found in [113]. However an important point to make clear is that, because both the pressure and the surface pressure are a function of the time and space, a fixed value of η does not correspond to a fixed altitude. But, due to the nature of the stratification in the atmosphere, decreasing values of the η coordinate can be associated with monotonically increasing altitudes.

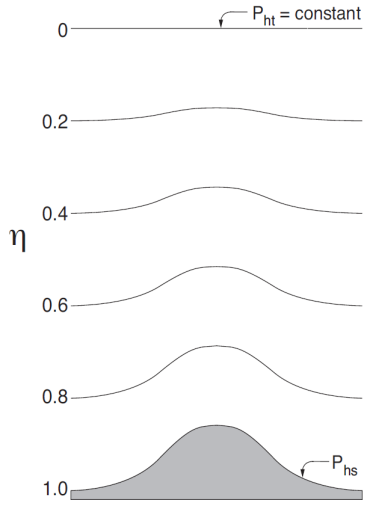

Figure 3.1 – WRF vertical coordinates [113].

3.2.2 Horizontal coordinates and map projection

Horizontally to Earth surface, regional NWP models use pseudo-cartesian coordinates (x, y) with horizontal resolutions Δx and Δy. Generally $\Delta x = \Delta y$.

The coordinates (x, y) are defined by a map projection, typically the Lambert Conformal Conic (LCC) projection. For the spherical Earth, the projection is specified thanks to the following functions of the latitude φ [120]

$$\left\{ \begin{array}{lcl} m(\varphi) & = & \cos(\varphi) \\ t(\varphi) & = & \tan(\pi/4 - \varphi/2) \end{array} \right. \tag{3.27}$$

which are computed at the projection's true latitudes φ_1 and φ_2 as $m_1 = m(\varphi_1)$, $m_2 = m(\varphi_2)$, $t_1 = t(\varphi_1)$, $t_2 = t(\varphi_2)$ and then further deliver

$$n = \left\{ \begin{array}{ll} \dfrac{\log(m_1/m_2)}{\log(t_1/t_2)} & \varphi_1 \neq \varphi_2 \\ \sin(\varphi_1) & \varphi_1 = \varphi_2 \end{array} \right. \tag{3.28}$$

$$F = m_1/(nt_1^n) \tag{3.29}$$

which are all that is needed to convert from a latitude-longitude point (φ, λ) to the maps coordinates (x, y) and back.

The forward conversion uses (ρ, τ) as a function of (φ, λ)

$$\left\{ \begin{array}{lcl} \rho & = & RF \tan^n(\pi/4 - \varphi/2) \\ \tau & = & n(\lambda - \lambda_0) \end{array} \right. \tag{3.30}$$

and then

$$\left\{ \begin{array}{lcl} x & = & \rho \sin(\tau) \\ y & = & \rho_0 - \rho \cos(\tau) \end{array} \right. \tag{3.31}$$

while the backward conversion uses (ρ, τ) as a function of (x, y)

$$\left\{ \begin{array}{lcl} \rho & = & \mathrm{sign}(n)\sqrt{x^2 + (\rho_0 - y)^2} \\ \tau & = & \mathrm{arctan2}(\mathrm{sign}(n)x, \mathrm{sign}(n)(\rho_0 - y)) \end{array} \right. \tag{3.32}$$

and then

$$\left\{ \begin{array}{lcl} \varphi & = & 2\arctan((\frac{RF}{\rho})^{1/n}) - \pi/2 \\ \lambda & = & \frac{\tau}{n} + \lambda_0 \end{array} \right. \tag{3.33}$$

where in both cases R is the radius of the Earth, and where the origin of the projection coordinates is written as either (φ_0, λ_0), (ρ_0, τ_0), or (x_0, y_0).

3.2.3 Simulation grids

Equipped with both the definition of the vertical coordinates in Sec. 3.2.1 and the horizontal coordinates in Sec. 3.2.2, the simulation grids are conceived as shown in the Fig. 3.2. The grids are Arakawa C-grid, where the thermodynamic variables (e.g. the potential temperature θ) are defined at the center of a grid cell, whereas the wind velocity components (u_g, v_g, w_g) are defined on the edges of the grid and are thus referred to as "staggered" variables.

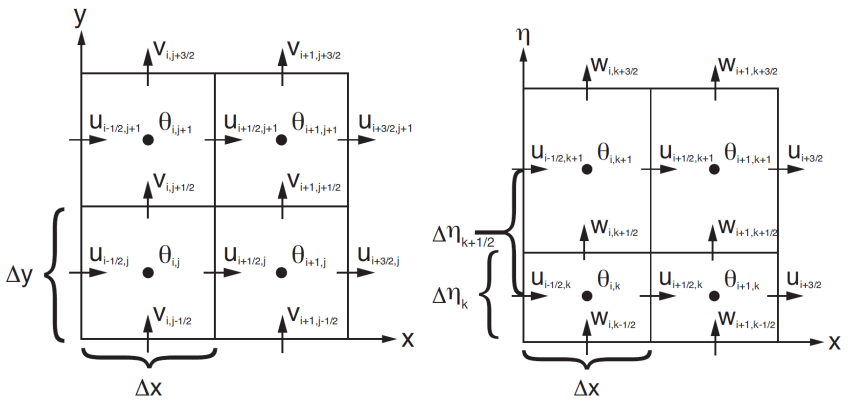

(a) Horizontal grid (b) Vertical grid

Figure 3.2 – WRF horizontal and vertical grids [113].

3.2.4 Nesting

WRF enables horizontal domains nesting when compiled with the proper option. This allows the spatial resolution to be increased locally at a reasonable cost in computing power/time. There are several ways to perform nested runs in WRF:

- 1-way nesting with consecutive runs. The output of a run on a coarse grid domain can be post-processed to start a run on a nested fine grid domain.

- 1-way nesting with concurrent runs. In a single run the information from a coarse grid domain is fed to nested fine grid domains at each time step.

- 2-way nesting with concurrent runs. In a single run the information from a coarse grid domain is fed to nested fine grid domains at each time step, and then fed back to the coarse grid domain.

Nesting follows simple inheritance (see Fig. 3.3). A parent domain can have many nested children domains, but a child domain can only have one parent. Nesting can span multiple levels in that a nested domain may be a parent to nested domains itself. For 2-way nesting it is also forbidden to have overlapping domains as it creates ambiguity regarding feedback.

Grid ratios are usually chosen to be odd integers so that parent grid points become coincident child grid points (see Fig. 3.4). Moreover, for 2-way nesting, this means there is no ambiguity regarding feedback. Preferred grid ratios are 3 or 5 as those have abundantly been tested and are reasonably small.

1-way nesting with concurrent runs will be the default choice in this work and feedback will be turned off.

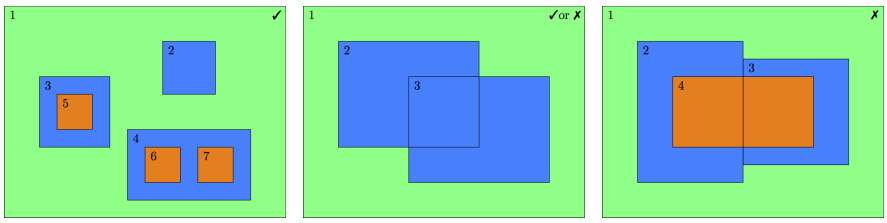

(a) Valid nests (b) Overlapping nests (c) Invalid nests

Figure 3.3 – WRF nesting rules

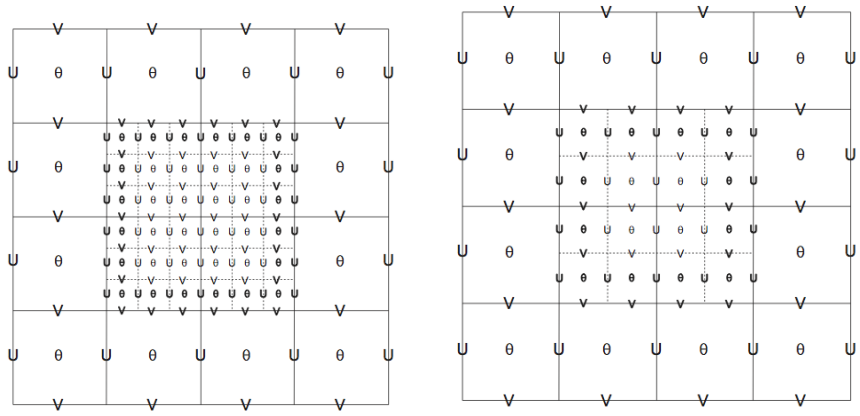

(a) Odd grid ratio (3) (b) Even grid ratio (2)

Figure 3.4 – WRF nesting grid ratios [113]

3.2.5 Discretisation in time

Besides the definition of the simulation grids with appropriate coordinates to discretise the problem in space, there is also the question on how to best integrate the PDEs in time. The example of the special Runge-Kutta 3 scheme in use by WRF-ARW is amply described in [113].

A more practical consideration here however concerns the option in WRF to use adaptive time steps. Thanks to the estimation of a stability criterion, the Courant–Friedrichs–Lewy (CFL) condition inside one of the simulation domain, it becomes possible to control the size of the temporal integration step. This approach has the first advantage to avoid that the instabilities due to strong winds cause a crash of the NWP run. It also has the second advantage to allow for a larger time step on average, unlike fixed time steps which much be small enough to avoid a crash in most circumstances. Therefore adaptive time steps permit to reduce the computing cost of NWP runs, while being generally safer. On the other hand, this is in some ways still an experimental feature of WRF. By using non-fixed time steps, an additional source of variability in the behaviour of the run is also added on top of the initial conditions.

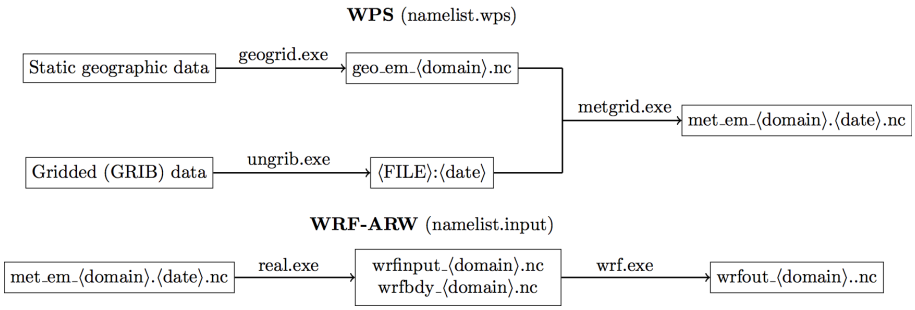

Figure 3.5 – WRF-ARW work flow

3.2.6 Initial and boundary conditions

In the workflow of WRF-ARW (see Fig. 3.5), the WRF Pre-processing System (WPS) requires two types of initialisation data:

- static geographic data (e.g. land use, vegetation, soil albedo) fed to `geogrid.exe`.
- dynamic atmospheric data (usually in GRIB format) fed to `ungrib.exe` and then, together with the output of `geogrid.exe`, to `metgrid.exe`.

The latter type of data must be provided by a global model. Here the choice, in line with earlier works [36], is made to solely use ECMWF data. The required time varying initialisation data include:

- data in volume (on pressure levels), the geopotential, the temperature, the relative humidity, and the wind components.
- data at the surface, surface geopotential and pressure, 2 m temperature and dewpoint temperature, skin temperature, 10 m winds, temperature and humidity in the soil, land-sea and sea-ice flags, and snow water.

Note that the output of `metgrid.exe` must further enter in `real.exe` (vertical interpolation from pressure to η levels) before `wrf.exe` can start.

To highlight some initialisation options, the configuration and other characteristics of two different ECMWF archives are presented in the the Tab. 3.1.

The ERA-Interim archive is a re-analysis of primary interest. As a re-analysis, it covers a long period of time with a fixed version of the IFS. It is thus ideal for simulations that must cover long periods such as multiple years. ERA-Interim has a relatively coarse spatial resolution ($\sim$ 80 km). And it is actually in the process of being replaced by ERA-5, which has better horizontal and temporal resolutions as well as using a newer version of the IFS. However, ERA-Interim, despite its name, stayed the best ECMWF's re-analysis available for years and is well trusted as there are many studies based on it.

ECMWF operational archive represents the day-to-day simulations including the most up to date version of the IFS with the best horizontal resolution. However, this means that over longer periods there are changes in the IFS cycle

Configuration	ERA-Interim	Operational (1)	Operational (2)
IFS cycle	31r2	38r2 (06/2013)	41r2 (03/2016)
Time period	Jan 1979-Aug 2019	Aug 1982-now	
Spectral grid	N128	N640	O1280
Gaussian grid	T_L255	$T_{CO}1279$	
Horizontal res.	$\sim 0.75°$(80 km)	$\sim 0.125°$(16 km)	$\sim 0.1°$(9 km)
Vertical res. (pl)	37	25	
Vertical res. (ml)	60	137	
Temporal res.	Data every 6 h (00:00, 06:00, 12:00, 18:00 UTC)		

Table 3.1 – Comparison between ECMWF ERA-Interim re-analysis archive and operational analysis archives

being used. The most notable recent change shown in the Tab. 3.1 is a change in horizontal resolution in March 2016 (from $\sim$ 16 km to $\sim$ 9 km).

Another point of note regarding the initialisation data is the spin-up time. Because all the initialisation data in use are available every 6 h, the spin-up time given to the to simulation for variables to settle must be a multiple of 6 h. Typically 12 h to 24 h will be considered in this work.

3.2.7 Physical parametrisations

Last but not least in this section, the physical parametrisations are of paramount importance to produce meaningful output with a NWP model. The subgrid processes that must be modelled are:

- water microphysics, the formation of water species and their concentration (water vapour, rain, cloud water, cloud ice, snow, graupel, hail, ...).
- cloud physics, the formation of clouds not resolved by the grid resolutions.
- radiation physics, both short-wave (solar) and long-wave (Earth surface, infrared) radiations.
- surface layer physics, for the friction velocity, exchange coefficients and heat and moisture fluxes at the surface.
- planetary boundary layer (PBL) physics, eddies and turbulent kinetic energy as well as vertical diffusion.
- soil layer physics, soil temperature and moisture content as well as the fluxes that drive them.
- horizontal diffusion and damping.

Documentation and references on the physical parametrisations are available for the different models of interest in this work. For WRF, there are the notes [113, 114], but also a webpage gathering links to most of the papers for each individual parametrisation [121]. For ALARO (also ARPEGE, ALADIN, and AROME) the documentation is available on the CNRM website [122]. For

ECMWF, the information is well detailed within the IFS documentation [123], in "Part IV: Physical Processes", with the specifics of a given dataset depending on a particular IFS cycle (e.g. 31r2 for ERA-Interim, see Tab. 3.1).

Though all the parametrisations have their importance for an accurate modelling of the atmosphere, the physics of water and clouds are of particularly high interest in the context of the atmospheric attenuation.

In WRF the water microphysics option used throughout this work will be WRF single-moment 6 (WSM6) [124] or WRF double-moment 6 (WDM6) [125]. The water species involved are represented in Fig. 3.6 along with the existence of a direct conversion process between two water species. The double-moment microphysics adds concentrations for rain and cloud water drops, as well a cloud condensation nuclei. For WRF cloud physics, the results in this document use the Tiedtke scheme [126] or the Grell-Freitas scheme [127]. Tiedtke parametrises the cloud convection and must in principle be turned off at cloud resolving scales ($\sim< 3\,\mathrm{km}$). Grell-Freitas is scale aware, deactivating the effects of the convective parametrisation when it is not needed.

In ALARO, the models for water and clouds physics are described in the documentations on "deep convection" and "cloudiness and large scale precipitation" in [122]. Convection is modelled with updraught and downdraught, entrainment and detrainment, ... in a column, with contributions moisture convergence/evaporation, buoyancy, turbulence, ... The convective cloud content is obtained from the convective precipitation. The stratiform (large scale, shallow convection) cloud content is obtained from the water vapour. Cloudiness (cloud fractions) are diagnosed from the cloud contents and total cloudiness follows Xu and Randall. The large scale precipitation scheme uses the Marshall-Palmer rain dropsize distribution with an empirical terminal velocity and models evaporation and condensation to obtain the partition between liquid (rain) and solid precipitations (snow).

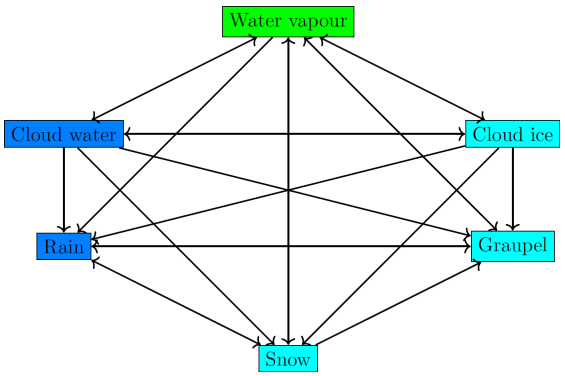

Figure 3.6 – WRF 6-species microphysics schemes (WSM6 and WDM6)

3.3 Description of the output

The last section of this chapter describes the typical output of a NWP run, especially variables useful for the modelling of propagation impairments. The output described is the one of WRF, though other models have similar output.

Variable	Description	Units	Dimensions	Symbol
`PH + PHB`	Geopotential	m^2/s	(nz+1, ny, nx)	ϕ_g
`T + 300`	Potential temperature	K	(nz, ny, nx)	θ
`P + PB`	Pressure	Pa	(nz, ny, nx)	p
`QVAPOR`	Vapour mixing ratio	kg/kg	(nz, ny, nx)	q_{vap}
`QCLOUD`	Cloud mixing ratio	kg/kg	(nz, ny, nx)	$q_{cloud,l}$
`QRAIN`	Rain mixing ratio	kg/kg	(nz, ny, nx)	q_{rain}
`RAINC`	Convective rain	mm	(ny, nx)	$\int_0^t R_{rain,c} dt$
`RAINNC`	Non-convective rain	mm	(ny, nx)	$\int_0^t R_{rain,nc} dt$
`U`	U wind (grid)	m/s	(nz, ny, nx+1)	u_g
`V`	V wind (grid)	m/s	(nz, ny+1, nx)	v_g
`W`	W wind	m/s	(nz+1, ny, nx)	w
`COSALPHA`	Map rotation cosine	/	(ny, nx)	$\cos\alpha$
`SINALPHA`	Map rotation sine	/	(ny, nx)	$\sin\alpha$
`XLAT`	Latitude	°E	(ny, nx)	φ
`XLONG`	Longitude	°N	(ny, nx)	λ

Table 3.2 – WRF output variables useful to model propagation impairments

3.3.1 Output variables

The NWP variables relevant to the computation of propagation impairments are given in the Tab. 3.2. Most of these variables are 3D variables, i.e. in volume, and have dimensions (nz, ny, nz) at any given time step. Notable exceptions are variables which are staggered along one dimension, such as the geopotential ϕ_g staggered in the vertical direction on nz+1 levels, or such as the grid wind component u_g staggered in the "east" direction on nx+1 levels. There are also some surface variables of dimensions (ny, nx) which have a particularly notable interest for propagation such as the accumulated rain.

Other useful surface variables are listed in the Tab. 3.3. They are mostly diagnostic variables, such as the 2 m temperature, i.e. used for comparison with other NWP models and/or synoptic measurements.

3.3.2 Geopotential

The geopotential ϕ_g [m^2/s] serves as the reference spatial vertical coordinate. It is converted to the geopotential height h [m] with

$$h = \frac{\phi_g}{g_0} \tag{3.34}$$

Variable	Description	Units	Dimensions
PSFC	Surface pressure	Pa	(ny, nx)
T2	2 m temperature	K	(ny, nx)
Q2	2 m vapour mixing ratio	kg/kg	(ny, nx)
U10	10 m U wind	m/s	(ny, nx)
V10	10 m V wind	m/s	(ny, nx)
QFX	Upward moisture flux	$\mathrm{kg\,m^{-2}\,s^{-1}}$	(ny, nx)
HFX	Upward heat flux	$\mathrm{W\,m^{-2}}$	(ny, nx)
LH	Latent heat flux	$\mathrm{W\,m^{-2}}$	(ny, nx)
GRDFLX	Ground heat flux	$\mathrm{W\,m^{-2}}$	(ny, nx)
SWDNB	Downwelling shortwave flux	$\mathrm{W\,m^{-2}}$	(ny, nx)
SWUPB	Upwelling shortwave flux	$\mathrm{W\,m^{-2}}$	(ny, nx)
LWDNB	Downwelling longwave flux	$\mathrm{W\,m^{-2}}$	(ny, nx)
LWUPB	Upwelling longwave flux	$\mathrm{W\,m^{-2}}$	(ny, nx)
TSLB	Soil temperature	K	(ns, ny, nx)
SMOIS	Soil moisture	$\mathrm{m^3\,m^{-3}}$	(ns, ny, nx)
SH2O	Soi liquid water	$\mathrm{m^3\,m^{-3}}$	(ns, ny, nx)

Table 3.3 – WRF surface and soil output variables useful for control

where $g_0 = 9.81\,\mathrm{m^2\,s^{-1}}$ is the standard Earth gravity. The geopotential height h is roughly equivalent to the altitude above mean sea level (amsl).

3.3.3 Thermodynamic state

In order to express the thermodynamic state of the atmosphere in a form convenient for the need of propagation computations, one has to first obtain the temperature T [K] from the potential temperature θ [K] and the pressure p [Pa] with

$$T = \theta \left(\frac{p}{10^5}\right)^{R/c_p} \tag{3.35}$$

where $R = 8.314\,\mathrm{J\,K^{-1}\,mol^{-1}}$ is the ideal gas constant, and $c_p = 29.07\,\mathrm{J\,K^{-1}\,mol^{-1}}$ is the isobaric specific heat capacity for dry air at sea level and 0 °C.

The water vapour partial pressure p_{vap} [Pa] is obtained from p and the water vapour mass mixing ratio q_{vap} [kg/kg] according to Dalton's law as in

$$p_{vap} = p\frac{q_{vap}}{q_{vap} + \frac{R_{air}}{R_{water}}} \tag{3.36}$$

with $R_{air} = 287.058\,\mathrm{J\,K^{-1}\,kg^{-1}}$ and $R_{water} = 461.52\,\mathrm{J\,K^{-1}\,kg^{-1}}$. The water vapour density ρ_{vap} [g/m^3] is alternatively further derived as

$$\rho_{vap} = \frac{p_{vap}}{R_{water}T} \times 10^3 \tag{3.37}$$

according to the ideal gas law. Furthermore, the relative humidity RH [%] is yet another formalism to express the humidity content and is given by

$$RH = 100\frac{p_{vap}}{p_{vap,s}} \tag{3.38}$$

where the water vapour pressure at saturation $p_{vap,s}$ [Pa] is obtained from [70]

$$p_{vap,s} = EF_{water} \times a \exp\left(\frac{(b - t/d)t}{t + c}\right) \tag{3.39}$$

with $t = T - 273.15$ [°C] and

$$EF_{water} = 1 + 10^{-4}(7.2 + 10^{-2}p(0.0320 + 5.9 \times 10^{-6}t^2)) \tag{3.40}$$

and $a = 611.21$ [Pa], $b = 18.678$ [/], $c = 257.14$ [°C], $d = 234.5$ [°C].

3.3.4 Liquid water

To obtain the densities of liquid water, it is first necessary to compute the dry air density ρ_{air} [g/m^3]

$$\rho_{air} = \frac{p}{R_{air}T} \times 10^3 \tag{3.41}$$

then the density of cloud liquid water $M_{cloud,l}$ [g/m^3] and the density of rain water M_{rain} [g/m^3] are simply obtained as

$$M_{cloud,l} = q_{cloud,l}\rho_{air} \tag{3.42}$$

$$M_{rain} = q_{rain}\rho_{air} \tag{3.43}$$

starting from the respective mass mixing ratio $q_{cloud,l}$ [kg/kg] and q_{rain} [kg/kg]/

In order to get the rain rate R_{rain} [mm/h] at a given time, one can use the accumulated rain rate at that time and at one output time interval Δt before. The contribution from the convective and non-convective rain must also be accounted for such that

$$R_{rain_c}(t) = \frac{\int_0^t R_{rain,c}dt - \int_0^{t-\Delta t} R_{rain,c}dt}{\Delta t} = \frac{\int_{t-\Delta t}^t R_{rain,c}dt}{\Delta t} \tag{3.44}$$

$$R_{rain_{nc}}(t) = \frac{\int_0^t R_{rain,nc}dt - \int_0^{t-\Delta t} R_{rain,nc}dt}{\Delta t} = \frac{\int_{t-\Delta t}^t R_{rain,nc}dt}{\Delta t} \tag{3.45}$$

$$R_{rain}(t) = R_{rain,c}(t) + R_{rain,nc}(t) \tag{3.46}$$

if $\Delta t \neq 1$ h (most often it is 5 min for WRF within this work) then the proper scaling factor must be applied to get the correct units.

3.3.5 Winds

The horizontal wind speeds u_g and v_g from WRF are grid relative, i.e. they follow the cartesian lines of the projection. In order to obtain instead the eastward horizontal wind speed u and the northward horizontal wind speed v, the local time-invariant rotation angle α of the map projection must be known. Then

$$u = u_g \cos\alpha - v_g \sin\alpha \tag{3.47}$$

$$v = u_g \cos\alpha + v_g \sin\alpha \tag{3.48}$$

after one has first unstaggered u_g and v_g by taking the means of each two consecutive points along their respective staggered direction.

3.3.6 Surface fluxes

The net surface radiative flux R_{net} [$\mathrm{W}^2\,\mathrm{m}^{-1}$] is found as

$$R_{net} = \texttt{SWDNB}\text{–}\texttt{SWUPB} + \texttt{LWDNB}\text{–}\texttt{LWUPB} \tag{3.49}$$

from the short- and long-wave radiative fluxes as defined in the Tab. 3.3.

The net surface flux E_{net} [$\mathrm{W}^2\,\mathrm{m}^{-1}$] is found as

$$E_{net} = \texttt{HFX} + \texttt{LX} - \texttt{GRDFLX} \tag{3.50}$$

from the heat fluxes as defined in the Tab. 3.3.

The surface energy balance is then attained when $R_{net} = E_{net}$.

3.4 Concluding remarks

In this section, the main considerations to have when running a NWP model were presented in relation with the WRF-ARW software.

The output of WRF-ARW for use with the propagation models of Chap. 2 and others were also listed:

- the geopotential height h in (3.34) is needed to convert the variables on a NWP grid to a grid suitable for the spatial integration of the propagation impairments (see Sec. 4.2.1).
- the equations of the LCC map projection in Sec. 3.2.2 also enter into the transformation of grid coordinates for the processing in Sec. 4.2.1.
- the temperature T in (3.35) intervenes in all the specific attenuation model of Chap. 2.
- the water vapour partial pressure p_{vap} in (3.36) or the water vapour density ρ_{vap} in (3.37) are needed for the water vapour specific attenuation in Sec. 2.2, for the line-by-line method or its approximation respectively.
- the relative humidity RH in (3.38) is needed for the Salonen and Mattioli models in Sec. 2.3.6 and 2.3.7.
- the cloud liquid water density $M_{cloud,l}$ in (3.42) is used for the cloud specific attenuation in Sec. 2.3.5.
- the rain liquid water density M_{rain} in (3.43) is used for the rain specific attenuation in Sec. 2.3.8.
- the rain rate R_{rain} in (3.46) is used for the alternative rain specific attenuation model in Sec. 2.3.9.
- the wind speeds (u, v) in (3.47) and (3.48) are used for the scintillation cut-off frequency in (2.109) and (2.111).
- an example of diagnostic involving one of the surface fluxes in (3.50), the latent heat flux `LH`, is shown in Sec. 5.2.1.

Chapter 4

Methods for NWP data processing and analysis

This chapter explains how the 4D data from NWP models (see Chap. 3) are to be processed in order to simulate propagation impairments on Earth-space links (see Chap. 2). The expected outputs of the method presented hereinafter are thus 1D time series of the propagation variables, as well as their underlying statistical distributions. If refraction can be neglected, the geometry of an Earth-space link is described by its azimuth and elevation at the ground terminal. Therefore, the method relies on multiple conversions between Earth-relative coordinate systems (see Sec. 4.1) combined with interpolations and integrations to transform the data from the time-varying NWP coordinates into azimuth and elevation maps (see Sec. 4.2). When combining those maps with the orbitography, time series of the impairments are obtained (see Sec. 4.3), and then the statistics are derived from the time series (see Sec. 4.4).

The core of the proposed method was already formulated by the participants to the ESA EODDL contract [37]. However, some modifications aimed to improve this method were implemented and will be mentioned when needed.

4.1 Earth coordinate systems and conversions

For the sake of modelling Earth-space links from NWP data, some coordinate systems, and the conversions between them, are particularly relevant.

Choosing a frame of reference naturally defines cartesian coordinates. However, considering the shape of the Earth, or the shapes of satellites' orbits, the more practical coordinates are usually curvilinear ones. The conversions which are the simplest and most ubiquitous in that respect are thus between cartesian and spherical coordinates (see Sec. 4.1.1).

For the purpose of locating points at a global scale near the surface of the Earth, i.e. geodesy, it is convenient to choose a frame of reference which is fixed relatively to reference points on the surface of the Earth. Such a frame of reference is non-inertial as it is rotating with the Earth (see Sec. 4.1.2). The systems of interest are the cartesian Earth-Centered Earth-Fixed (ECEF) coordinates and the curvilinear Latitude Longitude Altitude (LLA) coordinates. Those latter coordinates are nearly spherical but their definition will vary depending on how the Earth is modelled as an ellipsoid or geoid.

When the objects under scrutiny have their own motion relative to the Earth surface, as is of course the case with most satellites, it becomes more practical

to choose a frame of reference which is not rotating with the Earth but is fixed with respect to some cosmic reference points. An example of Earth global inertial coordinates (see Sec. 4.1.3) are the cartesian True-Equator Mean-Equinox (TEME) coordinates which are particularly useful to handle satellites' orbits described by Two-Line Elements (TLEs) (see Sec. 4.3.1).

In the context of Earth-space links, the point of view of their operations is relative to some specific location on the surface of the Earth where a terminal is located. Then the most important systems are ultimately Earth local coordinates (see Sec. 4.1.4), conventionally the cartesian East-North-Up (ENU) coordinates and the spherical Azimuth-Elevation-Range (AER) coordinates.

4.1.1 Cartesian and spherical coordinates

Considering the right-handed cartesian coordinates (x, y, z), the corresponding spherical coordinates (r, ϕ, θ) can be defined according to the following:

- r is the norm of the vector $\mathbf{r}$ from the origin to the point,
- ϕ is the angle between the x axis and the projection of $\mathbf{r}$ on the xy plane,
- θ is the angle between the projection of $\mathbf{r}$ on the xy plane and $\mathbf{r}$, or equivalently the complementary of the angle between the z axis and $\mathbf{r}$.

The cartesian and spherical coordinates are illustrated on the Fig. 4.1.

The conversion from spherical to cartesian coordinates is given by

$$\begin{cases} x &= r\cos(\phi)\cos(\theta) \\ y &= r\sin(\phi)\cos(\theta) \\ z &= r\sin(\theta) \end{cases} \tag{4.1}$$

and the conversion from cartesian to spherical coordinates is given by

$$\begin{cases} r &= \sqrt{x^2+y^2+z^2} \\ \phi &= \operatorname{arctan2}(y,x) = \operatorname{Arg}\{x+jy\} \\ \theta &= \begin{cases} \arcsin(z/r) & r \neq 0 \\ 0 & r = 0 \end{cases} \end{cases} \tag{4.2}$$

where by definition the origin is $(0, 0, 0)$ in both systems.

Note that it is not uncommon to define spherical coordinates using the complementary of θ instead. The $\cos(\theta)$ and $\sin(\theta)$ in (4.1) must then be switched, and similary for the inverse trigonometric function in (4.2).

4.1.2 Earth global non-inertial coordinates

The key interest behind a non-inertial frame of reference which is rotating with the Earth is to easily locate points on its surface at a global scale. The curvilinear geodetic coordinates described here are actually "nothing more" than the usual Latitude Longitude Altitude (LLA) coordinates used in geography. The corresponding cartesian coordinates are the Earth-Centered Earth-Fixed (ECEF) coordinates whose frame of reference is defined by an x and y axes

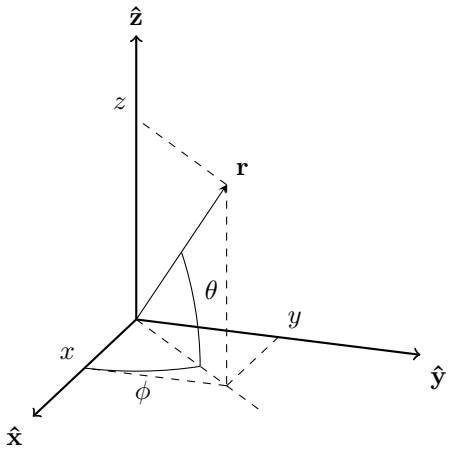

Figure 4.1 – Spherical coordinates (r, ϕ, θ) for the corresponding right-handed cartesian coordinates (x, y, z)

lying in Earth equatorial plane, the z axis pointing towards the geographical North pole, and the x axis additionally intersecting the Greenwich meridian. The exact nature of the LLA coordinates depends however on how the Earth is modelled. The Earth closely resembles a sphere, but it is more accurately modelled as an ellipsoid of revolution, a.k.a. a spheroid.

An ellipsoid of revolution is entirely characterized by the dimensions of the ellipse which is rotated during its construction. For example, it is enough to specify the semi-major axis a and the semi-minor axis b. Some other useful parameters are the flattening f, a.k.a. oblateness or ellipticity, given by

$$f = 1 - \frac{b}{a} \tag{4.3}$$

and also e and e', respectively the first and second eccentricities, given by

$$e = \sqrt{1 - \frac{b^2}{a^2}} \tag{4.4}$$

$$e' = \sqrt{\frac{b^2}{a^2} - 1} \tag{4.5}$$

with notably $f = 0$, $e = 0$ and $e' = 0$ in the case of a sphere. Another useful quantity regarding ellipsoids is the volumetric mean radius R as in

$$R = \sqrt[3]{ab} \tag{4.6}$$

which is one way to approximate a spheroid by a sphere.

The Earth is well modelled by an oblate $(a > b)$ spheroid. Typically, for a given ellispoid model, the dimensions are specified from a, the equatorial radius, and f the flattening. Such a model of the Earth is the World Geodetic System

Ellipsoid parameters	Spherical Earth	WGS 84
f [/]	0	1/298.257223563
a [km]	6371	6378.137
b [km]	6371	6356.752
R [km]	6371	6371.001
e [/]	0	0.08181919
e_2 [/]	0	0.08209444

Table 4.1 – Ellipsoid parameters for the Earth

1984 (WGS 84) [128]. The parameters of the WGS 84 and of the corresponding spherical Earth are given in Table 4.1.

If the Earth is modelled as a sphere of radius R, then the LLA coordinates (φ, λ, h) are rather straightforwardly converted from or into using (4.1) or (4.2) respectively. One has then indeed $\varphi = \theta$ for the latitude, $\lambda = \phi$ for the longitude, and $h = r - R$ for the altitude, keeping the same notation as earlier.

When considering the Earth as an ellipsoid with $a \neq b$, then the notions of latitude φ and altitude h become less clear. The altitude h is understood as the shortest distance between a point and the surface of the Earth. The geodetic latitude φ of that point is then defined as the angle between the equatorial plane and the normal to the Earth surface at that point. But one could consider also the angle φ_s between the equatorial plane and the line of length r_s joining the point's projection on the surface of the Earth and the center of the Earth. Making use of those different quantities it becomes possible to define the conversion from LLA to ECEF coordinates as

$$\begin{cases} x_{ECEF} &= x_\lambda \cos(\lambda) \\ y_{ECEF} &= x_\lambda \sin(\lambda) \\ z_{ECEF} &= r_s \sin(\varphi_s) + h \sin(\varphi) \end{cases} \tag{4.7}$$

where x_λ is the projection of the position vector on the equatorial plane with

$$x_\lambda = r_s \cos(\varphi_s) + h \cos(\varphi) \tag{4.8}$$

and where

$$r_s = \frac{a}{\sqrt{1 + \left(\left(\frac{a}{b}\right)^2 - 1\right) \sin^2 \varphi_s}} \tag{4.9}$$

$$\frac{\tan(\varphi_s)}{\tan(\varphi)} = \frac{b^2}{a^2} \tag{4.10}$$

to relate the two kinds of latitudes. These relationships between the LLA and ECEF coordinates are explained by the Fig. 4.2. From (4.10) it is furthermore possible to rewrite (4.7) and (4.8) so that they involve only φ. By introducing

$$r_c = r_s \frac{\cos(\varphi_s)}{\cos(\varphi)} \tag{4.11}$$

then it gives

$$\begin{cases} x_{ECEF} &= x_\lambda \cos(\lambda) \\ y_{ECEF} &= x_\lambda \sin(\lambda) \\ z_{ECEF} &= \big(r_c(1-e^2)+h\big)\sin(\varphi) \end{cases} \tag{4.12}$$

and

$$x_\lambda = (r_c + h)\cos(\varphi) \tag{4.13}$$

this new formulation proves more practical to reverse the equations.

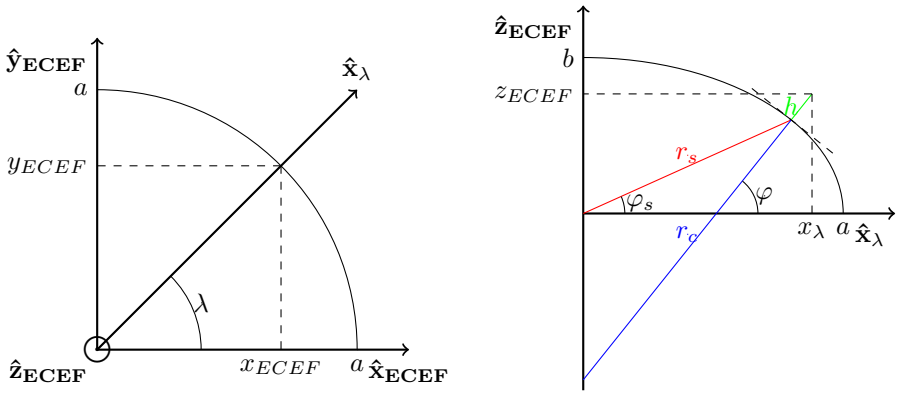

(a) Equatorial plane cut view

(b) Ellipsoid cut view

Figure 4.2 – ECEF and LLA coordinates

The reverse conversion, from ECEF to LLA, is harder to perform in closed form. For the longitude it remains simple such that

$$\lambda = \arctan2(y_{ECEF}, x_{ECEF}) \tag{4.14}$$

and with also

$$x_\lambda = \sqrt{x_{ECEF}^2 + y_{ECEF}^2} \tag{4.15}$$

but it is not as obvious for the latitude and altitude. A possibility is to use an iterative procedure. A guess for φ is obtained by assuming $h = 0$, that is

$$\varphi \approx \arctan2(z, x_\lambda/(1-e^2)) \tag{4.16}$$

and from (4.10) and (4.11) an approximative value for r_c is also known. Then, from (4.13)

$$h = \frac{x_\lambda}{\cos(\varphi)} - r_c \tag{4.17}$$

and, from these values of h and r_c, the value of φ can now be refined with

$$\varphi = \arctan2\left(\frac{z}{r_c(1-e^2)+h}, \frac{x_\lambda}{r_c+h}\right) \tag{4.18}$$

and a new iteration can be made to recompute new values of r_c and h. Usually the procedure converges quite fast in a few iterations (~ 5 gives good result).

Note that an aspect which has been neglected so far is that the geodetic altitude h is usually understood to mean the altitude above mean sea level (amsl). Because of the variations in the repartition of mass near the Earth surface, the mean sea level is not a simple uniform surface but a far more complex one known as the geoid. Considering the altitude relative to the ellipsoid instead of the geoid introduces an error around $\pm 100\,\mathrm{m}$ depending on the location. The Fig. 4.3 represents the geoid height undulations with respect to the WGS84 system according to the Earth Gravitational Model 2008 (EGM2008) [129, 130]. The relationship between the "true" amsl altitude h and the altitude h_{WGS84} relative to the WGS84 ellipsoid is thus

$$h = h_{WGS84} - \Delta h_{EGM2008} \tag{4.19}$$

where $\Delta h_{EGM2008}$ is the EGM2008 geoid height undulation. While taking these undulations into account is very important as far as accurate positioning goes, it is considered negligible here for the purpose of processing NWP data for propagation computations. Throughout this work it is assumed that $\Delta h_{EGM2008} \approx 0$, i.e. $h \approx h_{WGS84}$. One justification for this is that the NWP models under scope consider a spherical Earth for simplicity, hence they introduce an already larger error.

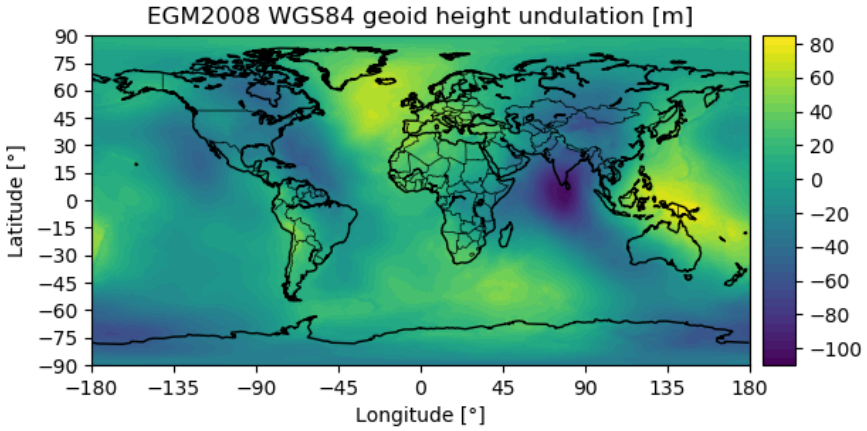

Figure 4.3 – EGM2008 geoid height undulation $\Delta h_{EGM2008}$ with respect to the WGS84 ellipsoid (2.5 min resolution)

4.1.3 Earth global inertial coordinates

If the primary point of interest is a satellite orbiting the Earth, its motion is more conveniently defined with respect to the center of an Earth fixed in the cosmos. It is important however to be able to convert those inertial coordinates into the non-inertial ones for the purpose of tracking the satellite from the surface of the Earth.

The two main motions of the Earth to consider are its rotation, and the displacement of its rotational axis. The non-inertial ECEF coordinates must thus

be transformed into inertial coordinates in two steps. The first step consists in obtaining Pseudo Earth-Fixed (PEF) coordinates by taking into account the polar motions. The second step consists in producing True-Equator Mean-Equinox (TEME) coordinates which do not rotate with the Earth anymore.

To convert ECEF coordinates into PEF coordinates, one uses

$$\begin{bmatrix} x_{PEF} \\ y_{PEF} \\ z_{PEF} \end{bmatrix} = \begin{bmatrix} \cos(x_p) & 0 & -\sin(x_p) \\ \sin(x_p)\sin(y_p) & \cos(y_p) & \cos(x_p)\sin(y_p) \\ \sin(x_p)\cos(y_p) & -\sin(y_p) & \cos(x_p)\cos(y_p) \end{bmatrix} \begin{bmatrix} x_{ECEF} \\ y_{ECEF} \\ z_{ECEF} \end{bmatrix} \tag{4.20}$$

where x_p and y_p are the polar motion angles such that the above transformation is composed of a rotation $R_2(x_p)$ and then a rotation $R_1(y_p)$. Using the fact that the angles are small, one has

$$\begin{bmatrix} x_{PEF} \\ y_{PEF} \\ z_{PEF} \end{bmatrix} \approx \begin{bmatrix} 1 & 0 & -x_p \\ 0 & 1 & y_p \\ x_p & -y_p & 1 \end{bmatrix} \begin{bmatrix} x_{ECEF} \\ y_{ECEF} \\ z_{ECEF} \end{bmatrix} \tag{4.21}$$

yet, in practice, it is not so simple to get the necessary data for x_p and y_p. The simplification $x_p = 0$, $y_p = 0$ shall actually be considered acceptable here (hence PEF $\equiv$ ECEF).

To convert PEF coordinates into TEME coordinates [131], the Greenwich Mean Sidereal Time (GMST) [s] must be known from

$$\begin{aligned} \text{GMST} = -6.2 \times 10^{-6} t_{UT1}^3 + 0.09104 t_{UT1}^2 + (3.155\,76 \times 10^9 + \\ + 8640184.812866) t_{UT1} + 67310.54841 \end{aligned} \tag{4.22}$$

where t_{UT1} [s] is the UT1 time such that

$$t_{UT1} = (jd_{UT1} - 2451545.0)/36525.0 \tag{4.23}$$

with jd_{UT1} the julian day. Once converted into the appropriate angular unit (accounting for 86 400 s in one turn), the GMST serves as the angle for the Earth rotation and then

$$\begin{bmatrix} x_{TEME} \\ y_{TEME} \\ z_{TEME} \end{bmatrix} = \begin{bmatrix} \cos(\text{GMST}) & \sin(\text{GMST}) & 0 \\ -\sin(\text{GMST}) & \cos(\text{GMST}) & 0 \\ 0 & 0 & 1 \end{bmatrix} \begin{bmatrix} x_{PEF} \\ y_{PEF} \\ z_{PEF} \end{bmatrix} \tag{4.24}$$

for the position vector. It is also useful to consider the velocity vector

$$\begin{bmatrix} v_{x,TEME} \\ v_{y,TEME} \\ v_{z,TEME} \end{bmatrix} = \begin{bmatrix} \cos(\text{GMST}) & \sin(\text{GMST}) & 0 \\ -\sin(\text{GMST}) & \cos(\text{GMST}) & 0 \\ 0 & 0 & 1 \end{bmatrix} \begin{bmatrix} v_{x,PEF} - \omega_E y_{PEF} \\ v_{y,PEF} + \omega_E x_{PEF} \\ v_{z,PEF} \end{bmatrix} \tag{4.25}$$

with ω_E [rad/s] the angular speed for the rotation of the Earth.

4.1.4 Earth local coordinates

For the purpose of processing Earth-space links for a given location, it is necessary to work with local coordinates. By local coordinates, it is understood

that the origin of the frame of reference is defined at the point $(\varphi_0, \lambda_0, h_0)$ in LLA coordinates, or (x_0, y_0, z_0) in ECEF coordinates.

The East-North-Up (ENU) coordinates are right-handed cartesian coordinates whose xy plane is the plane tangent to the surface of the Earth at $(\varphi_0, \lambda_0, h_0)$, whose x axis points towards the East, y axis points towards the North, and z axis points upwards from the center of the Earth. To the ENU coordinates are associated Azimuth Elevation Range (AER) coordinates, which are spherical coordinates but which defines the azimuth ψ as

$$\psi = (90° - \phi) \mod 360° \tag{4.26}$$

i.e. starting from the y North axis and going clockwise.

To convert ECEF to ENU coordinates the procedure is as follows

$$\begin{bmatrix} x_{ENU} \\ y_{ENU} \\ z_{ENU} \end{bmatrix} = \begin{bmatrix} -\sin(\lambda_0) & \cos(\lambda_0) & 0 \\ -\sin(\varphi_0)\cos(\lambda_0) & -\sin(\varphi_0)\sin(\lambda_0) & \cos(\varphi_0) \\ \cos(\varphi_0)\cos(\lambda_0) & \cos(\varphi_0)\sin(\lambda_0) & \sin(\varphi_0) \end{bmatrix} \begin{bmatrix} x_{ECEF} - x_0 \\ y_{ECEF} - y_0 \\ z_{ECEF} - z_0 \end{bmatrix} \tag{4.27}$$

with the different components of this conversion being:

1. The translation from the origin of the ECEF coordinates, i.e. the center of the Earth, to (x_0, y_0, z_0).
2. The rotation around $\hat{z}_{ECEF}$ of an angle λ_0, given by the rotation matrix $R_3(\lambda_0) = \begin{bmatrix} \cos(\lambda_0) & \sin(\lambda_0) & 0 \\ -\sin(\lambda_0) & \cos(\lambda_0) & 0 \\ 0 & 0 & 1 \end{bmatrix}$.
3. The rotation around $\hat{y}_{\lambda_0}$ of an angle $-\varphi_0$, given by the rotation matrix $R_2(-\varphi_0) = \begin{bmatrix} \cos(\varphi_0) & 0 & \sin(\varphi_0) \\ 0 & 1 & 0 \\ -\sin(\varphi_0) & 0 & \cos(\varphi_0) \end{bmatrix}$.
4. The permutation of the axes $\hat{x}_{\lambda_0,\varphi_0} \to \hat{y}_{\lambda_0,\varphi_0} \to \hat{z}_{\lambda_0,\varphi_0} \to \hat{z}_{\lambda_0,\varphi_0}$, given by the matrix $\begin{bmatrix} 0 & 1 & 0 \\ 0 & 0 & 1 \\ 1 & 0 & 0 \end{bmatrix}$.

4.2 Transforming NWP data into propagation impairments azimuth-elevation maps

The transformation of data on a NWP grid into azimuth-elevation maps follows two main steps. First, the data must be converted and interpolated into AER coordinates. Second, there must be an appropriate integration along the path.

4.2.1 Interpolation of NWP output into AER coordinates

For a given point in time, the NWP data are given on the "NWP" 3D grid which is regular in (x_{LCC}, y_{LCC}, η). The altitude $h(x_{LCC}, y_{LCC}, \eta)$ is known

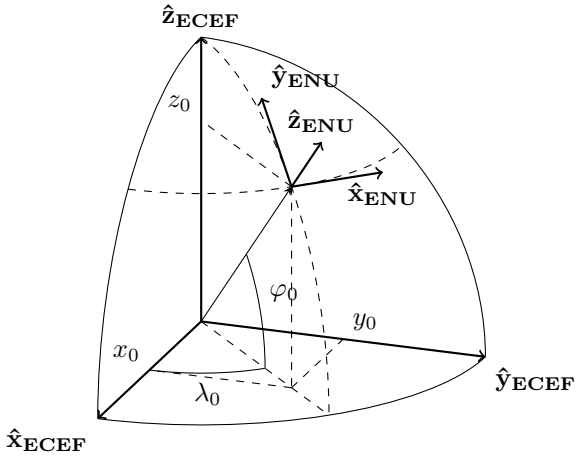

Figure 4.4 – ECEF and ENU coordinates

but is irregular and time varying. It is then useful to create a new grid "MAP" which is regular in (x_{LCC}, y_{LCC}, h), with the same horizontal coordinates as the "NWP" grid but where the vertical coordinate h is now defined by a monotonically increasing vector. To get from the "NWP" grid to the the "MAP" grid, a vertical linear interpolation must be performed at each grid point.

The main objective is to obtain the data on a local AER grid, the "SKY" grid, which is regular in (ψ, θ, r_z), for r_z the projection of r on the z axis (i.e. such that $r = r_z / \sin(\theta)$). The resolutions for that "SKY" grid can for example be $\Delta\psi = 1°$, $\Delta\theta = 1°$. For Δr_z it is preferable to have a higher resolution near the ground and a lower one farther away upward (e.g. $\Delta r_z = 50\,\text{m}$ for $r_z \in [0, 3]\,\text{km}$, $\Delta r_z = 100\,\text{m}$ for $r_z \in [3, 6]\,\text{km}$, and $\Delta r_z = 200\,\text{m}$ for $r_z \in [6, 12]\,\text{km}$).

Once the "SKY" grid has been created, a series of conversions between coordinate systems will produce a point cloud in the (x_{LCC}, y_{LCC}, h) coordinate system corresponding to the "SKY" grid:

1. Conversion from AER to ENU coordinates.
2. Conversion from ENU to ECEF coordinates.
3. Conversion from ECEF LLA coordinates.
4. Conversion from LLA to LCC map coordinates.

Then the NWP data on the "MAP" grid may be interpolated to that point cloud using a trilinear interpolation. As both the "SKY" and the "MAP" grid are not varying in time, the weights and indices of that trilinear interpolation may be saved to gain some computing time. As a general rule, it is more economical to save the weights and indices for the interpolations as they are used for many propagation variables.

Please note that the largest implementation difference with respect to [37] regarding the data processing is the absence of any triangulation and the use of regular grids exclusively.

4.2.2 Integration of AER variables as azimuth-elevation maps

The integration from AER to azimuth-elevation is mostly computationally trivial, even though the "SKY" grid is actually not regular in r but in r_z. It is suggested to simply use trapezoidal integrations. For specific attenuations, the integration is a simple one along the path. For some properties, such as brightness temperature, a cumulative integration of some variables is needed. For properties such a scintillation variance, the integrand is also a function of r.

4.3 Generation of propagation time series

In order to generate time series of a propagation impairments based on azimuth-elevation maps, two steps are necessary. The first step consists in providing the description over time of the propagation slant path in the form of time series of its azimuth and elevation. For a link between a Earth station and a satellite, the knowledge of the latter's orbit is then needed (see Sec. 4.3.1). The other step is to interpolate the impairments from the azimuth-elevation maps to the azimuth-elevation time series obtained from the orbitography (see Sec. 4.3.2).

4.3.1 Orbitography and SGP4

In the case of a truly Geostationary Earth Orbit (GEO), the question of the evolution over time of its azimuth and elevation is a rather simple one. Indeed as the position of the satellite is fixed from the point of view of an observer on the surface of the Earth, the azimuth and elevation are constant. In the more general case of a Geosynchronous Earth Orbit (GSO), the azimuth and elevation vary over time tracing an eight-shaped figure in the sky. However, for a GSO satellite with low inclination with respect to the equatorial plane, the variations in azimuth and elevation around the averages are small and they may be neglected. The orbitography of any nearly GEO satellite is thus well characterized by a fixed link whose azimuth and elevation can be computed once and for all. These values depend essentially on the longitude difference between the ground station and the satellite, and the latitude of the ground station. As a general rule, or everything else (i.e. longitude and altitude) being equal, a station at a higher latitude will see the satellite at a lower elevation.

For non-GSO satellites, on a Medium Earth Orbit (MEO) or a Low Earth Orbit (LEO), the orbitography must this time be fully detailed in order to accurately model the slant paths. A possibility is to obtain the orbital parameters at one epoch under the Two Line Elements (TLE) format (see e.g. [131] for a definition). For example, see the Fig. 4.5) where a TLE set for the METOP-A satellite is displayed. Then, from the TLE the position of the satellite may be known by applying the Simplified General Perturbations 4 (SGP4) algorithm [131, 132]. The present thesis will not go further into the description of the physics involved or the details of those models. It is recommended to use and trust the available implementations such as the `sgp4` python package [133].

```
METOP-A
1 29499U 06044A   18056.63584701 -.00000011  00000-0  14630-4 0  9992
2 29499  98.6430 116.5450 0001713 131.6411  22.4866 14.21517779588964
```

Figure 4.5 – Example of Two Line Elements (TLE) data for the METOP-A satellite on the 56th day of the year 2018 (February 25th 2018) [134]

The outputs of SGP4 are the position and velocity in TEME coordinates. For use in propagation they must first be converted into ECEF coordinates using (4.24) and (4.25), then converted into ENU coordinates using (4.27), and then into AER coordinates with (4.2) and (4.26). The result is thus a time series $(\psi(t), \theta(t))$ of the azimuth and elevation of an Earth-space link.

4.3.2 Link time series from azimuth-elevation maps

The output of the post-processed NWP data are 2D azimuth and elevation maps of the propagation impairments at a given radio-frequency for a given ground station. These maps $A_i(\psi, \theta)$ are known for each time $t_i = t_0 + iT_{NWP}$, with T_{NWP} the period at which NWP data is produced (typically every 5 min).

For GSO satellites, the azimuth and elevation are approximatively constant, i.e. $\psi(t) \approx \bar{\psi}(t)$ and $\theta(t) \approx \bar{\theta}(t)$. This simplifies grandly the problem, as it suffices to build a time series $A(t)$ with a resolution of T_{NWP} such that $A(t_i) = A_i(\bar{\psi}(t), \bar{\theta}(t))$ by bilinear interpolation of each $A_i(\psi, \theta)$ to $(\bar{\psi}(t), \bar{\theta}(t))$.

For non-GSO satellites, the time when the satellite is visible from a certain ground station may be only a few minutes, so of the same order as T_{NWP}, whereas the azimuth and elevation may vary significantly every few seconds. To use the maps $A_i(\psi, \theta)$ in this configuration, it must first be assumed they represent a frozen state of the atmosphere. Then, it is possible to derive the time series $A_i(t)$ by means of a bilinear interpolation of $A_i(\psi, \theta)$ in $(\psi(t), \theta(t))$. In order to produce a time series $A(t)$ which is representative of the Earth-space links for any period of time, and not just in a temporal window where the frozen atmosphere assumptions holds, it is proposed to construct $A(t)$ piecewise so that for $t \in [t_i, t_{i+1}]$ the time series $A_i(t)$ and $A_{i+1}(t)$ are combined linearly as

$$A(t) = (1 - w_i(t))A_i(t) + w_i(t)A_{i+1}(t) \tag{4.28}$$

with the linear weight in time $w_i(t)$ defined as

$$w_i(t) = (t - t_i)/T_{NWP} \tag{4.29}$$

meaning that $A(t)$ depends on the two nearest frozen atmospheres available.

4.4 Statistical analysis of NWP-derived propagation time series

Once time series of a propagation impairment are obtained from the NWP data, it opens the door to perform various statistical analyses of the simulated data and to compare with measurements and reference models.

4.4.1 Error metrics

Being given a simulated time series $A(t)$ of a propagation impairment, and being also given a reference time series $A_{ref}(t)$ for that same impairment, there are many well-known error metrics which can be computed. First, the instantaneous error is defined as

$$\epsilon_A = A(t) - A_{ref}(t) \tag{4.30}$$

and the relative error is

$$\epsilon_{A,r} = \frac{A(t) - A_{ref}(t)}{A_{ref}(t)} \tag{4.31}$$

which only make sense in the cases where it is guaranteed that $A_{ref} \geq 0$ (e.g. if A is the attenuation including the gases but not scintillation).

For a time series of N samples, the mean error (ME) is

$$\mathrm{ME}_A = \frac{1}{N} \sum_t \epsilon_A(t) \tag{4.32}$$

the mean absolute error (MAE) is

$$\mathrm{MAE}_A = \frac{1}{N} \sum_t |\epsilon_A(t)| \tag{4.33}$$

the root mean square error (RMSE) is

$$\mathrm{RMSE}_A = \sqrt{\frac{1}{N} \sum_t \epsilon_A^2(t)} \tag{4.34}$$

which relates to the variance σ_A^2 as

$$\mathrm{RMSE}_A^2 = \sigma_A^2 + \mathrm{ME}_A^2. \tag{4.35}$$

Moreover, the correlation coefficient ρ_A between A and A_{ref} is

$$\rho_A = \frac{N \sum_t A(t) A_{ref}(t) - \sum_t A(t) \sum_t A_{ref}}{\sqrt{N \sum_t A(t)^2 - \left(\sum_t A(t)\right)^2} \sqrt{N \sum_t A_{ref}(t)^2 - \left(\sum_t A_{ref}(t)\right)^2}}. \tag{4.36}$$

Other metrics tailored for some propagation variables are suggested in [135].

4.4.2 Complementary Cumulative Distribution Function for fixed elevation

The Complementary Cumulative Distribution Function (CCDF) of the propagation impairment A is characterized by the graph $(P(A \geq A^*), A^*)$ where for each exceeded level A^* of the impairment the probability of exceedance $P(A \geq A^*)$ is given.

From a time series $A(t)$ there are at least two different ways to compute the CCDF:

1. By sorting $A(t)$ in decreasing order, and then associating for each t a probability of exceedance corresponding to the natural frequency of occurrence in the sorted time series.

2. By binning $A(t)$ into consecutive intervals, and then obtaining the exceedance probability for each bin by performing a cumulative sum of the histogram count.

Moreover the ITU-R Study Group 3 (SG3) provides guidelines for the processing of propagation data into statistics [136]. Notably, as far as measurements are concerned, the CCDFs must be normalized with respect to the full observation period and not only the period for which there is valid data. If NWP-derived CCDFs are compared with experimental CCDFs, or CCDFs issued from the ITU-R models, this must be kept in mind.

4.4.3 Complementary Cumulative Distribution Function for varying elevation

The procedure to compute the CCDF of, e.g., a LEO satellite is not very different in principle from the one presented for the fixed links. However because the satellite is not visible 100 % of the time, the normalisation of the CCDF must include only the samples during the visibility periods.

Note that a procedure exists in [5] to approach the CCDF of a non-GSO links from the knowledge of the CCDFs at several fixed elevation angles. This procedure is summarized by

$$P(A \geq A^*) = \int_{\theta_{min}}^{\theta_{max}} P(A \geq A^* | \theta) P(\theta) d\theta \approx \sum_i P(A \geq A^* | \tilde{\theta}_i) P(\theta_{i+1} \geq \theta \geq \theta_i) \tag{4.37}$$

where the fixed elevation CCDFs $P(A \geq A^* | \tilde{\theta}_i)$ are assumed to be known for the angles $\tilde{\theta}_i \in [\theta_i, \theta_{i+1}]$, and where the histogram $P(\theta_{i+1} \geq \theta \geq \theta_i)$ is also known from the orbitography. With NWP data processed as azimuth-elevation maps, it is possible to compare this approach with the CCDFs computed directly from time series with varying azimuths and elevations.

4.5 Concluding remarks

This chapter bridged the propagation models of Chap. 2 to the output of NWP models as described in Chap. 3 by introducing the following procedures:

- in Sec. 4.1, the coordinate systems for the Earth and the conversion between them. First, Sec. 4.1.1 serves as a reminder on cartesian and spherical coordinates, with the conversion from spherical to cartesian in (4.1) and from cartesian to spherical in (4.2). The Earth non-inertial global coordinates (i.e. rotating with the Earth) are described in Sec. 4.1.2, the Latitude Longitude Altitude (LLA) coordinates and the Earth-Centered Earth Fixed (ECEF) coordinates, with the conversion from LLA to ECEF from (4.9) to (4.13) and the conversion from ECEF to LLA

from (4.14) to (4.18). The Earth is assumed to be an ellipsoid as the geoid height is neglected. Then the Earth inertial global coordinates (i.e. not rotating with the Earth) are described in Sec. 4.1.3: the Pseudo-Earth Fixed (PEF) coordinates are assumed to be equivalent to the ECEF coordinates as polar motions are neglected, and the conversion between PEF/ECEF and True-Equator Mean-Equinox (TEME) coordinates are given from (4.22) to (4.25) for position and velocity. Finally, the Earth local coordinates (i.e. corresponding to a plane tangent to the surface of the Earth) are described in Sec. 4.1.4, the East-North-Up (ENU) cartesian system and its corresponding Azimuth-Elevation-Range (AER) spherical system, with the conversion between them stated in (4.26) and (4.27). All these coordinate systems and conversions are needed in Sec. 4.2 and/or Sec. 4.3.1 as detailed below.

- in Sec. 4.2, a way to transform data given on the "NWP" model grid to the "SKY" grid suitable for the simulation of Earth-space links, i.e. AER coordinates associated with a given ground station. Data on the "NWP" grid is first interpolated into the "MAP" grid, a regular cartesian grid following the NWP map projection horizontally but replacing the time-dependent pressure-based vertical coordinates with fixed altitudes. The desired coordinates of the "SKY" grid are then converted from AER to LLA, and from there to the same coordinates as the "MAP" grid. Finally, the data is interpolated linearly from the "MAP" grid to the "SKY" grid. This procedure is applied throughout the thesis, with NWP data on the "NWP" grid first processed into propagation impairments as in Chap. 2, then transformed to the "SKY" grid, and then integrated as in Sec. 4.2.2.

- in Sec. 4.3, the generation of GSO or non-GSO propagation impairments time series by taking into account the orbitography and subsequent geometry of the Earth-space link. From a satellite's TLEs, its reconstructed orbit given in TEME coordinates is converted into azimuth-elevation time series. The propagation impairments on azimuth-elevation 2D maps integrated from the "SKY" grid, and corresponding to a visibility period of the satellite, are then interpolated to correspond to those azimuth-elevation time series. Considering the limits on the NWP data temporal resolution ($\sim 5\,\mathrm{min}$), a linear combination of maps is necessary for non-GSO links as given by (4.29) and (4.28).

- in Sec. 4.4, the error metrics most useful to the evaluation of the performances of NWP-derived propagation impairments time series, as well as the methods to obtain their Complementary Cumulative Distribution Functions (CCDFs). Particularly, the mean error in (4.32), root-mean-square error in (4.34) and correlation coefficient in (4.36) are the basis of the later results discussed from Tab. 5.1, Tab. 6.3 and Tab. 6.4. The methods to compute a CCDF given in Sec. 4.4.3 is relevant to the results from Sec. 5.2.4 to Sec. 5.2.8, in Sec. 6.2.3, in Sec. 7.1.3, 7.1.4 and 7.2.3. The formula in (4.37) to combine GSO CCDFs (i.e. at fixed elevations) so as to obtain non-GSO CCDFs is compared to the direct approach in both Sec. 5.2.8 and Sec. 7.2.3.

Chapter 5

Validation of total and rain attenuations with operational NWPs and radar measurements

This chapter presents a validation effort concerning the use of NWP data to generate time series and statistics of the different attenuation components over multiple years. For this purpose, two NWP models are compared: WRF, which is used throughout most of this thesis, and ALARO, used operationally by the Royal Meteorological Institute of Belgium (RMIB). Moreover, in the case of rain, 10 years of weather radar measurements serve as a reference.

The rain attenuation results produced from the Wideumont radar data were published on their own, in collaboration, by Lukach et al. [110].

5.1 Description of the experimental set-up

The goal of this validation is to provide evidence of the suitability of NWPs for the simulation of propagation impairments, or as means to detect weaknesses or insufficiencies present in the approaches discussed in Sec. 1.4 and whose re-implementations are described from Chap. 2 to Chap. 4. The impairments under scope here are most of the attenuation components: the attenuation due to gases (oxygen and water vapour), the attenuation due to clouds, the attenuation due to rain, and the "total" attenuation (excluding scintillation). Both GEO and LEO links are studied. There are three datasets involved:

- Wideumont single-polarisation C band (5.64 GHz) weather radar [137] reflectivity data for 10 years (2003-2012), every 5 min.
- ALARO 4 km NWP domain [138] for 10 years (2004-2013), every 1 h.
- WRF 4 km NWP domain for 5 years (2009-2013), every 5 min.

On the one hand, the focus is given to a large number of years. The aim is to form the basis for a sound statistical analysis by reducing the inter-annual variability of the weather and consequently of the propagation impairments, especially rain. To the author's knowledge, the use of such large periods with such high resolution NWP data (in both time and space), and in conjunction

with such a large radar database, is largely unprecedented. Indeed, the most relevant results as reviewed in Sec. 1.4 use either coarser models or rarely more than a year. On the other hand, results of this first validation remain limited to one zone, at a mid-latitude and temperate climate, and typical of the most studied zones in radio-propagation (in North America, Europe, Japan). This latter aspect means however that it is easier to trust the reference models of the ITU-R since more data were available for their calibration to this area.

5.1.1 Earth-space links' configuration

These are the characteristics of the space-to-Earth links that are simulated based on the radar and NWP data:

- the station is Louvain-la-Neuve (50.67°N, 4.61°E, 160 m a.m.s.l) (BE).
- the frequencies and polarisation tilt angles of the links are 19.701 GHz (linear vertical), 26 GHz (45°), 39.402 GHz (45°), or 75 GHz (45°).
- GEO links (i.e. fixed elevations) are simulated between 5° and 90°, and a reference elevation of 30° is selected for the main comparison.
- LEO links are simulated for the satellites METOP-A, -B and -C.

The choice of Louvain-la-Neuve as a site for a validation study of NWPs in this thesis is of course first motivated by the Belgian collaboration between UCLouvain and the RMIB within the F.R.S.-FNRS project NEWPORT. Louvain-la-Neuve is a historically notable location for propagation research due to its participation to the propagation experiments OTS and OLYMPUS. Louvain-la-Neuve is also a receiving station for the Alphasat Aldo Paraboni TDP5 propagation experiment since mid March 2017. Though no comparison with propagation beacon measurements is provided within this thesis for Louvain-la-Neuve, this is a clear perspective for future works, especially once Alphasat measurements from Louvain-la-Neuve are processed. On other considerations, Louvain-la-Neuve is situated $\sim$ 100 km to the North West of the Wideumont radar, with a range of $\sim$ 240 km, which results in an acceptable compromise in data availability in order to process the rain conditions for most of the elevation range from the ground station [110]. Louvain-la-Neuve also has a relatively central location within Belgium, and hence within the RMIB's ALARO domain and its WRF equivalent (see next Sec. 5.1.2 and Fig. 5.1), which ensures an adequate coverage for the processing here as well.

The 19.701 GHz and 39.402 GHz frequencies are chosen as they are the beacon frequencies used for the GSO Alphasat experiment. Both Alphasat TDP5 signals polarisations are linear, though the 39.402 GHz signal is tilted by 45°. The 26 GHz frequency is chosen as it is representative of bands allocated a.o. to non-GSO Earth observation satellites downlinks at the lower edge of the Ka band. The 75 GHz frequency is chosen as a representative of even higher frequencies expected for the future of SatCom, on the other side of the 60 GHz oxygen absorption peak, and because a European propagation experiment with a cubesat is planned near this frequency [30]. Because usually non-GSO links have a circular polarisation, all the other polarisation tilt angles are set to 45°.

The main interest of simulating GEO links with varying elevations is to be able to apply ITU-R P.618 algorithm in (4.37) as an alternative procedure to create LEO attenuation CCDFs. From NWPs, links every 2.5° steps are produced with a fixed southward azimuth of 180° (for Alphasat links the azimuth is $\sim 154°$). From radar measurements, a smaller subset of elevations $\{10°, 15°, 20°, 30°, 45°, 60°, 75°, 90°\}$ is available but the average over all the azimuthal directions is taken for them. For the actual link between Louvain-la-Neuve and Alphasat, the inclination of the latter's orbit creates a variation of a few degrees of the elevation between 27° and 31°, with a mean elevation of $\sim 29°$. An elevation of 30° is thus well representative of a typical GEO link in Louvain-la-Neuve, and in addition is convenient to get back to an approximation of the zenith attenuation (90°) by applying the cosecant scaling law, i.e. by dividing the attenuation by a factor of two.

For the LEO links, the choice of the METOP satellites is motivated by their typical sun-synchronous orbits for Earth observation satellites and also considering the similar upcoming METOP-SG satellites planned with Ka band downlink capabilities. Note that, for the 10 years periods considered for which the radar and ALARO are nearly concurrently available, some of the METOP satellites were not even actually deployed. Indeed, the launches of METOP-A, -B, and -C, took place in October 2006, September 2012 and November 2018 respectively. The emphasis is thus on representative orbits, albeit in part hypothetical. Moreover, because the durations of the METOP passes over Louvain-la-Neuve is ~ 10 min, the simulation of LEO attenuation time series does not use the ALARO hourly data but is restricted to the WRF data.

5.1.2 NWP model

The design of the NWP domains takes as reference the 20 km and 4 km Lambert Conformal Conic domains of the RMIB's ALARO model [138]. The Fig. 5.1 shows the equivalent domains d01 at 20 km and d02 at 4 km reproduced for WRF. Working with almost identical domains is useful to alleviate the differences that would likely arise from different boundaries. Furthermore, the selection of these boundaries and the size of the domains are backed up by the RMIB's former investigations to reproduce the Belgian weather faithfully.

Besides the horizontal domains described above, the details of the configuration of WRF for a daily run are as follows:

- initialisation data: ECMWF ERA-Interim analysis (0.75°) every 6 h.
- vertical coordinates: 50 automatic vertical levels, 50 hPa pressure top.
- spin-up time: 24 h (d01) and 12 h (d02).
- time steps: d01 start is 100 s (min. 50 s, max. 300 s), parent time step ratio is 5, i.e. d02 start is 20 s (min. 10 s, max. 60 s). The adaptation is driven by d01.
- water microphysics: WRF single-moment 6 (WSM6).
- cloud physics: Tiedtke (d01, d02), called at each time step.

- radiation physics: RRTMG schemes for long-wave and short-wave radiations. The schemes are called every 20 min for both domains (d01, d02).
- surface layer physics: revised MM5 Monin-Obukhov scheme.
- planetary boundary layer physics: Yonsei University (YSU) scheme, called at each time step.
- soil layer physics: unified Noah land-surface model, 4 layers.
- diffusion and damping: second order diffusion on coordinate surfaces, Rayleigh damping with damping coefficient (inverse time scale) 0.2 Hz.

Other parameters are left to their default values.

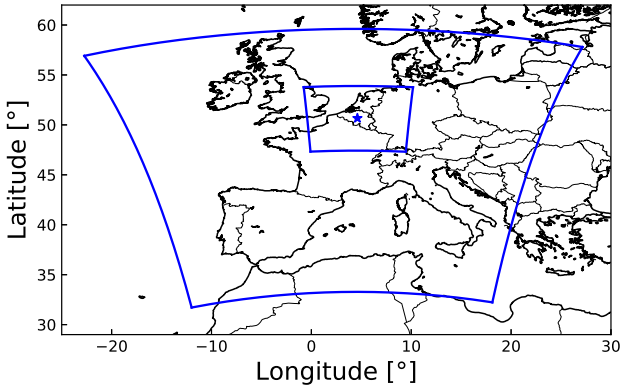

(a) 20 km parent domain with nested 4 km domain

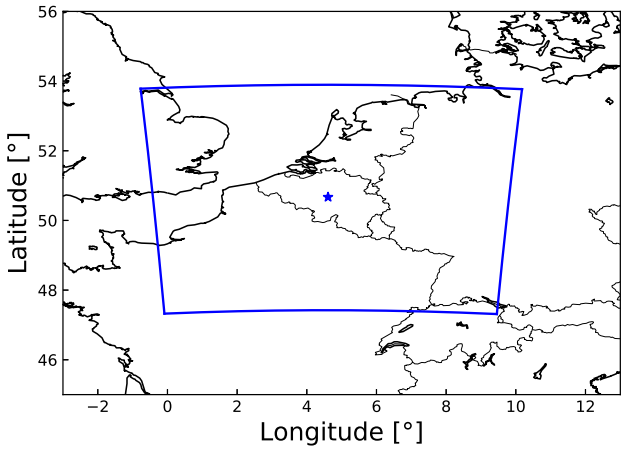

(b) 4 km nested

Figure 5.1 – "ALARO" WRF Lambert Conformal Conic (149 × 149) domain at 20 km, and (181 × 181) domain at 4 km, for Louvain-la-Neuve (50.67°N, 4.61°E)

5.2 Results

The results of the validation are presented as explained here. Firstly, some illustrative examples of WRF output and its post-processing are presented in the forms of NWP surface parameters (see Sec. 5.2.1), azimuth-elevation maps of the attenuation components (see Sec. 5.2.2), attenuation time series for both GEO and LEO links (see Sec. 5.2.3). Secondly, a comparison of error metrics and distributions of the GEO attenuation components at 30° of elevation is performed between ALARO, WRF, the ITU-R references, and the radar data when applicable, for the gaseous attenuation (see Sec. 5.2.4), the cloud attenuation (see Sec. 5.2.5), the rain attenuation (see Sec. 5.2.6), and the total attenuation (see Sec. 5.2.7). Thirdly, the consequences on the total attenuation for LEO links are shown (see Sec. 5.2.8).

5.2.1 Examples of NWP surface parameters

The Fig. 5.2 presents examples of surface parameters output of the WRF model with the configuration inspired by ALARO. The examples are for the 1st January 2013 at 3:00 UTC.

The Fig. 5.2 (a) shows the 2 m surface temperature over the 20 km domain d01. The distinction between land and sea is apparent with an outline of Western Europe, including the British Isles and the South of Scandinavia, and also parts of North Africa. The sea temperature is colder in the North and Baltic Seas, and warmer in the Mediterranean Sea or in the southern visible part of the Atlantic, with some of the highest temperatures over the Canary Islands. The temperature gets lower more inland and in mountainous areas, most noticeably in the Alps. The Fig. 5.2 (b) offers a zoomed in view of the temperature around Belgium thanks to the finer 4 km domain d02. The coasts of France, Belgium, the Netherlands and Germany, in the Channel and the North Sea, are partly identifiable. The temperature gets lower at higher altitudes inland towards Switzerland in the southeast corner. The colder temperature over England compared to most of the continent is also visible.

The Fig. 5.2 (c) presents the ground rain rate for d01. There is a large area of precipitation with a southwest to northeast extent over Western Europe, apparently as the result of a weather front. More details over Belgium an neighbouring countries are visible in Fig. 5.2 (d) for d02, with light to moderate rain up to $5\,\mathrm{mm\,h^{-1}}$ over roughly half of the domain.

The Fig. 5.2 (e) presents the latent heat flux for d01, and similarly the Fig. 5.2 (f) presents the latent heat flux for d02. The latent heat flux is seen to be high over sea during the night by the sea, especially to the northwest of the British Isles, or over mountains, where changes of phase in water can occur.

All these examples demonstrate the utility of the domains' dimensions and of the downscaling procedure. As much as possible, the boundaries of the domains are positioned so that there is enough distance between them and the land-sea interfaces, and so that they do not lie right on the steeper topography. As seen in Fig. 5.2 (a), large transitions in temperature are contained within d01, and, as seen in Fig. 5.2(c), it is big enough to include an entire front.

Consequently, the weather information outside of d02 is reproduced by the model and transferred to the nest with limited forcing.

At a glance, the output of WRF looks realistic. Synoptic measurements from Brussels National airport (WMO-06451) [139] agrees well (rain, temperature) with the examples. A thorough long-term comparison of WRF with ALARO, with ECMWF data, or with meteorological measurements (synoptic observations, radiosoundings, ...) would vastly improve the confidence in the model. Such an analysis is however not provided here, and the performances are assessed in the next sections solely using the derived propagation parameters.

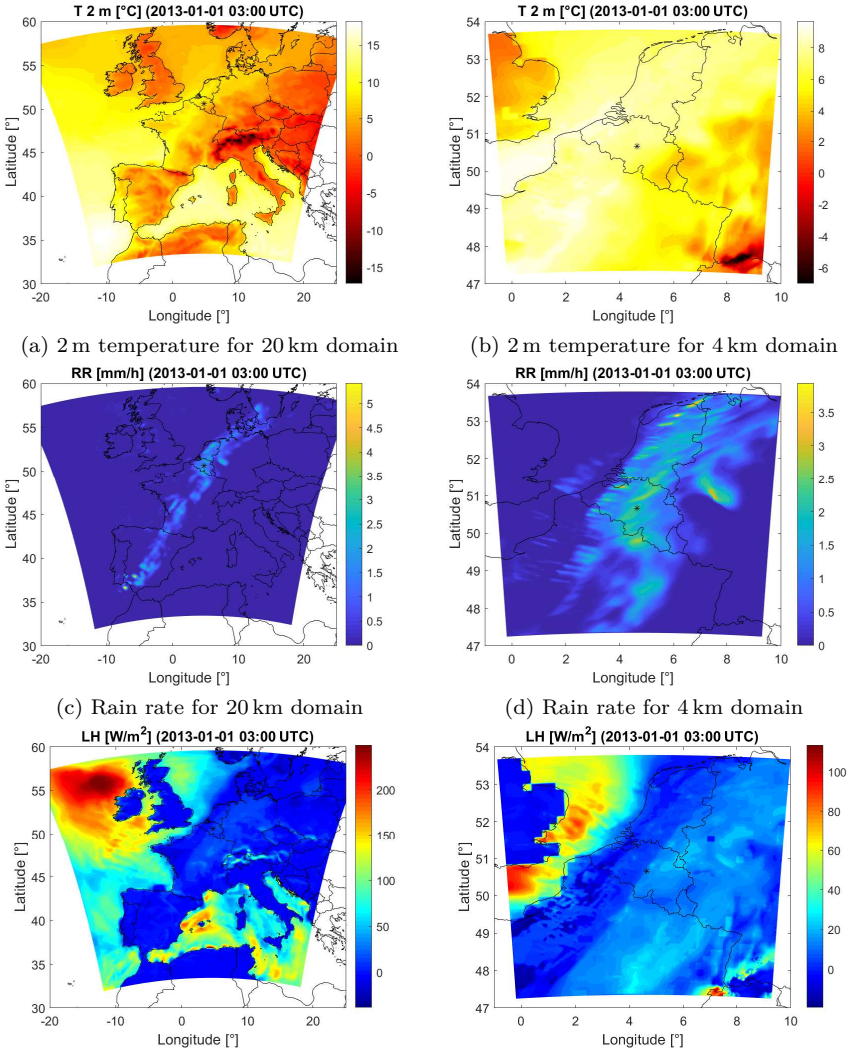

(a) 2 m temperature for 20 km domain

(b) 2 m temperature for 4 km domain

(c) Rain rate for 20 km domain

(d) Rain rate for 4 km domain

(e) Latent heat flux for 20 km domain

(f) Latent heat flux for 4 km domain

Figure 5.2 – Example of WRF ground variables for the 1st January 2013 at 3 AM UTC with the domains for the comparison with ALARO

5.2.2 Examples of propagation azimuth-elevation maps

The Fig. 5.3 shows azimuth-elevation maps of the attenuation components at 39.402 GHz for Louvain-la-Neuve on the 1st January 2013 at 2:20 UTC. Hence the maps shown here correspond to a time slightly before the maps of Fig. 5.2.

In Fig. 5.3 (a), the map for the gaseous attenuation is shown. The gaseous attenuation appears to have a high azimuthal symmetry, with a maximum difference of ~ 0.1 dB at 5° in elevation. The gaseous attenuation also follows very well the cosecant scaling law with e.g. ~ 0.40 dB for the zenith and ~ 0.79 dB at 30° of elevation (nearly the expected 0.80 dB). The deviations from the common assumptions of perfect azimuthal symmetry and scaling law are small. Moreover, for the lowest elevations, these deviations are likely affected by the path falling slightly short of the tropopause. Indeed, even though the "ALARO" WRF domain d02 is large enough for paths as low as 2° in elevation, in practice the post-processing was limited to a 240 km × 240 km subdomain centred on Louvain-la-Neuve. Considering also the lack of accurate modelling for the refraction, this explains why the statistical results shown in the next sections will be restricted to elevations $\geq 10°$. Otherwise, as far as the gaseous attenuation is concerned, it can be inferred that NWP information in 3D is not necessary for an accurate model. Local information to the station, such as 1D profiles, should already be enough instead of full azimuth-elevation maps. Nevertheless, the relative ease to model the gaseous attenuation also makes it a useful baseline performance marker for the NWP modelling strategy.

In Fig. 5.3 (b), the map for the cloud attenuation is shown. In this instance, the cloud attenuation is computed from the model cloud liquid water content according to the method discussed in Sec. 2.3.5. Clearly the cloud attenuation is not particularly high here, of the order of a fourth (0.12 dB) of the gaseous attenuation in the zenith direction. However, a much larger azimuthal dependence than for the gases is observed, with a higher presence of clouds in the southeastern half of the map. The cloud attenuation varies between 0.19 dB and 0.3 dB for 30° in elevation (0.24 dB expected from the scaling law), and between 0.45 dB and 2.32 dB for 5° in elevation (1.38 dB expected from the scaling law). The scaling law is seen to give a good average perspective of the cloud attenuation but is insufficiently accurate to capture its spatial variability. Clearly, it shows, as can be expected, that 3D data is valuable to obtain the cloud attenuation on an instantaneous basis.

In Fig. 5.3 (c) and (d), maps for the rain attenuation are shown, respectively based on the approaches detailed in Sec. 2.3.8, using the volumetric rain water content, and in Sec. 2.3.9, using the ground rain rate. The values of the estimated rain attenuations are similar in both models, but the second one provide higher estimates. In the zenith direction, the rain attenuations are respectively 1.0 dB and 1.2 dB. The rain is not very strong, as seen from 5.2 (d) it does not exceed $\sim 5\,\mathrm{mm\,h^{-1}}$ in the entire domain, but the attenuation is markedly higher than both gaseous and cloud attenuations. There is an azimuthal dependence for rain, with higher attenuations in the southwest direction. For the approach in Sec. 2.3.8, the attenuation varies actually little in azimuth for 30° in elevation, from 2.0 dB to 2.1 dB (2.0 dB expected from scaling law), but more strongly for 5° from 9.4 dB to 12.6 dB (11.5 dB expected

from scaling law). For the approach in Sec. 2.3.9, the variations are a bit larger, partly due to the larger values compared to the previous approach: for 30° in elevation the range is from 2.3 dB to 2.5 dB (2.4 dB expected from scaling law), and for 5° in elevation the range is from 9.7 dB to 15.2 dB (13.8 dB expected from scaling law). Here, as for the clouds, the knowledge of the atmosphere in 3D is important to make an instantaneous estimate of the rain attenuation. However, except at lower elevations, the azimuthal dependence and scaling law appear to hold slightly better than for the clouds. A possible reason is that, since rain is expected to be found mostly below the 0 °C isotherm, the rain contributing to the slant path attenuation is for the greater part the one in close proximity to the station. Hence, from the look a this example, commonly used modelling strategies involving only the measured ground rain rate at the station appear to follow a sensible assumption. It is expected however that other types of rain, such as localised convective precipitations, will cause a higher azimuthal dependence and stronger deviations from the scaling law.

In summary, the attenuation components benefit differently from 3D data. For the gases, the added value appears low, but this makes it easier to validate and serve as a first benchmark. For the clouds and rain, the spatial variability is as expected higher and shows clearer advantages to the 3D NWP data.

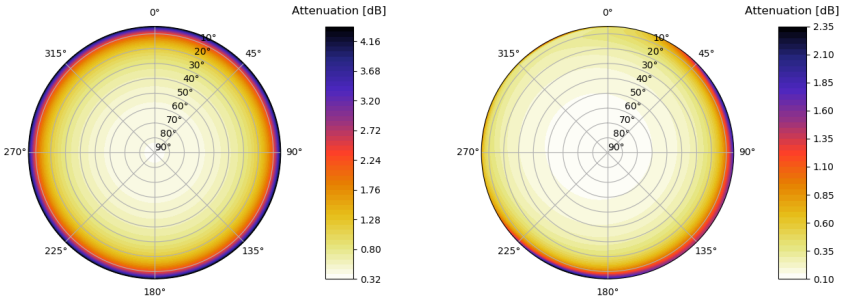

(a) Gases (b) Cloud

(c) Rain (Mie) (d) Rain (RR)

Figure 5.3 – Example of WRF-derived attenuation maps at 39.402 GHz for Louvain-la-Neuve on the 2013-01-01 at 02:20 UTC

5.2.3 Examples of attenuation time series

The Fig. 5.4 presents an example of simulated 39.402 GHz GEO attenuation time series for Louvain-la-Neuve on the 1st January 2013. The elevation is 30° and the azimuth 180°, with each point in time taken from the azimuth-elevation maps every 5 min. The curves represent the progressive addition of the attenuation components, first the gaseous attenuation, then the gaseous and cloud attenuations, and finally the "total" attenuation (not including scintillation). As is already known from Sec. 5.2.1 and 5.2.2, a light rain event is present during the night and into the morning. The peak is observed at 02:20 UTC. The results with the methods from Sec. 2.3.8 (Mie) and from Sec. 2.3.9 (RR) are consistent and in appearance well correlated. However, the rain attenuation obtained from the rain rate method (RR) is higher than the one from the volumetric method (Mie). This was already observed from Fig. 5.3 (c) and (d). There is also cloud attenuation present in the morning, predictably cloud and rain show some degree of correlation. The cloud attenuation is smaller than the rain attenuation in the earliest hours and the thick of the rain event. Later, as hardly any rain is predicted, the small cloud attenuation has a stronger contribution. This example illustrates why it is difficult to distinguish light rain from cloud attenuation, especially as the two of them often get mixed together. Concerning the gaseous attenuation, it appears very stable throughout the day, at least in comparison to the cloud and rain components. The variations are of the order of ~ 0.2 dB, from ~ 0.8 dB at the beginning of the day to ~ 0.6 dB around noon. The variations are also slow enough that the WRF selected output temporal resolution of 5 min is not really needed, unlike for the clouds and rain where it helps to capture the finer details of the peaks.

The Fig. 5.5 (a) also shows WRF results at 39.402 GHz for Louvain-la-Neuve on the 1st January 2013. The radio-links simulated here are however LEO links, for METOP-A, -B, and -C. The Fig. 5.5 (b) accompanies the LEO attenuation curves by showing the temporal evolution of the satellites' elevations as seen from Louvain-la-Neuve. Considering here the satellites become visible above 10° in elevation, the correspondence can be made between the attenuation curves representative of the individual passes of the satellites, and their actual movement in the sky. In this instance, the conditions of the satellites' passes exclude the rain event in the beginning of the day, so all the passes correspond to gaseous attenuation only. All the passes start at 10° in elevation at an attenuation within 1.7-2 dB, which is a consistent scaling with the gaseous attenuation range of 0.6-0.8 dB observed for the GEO case at 30°. However, the attenuation curves display a wider range of the lowest values reached as the satellite is at its highest elevation in the sky, as this elevation varies for each of the passes. There are six passes for each satellite, three between 8:00 to 13:00 UTC, three between 18:00 to 24:00 UTC. Because the orbits under scope are sun-synchronous, these passes happen approximatively always at the same time and in the same numbers, with here an actual repeat cycle of about one month. Interestingly, note that there is no overlap between the passes of the METOP satellites, which remains true on other days. It means the scenario is not one of a constellation with multiple satellites visible at the same time and options for satellite diversity. Furthermore, the fact that no rain or cloud

attenuation are predicted to affect the LEO links in spite of long-lasting light rain and cloudy conditions in the morning is an interesting situation in and of itself. It means that an approach based on GEO statistics with 100 % uptime will, by including this day, incorrectly consider some rain/cloud attenuation which are not actually encountered during the passes.

More time series for GSO and non-GSO links are shown in the Figs 5.6 and 5.7 respectively. The time series contains three days in the four seasons, with cloud and rain events of varying strengths. As before, the rain attenuation is a bit higher with the RR method than with the Mie method, and some light rain events are even absent from the Mie method (see middle of Fig. 5.6 (b)).

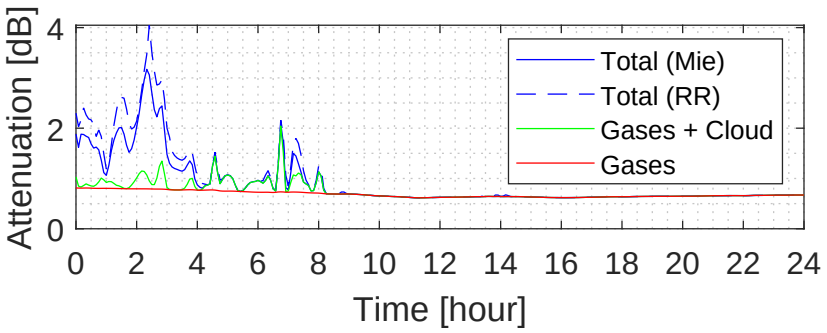

Figure 5.4 – Example of WRF-derived attenuation time series at 39.402 GHz for Louvain-la-Neuve, at 30° in elevation and 180° in azimuth, on the 2013-01-01

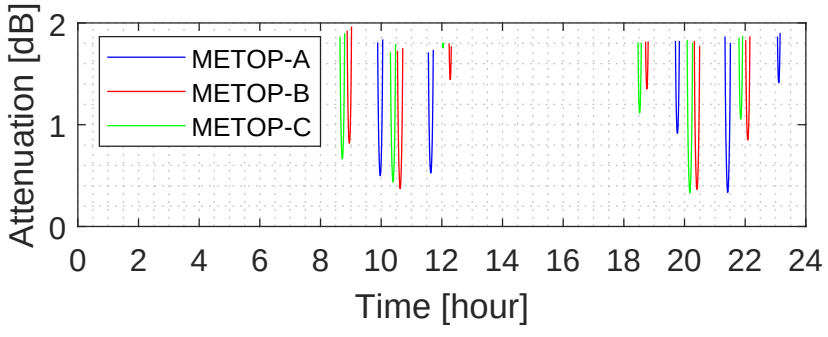

(a) Attenuation

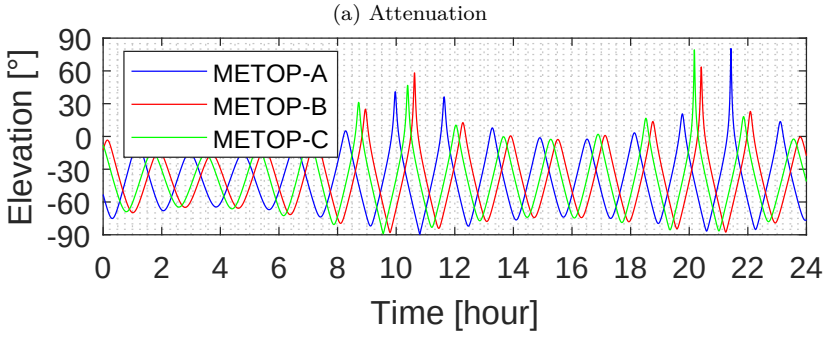

(b) Elevation

Figure 5.5 – Example of WRF-derived attenuation time series at 39.402 GHz for Louvain-la-Neuve, for the satellites METOP-A, -B, and -C, on the 2013-01-01

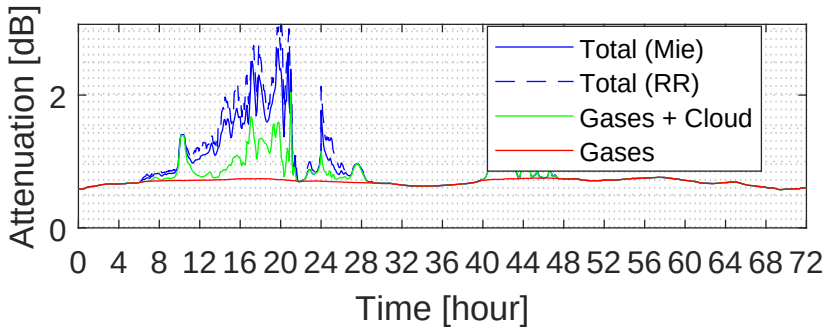

(a) 2010-02-03 to 2010-02-04 (Winter)

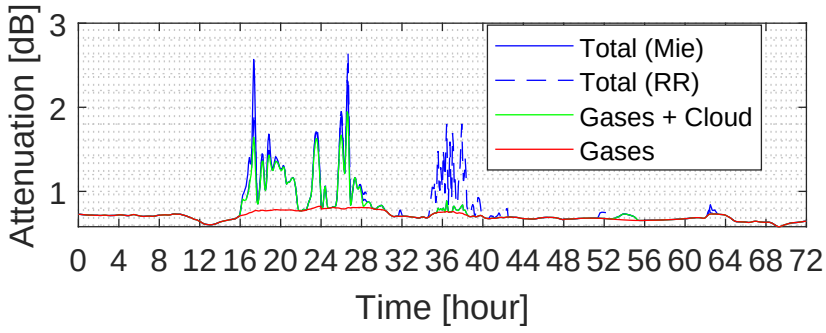

(b) 2010-05-16 to 2010-05-18 (Spring)

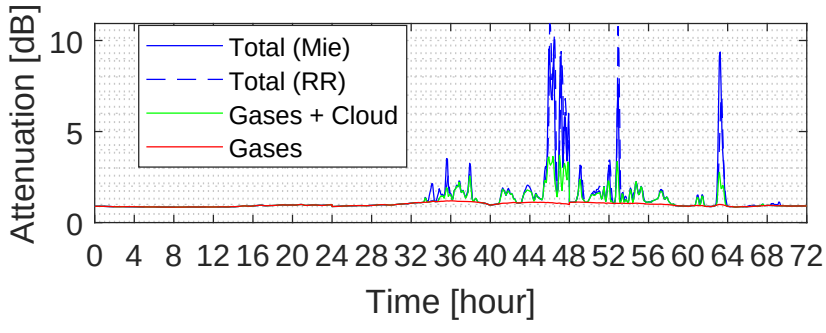

(c) 2010-07-20 to 2010-07-22 (Summer)

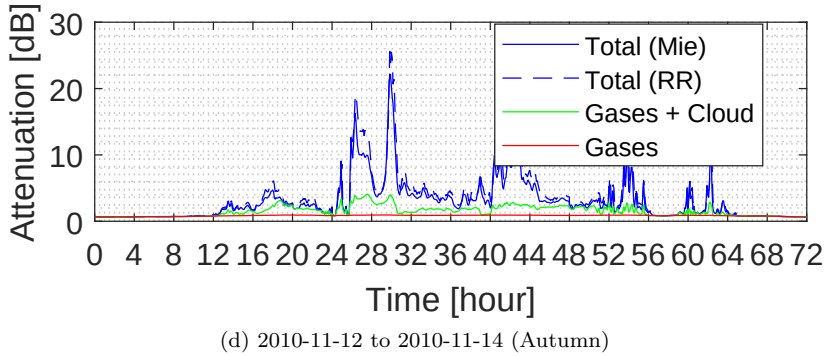

(d) 2010-11-12 to 2010-11-14 (Autumn)

Figure 5.6 – Examples of WRF-derived attenuation time series at 39.402 GHz for Louvain-la-Neuve, at 30° in elevation and 180° in azimuth (over 3 days)

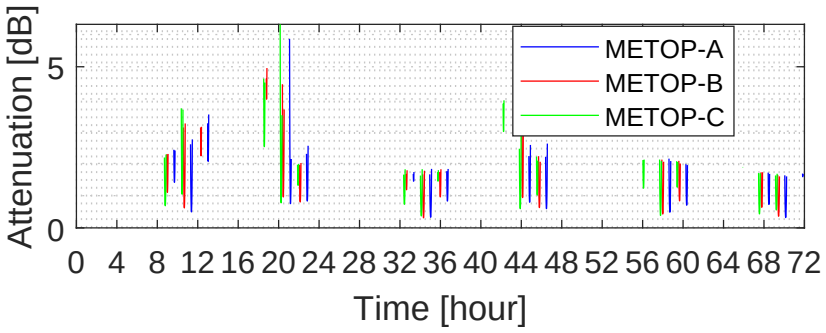

(a) 2010-02-03 to 2010-02-04 (Winter)

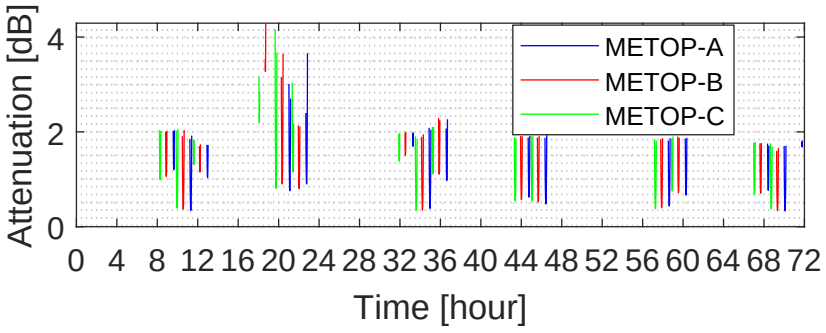

(b) 2010-05-16 to 2010-05-18 (Spring)

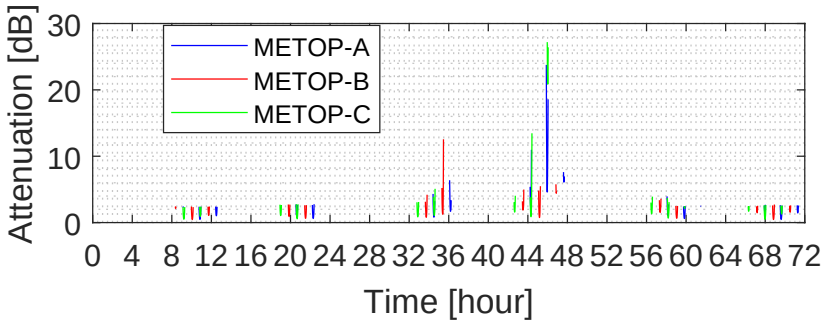

(c) 2010-07-20 to 2010-07-22 (Summer)

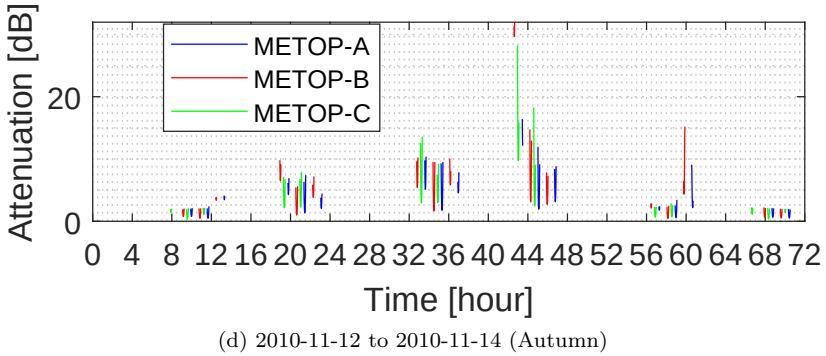

(d) 2010-11-12 to 2010-11-14 (Autumn)

Figure 5.7 – Examples of WRF-derived attenuation time series at 39.402 GHz for Louvain-la-Neuve, for the satellites METOP-A, -B, and -C, over 3 days

Frequency (GHz)	Attenuation	Error metric		
		RMSE (dB)	ME (dB)	ρ^{NWP} (-)
19.701	Oxygen	0.0019	0.0002	0.909
	Water vapour	0.1194	0.0202	0.790
	Gases	0.1185	0.0204	0.785
	Cloud	0.1022	-0.0214	0.112
	Rain (Mie)	0.3137	-0.0109	0.037
	Rain (RR)	0.5027	0.0048	0.037
	Total (Mie)	0.3933	-0.0118	0.342
	Total (RR)	0.5629	-0.0150	0.299
26.0	Oxygen	0.0027	0.0003	0.910
	Water vapour	0.1415	0.0248	0.792
	Gases	0.1403	0.0251	0.786
	Cloud	0.1704	-0.0344	0.114
	Rain (Mie)	0.5466	-0.0198	0.041
	Rain (RR)	0.7440	0.0068	0.048
	Total (Mie)	0.6557	-0.0290	0.251
	Total (RR)	0.8361	-0.0361	0.260
39.402	Oxygen	0.0082	0.0009	0.911
	Water vapour	0.1017	0.0190	0.786
	Gases	0.0984	0.0199	0.757
	Cloud	0.3522	-0.0654	0.118
	Rain (Mie)	1.1268	-0.0551	0.056
	Rain (RR)	1.3797	0.0059	0.070
	Total (Mie)	1.3022	-0.1006	0.129
	Total (RR)	1.5354	-0.1223	0.185
75.0	Oxygen	0.0173	0.0022	0.916
	Water vapour	0.3182	0.0598	0.784
	Gases	0.3115	0.0620	0.764
	Cloud	0.9385	-0.1468	0.127
	Rain (Mie)	2.343	-0.1451	0.089
	Rain (RR)	2.605	-0.0178	0.1096
	Total (Mie)	2.9151	-0.2299	0.193
	Total (RR)	3.1482	-0.2765	0.260

Table 5.1 – Root means square errors (RMSE), mean errors (ME), and correlation coefficients (ρ^{NWP}), between the attenuation components estimated by WRF or ALARO, for Louvain-la-Neuve at 30° in elevation and for 2009-2013

5.2.4 Comparison of GEO gaseous attenuation

As a first step towards the validation of GEO attenuation with the WRF and ALARO NWP models, the gaseous attenuation is here considered. The contributions of oxygen and water vapour are first investigated separately.

The error metrics of WRF against ALARO over the 5 years period 2009-2013 are reported in Tab. 5.1 p. 87 for the oxygen attenuation (as well as for the other attenuation components). CCDFs of the oxygen attenuation at 30° in elevation are presented in the Fig. 5.8-5.11 pp. 91-92 for the four reference frequencies of interest. A general observation concludes to an essential agreement between WRF and ALARO. Indeed the correlation over 5 years is rather high at ~ 0.91 for the four frequencies considered. Though, it must be noted, a prior analysis of the last 3 years (2011-2013) showed lower correlations ~ 0.85 which were improved upon by considering the longer 5 years period.

Looking at the left panel of the Fig. 5.8 p. 91, the WRF and ALARO oxygen attenuation CCDFs at 19.701 GHz for each individual year stay within ~ 0.001 dB from one another over the probability range from 0.1 to 100 %. This level agreement is also shown by the RMSE of 0.002 dB given by the Tab. 5.1. The attenuation varies between 0.09 dB and 0.12 dB from high to low probabilities of exceedance. The CCDFs from WRF are all slightly above the ones from ALARO. The year to year variability is small as it does not exceed 0.007 dB for 0.1 % of the time, with the years 2010 and 2012 in particular showing larger deviations with respect to the three other years. From the right pannel of Fig. 5.8, the CCDFs of WRF and ALARO over the 5 years period are in excellent agreement, deviating by only as much as ~ 0.001 dB at the 10 % probability level, and with the WRF curve standing above ALARO's. As per Tab. 5.1 the mean error between WRF and ALARO is only 0.0002 dB. The CCDFs of ALARO for the 5 years period and the full 10 years period agree very well, to the point they are nearly indistinguishable on the figure, which suggests no too large discrepancies are found over the longer period, and that 5 years is suitable to predict the oxygen attenuation down to a very accurate level. Note, finally, that the ITU-R prediction, which is a constant value for oxygen, is higher than the NWP CCDFs even for the lowest represented probability of 0.1 % for which the plateau appears. Here at 19.701 GHz the difference is minute and so, in the case of Louvain-la-Neuve, the ITU-R model would then act as a worst case scenario for the oxygen contribution to the attenuation margin. Considering the very low value of oxygen attenuation at this frequency, the approach is perfectly sound from the practical point of view of a general link budget. It remains that from the analyses with NWP data a more accurate picture is obtained which, as will be shown now, can have more impact at higher frequencies where the contribution from oxygen becomes more important.

The Fig. 5.9-5.11 pp. 91-92 for the other frequencies corroborate for the most part the observations made at 19.701 GHz in terms of agreement between WRF and ALARO, low year to year variability, and relation to the ITU-R reference. As the frequency increases, so does the oxygen attenuation, and the absolute differences become thus larger. The observed variability between the 5 years for 0.1 % of the time are ~ 0.009 dB, 0.03 dB, and 0.07 dB, at 26 GHz, 39.402 GHz and 75 GHz respectively. The RMSEs are ~ 0.003 dB, 0.008 dB,

and 0.017 dB for those same frequencies respectively. There are also more noticeable differences between the two ALARO curves on the right part of the figures, for 5 and 10 years, to the point where the agreement between WRF and ALARO CCDFs over the 5 years becomes better than ALARO CCDFs for the two periods. However, the difference does not exceed 0.02 dB even for 75 GHz and 0.1 % of the time. The previous assertion that 5 years is largely sufficient for a stable characterisation of the oxygen contribution remains in practice, though this should be kept in mind, and also considering the context of climate change. It is still worth noting that, depending on the frequency, the ITU-R constant oxygen attenuation level varies in relative position. For example, in Fig. 5.10 p. 92 at 39.402 GHz the ITU-R attenuation corresponds to $< 1\%$ of the time. In Fig. 5.11 p. 92 at 75 GHz, the ITU-R is still $\sim 20\%$ higher than the NWP models for 0.1% of the time. Note that the ITU-R reference's algorithm differs for frequencies below or above 70 GHz.

Being given that the oxygen attenuation depends only on the temperature and pressure, the small differences found in the comparison between the two NWP models indicate that those basic atmospheric variables must be sufficiently well predicted for the needs of propagation models. The systematic small overestimation of WRF with respect to ALARO suggest however a small bias exist between them, likely in temperature.

Regarding the water vapour attenuation, the error metrics are found, as for the oxygen, in the Tab. 5.1 p. 87. The correlations are > 0.78 and therefore weaker than for oxygen, and also more affected by the differences in frequencies. This correlation level is intermediate between typical correlations of ~ 0.7 (summer) and ~ 0.9 (winter) found by Memmo et al. [57] for the integrated water vapour (IWV) between NWPs and RAOBS in Italy. However, still according to [57], higher correlations > 0.9 are usually found for IWVs between other datasets/instruments (such as MWRs and GNSS) and RAOBS, pointing towards a poorer performance of NWPs in that regard. Luini et al. [112] (including the present thesis' author) also found high correlations, > 0.97, for IWVs in both Milano (IT) and, of interest here, Louvain-la-Neuve (BE). Similar IWV correlations were reported by Berckmans *et al.* [140]. It must be noted as well that the correlations between WRF and ALARO were even weaker, > 0.67,for the last 3 years (2011-2013). In this context, the correlations on water vapour between this thesis' NWP datasets appear mediocre and it is important to check the CCDFs to see how they are or are not affected.

The 30° elevation CCDFs are in the Fig. 5.12-5.15 pp. 93-94. In Fig. 5.12, at 19.701 GHz, the left panel with the CCDFs for 5 individual years present consistently higher water vapour attenuation for WRF than for ALARO. The former varies roughly by 0.125 dB between 0.950 dB and 1.075 dB for 0.1 % of the time, while the latter has a similarly variability but with lower extreme between 0.875 dB and 1.0 dB. This variability is on par with the RMSE of ~ 0.12 dB between WRF and ALARO. To put it in perspective in another way, it is also the same order of magnitude as the gaseous attenuation at this frequency. The higher water vapour attenuation is of course found as well in the right panel of the Fig. 5.12 with the CCDF over multiple years. The gap between WRF and ALARO is small at first near 100 % of the time but then

increase up to ~ 0.3 dB for 0.1 %, for a corresponding mean error of 0.02 dB. As was observed for the gases however, the agreement between ALARO in 5 or 10 years is still excellent, showing the selected period suffices for a stable distribution. Note the ITU-R reference CCDF for water vapour attenuation is even further below ALARO, with a similar margin as the one between WRF and ALARO, though the lowest exceedance probabilities remain in good agreement between the three models. Based on those results it may be assumed the water vapour generated by WRF in this configuration is too high. It must be kept in mind the ITU-R model uses information only at a resolution 1.125° of latitude-longitude. It will also be seen in Chap. 7.1 that this apparent overestimation is not found universally in every site. But the behaviour of WRF in this regard is a point of concern, not so much perhaps for the water vapour attenuation itself, but as it could translate into a weaker conversion of water vapour into clouds and rain by the WRF parametrisations, or conversely into too much cloud content by the cloud detection algorithms during the post-processing.

The Fig. 5.13-5.15 pp. 93-94 for the other frequencies confirm the observations on water vapour attenuation made at 19.701 GHz with very little of note to mention. The relative positions of the curves are the same with WRF above ALARO and ALARO above the ITU-R, and the two curves for ALARO still agree very well with each other. The RMSEs given in the Tab. 5.1 p. 87 are ~ 0.14 dB, 0.10 dB, and 0.32 dB, for 26.0 GHz, 39.402 GHz, and 75.0 GHz respectively. As expected the gaseous attenuation is weakest at 39.402 GHz due to the position of the frequencies relatively to the 22.2 GHz water vapour absorption peak (see also the Fig. 2.1 on p. 14).

Considering the two contributions to the gaseous attenuation, from oxygen and from water vapour, the Tab. 5.1 p. 87 shows a distinct dominance on the error metrics by the water vapour. The correlations > 0.75 for the gaseous attenuation are very similar to those for the water vapour attenuation, albeit slightly lower. The RMSEs are ~ 0.12 dB, 0.14 dB, 0.10 dB, and 0.31 dB at 19.701 GHz, 26.0 GHz, 39.402 GHz, and 75.0 GHz respectively. The RMSEs are slightly lower for the gaseous attenuation than for the water vapour attenuation alone, but practically equal to the latter. There is a clear influence of the 22.2 GHz water vapour peak on the relative magnitude of the gaseous attenuation RMSEs, with 39.402 GHz having the lowest. The MEs are ~ 0.020 dB, 0.025 dB, 0.020 dB, and 0.060 dB respectively for each of the same frequencies. The MEs are logically a bit higher for the gaseous attenuation than for only the water vapour attenuation, as both the oxygen attenuation and the water vapour attenuation are found to be overestimated in WRF with respect to ALARO, and as the MEs for the gaseous attenuation are equal to the the sum of the MEs for both of the gaseous components. In terms of CCDFs, the agreements found for both components are rather satisfactory between WRF and ALARO, and both are similar to the ITU-R, with the exception of the too high gaseous attenuation ITU-R reference value at 75 GHz.

As a first conclusion of this validation effort, WRF appears to be a suitable tool to generate gaseous attenuation estimates, with acceptable errors and correlations. However, the analysis so far suggest some bias in temperature and water vapour which could have consequences on the other water species.

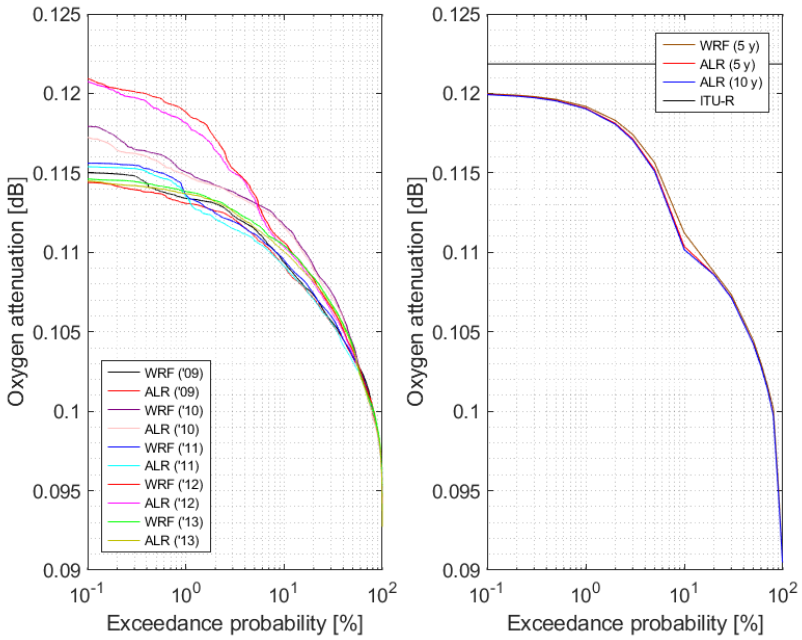

Figure 5.8 – Oxygen attenuation CCDFs with WRF, ALARO (ALR) and the ITU-R reference, at 19.701 GHz and 30° in elevation, for Louvain-la-Neuve in 2009-2013 (+ 2004-2013 for ALR)

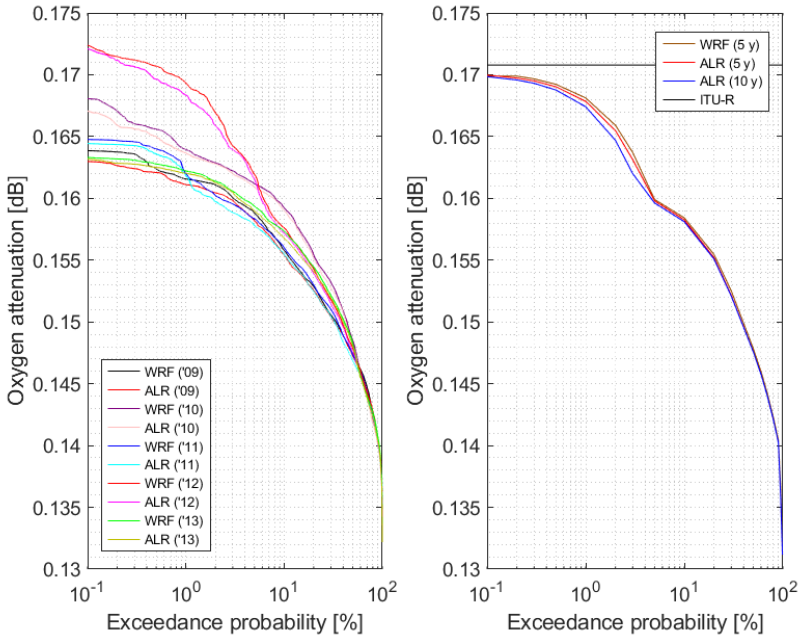

Figure 5.9 – Oxygen attenuation CCDFs with WRF, ALARO (ALR) and the ITU-R reference, at 26.0 GHz and 30° in elevation, for Louvain-la-Neuve in 2009-2013 (+ 2004-2013 for ALR)

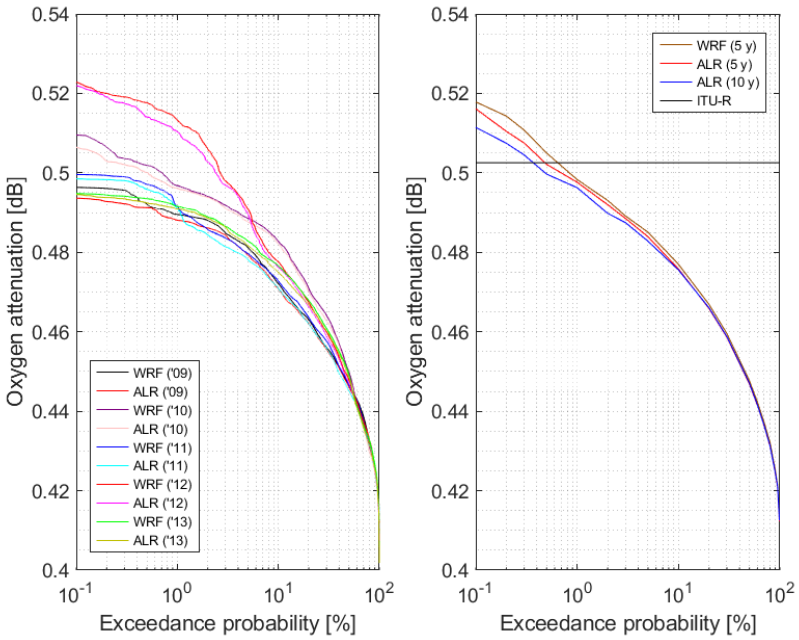

Figure 5.10 – Oxygen attenuation CCDFs with WRF, ALARO (ALR) and the ITU-R reference, at 39.402 GHz and 30° in elevation, for Louvain-la-Neuve in 2009-2013 (+ 2004-2013 for ALR)

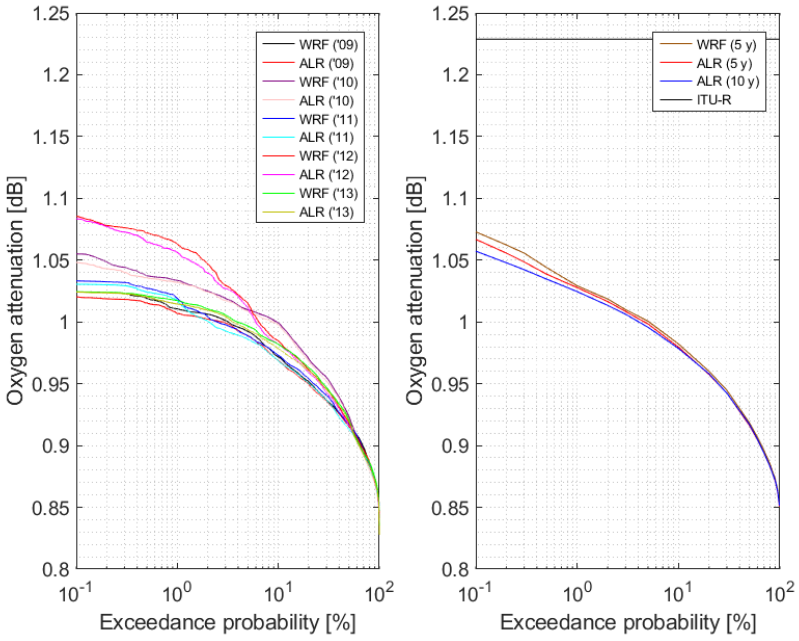

Figure 5.11 – Oxygen attenuation CCDFs with WRF, ALARO (ALR) and the ITU-R reference , at 75.0 GHz and 30° in elevation, for Louvain-la-Neuve in 2009-2013 (+ 2004-2013 for ALR)

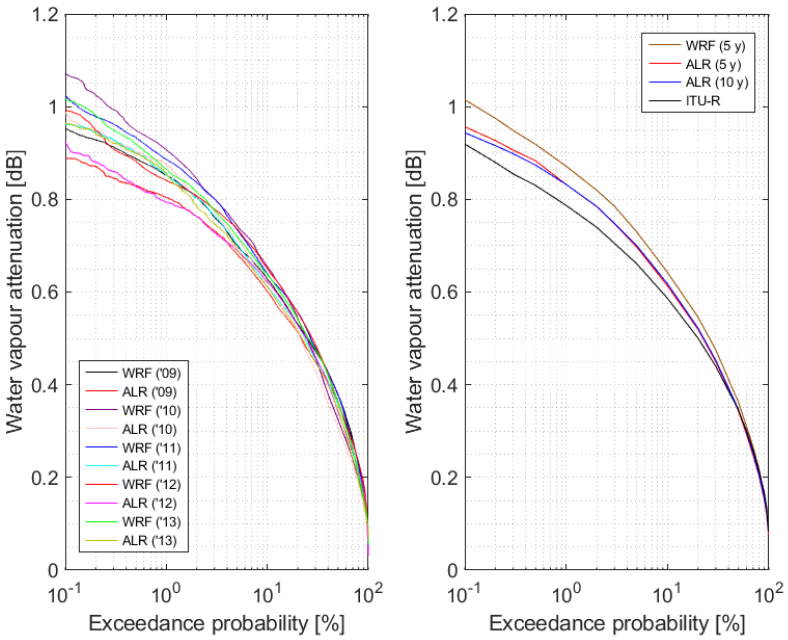

Figure 5.12 – Water vapour attenuation CCDFs with WRF, ALARO (ALR) and the ITU-R reference, at 19.701 GHz and 30° in elevation, for Louvain-la-Neuve in 2009-2013 (+ 2004-2013 for ALR)

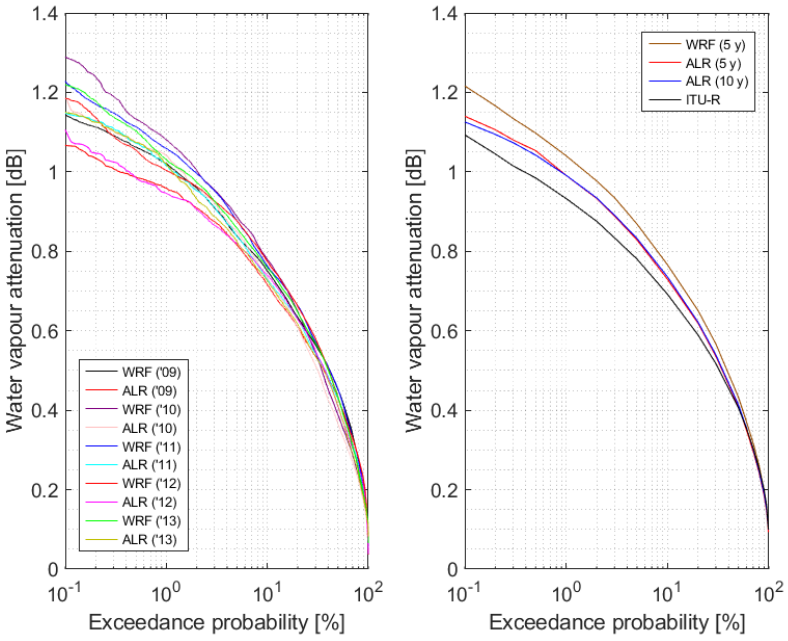

Figure 5.13 – Water vapour attenuation CCDFs with WRF, ALARO (ALR) and the ITU-R reference, at 26.0 GHz and 30° in elevation, for Louvain-la-Neuve in 2009-2013 (+ 2004-2013 for ALR)

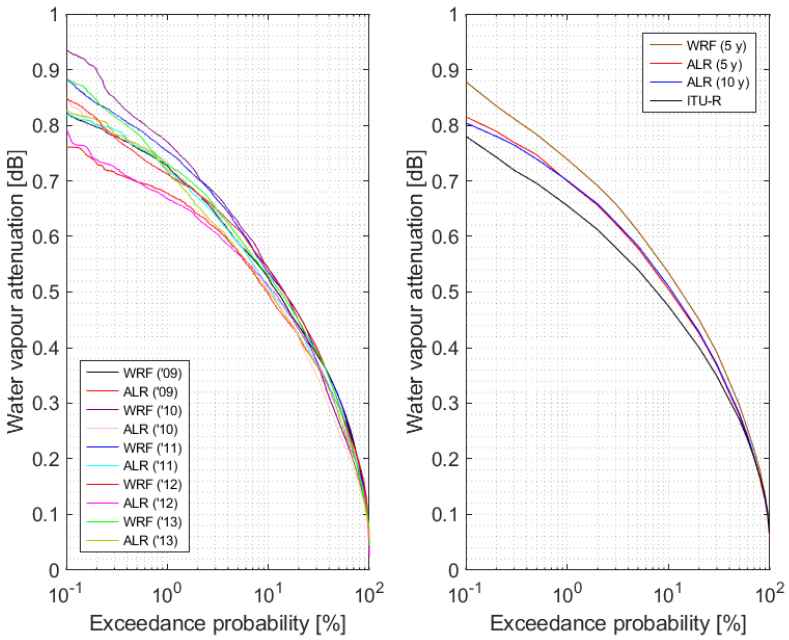

Figure 5.14 – Water vapour attenuation CCDFs with WRF, ALARO (ALR) and the ITU-R reference, at 39.402 GHz and 30° in elevation, for Louvain-la-Neuve in 2009-2013 (+ 2004-2013 for ALR)

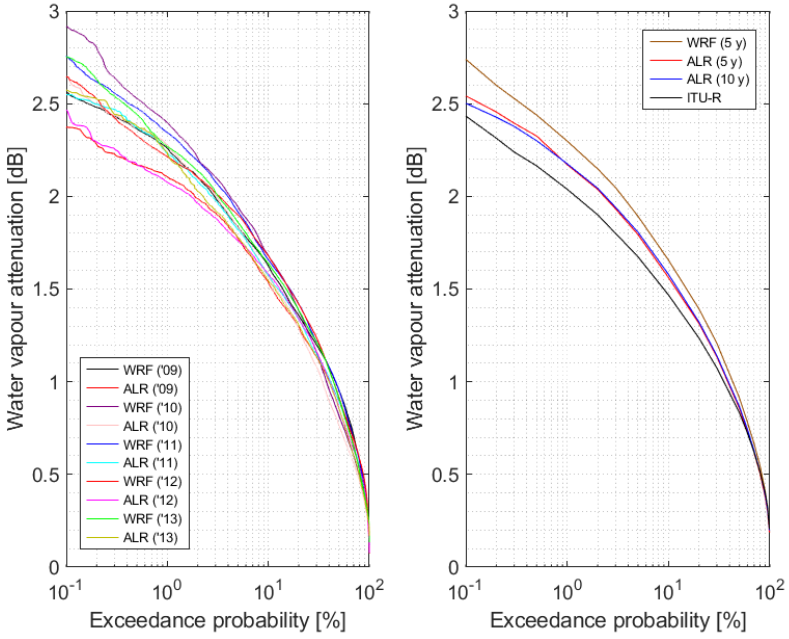

Figure 5.15 – Water vapour attenuation CCDFs with WRF, ALARO (ALR) and the ITU-R reference , at 75.0 GHz and 30° in elevation, for Louvain-la-Neuve in 2009-2013 (+ 2004-2013 for ALR)

5.2.5 Comparison of GEO cloud attenuation

The cloud attenuation is, as illustrated in Sec. 5.2.2 and 5.2.3, a phenomenon with a much higher degree of localisation in time and space than the gaseous attenuation. The probability of occurrence of clouds can nevertheless be high, tens of percents of the time, depending of the location and season, and with contributions ranging from less than the gases to a substantial fraction of the rain attenuation. As explained in Sec. 2.5.2, and at the frequencies studied in this work, the cloud attenuation is therefore an integral part of the nonrainy attenuation that cannot easily be recovered from beacon measurements alone and must be estimated independently from them. As further discussed in Sec. 2.6 and 2.7 there are few options to estimate the cloud attenuation besides radiometers and NWPs. While it is more challenging than for the gases, it is especially important to validate the use of the NWP cloud attenuation.

As before, the Tab. 5.1 p. 87 contains the error metrics, for 2009-2013, of the cloud attenuation produced by WRF when compared to ALARO. For both NWP models, the cloud attenuation is computed from the cloud liquid water content generated from the model itself and its parametrisations. A first observation is that the correlations, which vary slightly between 0.11 and 0.13 depending on the frequency, are very low, especially when compared to the correlation for the gases. This already gives a low confidence on the capability to create accurate time series estimate of the instantaneous cloud attenuation. Similarly, the RMSEs are $\sim 0.10\,\mathrm{dB}$, $0.17\,\mathrm{dB}$, $0.35\,\mathrm{dB}$, $0.94\,\mathrm{dB}$ at $19.701\,\mathrm{GHz}$ $26.0\,\mathrm{GHz}$, $39.402\,\mathrm{GHz}$, and $75.0\,\mathrm{GHz}$ respectively. For the two lowest frequencies, the RMSEs are not too high and of the same order of magnitude as the RMSEs for the gaseous attenuation. However, the RMSEs on the cloud attenuation for the higher frequencies are far higher as the cloud attenuation itself get higher. Considering the MEs, they are $\sim -0.02\,\mathrm{dB}$, $-0.03\,\mathrm{dB}$, $-0.07\,\mathrm{dB}$, and $-0.15\,\mathrm{dB}$ for each of the frequencies of interest. There is therefore a marked negative bias of WRF against ALARO, with the latter generating cloud liquid water either in higher quantities or more often. Once more, the higher frequencies are more strongly impacted. To understand better the perceived limits on the performances, it is essential to look at the distributions.

The Fig. 5.16 p. 97 presents the cloud attenuation CCDFs for the first $19.701\,\mathrm{GHz}$ frequency. For WRF two other cloud attenuation estimates are included: one estimate using the Salonen cloud detection model (see Sec. 2.3.6) instead of the WRF cloud content, and another estimate using the Mattioli cloud detection model (see Sec. 2.3.7). They were not included into the error metrics table because of their tendency to overestimate the cloud attenuation so much with respect to the NWP cloud output, hence it suffices to say their errors with respect to ALARO are even higher than the ones reported.

Back to the full picture however, it appears on the left panel of the Fig. 5.16 that the cloud attenuation CCDF from ALARO cloud content is indeed generally higher than the cloud attenuation CCDF from WRF cloud content. Very importantly, the probability of having cloud attenuation is consistently higher, ~ 80 % each year, for the CCDFs from ALARO than for the CCDFs from WRF, where it reaches ~ 30 %. It means here the CCDFs from ALARO are already at $\sim 0.05\,\mathrm{dB}$ for more than 30 % of the time while the WRF CCDF

is still at 0 dB. Otherwise the ALARO and WRF curves seem to almost merge at lower probabilities, with an attenuation ~ 0.6 dB more than 0.1 % of the time for most of the year. Excluding some years such as 2009, 2010, and especially 2013, the year to year variability of the cloud attenuation is not so high and the differences between WRF and ALARO are of a similar order of magnitude, within ~ 0.1 dB for an exceedance probability of 0.1 %.

Interestingly, the WRF CCDFs using the Salonen and Mattioli models also display some characteristics of the other cloud CCDFs, in spite of them predicting attenuations more than twice higher for most of the probability range, and with the Mattioli model predicting even higher attenuation than the Salonen model. For both the Salonen and the Mattioli model, the year to year variability is similar to NWP cloud content models. The probability of having cloud attenuation is also higher than for the native WRF output, and aligns rather well with the prediction of the ALARO cloud content. If one now pays attention to the right panel of the Fig. 5.16, with the CCDFs over 5 years (and also 10 years for ALARO), the general behaviour observed from the CCDFs for individual years emerge clearly. The WRF and ALARO CCDFs using their own cloud content output show a marked difference in the probability of cloud attenuation, as well as the cloud attenuation from ALARO being higher, thank to a few years in particular. The year-to-year variability of the cloud attenuation is also confirmed to be low as the ALARO CCDF over 10 years is only slightly below the one over 5 years. The WRF CCDFs with the Salonen and Mattioli models are again largely over both cloud content CCDFs, but what is also notable is their shape which sees some sort of plateau appearing near 0.1 % of the time whereas the other CCDFs would keep increasing. Hence while the Mattioli model is higher than the Salonen model, both of them almost join at an exceedance probability of 0.1 %.

Due to all the curves sometimes radically different behaviours, and in the absence of measurements, it is difficult to identify which model could be the (more) correct one. Therefore a comparison with the ITU-R reference CCDF for the cloud attenuation is needed. The ITU-R CCDF presents a probability of cloud attenuation ~ 50 % that is intermediate between WRF and ALARO cloud content CCDFs, but aligning more with the latter. Strikingly, the cloud attenuation rises very fast in comparison to the native NWP CCDFs, and even overshoots both the Salonen and Mattioli model after an exceedance probability of ~ 1 %. Having a look at the other frequencies in the Fig. 5.17-5.19 pp. 97-98, the previous observations stands albeit scaled to higher attenuations. This latter aspect is however of a tremendous importance as e.g. the difference for 0.1 % of the time is from 0.6 dB (WRF cloud content) to 1.3 dB (ITU-R) at 19.701 GHz, but from 6 dB (WRF cloud content) to 12.5 dB (ITU-R) at 75.0 GHz. The rough observation that the ITU-R predicts double the cloud attenuation is a bigger issue as the attenuation increases roughly tenfold.

There are many unresolved questions here. Is the NWP cloud production insufficient, especially WRF's? Is the NWP resolution/parametrisation at cause? Are the cloud detection algorithms or ITU-R reference overestimating? To clarify the situation, radiometric measurements are needed. Answering some of these questions will be a goal of Chap. 6.

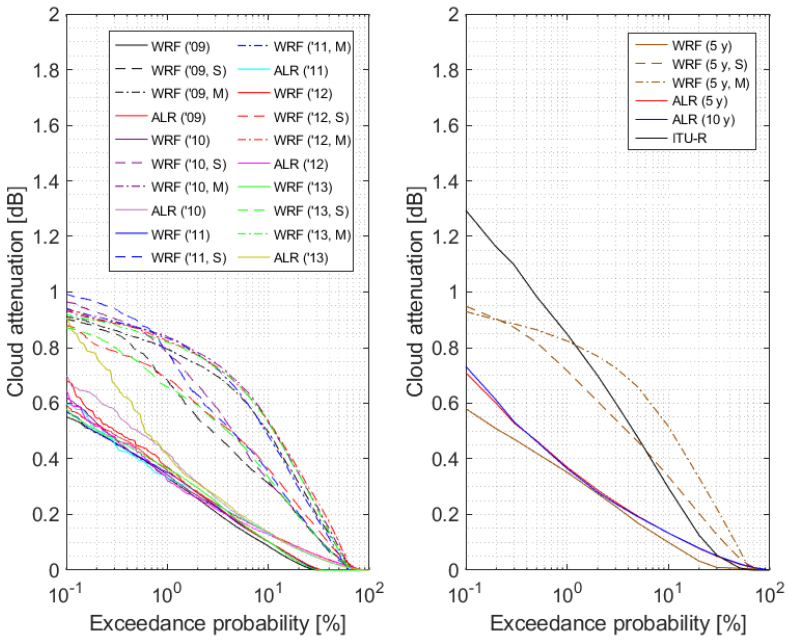

Figure 5.16 – Cloud attenuation CCDFs with WRF (Salonen or Mattioli), ALARO (ALR) and the ITU-R reference, at 19.701 GHz and 30° in elevation, for Louvain-la-Neuve in 2009-2013 (+ 2004-2013 for ALR)

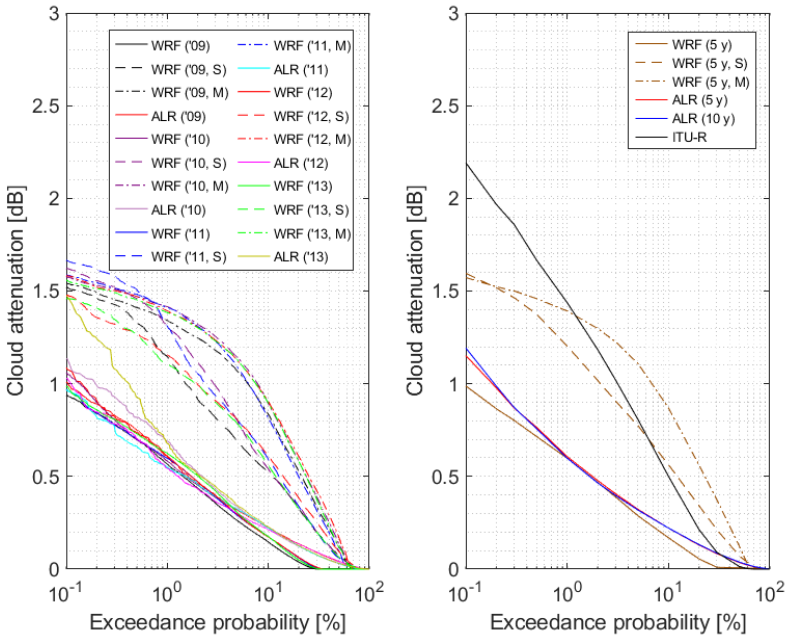

Figure 5.17 – Cloud attenuation CCDFs with WRF (Salonen or Mattioli), ALARO (ALR) and the ITU-R reference, at 26.0 GHz and 30° in elevation, for Louvain-la-Neuve in 2009-2013 (+ 2004-2013 for ALR)

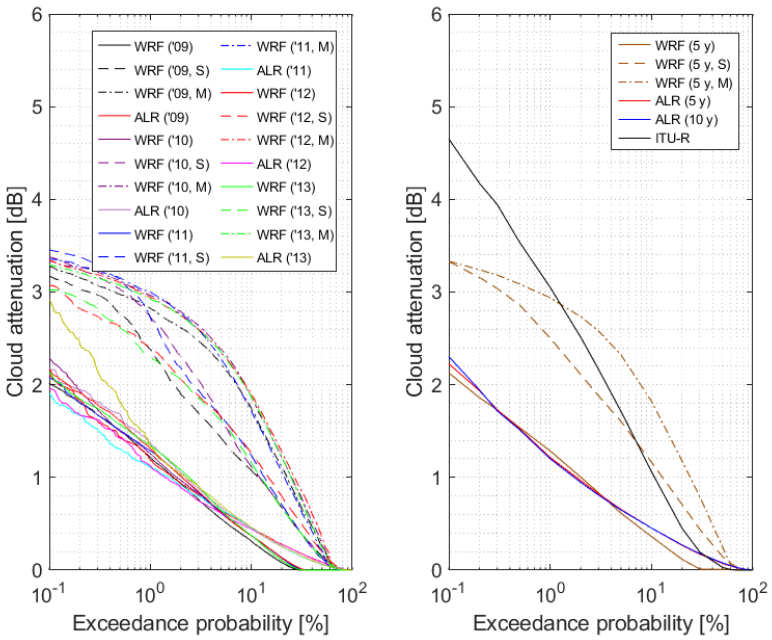

Figure 5.18 – Cloud attenuation CCDFs with WRF (Salonen or Mattioli), ALARO (ALR) and the ITU-R reference, at 39.402 GHz and 30° in elevation, for Louvain-la-Neuve in 2009-2013 (+ 2004-2013 for ALR)

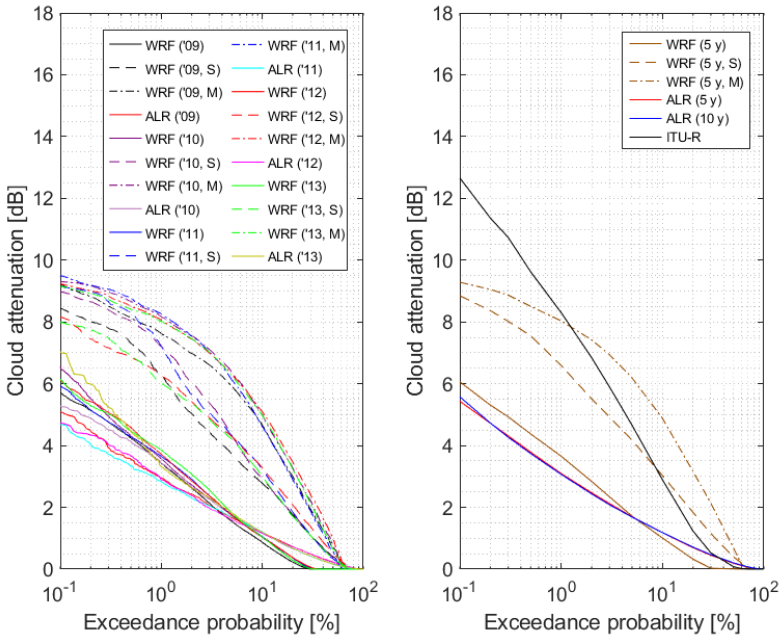

Figure 5.19 – Cloud attenuation CCDFs with WRF (Salonen or Mattioli), ALARO (ALR) and the ITU-R reference, at 75.0 GHz and 30° in elevation, for Louvain-la-Neuve in 2009-2013 (+ 2004-2013 for ALR)

5.2.6 Comparison of GEO rain attenuation

The rain attenuation is in many ways the most important attenuation component an engineer may wish to model, as it the main cause of signal loss in a system or the reason to adapt the coding to avert it. Performing the prediction at the level of time series with NWPs is a difficult task, as was reviewed among other things in Sec. 1.4. But there is at least hope for the long-term simulated CCDFs of rain attenuation to match the long-term CCDFs from propagation beacon measurements or from the derived ITU-R models. Another type of measurements relevant to the rain attenuation are weather radar measurements such as those from Wideumont radar included here in the comparison.

Referring again to the Tab. 5.1 p. 87, it is easy to see why the accuracy of NWPs for instantaneous rain attenuation prediction is less than assured. Firstly, note that there are two models for the rain attenuation in use, the model using the rain content in volume with Mie scattering (see Sec. 2.3.8), only for WRF, and the model using the ground rain rate (RR) (see Sec. 2.3.9), used both for WRF and for ALARO. The correlations for WRF (Mie) vs ALARO (RR) are ~ 0.04, 0.04, 0.06, 0.09 at $19.701\,\mathrm{GHz}$ $26.0\,\mathrm{GHz}$, $39.402\,\mathrm{GHz}$, and $75.0\,\mathrm{GHz}$ respectively. The correlations for WRF (RR) vs ALARO (RR) are ~ 0.04, 0.05, 0.07, 0.11 at those same frequencies. The main conclusion is that the correlations are very poor. They are a bit better between the two estimates using the same model (RR), but they are otherwise very similar, which is to say at least both models correlate well from the same WRF runs but not between WRF and ALARO. The correlation improves with the frequency, which suggests there is at least some overlap in the predictions of the strongest rain events associated with very high attenuations and having the most influence on the correlations. For comparison, a correlation ~ 0.1, while poor, arrives at the same level as what was found for the clouds. The RMSEs at these frequencies of interest are for WRF (Mie) vs ALARO (RR), $0.314\,\mathrm{dB}$, $0.547\,\mathrm{dB}$, $1.13\,\mathrm{dB}$, $2.34\,\mathrm{dB}$, and for WRF (RR) vs ALARO (RR), $0.503\,\mathrm{dB}$, $0.744\,\mathrm{dB}$, $1.38\,\mathrm{dB}$, $2.60\,\mathrm{dB}$. These RMSEs are high, increasing with the frequency as expected, none of which is surprising. However, it is notable that the RMSEs are a bit higher between the two models using the ground rain rate. Without entering into their details, the MEs are smaller than for the clouds, due to rain having lower probability of occurence; they are negative for WRF (Mie) vs ALARO (RR), but generally positive for WRF (RR) vs ALARO (RR). The MEs thus already suggest which models result in higher rain attenuations.

For a better understanding, one needs to refer to the CCDFs. The rain attenuation CCDFs for $19.701\,\mathrm{GHz}$ are in the Fig. 5.20 p. 102. A striking feature of the left part of the figure, containing the CCDFs for individual years, is the strong inter-annual variability. For example, at an exceedance probability of 0.01 %, ALARO in 2011 estimates $\sim 3\,\mathrm{dB}$ of rain attenuation, but in 2013 $\sim 12.5\,\mathrm{dB}$. As another example, still at 0.01 %, WRF (Mie) estimates $\sim 15\,\mathrm{dB}$ in 2011, but only $\sim 5\,\mathrm{dB}$ in 2013. From these examples it is clear that the CCDFs differ widely between the different models for the same year. Due to the number of curves, it is not clear at a glance whether WRF (Mie) or ALARO presents higher values on average. Another feature of the models is the systematically higher WRF (RR) attenuation with respect to WRF (Mie).

A cleaner picture of the performances of each model is obtained on the right side of the Fig. 5.20, with the long-term CCDFs. WRF (Mie) and WRF (RR) are both over the 5 years dataset (2009-2013), ALARO (RR) is represented for both those 5 years and for the extended 10 years period (2004-2013). Importantly, the Wideumont weather radar rain attenuation CCDF is also represented for the period (2003-2012), with a near concurrency between ALARO and the radar. The ITU-R reference rain attenuation CCDF is also shown, as was the case for the other impairments. On the topic of the agreement between the two non-NWP references, the radar curve behaves very similarly to the ITU-R, as was discussed further in [110]. It must be recalled the ITU-R rain CCDF is actually presumed to be valid only up to 5 % of the time (see Sec. 2.3.10). The probability of rain itself for Louvain-la-Neuve was given coincidentally as 5 % by the ITU-R P.837-6, and is now adjusted as 6.96 % by the ITU-R P.837-7 [87]. The ITU-R CCDF is ~ 0.5 dB above the radar CCDF down to ~ 0.03 % of the time after which the radar CCDF catches up. Being built from a large database of local measurements, the radar CCDF could be considered as the more trustworthy reference. The ITU-R CCDF is indeed reconstructed from a simplified model, even though direct beacon measurements entered into its development. The ITU-R curve is based on the rain rate exceeded 0.01 % of the time, and the agreement with the radar is better for this part of the CCDFs. Also since both the radar and ITU-R rain attenuation models are based on the rain rate, another aspect likely to affect the curves is the integration time of said rain rate. For the ITU-R it is 1 min. For the radar there is not a comparable notion considering the scan in elevation, but the output temporal resolution is 5 min. The agreement of the WRF (RR) CCDF, using a rain rate integrated over the model resolution of 5 min, with the radar CCDF is actually even better than the agreement between the radar and the ITU-R CCDFs. Indeed the WRF (RR) CCDF is only slightly below the radar CCDF. This results is a great confidence boost in the capability of NWP models to produce long-term CCDFs of the rain attenuation, and the importance of ~ 5 years of data is also clear to reduce the inter annual variability. Speaking of which, if one takes now an interest in the other CCDFs on the right, the two ALARO CCDFs over 5 and 10 years are still in good agreement, as was the case for the gases and the cloud attenuations. The discrepancies, of the order of 1 dB for 0.01 % of the time, are higher than for the other impairments. It tends to show that, while 5 years is enough to reduce the inter-annual variability significantly, a larger number of years is beneficial to reduce it further in the case of rain (see [141, 142] on that topic). The ALARO CCDFs are nevertheless clearly below the references for probabilities lower than 1 %. Part of this underestimation may come from the rain rate integration time of 1 h imposed by the ALARO output step. The WRF (Mie) CCDF is not in the same scenario regarding its temporal resolution, but it also underestimates the reference CCDFs, from ~ 0.5 dB for 1 % of the time, and by as much as 5 dB for 0.01 % of the time.

Though CCDFs from the radar are not available for them, the frequencies 26.0 GHz, 39.402 GHz, and 75.0 GHz are represented by the rain attenuation CCDFs from the other models in the Fig. 5.21-5.23 pp. 102-103. All

the features observed at 19.701 GHz are still present: the large year-to-year variability of the rain attenuation CCDFs on the left side of the figures, the long-term NWP CCDFS being below the ITU-R reference on the right side of the figures, with the best agreement with the ITU-R found for the WRF (RR) model, and with the other two NWP models underestimating them. It must be noted that, as given in Sec. 2.3.10, the ITU-R rain attenuation CCDF is not designed to work for a frequency as high as 75 GHz. In practice however there is no sign that the ITU-R model behaves differently in Fig. 5.23 than for the lower frequencies.

In summary of the results for the rain, a NWP model, WRF (RR), is seen to yield long-term CCDFs of the rain attenuation in acceptable agreement with both the ITU-R reference CCDF and the CCDF derived from weather radar reflectivity measurements, though with some underestimation. The other models, WRF (Mie) and ALARO (RR), underestimate the references more severely. The statistical agreement is found in spite of low correlations and high RMSEs between the NWP models, which suggest poor instantaneous performances.

5.2.7 Comparison of GEO total attenuation

To conclude the GEO part of the NWP validation about the total attenuation, it is useful to have a look at its corresponding error metrics and statistics.

In the Tab. 5.1 p. 87, the correlations on the total attenuation vary both in terms of the frequency and if the rain attenuation is considered to come from the Mie scattering approach, or the rain rate approach. The cloud attenuation is only considered as coming from the NWP models native cloud contents. The correlation on total attenuation is lowest with $\sim$ 0.13 for WRF (Mie) at 39.402 GHz, and correspondingly highest with $\sim$ 0.34 for WRF (Mie) at 19.701 GHz. The correlations are similar to the $\sim$ 0.2 that Jeannin et al. [36] reported between WRF and 18.7 GHz ITALSAT data, which were already mentionned in Sec. 1.4. Unsurprisingly the RMSEs are higher than even for rain, as the variability from all the impairments are encompassed into the total attenuation. The MEs are naturally the sum of the MEs for each component, which results in negative values as the errors from the cloud dominates.

In the Fig. 5.24-5.27 pp. 104-105, the CCDFs for the total attenuation are shown in a similar fashion as before, at the four frequencies of interest in this study. The left parts of the figure emphasize the inter-annual variability seen to affect the attenuation component to diverse degrees, though rain is the strongest contributor. Considering the right parts of the figure, for the long-term CCDFs, an observation made e.g. in the Fig. 5.24 is the excellent agreement at high probabilities of exceedance brought up by the gaseous attenuation. The higher cloud attenuation predicted by the ITU-R starts to visibly affect the CCDFs for $\sim$ 20 to 30 % of the time and create a gap between the reference and the NWP models. The gap is then further increased as rain starts to affect the reference statistics. The cloud attenuation is artificially plateaued below 1 % of the time (see Sec. 2.3.10), which allows the NWP model to partially catch up to the ITU-R. The WRF (RR) CCDF is the closest to the reference, with the WRF (Mie) and ALARO CCDFs below it.

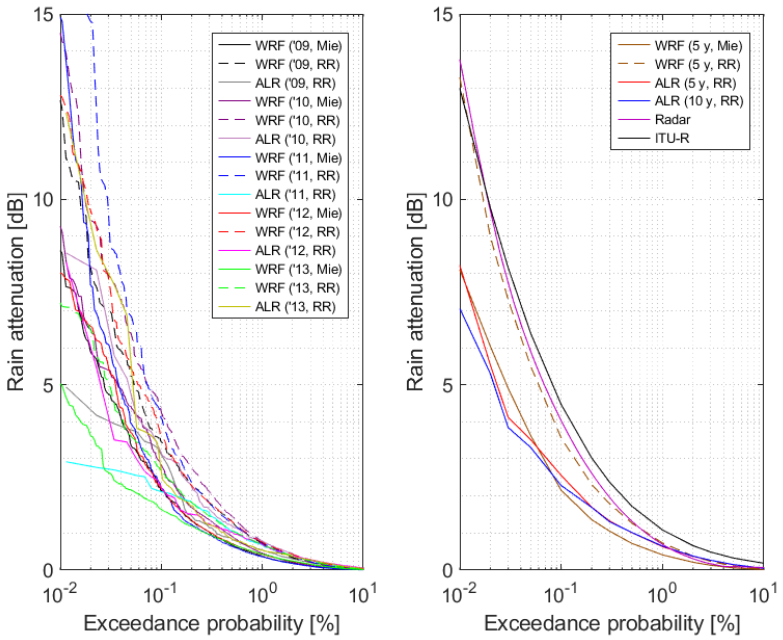

Figure 5.20 – Rain attenuation CCDFs with WRF (Mie or Rain Rate), ALARO (ALR), and the ITU-R reference, at 19.701 GHz and 30° in elevation, for Louvain-la-Neuve in 2009-2013 (+ 2004-2013 for ALR, 2003-2012 for Radar)

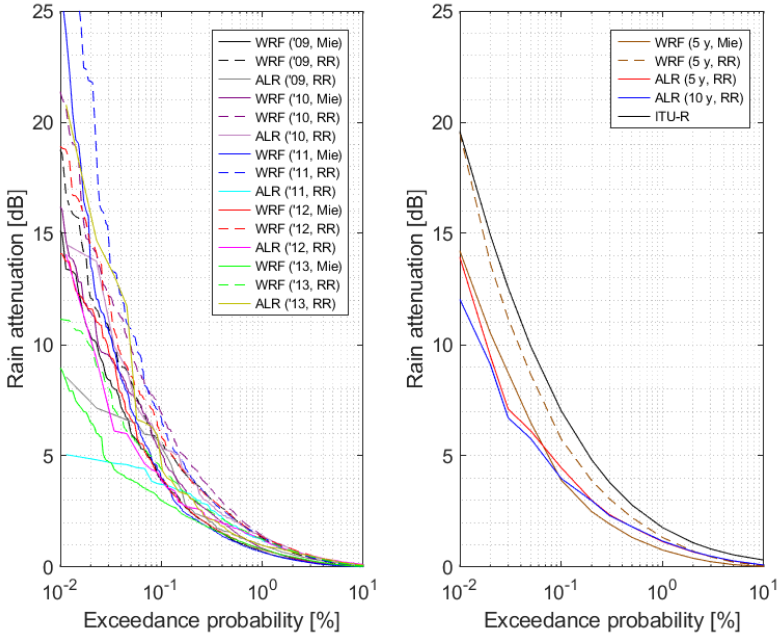

Figure 5.21 – Rain attenuation CCDFs with WRF (Mie or Rain Rate), ALARO (ALR) and the ITU-R reference, at 26.0 GHz and 30° in elevation, for Louvain-la-Neuve in 2009-2013 (+ 2004-2013 for ALR)

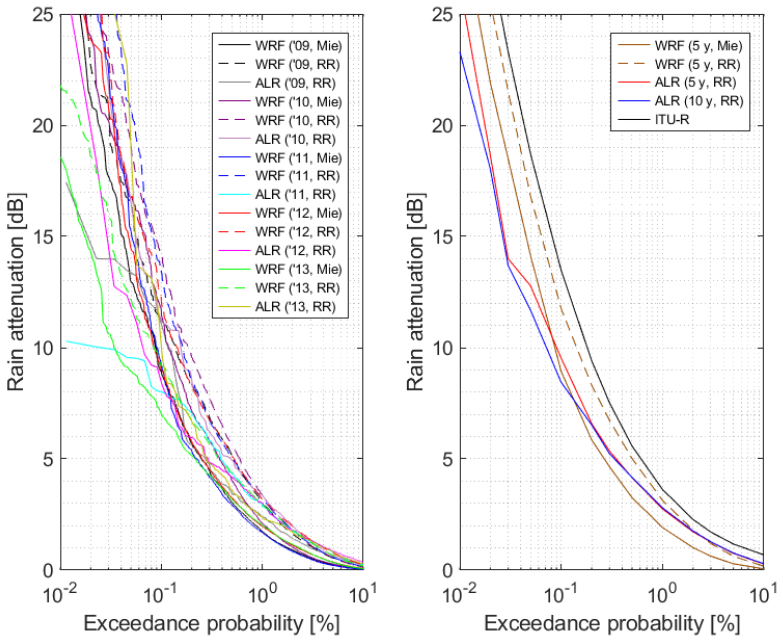

Figure 5.22 – Rain attenuation CCDFs with WRF (Mie or Rain Rate), ALARO (ALR) and the ITU-R reference , at 39.402 GHz and 30° in elevation, for Louvain-la-Neuve in 2009-2013 (+ 2004-2013 for ALR)

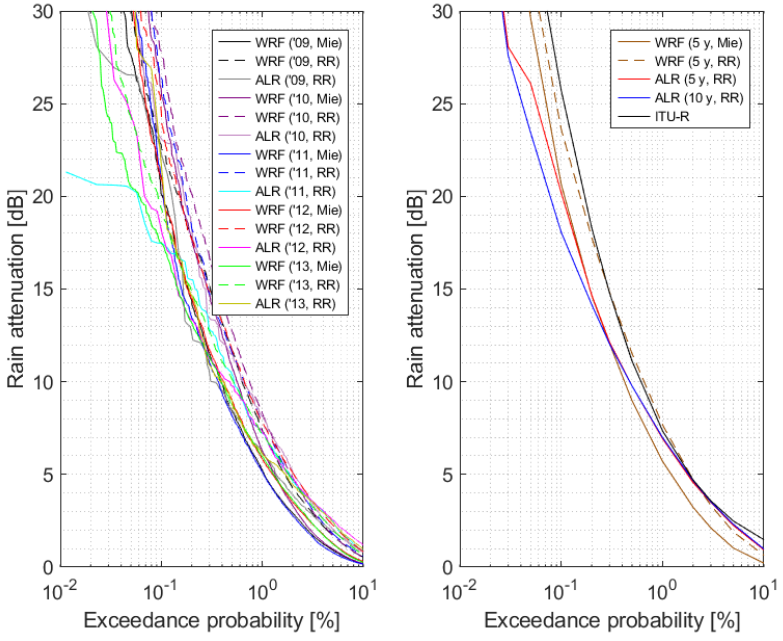

Figure 5.23 – Rain attenuation CCDFs with WRF (Mie or Rain Rate), ALARO (ALR) and the ITU-R reference , at 75.0 GHz and 30° in elevation, for Louvain-la-Neuve in 2009-2013 (+ 2004-2013 for ALR)

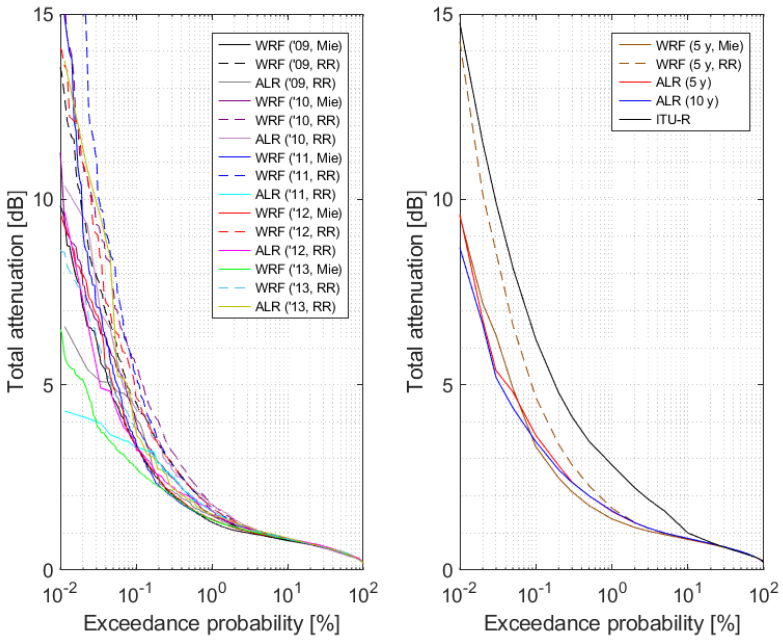

Figure 5.24 – Total attenuation CCDFs with WRF, ALARO (ALR) and the ITU-R reference, at 19.701 GHz and 30° in elevation, for Louvain-la-Neuve in 2009-2013 (+ 2004-2013 for ALR)

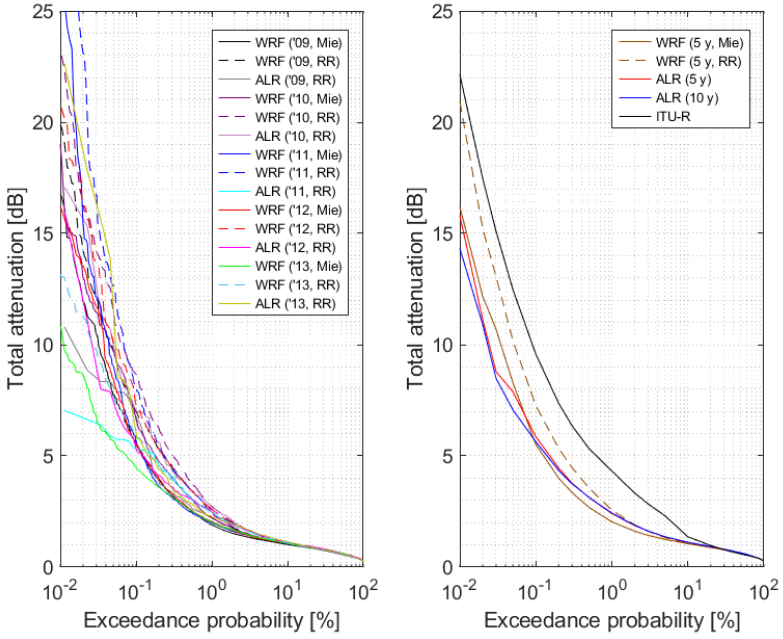

Figure 5.25 – Total attenuation CCDFs with WRF, ALARO (ALR) and the ITU-R reference, at 26.0 GHz and 30° in elevation, for Louvain-la-Neuve in 2009-2013 (+ 2004-2013 for ALR)

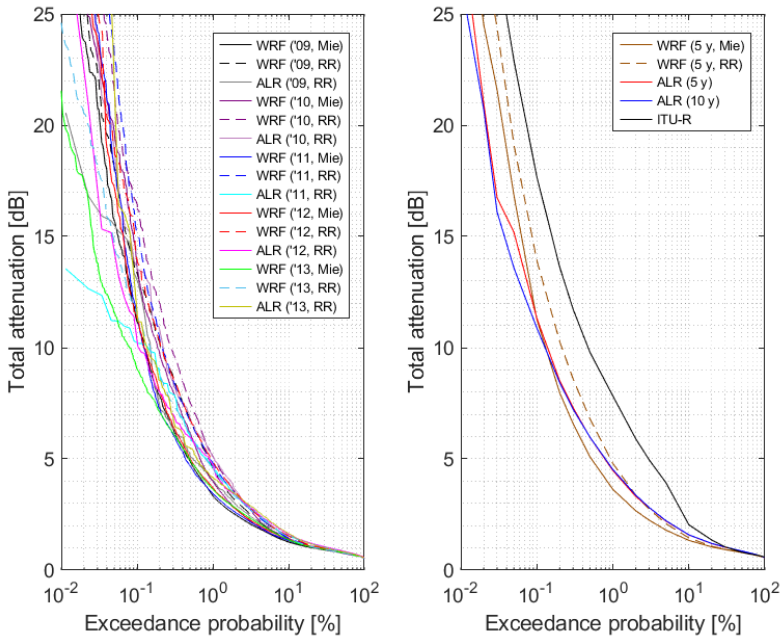

Figure 5.26 – Total attenuation CCDFs with WRF, ALARO (ALR) and the ITU-R reference, at 39.402 GHz and 30° in elevation, for Louvain-la-Neuve in 2009-2013 (+ 2004-2013 for ALR)

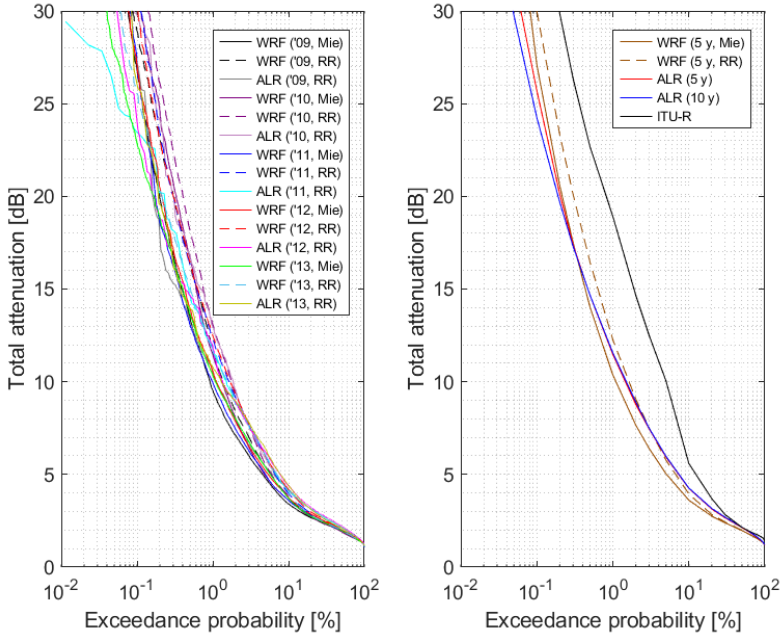

Figure 5.27 – Total attenuation CCDFs with WRF, ALARO (ALR) and the ITU-R reference, at 75.0 GHz and 30° in elevation, for Louvain-la-Neuve in 2009-2013 (+ 2004-2013 for ALR)

5.2.8 Comparison of LEO total attenuation

Now that the validation for the GEO attenuation has been conducted at 30° in elevation, it is possible to consider what happens in the case of LEO satellites. As was discussed previously, the CCDF of a LEO satellite can be derived from LEO time series generated according to 4.37 (see Sec. 4.3.2 p. 71), or from a set of GEO CCDFs at multiple elevation angles (see Sec. 4.4.3 p. 73).

Concerning the time series approach, it is desirable to have a temporal resolution corresponding both to stable atmospheric conditions and shorter than the duration of the satellites passes. So, the ALARO hourly dataset does not offer a sufficient resolution for direct LEO modelling. Concerning the GEO CCDFs approach, it is necessary to establish the histogram of the elevation at which the LEO satellite is visible. Because METOP-A, -B, and -C share almost the same orbit, the elevation histogram is essentially the same for all of them over a sufficiently long period of time. The Fig. 5.28 shows the normalized elevation histogram for the METOP-A satellite for the 5 years period 2009-2013. The probability associated to the given elevation bins is higher for lower elevations than for higher ones, i.e. the satellite is visible most of the time at low elevations but very rarely close to the zenith (see also the example of passes in Fig. 5.5). It is worthwhile to also investigate the histogram for the azimuth, which is shown in Fig. 5.29. There is a clear preference for the 0° azimuth, i.e. towards the north, with about twice the probability to see the satellite from that direction than from the 180° azimuth, i.e. from the south. This could be an issue considering all the GEO CCDFs were computed with an azimuth of 180°, as it is a good approximative direction for GEO links from the northern hemisphere. However, generally, the azimuthal dependence of the attenuation on the long-term is assumed to be weak: for the gases it is clearly the case even instantaneously in Sec. 5.2.2, for rain the dependence on radar-derived specific rain attenuation is shown to be very small in Louvain-la-Neuve by Lukach et al. [110], similarly to e.g. observations that were made with radar derived rain rate in Vienna by Teschl et al. [143].

The resulting LEO total attenuation CCDFs, for which 100 % of the time represent the visibility period of the satellite (i.e. here an elevation $> 10°$), are given in the Fig. 5.30-5.33 pp. 108-109. The total attenuation CCDFs are obtained for WRF, considering its native cloud content, using either the rain attenuation obtained from Mie scattering or from the rain rate, and for the statistics corresponding either to the time series of the three METOP satellites, or corresponding to weighted conditional combinations of GEO CCDFs. For the conditional method, the ITU-R reference CCDFs are also considered. Unsurprisingly, some of the features observed on the 30° CCDFs are also present for the LEO attenuations. The WRF total attenuation using Mie scattering is below the one using the NWP rain rate. There is a gap in the central part of the probabilities between the WRF CCDFs and the ITU-R one, due to the lower cloud attenuation from WRF.

More interesting observations specific to the LEO are, however, the lack of convergence of the CCDFs of METOP-A, -B and -C to a single statistics even over 5 years. Indeed, while the CCDFs are in good agreement for high probabilities of exceedance, the LEO CCDFs diverge at lower probabilities.

It is not clear if this is influenced more by the inter-annual variability, as the visibility of the LEO satellite is only 3.06 % of the time it is much less than even a year, or rather by regular passes on different parts of the day imposed by the sun-synchronous orbits. It remains that the conditional probability CCDF of WRF either over- or underestimate the individual satellite CCDFs. The limits on those performances, with sometimes 5 dB to 10 dB of discrepancies between certain model, must however be put in the context of the quasi-absence of LEO measurements. On the one hand, the ITU-R reference offer a safe link budget as it it almost always higher than WRF. On the other hand, the variability obtained in the simulations suggests more economical models can be devised.

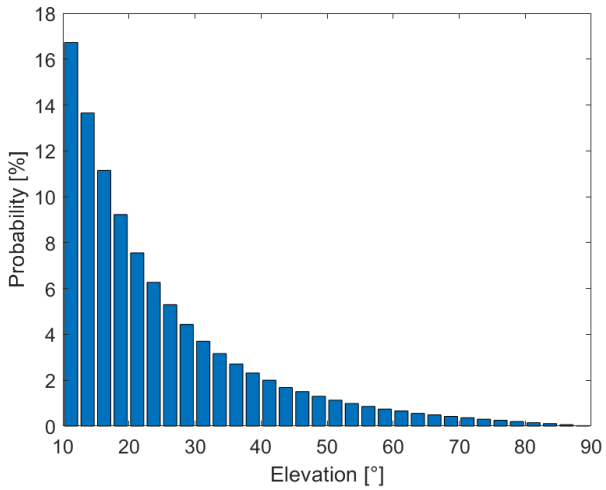

Figure 5.28 – Elevation PDF for METOP-A and Louvain-la-Neuve in 2009-2013

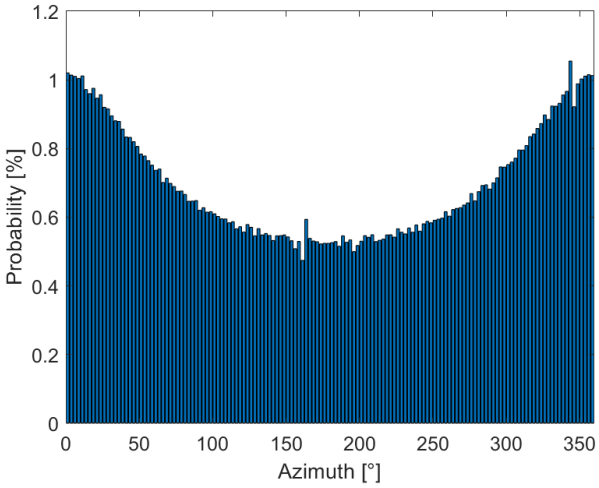

Figure 5.29 – Azimuth PDF for METOP-A and Louvain-la-Neuve in 2009-2013

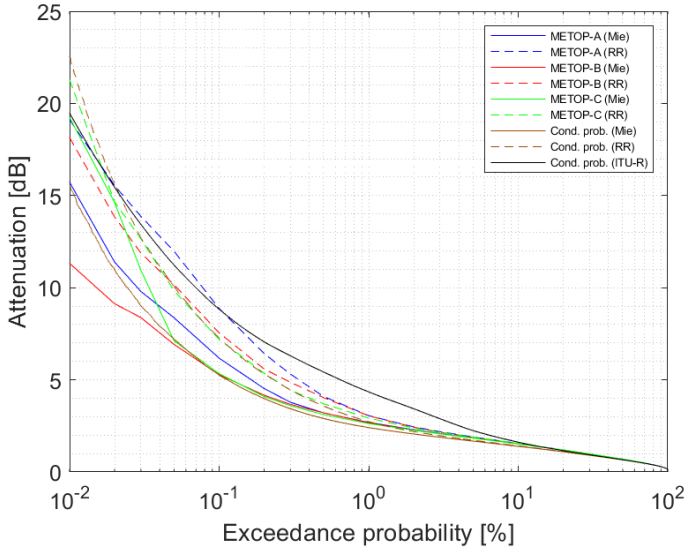

Figure 5.30 – Total attenuation CCDFs with WRF and the ITU-R reference, at 19.701 GHz for METOP-A, -B, and -C, for Louvain-la-Neuve in 2009-2013

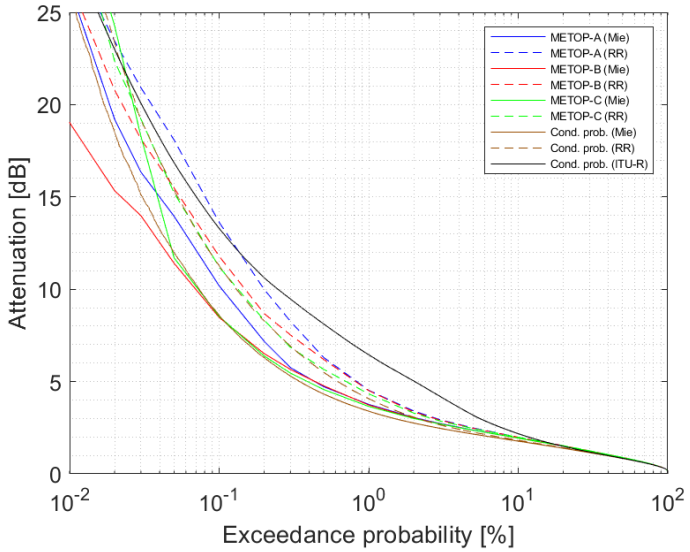

Figure 5.31 – Total attenuation CCDFs with WRF and the ITU-R reference, at 26.0 GHz for METOP-A, -B, and -C, for Louvain-la-Neuve in 2009-2013

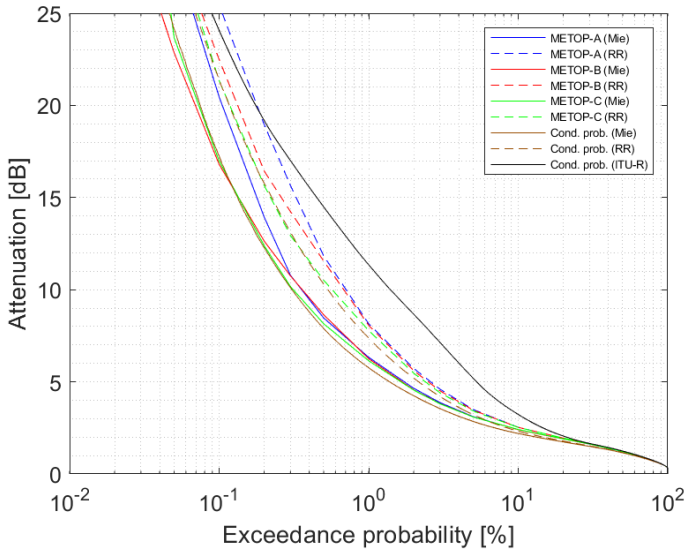

Figure 5.32 – Total attenuation CCDFs with WRF and the ITU-R reference, at 39.402 GHz for METOP-A, -B, and -C, for Louvain-la-Neuve in 2009-2013

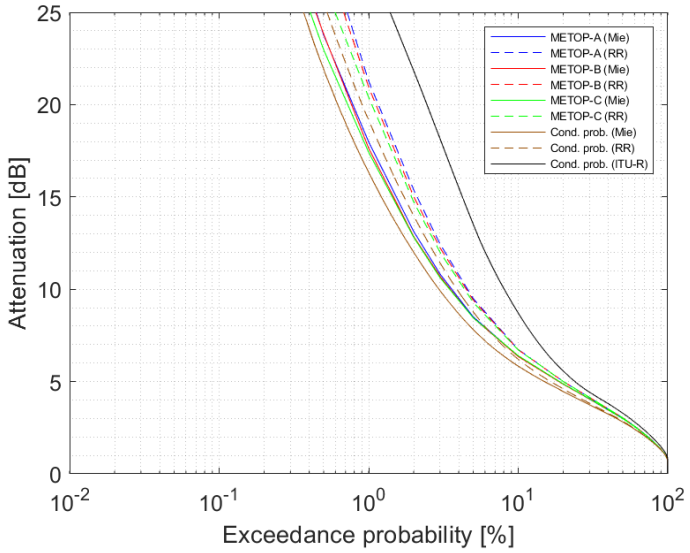

Figure 5.33 – Total attenuation CCDFs with WRF and the ITU-R reference, at 75.0 GHz for METOP-A, -B, and -C, for Louvain-la-Neuve in 2009-2013

5.3 Concluding remarks

This chapter was dedicated to the validation of the principal attenuation components (gases, cloud, rain) and their combination (total) derived from NWP data with two solvers, WRF and ALARO, by comparison between these models and also with weather radar data and the ITU-R references. The NWP models have a high spatial resolution (4 km) and a high temporal resolution (5 min for WRF, 1 h for ALARO). The validation is based on long-term datasets for a single ground station in Louvain-la-Neuve (5 years for WRF, 10 years for ALARO and the weather radar). To the author knowledge, a similar approach, and over such a long period, has not been reported before.

In order to summarize the results of the validation, some important conclusions are recapitulated here point by point. Regarding the observations made on sample output from WRF and the corresponding post-processed propagation variables (from Sec. 5.2.1 to 5.2.3), it is found that:

- WRF shows a realistic behaviour for common NWP ground variables (2 m temperature, ground rain rate, surface energy balance). A long-term comparison (e.g. with ALARO) would be more enlightening however.
- the attenuation azimuth-elevation maps show varying degree of azimuthal dependence and deviations from the cosecant scaling law. For the gases, both of the latter effects are almost negligible. For the clouds and rain, there are localized features showing the use of 3D data.
- GSO time series presents a slow varying gaseous attenuation baseline and correlated cloud and rain events. Non-GSO time series may exclude propagation events seen by GSO links outside of passes, so that one must be careful when studying non-GSO links from GSO results.

Regarding the comparison of the CCDFs of the attenuation components for GEO links at 30° in elevation (from Sec. 5.2.4 to 5.2.7), it is found that:

- the gaseous attenuation is well modelled (correlations > 0.75) with low errors at any frequency, though some biases are possible.
- the cloud attenuation CCDF is lower than predicted by the ITU-R reference for both WRF and ALARO, except when using the Salonen or Mattioli models which exceed the ITU-R at high probabilities of exceedance. WRF probability of clouds is lower than ALARO's, and the time series are not well correlated (~ 0.11) but have otherwise similar amplitudes.
- the rain attenuation shows a strong inter-annual variability, though 5 years stabilise the CCDFs. The CCDFs underestimate the ITU-R reference, though the method based on the rain rate with WRF approaches it best by ~ 1 dB and is close to the radar results at 20 GHz.

Regarding the comparison of the CCDFs of the total attenuation for LEO links based on the METOP satellites (in Sec. 5.2.8), it is found that:

- the CCDFs obtained directly from non-GSO time series differ from the ones obtained from a combination of GSO CCDFs at different elevations.

Chapter 6

Validation of nonrainy attenuation with beacon and radiometric measurements

This chapter presents another validation for the use of NWP data in propagation studies. The validity of the nonrainy attenuation components, understood here as the contribution from the gases and cloud, are investigated by comparison with measurements from a microwave radiometer (see Sec. 6.2.1 and 6.2.2). Because the nonrainy attenuation is typically unknown in a propagation experiment without a radiometer, it is then of interest to see how well the total attenuation is recovered by adding the different nonrainy attenuation estimates to the excess attenuation measured from a propagation beacon (see Sec. 6.2.3).

The content of this chapter is mostly similar to what is found in the papers by Quibus et al. [81, 144].

6.1 Description of the experimental set-up

The validation experiment relies on the presence of the following datasets:

- Alphasat propagation beacon measurements (19.701 GHz and 39.402 GHz) at Spino d'Adda (IT), with a 16 Hz sampling rate.
- concurrent RPG HATPRO radiometric measurements of the brightness temperature at Spino d'Adda, with a 1 Hz sampling rate.
- concurrent rain rate measurements at Spino d'Adda, every 1 min.
- WRF 2 km NWP domain, every 5 min.

Thanks to the combination of beacon and radiometric data, and also thanks to the ancillary rain rate information, a classic retrieval of the excess and total attenuations as presented in Sec. 2.5 and 2.6 was performed by PoLiMi. The date were then transmitted to UCLouvain. Unlike in Chap. 5 where even the radar attenuation was a derived quantity, the current ground for the evaluation of NWP performances is therefore based on data coming as close as possible from direct measurements of the atmospheric attenuation.

Due to the intrinsic value and relative exclusivity of a full propagation dataset of such a high quality as Spino's, an agreement was reached to base the study on a subset of measurements during four months. Those four months were selected for their high availability and representativeness of different weather and seasonal conditions. The following months in 2015, given with the data availability and occurrence of rain, are selected for the comparison:

- January (97.4 % availability, 0.36 % rain), a cloudy and foggy winter month, with some light rain and an event on the 17^{th}.
- May (95.3 % availability, 1.64 % rain), a rainy spring month with high attenuations from showers and thunderstorms.
- July (89.9 % availability, 0.10 % rain), a mostly dry and clear-sky summer month, with one thunderstorm on the 25^{th}.
- October (86.9 % availability, 2.94 % rain), a rainy autumn month.

Because the emphasis is given on validating the performances of NWPs for non-rainy attenuation, it is essential to verify that the selected four months are at least sufficiently representative of the cloud conditions found near Spino. As a way to evaluate this, the Fig. 6.1 illustrates the characteristics of the low clouds cover observed at the Milano Linate Airport ($\sim$ 20 km from Spino d'Adda) for the full year 2015 against the four months, and for the individual month against their containing quarter or "season" [139]. At a glance, one sees there is an overall mix of stratiform and convective clouds, for a total probability of low clouds $> 40\%$. Stratiform clouds are more common in the colder seasons, winter and autumn, while convective clouds are more common in the warmer seasons, spring and summer, with also the presence of cumulonimbuses and thunderstorms. Comparatively, July has a noticeably clearer sky than its containing quarter, while on the other hand May and October have more convective clouds than their respective quarters. Ultimately, none of the cloud type fractions differs by more than 2.5 % between the year and the four months period. It can be concluded that the four months indeed offer representative cloudy conditions and form a sound basis for the study.

6.1.1 Earth-space links' configurations

For more details on the Earth-space links, the site of Spino d'Adda (45.41°N, 9.49°E, 84 m a.m.s.l.) actually coincides with the boresight of the Alphasat antenna for the 39.402 GHz beacon signal. The reason behind this exceptional situation is the status of Spino d'Adda as one of the principal ground station of the Alphasat experiment, and a consequence of this is again the especially high quality of the measurements. Being given the position in longitude of the Alphasat satellite (25°E), the links are modelled as 19.701 GHz and 39.402 GHz GEO links received on average at 159° in azimuth and 35.5° in elevation. Alphasat being geosynchronous, the assumptions of average azimuth and elevation are followed as was described in Sec. 4.3.2.

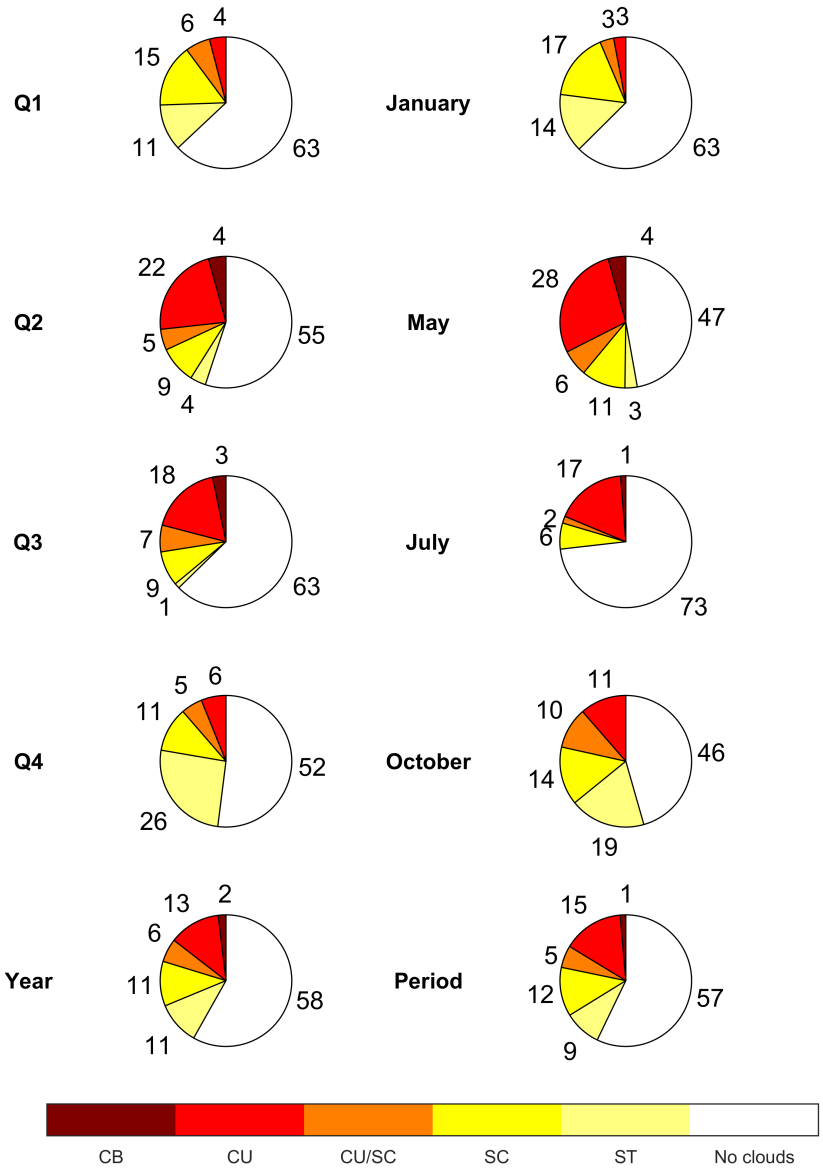

Figure 6.1 – Fractions (%) of low clouds observed in synoptic reports at Milano Linate Airport in 2015 for each quarter of the year and for the period comprising the months of January, May, July and October (CB = cumulonimbus, CU = cumulus, SC = stratocumulus, ST = stratus)

6.1.2 Radiometric data description

The procedure of PoLiMi for the estimation of the non-rainy attenuation from the radiometer measurements is the one detailed in Sec. 2.6. The subset of frequencies taken from the multi-channels RPG HATPRO is { 23.84, 27.84, 31.4, 51.26, 52.28 } GHz for the separation of water vapour, clouds and oxygen.

The RAOBS-based regression coefficients to apply (2.123) and retrieve the attenuation at the frequencies {19.701, 39.402 } GHz are given in the Tab. 6.1. The root-mean-square errors of those regressions are 0.0006 dB at 19.701 GHz and 0.0029 dB at 39.402 GHz. These errors are very small in comparison to instrumental and modelling errors and can safely be neglected from now on.

The average mean radiative temperatures (yearly) and average brightness temperature (over four months) for each of the selected radiometric channels, which are required to estimate the radiometric accuracy according to Sec. 2.6.3, are given in the Tab. 6.2. The standard deviations of the errors on the brightness temperature σ_ζ and on the mean radiative temperature σ_ξ are also needed to estimate the radiometric accuracy. For an ideally calibrated RPG-HATPRO $\sigma_\zeta \approx 0.5\,\mathrm{K}$ [145]; however, due to calibration limitations, in practice, $\sigma_\zeta \approx 2\,\mathrm{K}$ is a more common value [104]. Based on the monthly $\bar{T}_{mr}$ from radio-soundings, $\sigma_\xi \approx 4\,\mathrm{K}$. The resulting standard deviations of the error on radiometric attenuations are evaluated as $\sigma_{\epsilon_{nr}} \in [0.028, 0.043]$ dB at 19.701 GHz and $[0.050, 0.084]$ dB at 39.402 GHz, assuming as in Sec. 2.6.3 positive correlations of the errors at the different radiometric channel frequencies. These values are lower than the ~ 0.1 dB that were reported, using an almost identical method, by Martellucci in the 20-30 GHz band from measurements in Cabauw (NL) [105]. The difference is explained by a lower value of σ_ξ (from 7 K to 4 K) from monthly $\bar{T}_{mr}$, and by an average instead of highest scenario for the brightness temperature.

These estimates of the radiometric attenuation accuracy are particularly important in this context of a validation of the NWP performances. Indeed, since all the reported errors, as defined in Sec. 4.4.1, will be taken with the radiometric attenuation as a reference, its limits must be kept in mind.

Table 6.1 – Characteristics of Spino d'Adda radiometer for attenuation retrieval ($a_0(19.701\,\mathrm{GHz}) = 0.017, a_0(39.402\,\mathrm{GHz}) = -0.038$)

f_i (GHz)	23.84	27.84	31.4	51.26	52.28
$a_i(19.701\,\mathrm{GHz})$	0.247	0.970	-0.517	0.010	-0.005
$a_i(39.402\,\mathrm{GHz})$	0.040	-0.875	1.989	0.107	-0.033

Table 6.2 – Average mean radiative and brightness temperatures used for the estimation of the radiometric attenuation accuracy

f_i (GHz)	23.84	27.84	31.4	51.26	52.28
$\bar{T}_{mr}(f_i)$ (K)	274.33	272.11	270.64	269.11	271.23
$\bar{T}_b(f_i)$ (K)	60.75	37.07	35.63	165.96	209.84

6.1.3 NWP model

The NWP model to be validated here uses a WRF configuration with 3 successively nested domains at 18 km, 6 km and 2 km centered on Spino d'Adda ground station. The domains are shown in the Fig. 6.2.

It is very notable the domains are much smaller than the ones designed previously in Sec. 5.1.2 for the validation comparing the NWP models WRF and ALARO. The final horizontal resolution is however better (from 4 km to 2 km). Both of these differences are expected to have an impact on the NWP performances and their subsequent processing into propagation variables. However the modelling strategy with similarly smaller domains at a higher resolution is inspired by the already positive results of that approach found by the participants of the EODDL ESA contract [37]. The d03 domain is also sufficiently large to contain the paths of the Earth-space links within the troposphere.

Besides the horizontal domains described above, the details of the configuration of WRF for a daily run are as follows:

- initialisation data: ECMWF operational analysis (0.125°) every 6 h.
- vertical coordinates: 50 automatic vertical levels, 50 hPa pressure top.
- spin-up time: 12 h (d01, d02, d03).
- time steps: d01 start is 90 s (min. 45 s, max. 270 s), parent time step ratio is 3, i.e. d02 start is 30 s (min. 15 s, max. 90 s) and d03 start is 10 s (min. 5 s, max. 30 s). The adaptation is driven by d03.
- water microphysics: WRF single-moment 6 (WSM6) or WRF double-moment 6 (WDM6).
- cloud physics: Tiedtke (d01, d02) or Grell-Freitas (d01, d02, d03). The schemes are called at each time step.
- radiation physics: RRTM long-wave radiation, Dudhia short-wave radiation. The schemes are called every 18 min (d01), 6 min (d02), and 2 min (d03).
- surface layer physics: revised MM5 Monin-Obukhov scheme.
- planetary boundary layer physics: Yonsei University (YSU) scheme. The scheme is called at each time step.
- soil layer physics: thermal diffusion, 5 layers.
- diffusion and damping: second order diffusion on coordinate surfaces, diffusive damping with coefficient 0.1.

Other parameters are left to their default values.

Notably, there are two sets of parametrisations for the water microphysics and cloud physics: WSM6 + Tiedtke, or WDM6 + Grell-Freitas. The test of more than one parametrisation is motivated by the apparent underestimation of the cloud attenuation found in other results (see e.g. Sec. 5.2.5 or 7.1.4).

The use of the double-moment water microphysics scheme WDM6 instead of WSM6, and of the scale-aware Grell-Freitas cloud physics scheme, is an attempt at generating higher cloud contents, which are found by some studies comparing WRF schemes with cloud radar measurements [146]. The approach offers at least a possibility to observe if there are important differences between the two schemes, with or without an improvement.

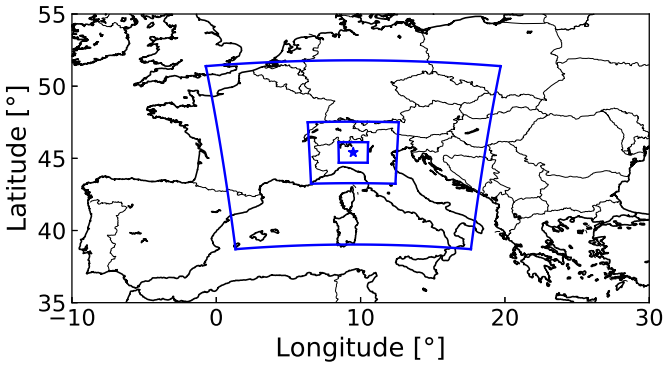

Figure 6.2 – WRF Lambert Conformal Conic (79×79) domains at 18 km, 6 km, and 2 km centered at Spino d'Adda (45.41°N, 9.49°E)

6.2 Results

The results are reported first in terms of examples of time series (6.2.1), then error metrics (6.2.2), and then total attenuation CCDFs (6.2.3).

6.2.1 Examples of nonrainy attenuation time series

The Fig. 6.3 shows some examples of 19.701 GHz nonrainy attenuation estimated either with the microwave radiometer (MWR) or with the NWP model.

In the Fig. 6.3 (a), for the 21/01/2015, the nonrainy attenuation estimate from the radiometer starts to increase at around 4 am from a base value of $\sim$ 0.35 dB, with peaks around 9 am, 6:30 pm and 11:30 pm, reaching up to 1.2 dB. The NWP curves using the Tiedtke and Grell-Freitas parametrisations present some cloud attenuation peaks but are below the radiometer. The NWP curves using the Salonen and Mattioli models get closer, with some overestimation by the Mattioli model. Based on the Linate reports and the rain gauge at Spino, this day has a mix of overcast stratiform clouds and some light rain (up to 2.5 mm h^{-1}) starting around 8 am. This is a situation where defining flags is difficult, because the events last so long. For the radiometer, (2.122) p. 39 can be assumed to still hold despite the presence of some scatterers [101]. But for the NWP estimates, the light rain is not modelled; this explains the deviations.

In the Fig. 6.3 (b), for the 23/05/2015, a rain event occurs at the end of the day and, as shown by the linear interpolation, is taken out. Tiedtke and Grell-Freitas follow the radiometer trend well, though not with a very good match on an instantaneous basis. Here, Salonen and Mattioli largely overestimate the

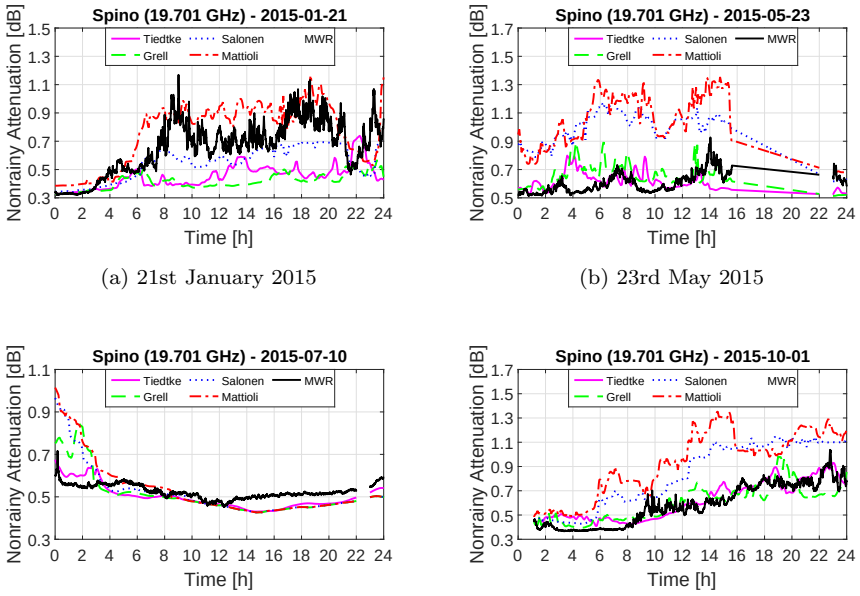

(a) 21st January 2015

(b) 23rd May 2015

(c) 10th July 2015

(d) 1st October 2015

Figure 6.3 – Examples of Spino d'Adda Alphasat 19.701 GHz nonrainy attenuation time series. Nonrainy attenuation is estimated from a radiometer (MWR) or from WRF. There are four separate WRF results: Tiedtke + WSM6 or Grell-Freitas + WDM6, and the latter with either the Salonen or Mattioli model.

nonrainy attenuation. Linate reports suggest the sky has a medium cover of altocumuli throughout the day, and that cumuli start to form around noon and persist during the event.

In the Fig. 6.3 (c), for the 10/07/2015, the sky appears mostly clear, but at the very beginning of the day. The Tiedtke model has the most reasonable behaviour, whereas the other models overestimate the radiometer in the first 3 hours by up to 0.3 dB. The observations point to the presence of only a few scattered (strato-)cumuli and no clouds in the afternoon.

In the Fig. 6.3 (d), for the 01/10/2015, the radiometer estimate is at ~ 0.35 dB in the early morning and starts to rise after 8 pm. The Tiedtke and Grell-Freitas models behave similarly. The Salonen and Mattioli models once more overestimate the cloud attenuations. Here the cloud reports describe the progressive build-up of an overcast of stratocumuli and altocumuli.

The Fig. 6.4 presents the equivalent time series but for 39.402 GHz.

From these examples, the NWP nonrainy attenuation estimated directly from the NWP output shows cloud peaks similar in amplitude to the radiometer, albeit with temporal shifts. The Salonen and Mattioli algorithms often overestimate the cloud attenuation, especially near rainy periods.

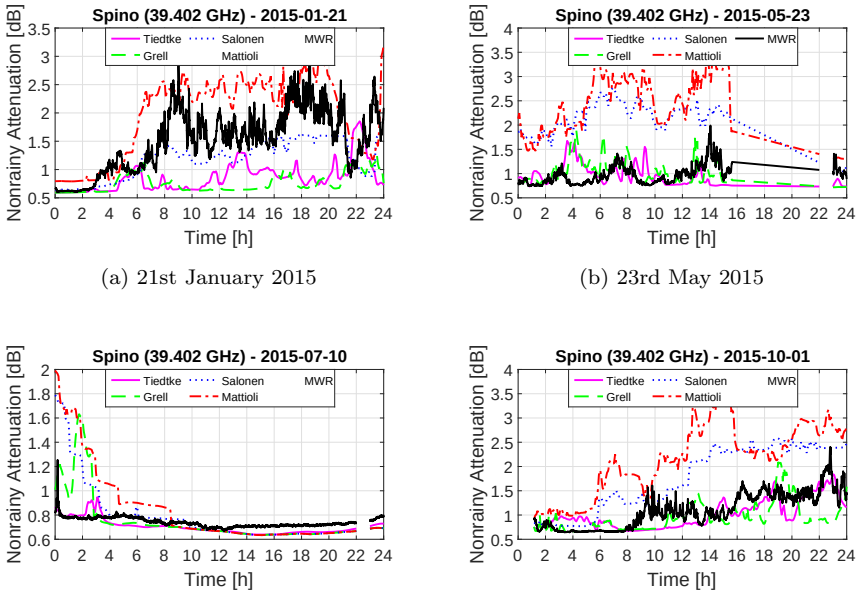

(a) 21st January 2015

(b) 23rd May 2015

(c) 10th July 2015

(d) 1st October 2015

Figure 6.4 – Examples of Spino d'Adda Alphasat 39.402 GHz nonrainy attenuation time series. Nonrainy attenuation is estimated from a radiometer (MWR) or from WRF. There are four separate WRF results: Tiedtke + WSM6 or Grell-Freitas + WDM6, and the latter with either the Salonen or Mattioli model.

6.2.2 Errors on the attenuation time series

The Tab. 6.3 and the Tab. 6.4 list some error figures for the four months under study, at 19.701 GHz (Ka band) and 39.402 GHz (Q band) respectively, with the best individual figures in bold.

For January, the NWP estimates with Tiedtke, Grell-Freitas and Salonen show very similar performances, and all have negative ME. The RMSE is below 0.1 dB in Ka band and below 0.3 dB in Q band. ρ^{NWP} is around 0.8 in Ka band and down to 0.6 in Q band. The Salonen model is the overall best with the lowest ME, but not by a very significant margin. The Mattioli RMSE is the worst, by 0.1 dB at Q band, and it has a slightly positive ME, but it has the highest ρ^{NWP}.

For May, the Tiedtke model is the best in RMSE: 0.11 dB in Ka band and 0.28 dB in Q band. The Grell-Freitas model is similar while slightly better in ME. The NWP estimates using the Salonen and Mattioli models perform far less favourably: as pointed out by their large positive ME, they largely overestimate the clouds. This is understandable given that their critical humidity thresholds are designed for nonrainy periods, yet May 2015 was a very rainy month. The correlations are here around 0.7 in Ka band and around 0.3 or

Period	NWP estimate	Error metric (19.701 GHz)		
		RMSE (dB) [%]	ME (dB) [%]	ρ^{NWP} (-)
January	Tiedtke	0.09 [**15.5**]	-0.03 [-5.5]	0.808
	Grell-Freitas	0.09 [15.8]	-0.02 [-4.3]	0.805
	Salonen	**0.08** [17.1]	**-0.01** [**-2.9**]	0.823
	Mattioli	0.11 [24.7]	0.02 [3.9]	**0.842**
May	Tiedtke	**0.11** [**17.4**]	-0.04 [-6.5]	**0.725**
	Grell-Freitas	0.12 [18.6]	**-0.03** [**-4.8**]	0.678
	Salonen	0.19 [29.3]	0.06 [8.6]	0.714
	Mattioli	0.23 [37.3]	0.09 [13.6]	0.677
July	Tiedtke	**0.13** [**16.0**]	-0.05 [-6.5]	**0.608**
	Grell-Freitas	0.14 [17.3]	-0.05 [-6.0]	0.571
	Salonen	0.14 [17.9]	**-0.03** [**-3.9**]	0.573
	Mattioli	0.14 [17.9]	**-0.03** [-4.0]	0.562
October	Tiedtke	**0.11** [**17.3**]	**-0.01** [-0.9]	0.788
	Grell-Freitas	0.13 [21.3]	**-0.01** [**0.4**]	0.705
	Salonen	0.15 [24.3]	0.05 [9.6]	**0.818**
	Mattioli	0.17 [30.2]	0.07 [12.3]	0.779
4 months	Tiedtke	**0.11** [**16.5**]	-0.03 [-4.9]	**0.878**
	Grell-Freitas	0.12 [18.3]	-0.03 [-3.8]	0.849
	Salonen	0.15 [22.7]	**0.02** [**2.8**]	0.826
	Mattioli	0.17 [28.5]	0.04 [6.4]	0.791

Table 6.3 – Absolute/relative root means square errors (RMSE), absolute/relative mean errors (ME), and correlation coefficients (ρ^{NWP}), between the Alphasat nonrainy attenuation estimated by the NWP model WRF or by a microwave radiometer (MWR), for Spino d'Adda at 19.701 GHz (Ka band). The best NWP attenuation estimates for each metric in each period are in bold.

0.55 in Q band for the Tiedtke/Grell-Freitas or Salonen/Mattioli results.

For July, the Tiedtke model is once again the best in RMSE with 0.13 dB in Ka band, and no more than 0.17 dB in Q band. The performances of the other models are not too far from that however. The Salonen and Mattioli models actually provide the best ME, and in Q band they have a slightly positive ME. The correlations are however especially poor, around 0.6 and 0.35.

For October, the Tiedkte model is also the overall best, with the Grell-Freitas model being worst in RMSE and ρ^{NWP}. As for May, the Salonen and Mattioli model have high RMSE and ME, though they maintain a better correlation in Q band.

Looking at the four months together, the best model appears to be Tiedtke

Period	NWP estimate	Error metric (39.402 GHz)		
		RMSE (dB) [%]	ME (dB) [%]	ρ^{NWP} (-)
January	Tiedtke	**0.26** [**19.3**]	-0.09 [-7.9]	0.607
	Grell-Freitas	**0.26** [21.4]	-0.05 [-4.7]	0.596
	Salonen	**0.26** [23.6]	**-0.03** [**-2.5**]	0.658
	Mattioli	0.37 [40.9]	0.09 [9.4]	**0.725**
May	Tiedtke	**0.28** [**26.1**]	-0.09 [-7.5]	0.315
	Grell-Freitas	0.31 [29.5]	**-0.05** [**-5.1**]	0.282
	Salonen	0.57 [59.4]	0.26 [26.4]	0.573
	Mattioli	0.76 [80.6]	0.38 [39.0]	**0.542**
July	Tiedtke	**0.17** [**16.1**]	-0.05 [-5.2]	0.380
	Grell-Freitas	0.20 [19.2]	-0.04 [-3.8]	0.320
	Salonen	0.26 [24.5]	**0.02** [2.5]	**0.383**
	Mattioli	0.26 [25.3]	**0.02** [**2.2**]	0.359
October	Tiedtke	**0.32** [**25.6**]	-0.08 [-5.2]	0.631
	Grell-Freitas	0.41 [36.2]	**-0.05** [**-2.2**]	0.478
	Salonen	0.41 [38.9]	0.17 [17.1]	**0.767**
	Mattioli	0.52 [53.6]	0.23 [23.3]	0.716
4 months	Tiedtke	**0.26** [**22.2**]	-0.08 [-6.5]	0.590
	Grell-Freitas	0.31 [27.2]	**-0.05** [**-2.2**]	0.502
	Salonen	0.40 [39.6]	0.10 [10.8]	**0.637**
	Mattioli	0.51 [54.4]	0.18 [18.6]	0.618

Table 6.4 – Absolute/relative root means square errors (RMSE), absolute/relative mean errors (ME), and correlation coefficients (ρ^{NWP}), between the Alphasat nonrainy attenuation estimated by the NWP model WRF or by a microwave radiometer (MWR), for Spino d'Adda at 39.402 GHz (Q band). The best NWP attenuation estimates for each metric in each period are in bold.

with RMSEs of 0.11 dB (Ka) and 0.26 dB (Q). This is 3 to 5 times higher than the radiometric accuracy estimated in Sec. 6.1.2. As another reference point, [111] proposes a 0.165 dB threshold for the agreement between MWR and GNSS as a way to detect malfunctions of the radiometer at 19.7 GHz and for clear-sky conditions. In that regard, the RMSEs found here are large (and also as relative values $\sim 15-25$ %) yet physically acceptable. The Grell-Freitas model performs similarly to Tiedtke, but the Salonen and Mattioli models are confirmed to overestimate the cloud attenuation, particularly close to rainy periods, and especially the Mattioli model. Part of the overestimation may be explained by the not so high number (i.e. 50) of vertical levels used for WRF, yielding larger apparent cloud thicknesses.

To understand the correlations, and as was already reported in Chap. 5, water vapour is typically correlated > 0.9 between MWR/GNSS/RAOBS/NWP data, though there is some seasonal variability and values ~ 0.7 were observed with NWP models in summer [57]. For the NWP nonrainy attenuation estimates, the presence of the clouds reduces the correlation with the radiometer, as the cloud events are not always predicted at the right time (see e.g. Fig. 6.3 (b)). Because the cloud attenuation increases faster with the frequency, its contribution degrades the correlation further at Q band. The especially poor correlations in May and July suggest indeed difficulties during the warmer seasons and/or regarding convective clouds, present in majority during those months. Cases when light rain is mixed with clouds and not flagged (see e.g. Fig. 6.3 (d)) also negatively affect the correlation.

For the purpose of obtaining the total attenuation from the NWP estimates, an important point to consider here is also the accuracy of the excess attenuation. When using a procedure similar to the one in Sec. 2.5.2, the retrieval accuracy is estimated to be $\sim 0.2-0.5$ dB in the $20-50$ GHz band [16]. In that regard, it appears that the results, at least those from the Tiedtke/Grell-Freitas models, are realistic enough to be considered statistically.

6.2.3 Errors on the attenuation statistics

Ultimately, what is expected as the primary output of a propagation experiment is the Complementary Cumulative Distribution Function (CCDF) of the total attenuation. Some standardized details of the CCDF computation are within the ITU-R SG3 Table II-1 template [136] as stated in Sec. 4.4.3. Notably, the CCDFs must be normalized with respect to the total observation period, here one month, and not the total number of available samples. Also of interest here are the CCDFs of the nonrainy attenuation only, outside of rain events.

The Figs. 6.5 to 6.8 compare the 19.701 GHz and 39.402 GHz total and nonrainy attenuation CCDFs, for each of the four months, for the radiometer and the NWP-based models (Tiedtke, Grell-Freitas, Salonen, Mattioli).

In the Figs 6.5 (a) and (b), showing the total attenuation CCDFs for January, the mostly cloudy conditions and the absence of strong rain events highlight some differences in behaviour between the NWP models. The Tiedtke model follows the radiometric curve with a small underestimation over the whole probability range reaching -20 %/-30 % (-0.2 dB/-0.6 dB) between 1 and 10 %. Grell-Freitas is slightly above Tiedtke. The Salonen and Mattioli models present an overestimation of the central part of the radiometric curve, Mattioli being above Salonen, with respective errors around 10 %/15 % (0.2 dB/0.8 dB) and 20 %/25 % (0.4 dB/1.4 dB) for 10^{-1} %.

From the Figs 6.5 (c) and (d), showing the nonrainy attenuation CCDFs for January, some more insight is gained on the relative performances of the NWP models and their impact on the total attenuation CCDFs described above. Both the Tiedtke and Grell-Freitas CCDFs are below the radiometer's over the full probability range, but they catch up with it near 10^{-3} %. As seen in the total attenuation CCDFs, Grell-Freitas is above Tiedkte at high probabilities. There is some overestimation of the radiometer by the Salonen and Mattioli models in the 1 % to 10 % probability range. Mattioli continues to overestimate the

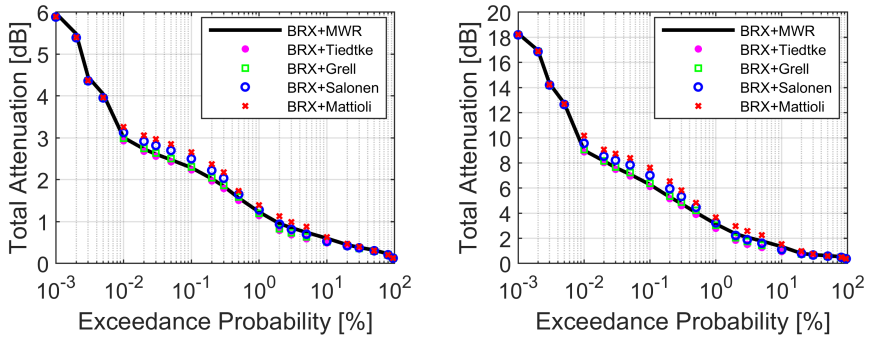

(a) Total (19.701 GHz)

(b) Total (39.402 GHz)

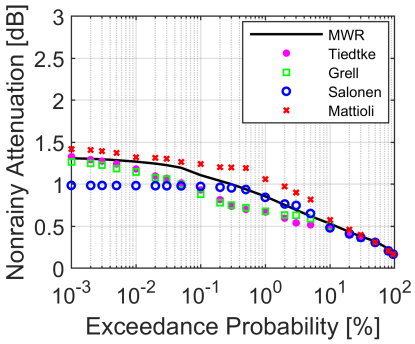

(c) Non-rainy (19.701 GHz)

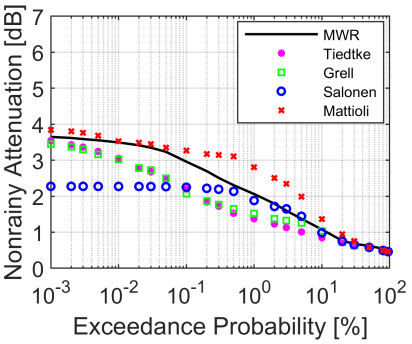

(d) Non-rainy (39.402 GHz)

Figure 6.5 – Alphasat total (incl. BRX) and nonrainy attenuation monthly CCDFs at Spino d'Adda in January 2015. The nonrainy attenuation estimates are from the MWR or NWP-based (Tiedtke, Grell-Freitas, Salonen, Mattioli)

radiometer, but Salonen actually underestimates it at lower probabilities. The relative position of the CCDFs is close to what is seen for the time series in the Fig. 6.3 (a), where stratiform clouds are mixed with light rain. Generally, the fact that the Salonen model is closer to Tiedtke/Grell, as seen in the Tabs.6.3 and 6.4, appears to be due to the prevalence of stratiform clouds in January.

In the Figs 6.6 (a) and (b), showing the total attenuation CCDFs for May, the Tiedtke model has an error of -10 %/-20 % (-0.1 dB/-0.4 dB) between 1 and 10 %, while Grell-Freitas is slightly above it until 10^{-1} %. The Salonen and Mattioli models on the contrary overestimate that part of the curve, with errors up to 40 %/90 % (0.4 dB/1.1 dB) and 45 %/120 % (0.4 dB/1.5 dB) near 10 % of the time.

From the Figs 6.6 (c) and (d), showing the nonrainy attenuation CCDFs for May, a more detailed outlook is once more possible. The underestimation by Tiedtke and Grell, and the large overestimation by Salonen and Mattioli, are more clearly visible. It is notable however that Tiedtke and Grell CCDFs are driven up at the lowest probability, most likely due to a few cloud events

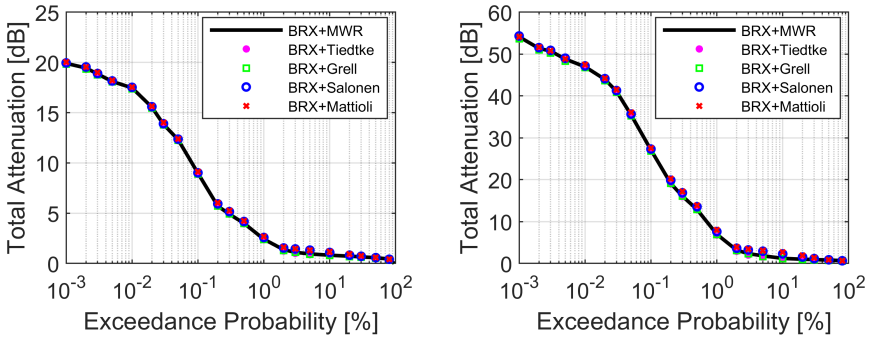

(a) Total (19.701 GHz) (b) Total (39.402 GHz)

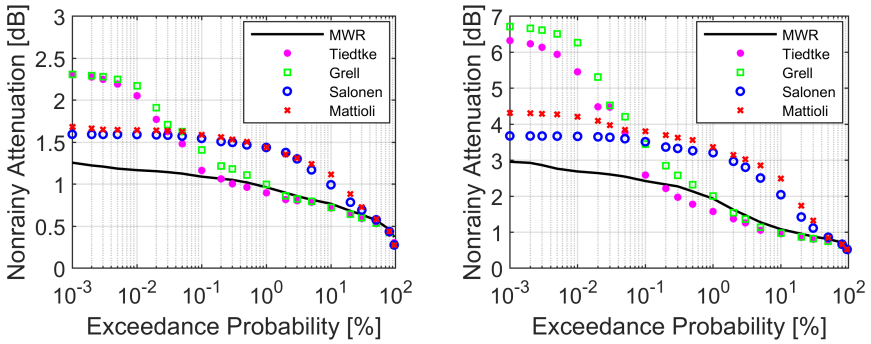

(c) Non-rainy (19.701 GHz) (d) Non-rainy (39.402 GHz)

Figure 6.6 – Alphasat total (incl. BRX) and nonrainy attenuation monthly CCDFs at Spino d'Adda in May 2015. The nonrainy attenuation estimates are from the MWR or NWP-based (Tiedtke, Grell-Freitas, Salonen, Mattioli)

predicted with too much intensity or at the wrong time. These affirmations are consistent with the example in the Fig. 6.3 (b).

In the Figs 6.7 (a) and (b), showing the total attenuation CCDFs for July, the curves remains at low attenuation values until the single rain event appears between 10^{-2} and 10^{-1} % where all the NWP results underestimate the radiometer by −10 %/−15 % (−0.3 dB/−1 dB). Once again for the central part curve, between exceedance probabilities of 10^{-1} and 1 %, the Salonen and Mattioli models overestimate the radiometer by up to about 10 %/45 % (0.15 dB/0.9 dB) and 15 %/60 % (0.2 dB/1.1 dB) respectively. The Grell-Freitas model has an error of 5 %/30 % (0.05 dB/0.5 dB) in the same range, but Tiedtke stays below the radiometer at all probabilities.

From the Figs 6.7 (c) and (d), showing the nonrainy attenuation CCDFs for July, some similarities with May are observed. Indeed the cloud cover is also largely convective, though it less frequent and with only one thunderstorm. The Tiedtke and Grell models are in particularly good agreement with the radiometer from 100 down to 1 % of the time. For Tiedtke, the agreement

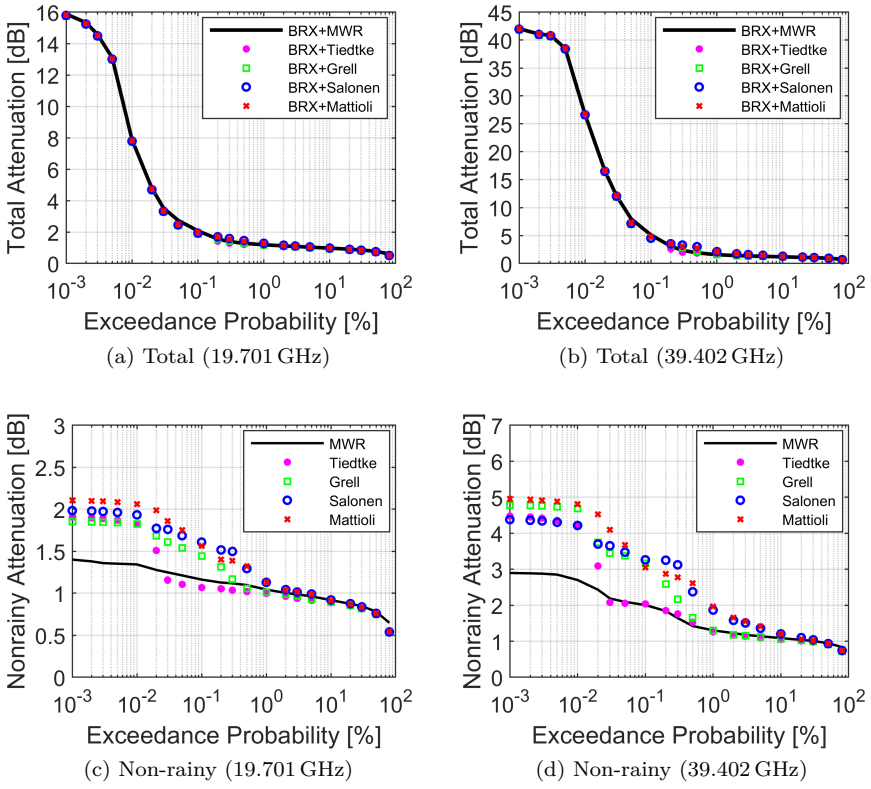

(a) Total (19.701 GHz)

(b) Total (39.402 GHz)

(c) Non-rainy (19.701 GHz)

(d) Non-rainy (39.402 GHz)

Figure 6.7 – Alphasat total (incl. BRX) and nonrainy attenuation monthly CCDFs at Spino d'Adda in July 2015. The nonrainy attenuation estimates are from the MWR or NWP-based (Tiedtke, Grell-Freitas, Salonen, Mattioli)

remains good until the onset of the thunderstorm event in between 10^{-2} and 10^{-1} %. All the NWP results produce events causing an overestimation of the MWR CCDF below 10^{-2} of the time. However, in the total attenuation CCDFs they boost the NWP estimates in the central probability range instead.

In the Figs 6.8 (a) and (b), showing the total attenuation CCDFs for October, Tiedtke remains below the radiometer, with its highest relative error -10 % (-0.2 dB/-0.5 dB) between 1 and 10 %. Grell-Freitas is slightly above Tiedtke and has an error up to 5 % (0.4 dB/1.1 dB) between 10^{-3} and 10^{-1} %, due to misplaced high attenuation NWP cloud events. Both Salonen and Mattioli make errors of 25 %/45 % (0.2 dB/0.7 dB) for 10 % of the time.

From the Figs 6.8 (c) and (d), showing the nonrainy attenuation CCDFs for October, the NWPs show a mix of tendencies seen in the other months. This is a month with a balance of stratiform and convective clouds and more rain but no thunderstorms. As for May and July, Tiedtke and Grell-Freitas underestimates slightly the radiometer at higher probabilities, but strong clouds events absent from the radiometric measurements are generated. Salonen and

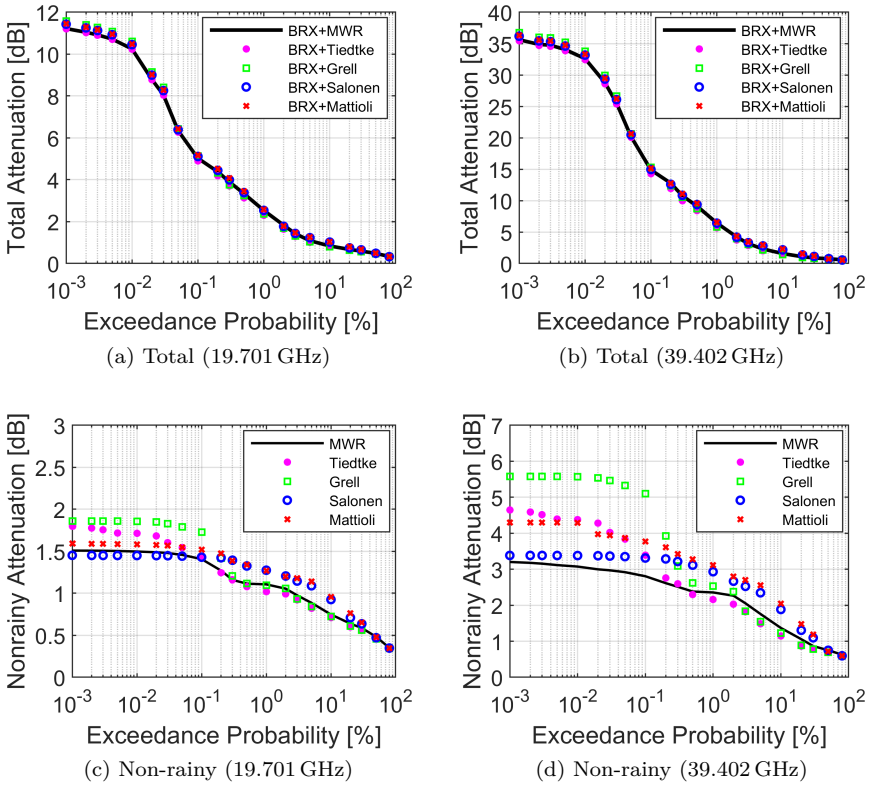

(a) Total (19.701 GHz)

(b) Total (39.402 GHz)

(c) Non-rainy (19.701 GHz)

(d) Non-rainy (39.402 GHz)

Figure 6.8 – Alphasat total (incl. BRX) and nonrainy attenuation monthly CCDFs at Spino d'Adda in October 2015. The nonrainy attenuation estimates are from the MWR or NWP-based (Tiedtke, Grell-Freitas, Salonen, Mattioli)

Mattioli overestimate the radiometer on nearly the full probability range, but Salonen plateaus near 10^{-1} % of the time as in January.

From all these observations, it is concluded that the NWP estimates from the Tiedtke and Grell-Freitas cumulus schemes allow to reproduce the monthly total attenuation CCDFs with a relative error better than ±30 % at any reference exceedance probability level. The highest errors are usually located in the 1 to 10 % exceedance probability range, July being the exception. Tiedtke almost never overestimates the radiometer's total attenuation, whereas Grell-Freitas does in a few instances and is almost always above Tiedtke. In the practical view of designing systems or fade mitigation techniques, both schemes are similarly useful, Tiedtke is more consistent but Grell-Freitas introduces a lower risk of underestimation. On the other hand, the NWP estimates from the Salonen and Mattioli cloud detection algorithms can largely overestimate the radiometer anywhere in the 10^{-2} to 10 % probability range. For the Mattioli model, it goes up to 120 % (1.5 dB) for 10 % of the time in May at Q band. Extracted system margins would be safe, but not economically optimal.

6.3 Concluding remarks

In order to obtain the total atmospheric attenuation, propagation experiments require independent estimates of the attenuation in nonrainy conditions. Radiometric measurements are the classic way to tackle the problem. Numerical Weather Prediction data, as input to propagation models, can provide such estimates as well. To this aim, either an appropriate NWP parametrisation for the clouds is selected, or a cloud detection algorithm is applied.

The comparisons of NWP-derived against radiometric estimates, using four months of beacon and radiometric data collected at Spino d'Adda, at 16 and 1 samples per second respectively, show the best overall results are obtained with the Tiedtke NWP scheme: the root mean-square errors are 0.11 dB (16.5 %) and 0.26 dB (22.2 %), the mean errors -0.03 dB (-4.9 %) and -0.08 dB (-6.5 %), and the correlations 0.878 and 0.590, at the frequencies of 19.701 GHz and 39.402 GHz respectively. The root mean-square errors are estimated here to be roughly 3 to 5 times higher than the standard deviation of the radiometric attenuation. Other practical estimates of the radiometric accuracy amount typically to ~ 0.1 dB[111]. The correlations are not excellent, but in Ka band they are still commensurable to the correlations > 0.9 observed for water vapour [57]. Analyses of individual NWP nonrainy attenuation time series reveal the cloud events have a poor instantaneous correlation. It explains why the nonrainy attenuation correlation is poorer than what is expected in clear-sky, and why it degrades with increased frequency as the cloud attenuation becomes relatively higher. Despite this, the errors remain acceptable at the statistical level, for the purpose of building the total attenuation distribution, and considering that extracing the excess attenuation in a propagation experiment has an estimated accuracy of $0.2 - 0.5$ dB in the 20-50 GHz band [16]. Indeed, for both the Tiedtke and Grell-Freitas schemes, the relative error on the total attenuation distribution never exceeds ± 30 % for the reference ITU-R exceedance probabilities. On the other hand, the estimates obtained using cloud detection algorithms (proposed by Salonen and Mattioli) strongly overestimate the cloud attenuation, especially near rainy conditions.

In conclusion, using two different NWP parametrisations did not result in very significant differences, while cloud detection algorithms seem too pessimistic when used with the NWP data. Overall, the accuracy of the method can be considered satisfactory for use by the EM wave propagation community in order to complement propagation beacon measurements, and subsequently to guide satellite system designers. A more careful design of the NWP domains might lower the error further, though part of the appeal of the domains presented in this chapter is that they are small and automatically defined.

Chapter 7

Applications of NWPs to the modelling of propagation impairments

This chapter goes through some applications of the methodology defended in this thesis. The first application (see Sec. 7.1) concerns the simulation of one year nonrainy attenuation CCDFs in the context of a large-scale GSO propagation experiment. The second application (see Sec. 7.2) concerns the simulation of one year total attenuation CCDF for LEO links. The last application (see Sec. 7.3) concerns the identification of scintillation at low elevations, a topic absent from the validations and for which only preliminary results are obtained.

7.1 Simulation of propagation impairments for a large-scale propagation experiment

This first application is linked to the conclusions of Chap. 6. As has already been stated, the production of time series of the nonrainy attenuation is of interest for propagation experiments where no radiometric measurements are/were being made. NWP models were shown to be sufficiently accurate for this task.

The ASALASCA extended consortium has a network of European ground stations and performs coordinated propagation measurements with the satellite Alphasat, already mentioned beforehand i.a. in Sec. 1.2, 5.1.1, and 6.1.1, and in one case also with Ka-Sat. The ASALASCA group, with up to ten participating stations, is a large subset of the ASAPE group which reports measurements carried out or in progress at ~ 20 locations (see Fig. 7.1). The ASALASCA stations present a variety of climatological conditions, elevation angles, and possibilities for small to large scale site diversity. However, the members of ASALASCA are in this situation where no suitable radiometric measurements where performed concurrently with their beacon measurements.

NWP-derived nonrainy attenuation statistical results are shown here for the ASALASCA stations. The lack of measurements with microwave radiometers for ASALASCA means however that the soundness of the results presented here cannot be assessed directly as in Chap. 6. However, the results will still be compared with the references from the ITU-R recommendations.

More information about the ASALASCA campaign and examples of NWP-based results were given, in collaboration, by Ventouras et al. in [147, 148].

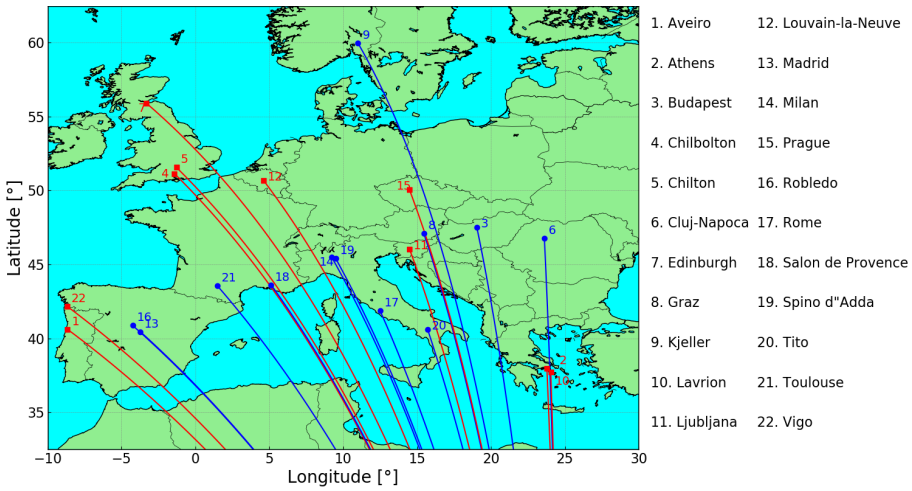

Figure 7.1 – Locations and projections of the path for the ground stations of the Alphasat propagation experiment. Links and stations in red are members of the ASALASCA extended network, other ASAPE experimenters are in blue.

7.1.1 Earth-space links' configurations

Alphasat frequencies are 19.701 GHz (Ka band) and 39.402 GHz (Q band). Ka-Sat frequency is 19.68 GHz and only concerns Aveiro at Ka band. The list of the ASALASCA ground stations with their coordinates and mean elevation angles to see Alphasat (or Ka-Sat) are given in the Tab. 7.1. The Ka and Q band links for Aveiro do not share the same path and have different elevations. As no results are shown here for Edinburgh, the range in elevation studied goes from $\sim 45°$ for Athens and Lavrion to $\sim 25°$ for Chilton and Chilbolton. The sites of Athens/Lavrion and Chilton/Chilbolton are meant to study small scale site diversity. The simulation period has a duration of one year, from July 2016 to June 2017, and for which measurements exist at most of the stations.

Ground station	Latitude	Longitude	Altitude	Mean elevation
Athens	37.975°N	23.785°E	210 m	45.97°
Lavrion	37.723°N	24.048°E	20 m	46.26°
Ljubljana	46.04°N	14.49°E	292 m	36.00°
Prague	50.04°N	14.48°E	274 m	31.80°
Aveiro	40.612°N	8.662°W	12 m	39.67° (Ka)
				31.85° (Q)
Vigo	42.170°N	8.688°W	447 m	30.60°
Louvain-la-Neuve	50.67°N	4.61°E	160 m	29.02°
Chilton	51.57°N	1.29°W	100 m	26.07°
Chilbolton	51.15°N	−1.43°W	100 m	26.40°
Edinburgh	55.91°N	−3.32°W	94 m	21.47°

Table 7.1 – List and coordinates of the ASALASCA ground stations

7.1.2 NWP model

The NWP modelling approach is almost identical to the one described in Sec. 6.1.3. For each ground station, a succession of three WRF Lambert Conformal Conic (LCC) domains centered on the station is created with resolutions of 18 km, 6 km, and 2 km. Examples of domains are given in the Fig. 7.2 (Athens),

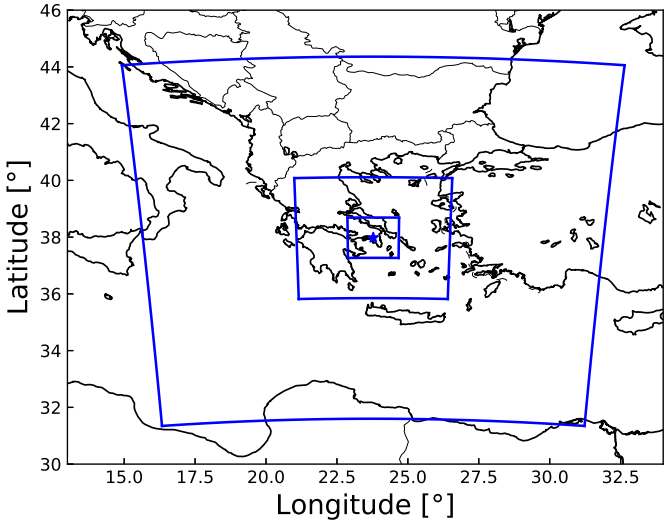

Figure 7.2 – WRF Lambert Conformal Conic (79×79) domains at 18 km, 6 km, and 2 km centered at Athens (37.975°N, 23.785°E)

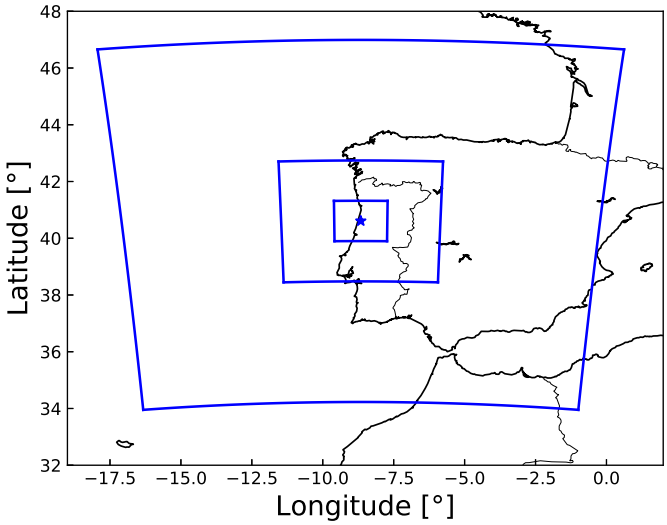

Figure 7.3 – WRF Lambert Conformal Conic (79×79) domains at 18 km, 6 km, and 2 km centered at Aveiro (40.612°N, 8.662°E)

the Fig. 7.3 (Aveiro), the Fig. 7.4 (Chilbolton), and the Fig. 7.5 (Louvain-la-Neuve). Note that the domains for Louvain-la-Neuve are much smaller than in Fig. 5.1. As in Sec. 6.1.3, the input data is ECMWF operational analysis every 6 h, though the resolution is increased from 0.125° to 0.1°. The operational model is preferred to a re-analysis due to the interest in generating NWP time series regularly and updating the statistics while the beacon measurements were collected. Unlike in Sec. 6.1.3, only one parametrisation is selected for the water microphysics (WSM6), and only one is selected for the cloud physics (Tiedtke for the two outermost domains, d01 at 18 km and d02 at 6 km).

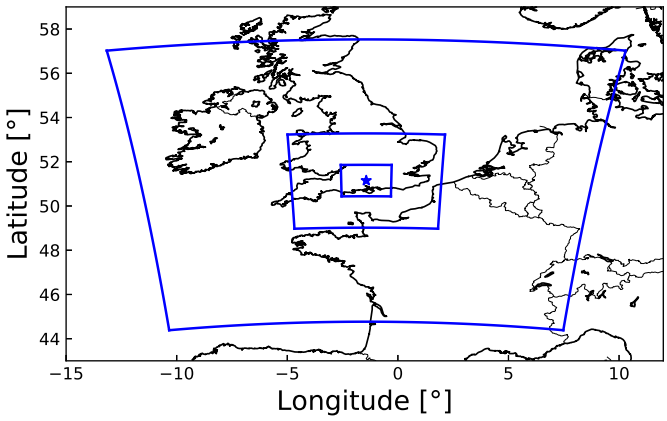

Figure 7.4 – WRF Lambert Conformal Conic (79 × 79) domains at 18 km, 6 km, and 2 km centered at Chilbolton (51.15°N, -1.43°W)

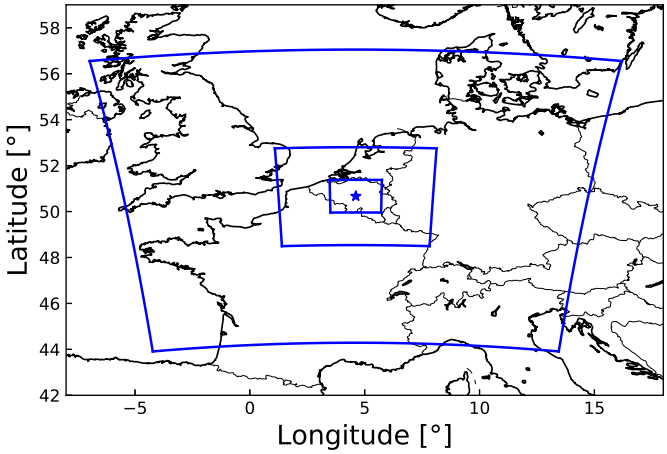

Figure 7.5 – WRF Lambert Conformal Conic (79 × 79) domains at 18 km, 6 km, and 2 km centered at Louvain-la-Neuve (50.67°N, 4.61°E)

7.1.3 Gaseous attenuation statistics

The gaseous attenuation CCDFs at Ka and Q bands for nine stations are given from the Fig. 7.6 for Athens to the Fig. 7.14 for Chilbolton. The figures are sorted by decreasing elevation, as in Tab. 7.1. CCDFs are shown both for the NWP simulations, and for the ITU-R CCDFs according to Sec. 2.2.4:

- Figs 7.6 and 7.7 are for Athens and Lavrion. Due to the proximity of the stations, their CCDFs are almost identical. The NWP and ITU-R start in excellent agreement for 100 % of the time. Nevertheless, the NWP is above the ITU-R by up to ~ 0.1 dB at lower exceedance probabilities. An overestimation of the NWP humidity is thus possible. Also, the CCDFs are higher at Q band for 100 % of the time, but they reach similar exceeded attenuations at both frequencies for 0.1 % of the time. This is explained by the absorption spectra (see Fig. 2.1): the water vapour attenuation is slightly higher at 19.701 GHz than at 39.402 GHz, but the oxygen attenuation increases with frequency until 60 GHz.
- Fig. 7.8 is for Ljubljana. The NWP and ITU-R CCDFs agree well at Ka band, though the ITU-R curve is higher than the NWP one by ~ 0.05 dB at Q band, likely due to the scaling of the constant ITU-R contribution from oxygen, or possibly a bias in the NWP temperature.
- Fig. 7.9 is for Prague. Prague has almost the same longitude and altitude as Ljubljana, though its elevation angle is $> 4°$ lower. The CCDFs behaves as Ljubljana's but with higher attenuations.
- Fig. 7.10 is for Aveiro. The Ka band CCDF from Ka-Sat is lower than it would be for Alphasat (lower elevation). The NWP curve is above the ITU-R's at Ka band, while the opposite happens at Q band.
- Fig. 7.11 is for Vigo. Vigo has almost the same longitude as Aveiro and a $\sim 1°$ higher elevation for Alphasat. The NWP and ITU-R CCDFs agree well, and the Q band results agree with Aveiro's.
- Fig. 7.12 is for Louvain-la-Neuve. The CCDFs appear in line with previous stations' CCDFs, e.g. Prague with almost the same latitude but a lower elevation. The results are comparable to the CCDFs for oxygen and water vapour in the Figs 5.8 and 5.10 (Ka) and in the Figs 5.12 and 5.14 (Q). This corroborates those previous findings, and illustrates further how the attenuation components differ at Ka and Q bands.
- Figs 7.13 and 7.14 are for Chilton and Chilbolton. They differ slightly from 1 to 0.1 %, perhaps as they are further apart (47.9 km) than Athens and Lavrion (36.3 km) [148]. They otherwise behave like Prague and Louvain-la-Neuve, but with yet higher attenuations.

Generally, the results show a good agreement between the NWPs and the ITU-R. NWPs tend to exceed the ITU-R at Ka band, sometimes the opposite at Q band. NWP biases in temperature or humidity are possible, but negligible for the gaseous attenuation itself. Estimating the gaseous attenuation acceptably for multiple stations re-affirms the confidence in the processing.

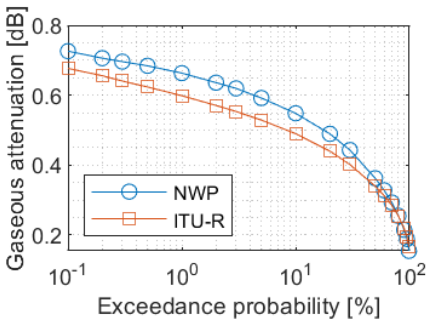

(a) 19.701 GHz

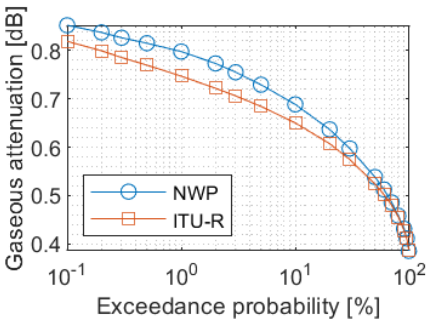

(b) 39.402 GHz

Figure 7.6 – CCDFs of the attenuation due to gases for Alphasat at Athens from 2016-07-01 to 2017-06-30, comparison between WRF-based simulations (NWP) and the reference from ITU-R recommendations (ITU-R)

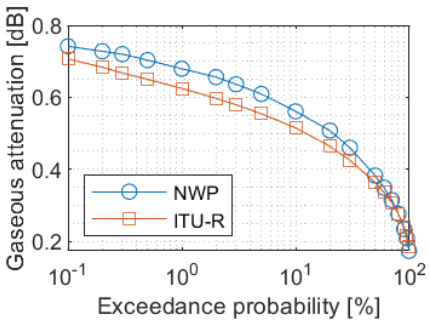

(a) 19.701 GHz

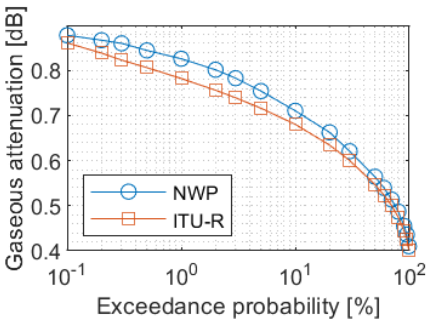

(b) 39.402 GHz

Figure 7.7 – CCDFs of the attenuation due to gases for Alphasat at Lavrion from 2016-07-01 to 2017-06-30, comparison between WRF-based simulations (NWP) and the reference from ITU-R recommendations (ITU-R)

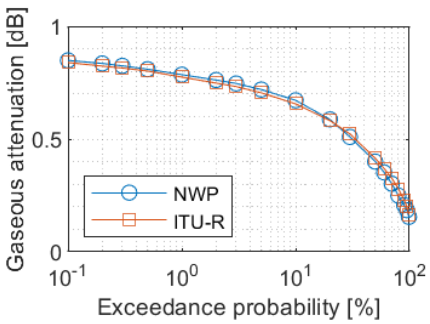

(a) 19.701 GHz

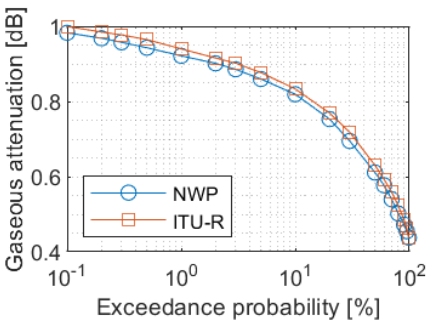

(b) 39.402 GHz

Figure 7.8 – CCDFs of the attenuation due to gases for Alphasat at Ljubljana from 2016-07-01 to 2017-06-30, comparison between WRF-based simulations (NWP) and the reference from ITU-R recommendations (ITU-R)

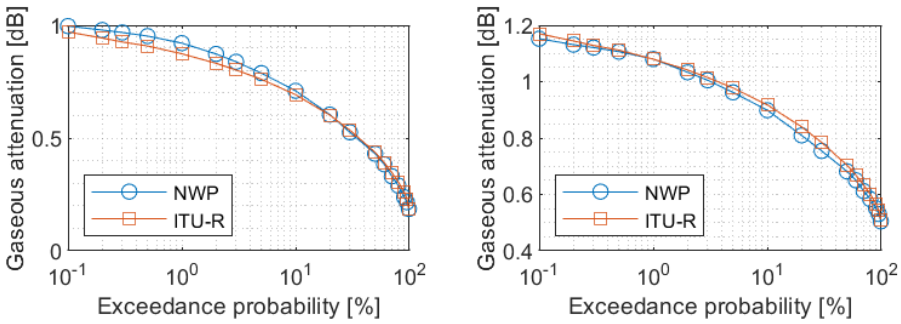

(a) 19.701 GHz (b) 39.402 GHz

Figure 7.9 – CCDFs of the attenuation due to gases for Alphasat at Prague from 2016-07-01 to 2017-06-30, comparison between WRF-based simulations (NWP) and the reference from ITU-R recommendations (ITU-R)

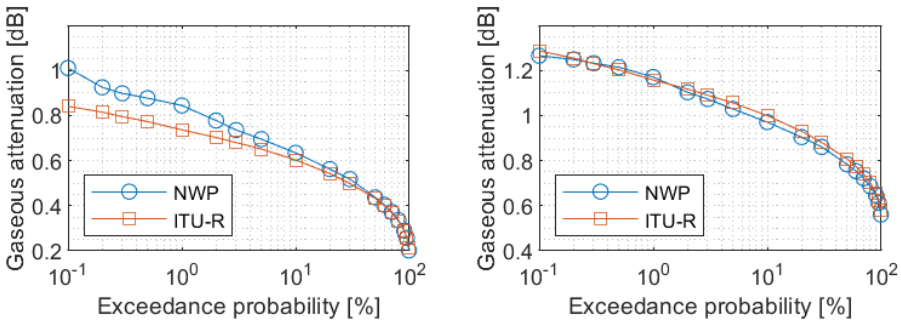

(a) 19.68 GHz (b) 39.402 GHz

Figure 7.10 – CCDFs of the attenuation due to gases for KaSAT and Alphasat at Aveiro from 2016-07-01 to 2017-06-30, comparison between WRF-based simulations (NWP) and the reference from ITU-R recommendations (ITU-R)

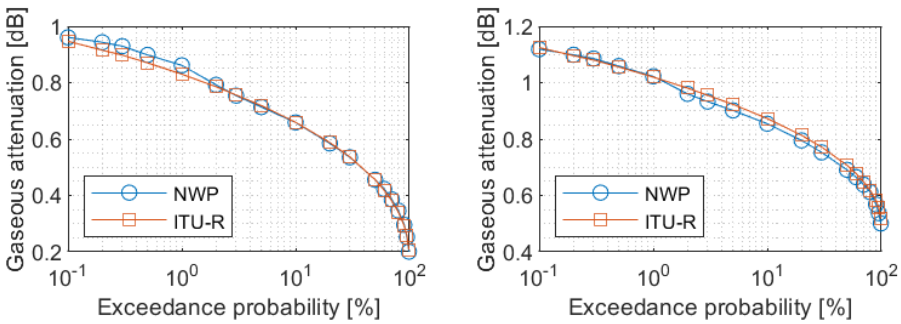

(a) 19.701 GHz (b) 39.402 GHz

Figure 7.11 – CCDFs of the attenuation due to gases for Alphasat at Vigo from 2016-07-01 to 2017-06-30, comparison between WRF-based simulations (NWP) and the reference from ITU-R recommendations (ITU-R)

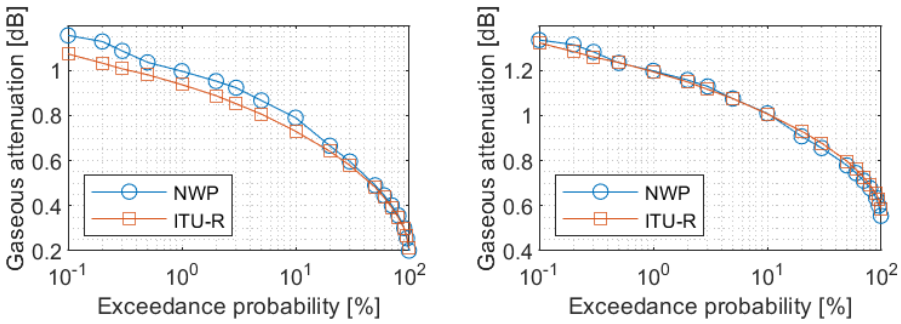

(a) 19.701 GHz (b) 39.402 GHz

Figure 7.12 – CCDFs of the attenuation due to gases for Alphasat at Louvain-la-Neuve from 2016-07-01 to 2017-06-30, comparison between WRF-based simulations (NWP) and the reference from ITU-R recommendations (ITU-R)

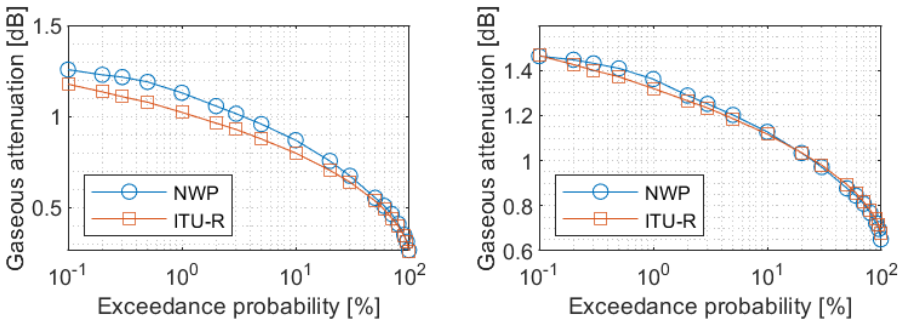

(a) 19.701 GHz (b) 39.402 GHz

Figure 7.13 – CCDFs of the attenuation due to gases for Alphasat at Chilton from 2016-07-01 to 2017-06-30, comparison between WRF-based simulations (NWP) and the reference from ITU-R recommendations (ITU-R)

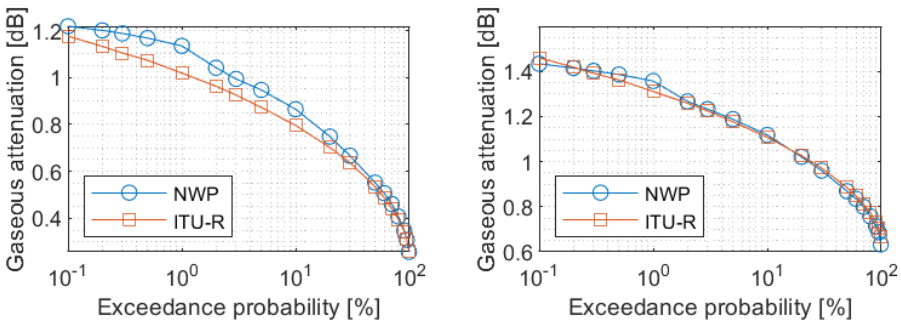

(a) 19.701 GHz (b) 39.402 GHz

Figure 7.14 – CCDFs of the attenuation due to gases for Alphasat at Chilbolton from 2016-07-01 to 2017-06-30, comparison between WRF-based simulations (NWP) and the reference from ITU-R recommendations (ITU-R)

7.1.4 Cloud attenuation statistics

Similarly to the previous section, the cloud attenuation CCDFs at Ka and Q bands for the nine stations under scope are given starting with the Fig. 7.15 for Athens and ending with the Fig. 7.23 for Chilbolton (see also Sec. 2.3.10):

- Figs 7.15 and 7.16 are for Athens and Lavrion. They produce almost identical results, slightly lower in Lavrion. The cloud attenuation is low, lower than for the gases in Ka band, but increases at Q band. Of course, the most important observation is the large underestimation by the NWPs of the ITU-R CCDFs. The probability to have a non-zero cloud attenuation is ~ 30 % from the ITU-R but only ~ 10 % from the NWPs.
- Fig. 7.17 is for Ljubljana. As for Athens/Lavrion, the NWP CCDFs are below the ITU-R CCDFs, but the cloud attenuations and their probability are higher, at ~ 50 % for the ITU-R and ~ 20 % for the NWPs.
- Fig. 7.18 is for Prague. They are once more similar to Ljubljana, though the attenuations are higher. The NWP probability of cloud attenuation is higher too at ~ 30 % while for the ITU-R it stays at ~ 50 %.
- Fig. 7.19 is for Aveiro. The different elevations mean the CCDF at Ka band is more similar to Ljubljana's, whereas the CCDF at Q band shows increased attenuations with respect to Prague. The probability of cloud attenuation is lower, ~ 30 % for the ITU-R and ~ 20 % for the NWPs.
- Fig. 7.20 is for Vigo. The results are very similar to Aveiro's, if the larger differences in elevation at Ka band are accounted for, though the ITU-R predicts a larger probability of cloud attenuation of ~ 40 %.
- Fig. 7.21 is for Louvain-la-Neuve. The ITU-R cloud attenuation CCDFs resemble Vigo's but with a higher cloud probability $\sim$ 50-60 %. The probability for NWP clouds is ~ 30 %, and the attenuation underestimates the ITU-R more significantly than for Vigo or Aveiro. It can be verified however in the Figs. 5.16 and 5.18 that the NWP CCDFs are consistent with simulations over a longer period and larger domains.
- Figs 7.22 and 7.22 are for Chilton and Chilbolton. Both stations agree with each other. The CCDFs looks like Louvain-la-Neuve's with higher attenuations. However the probability to have cloud attenuation is almost in agreement between the ITU-R and NWPs, at $\sim 50 - 60$ %.

The observations for the cloud are unanimous: the agreement between the NWPs and the ITU-R is poor, WRF systematically underestimates the ITU-R cloud attenuation and probability of non-zero cloud attenuation. The variety of climates (Mediterranean, continental, oceanic) represented affects the cloud variety, such as weaker and rarer events for Athens/Lavrion than for Chilton/Chilbolton. For Louvain-la-Neuve, the underestimation of the cloud attenuation from WRF output is also seen in Chap. 5 and Chap. 6, but the comparison with the radiometer for nonrainy periods is far more optimistic. Note that the contribution of clouds to the ITU-R total attenuation CCDF is plateaued at 1 % of the time (see Sec. 2.3.10) which suggests it has redundancy.

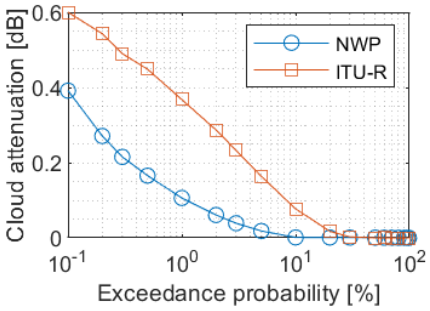

(a) 19.701 GHz

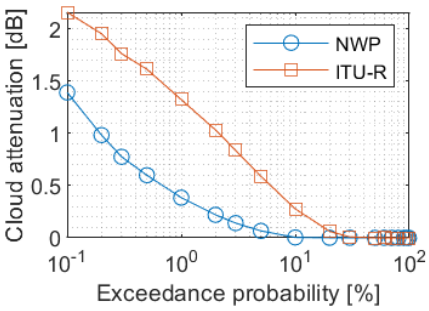

(b) 39.402 GHz

Figure 7.15 – CCDFs of the attenuation due to clouds for Alphasat at Athens from 2016-07-01 to 2017-06-30, comparison between WRF-based simulations (NWP) and the reference from ITU-R recommendations (ITU-R)

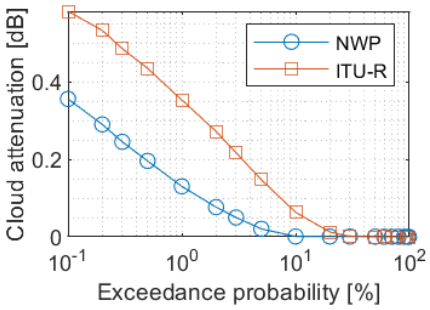

(a) 19.701 GHz

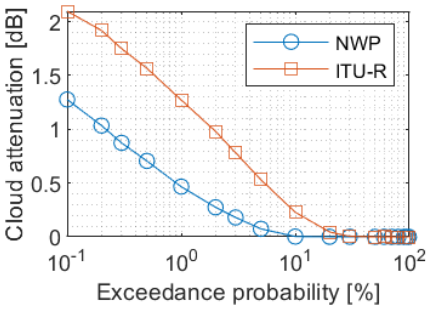

(b) 39.402 GHz

Figure 7.16 – CCDFs of the attenuation due to clouds for Alphasat at Lavrion from 2016-07-01 to 2017-06-30, comparison between WRF-based simulations (NWP) and the reference from ITU-R recommendations (ITU-R)

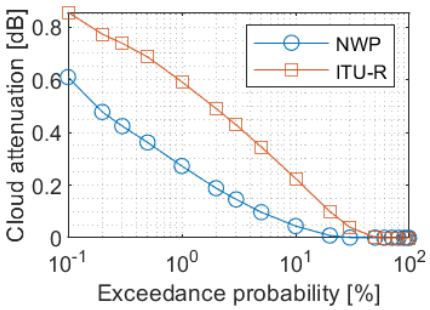

(a) 19.701 GHz

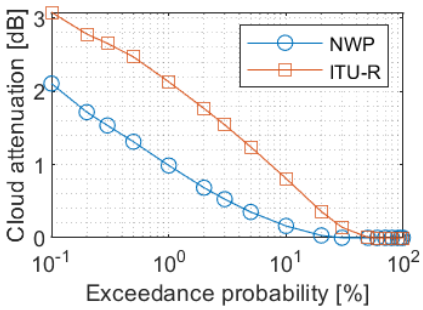

(b) 39.402 GHz

Figure 7.17 – CCDFs of the attenuation due to clouds for Alphasat at Ljubljana from 2016-07-01 to 2017-06-30, comparison between WRF-based simulations (NWP) and the reference from ITU-R recommendations (ITU-R)

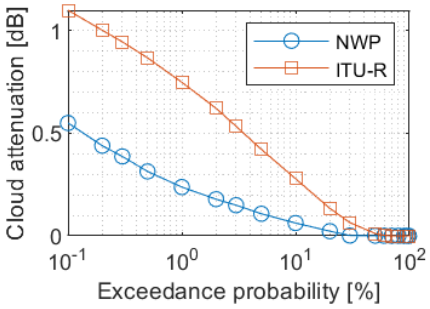

(a) 19.701 GHz

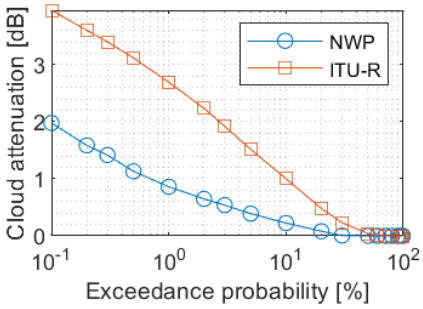

(b) 39.402 GHz

Figure 7.18 – CCDFs of the attenuation due to clouds for Alphasat at Prague from 2016-07-01 to 2017-06-30, comparison between WRF-based simulations (NWP) and the reference from ITU-R recommendations (ITU-R)

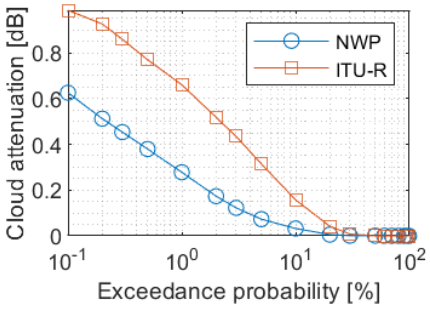

(a) 19.68 GHz

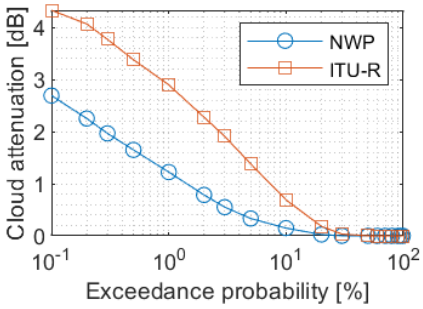

(b) 39.402 GHz

Figure 7.19 – CCDFs of the attenuation due to clouds for KaSAT and Alphasat at Aveiro from 2016-07-01 to 2017-06-30, comparison between WRF-based simulations (NWP) and the reference from ITU-R recommendations (ITU-R)

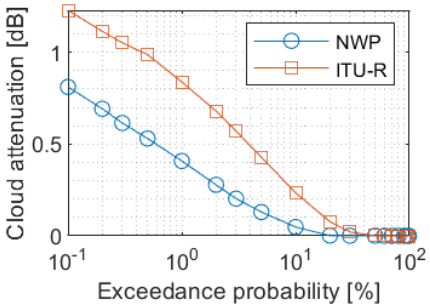

(a) 19.701 GHz

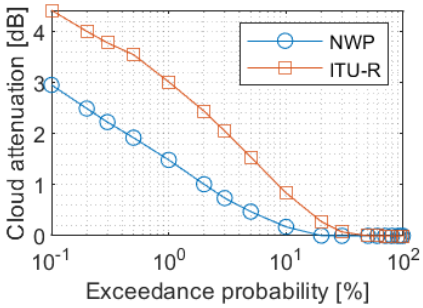

(b) 39.402 GHz

Figure 7.20 – CCDFs of the attenuation due to clouds for Alphasat at Vigo from 2016-07-01 to 2017-06-30, comparison between WRF-based simulations (NWP) and the reference from ITU-R recommendations (ITU-R)

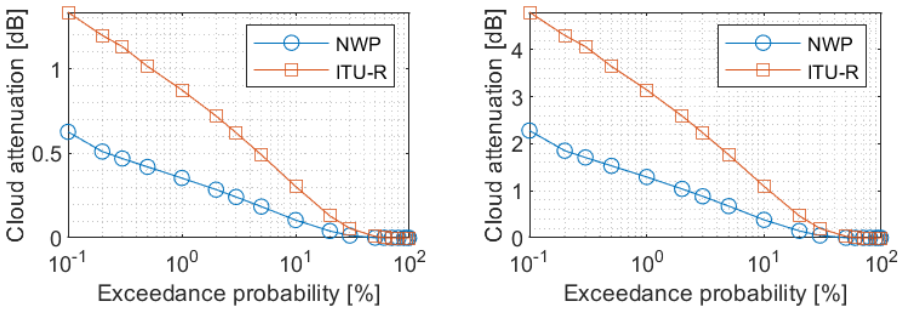

(a) 19.701 GHz (b) 39.402 GHz

Figure 7.21 – CCDFs of the attenuation due to clouds for Alphasat at Louvain-la-Neuve from 2016-07-01 to 2017-06-30, comparison between WRF-based simulations (NWP) and the reference from ITU-R recommendations (ITU-R)

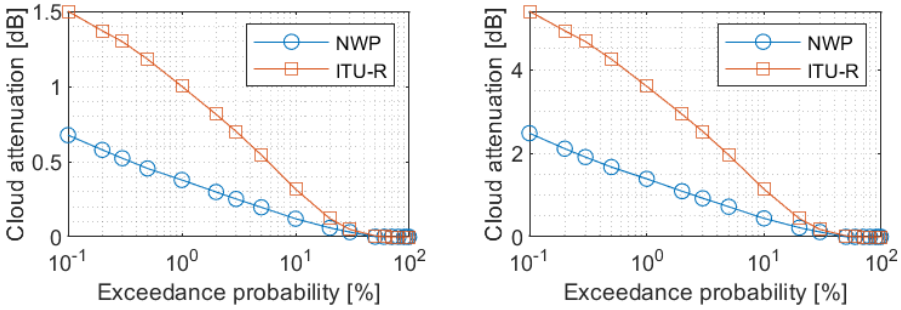

(a) 19.701 GHz (b) 39.402 GHz

Figure 7.22 – CCDFs of the attenuation due to clouds for Alphasat at Chilton from 2016-07-01 to 2017-06-30, comparison between WRF-based simulations (NWP) and the reference from ITU-R recommendations (ITU-R)

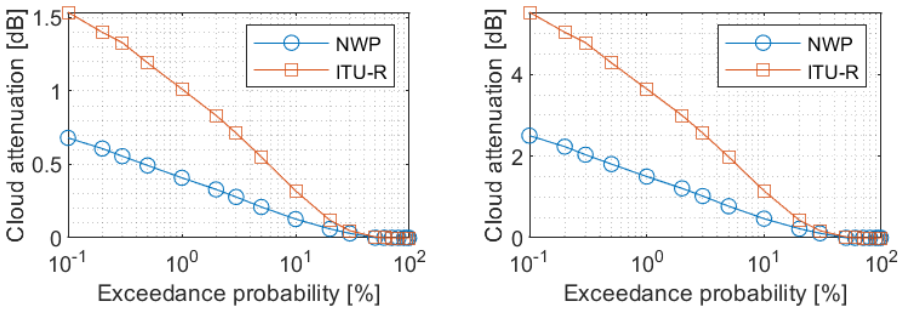

(a) 19.701 GHz (b) 39.402 GHz

Figure 7.23 – CCDFs of the attenuation due to clouds for Alphasat at Chilbolton from 2016-07-01 to 2017-06-30, comparison between WRF-based simulations (NWP) and the reference from ITU-R recommendations (ITU-R)

7.2 Simulation of propagation impairments for LEO links

The second application developed in this section takes the same approach for LEO links as the one reported in Sec. 5.2.8 but for another ground station. This application is explored more in details in Razavian et al. [149].

7.2.1 Earth-space links' configurations

Graz currently hosts ground stations measuring the Alphasat GSO propagation beacon signal at Ka and Q bands (19.701 GHz and 39.402 GHz) [150] and another non-GSO propagation experiment is in preparation with a cubesat at Q and W bands ($\sim$ 37.5 GHz and 75 GHz) [30]. It makes Graz a particularly interesting location to investigate the performances of non-GSO links simulated by the NWP-based simulator.

As in Sec. 5.2.8, the total attenuation on Earth-space links are simulated for the orbits of the Earth-observation LEO satellites METOP-A, -B and -C. These orbits are not meant to mimic the one of the cubesat, which will depend on its launch conditions. Three frequencies are selected: 19.701 GHz, 39.402 GHz and 75 GHz. The study period is shorter than in Sec. 5.2.8: only one year (2017). In order to compare with the model given by (4.37), southward GSO links (180° in azimuth) are also simulated every 2.5° in elevation from 10° and upwards.

7.2.2 NWP model

The WRF domains around Graz are shown in the Fig. 7.24. The configuration is the same as in Sec. 6.1.3 and 7.1.2. An exception to this regards the initialisation data: here ERA-Interim data was used, as in Chap. 5.

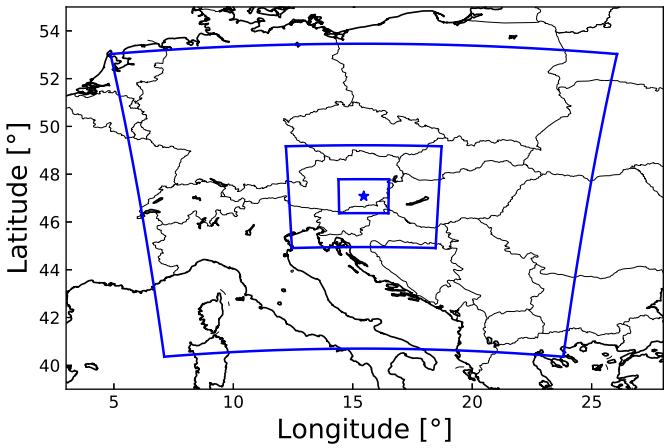

Figure 7.24 – WRF Lambert Conformal Conic (79 × 79) domains at 18 km, 6 km, and 2 km centered at Graz (47.06°N, 15.46°E)

7.2.3 Total attenuation statistics

To understand the behaviour of the LEO links based on the METOP orbits, the histogram of the elevation during the 2017 visibility periods (elevation $\geq 10°$) is presented in the Fig. 7.25 for METOP-A. Considering the three METOP orbits are nearly identical with different epochs, the elevation histograms for METOP-B and -C would be nearly indistinguishable from METOP-A's. Clearly, the visibility during the passes occurs mostly at low elevations, in a similar fashion to the configuration studied for Louvain-la-Neuve in the Fig. 5.28.

The total attenuation CCDFs at each frequency are provided from the Figs 7.26 to 7.28. The WRF total attenuation is here solely obtained from the WRF volumetric cloud content as in Sec. 2.3.5 (not using the Salonen or Mattioli model), and from the WRF volumetric rain content as in Sec. 2.3.8 (not using the rain rate). The computations of the CCDFs are done from the non-GSO time series for each individual METOP satellite (A, B, C) or from the GSO CCDFs combined with the histogram of the Fig. 7.25 according to the conditional probability approach of (4.37). The conditional probability approach is also applied to the reference ITU-R GSO CCDFs as per Sec. 2.3.10.

The Fig. 7.26 presents the total attenuation CCDFs at 19.701 GHz. Looking first at the four NWP CCDFs, a good agreement is found for the highest probabilities corresponding to the presence of gases only (clear-sky). However, it is observed that the brown CCDF based on conditional probabilities underestimates slightly the CCDFs for the individual satellites in the probability range from ~ 10 to 1 % corresponding to the highest influence from the clouds. The reason for this underestimation is not clear but seems to be caused by the histogram-based procedure, or linked to the METOP passes being localized at the same hours of a given day (sun-synchronous orbit). At lower exceedance probabilities, with growing influence from the rain, the brown CCDF becomes intermediate between the the CCDFs for METOP-A, -B and -C. METOP-A and -C have lower highest values of the exceeded attenuation, whereas METOP-B exceeds the brown curve below ~ 0.04 % of the time. The ITU-R conditonal probability CCDF agrees quite well with the NWP one for high and low probabilities, though it is underestimated by the NWPs from ~ 10 to 0.1 %, in parts due to low NWP cloud contents as discussed before in this document.

The Fig. 7.27 presents the total attenuation CCDFs at 39.402 GHz. Most of the observations made at 19.701 GHz holds but the higher attenuation from each atmospheric effect shift the probability range of interest, with attenuations that can reasonably be compensated, to ≥ 0.1 %.

The Fig. 7.28 presents the total attenuation CCDFs at 75.0 GHz. Here the workable range for the probabilities of exceedance is even shorter ≥ 0.5 %. The ITU-R is above WRF on most of that range, due to the ITU-R oxygen attenuation being a bit pessimistic at 75 GHz (as seen in Fig. 5.33),

As the Earth-space links configuration is nearly the same, the observations made here are in line with those in Sec. 5.2.8. As the period considered here is shorter (only one year) the inter-annual variability plays a larger role, though for the gases and clouds this is a lesser concern. In the absence of non-GSO measurements, the simulations suggest again the ITU-R procedure gives a safe estimate which could be improved by including more link information.

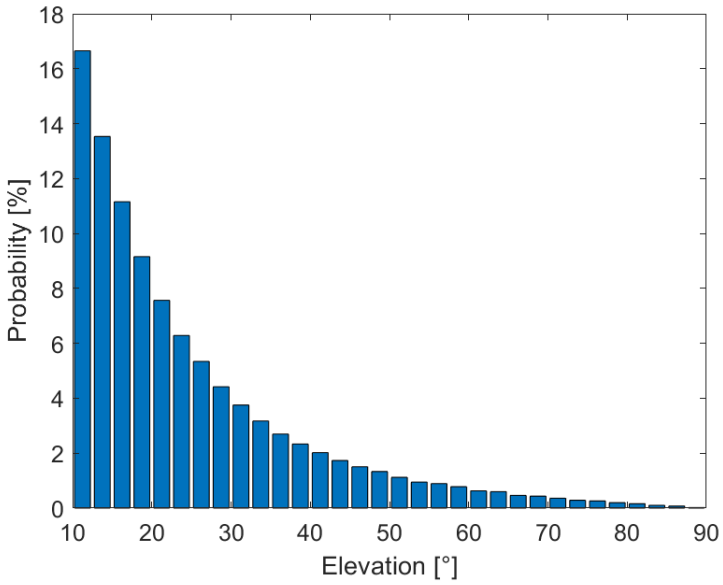

Figure 7.25 – Elevation PDF for METOP-A and Graz in 2017

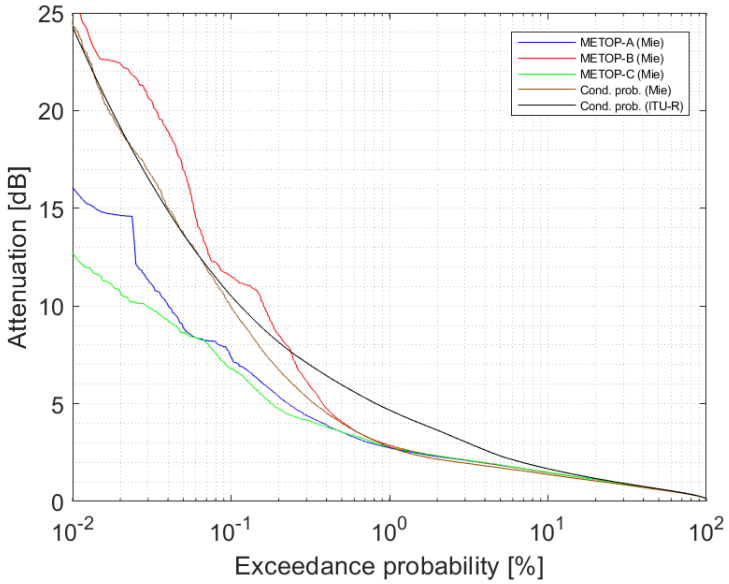

Figure 7.26 – Total attenuation CCDFs with WRF and the ITU-R reference, at 19.701 GHz for METOP-A, -B, and -C, for Graz in 2017

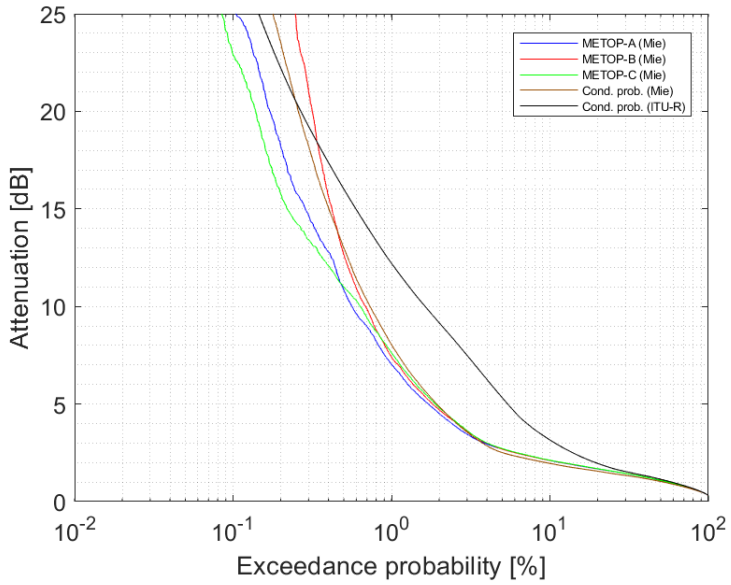

Figure 7.27 – Total attenuation CCDFs with WRF and the ITU-R reference, at 39.402 GHz for METOP-A, -B, and -C, for Graz in 2017

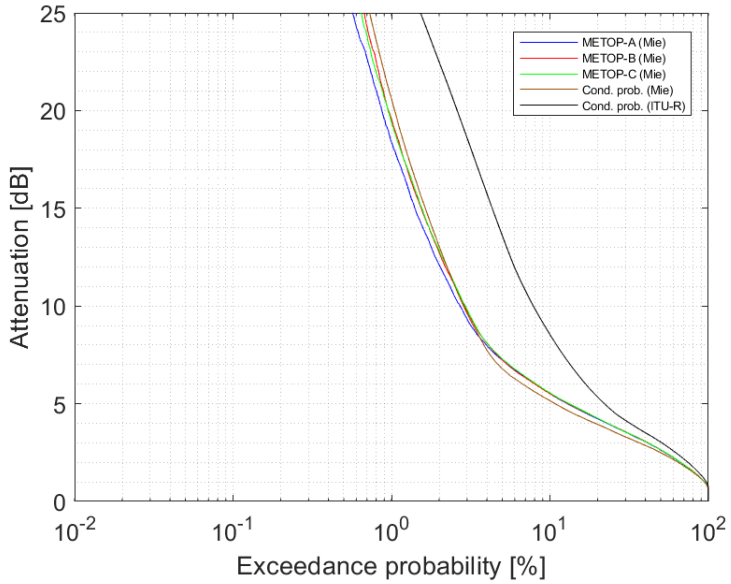

Figure 7.28 – Total attenuation CCDFs with WRF and the ITU-R reference, at 75.0 GHz for METOP-A, -B, and -C, for Graz in 2017

7.3 Identification of amplitude scintillation at low elevation

This third application treats a topic not investigated here so far. It explores briefly, by a comparison with measurements at low elevation, the possibility to detect conditions of strong scintillation from NWP data. The results of this section are based on the contribution by Vanhoenacker-Janvier et al. [151].

7.3.1 Earth-space link's configuration

At Isjord radio (78.1°N), in Svalbard, propagation measurements at 19.68 GHz with the GSO satellite Ka-Sat (9°E) were conducted by the Norwegian Defence Research Establishment (Forsvarets forskninginstitutt, FFI). The slant path is mostly over the sea (see Fig. 7.29 (c) at at very low elevation angle of 3.2°. The amplitude scintillation of the signal, especially significant in those conditions, was extracted from the beacon signal for its independent investigation.

7.3.2 NWP model

The NWP model in use for this application is distinct from most of the other results in this thesis based on the WRF model. Here the NWP data comes from the AROME-Arctic forecast at resolutions of 2.5 km and 1 h [116]. The AROME-Arctic domain includes Northern Scandinavia, Novaya Zemlya, Franz Josef Land, Jan Mayen, and, for what is of interest here, Svalbard.

7.3.3 Refractive index structure constant profiles

The Fig. 7.29 (a) shows an example of 19.68 GHz scintillation signal at 3.2° between Isfjord and Ka-Sat on the 24/07/2016. Periods of weak scintillation (around 2 AM, green arrow) and strong scintillation (around 9 AM, red arrow) are identified. Extracting the power spectral density at 2 AM (see Fig. 7.29 (b) gives a flattening of the spectrum for $-180\,\mathrm{dB\,Hz^{-1}}$ which proves the scintillation is always above the noise floor and correctly extracted.

AROME-Arctic data serve to estimate the refractive index structure constant. First, N_0 is computed as in (2.6) from vertical profiles of (T, p, p_{vap}) for some grid points encountered along the path. N_0 is then converted to n as in (2.4), and then interpolated up to and altitude of 3 km with a fixed vertical spacing $\delta r = 25\,\mathrm{m}$ (roughly the best resolution available). Then profiles of C_n^2 are estimated according to (2.103). This method is simpler than other approaches [93, 95] but is unlikely to produce a very accurate C_n^2. Likely $\delta r > L_0$, for the outer scale L_0, which contradicts the assumptions made for (2.103).

At 9 AM there is a layer of strong turbulence around 1 km (see Fig. 7.29 (d)) which is found for all selected profiles along the radio-path (see 7.29 (c)). This result is encouraging regarding the possibilities of NWPs to model scintillation, but so far attempts to reproduce reliably σ_χ or W_χ were not very conclusive. Some research in that direction was reported, indepently from the present work, by two master's theses completed at UCLouvain [152, 153].

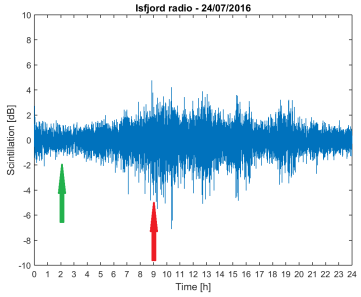

(a) Scintillation signal on the 24/07/2016

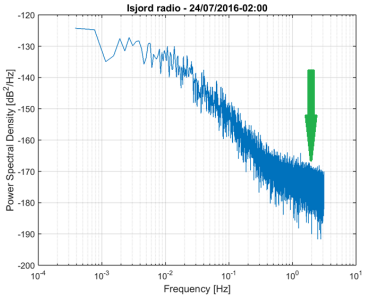

(b) Spectral density estimated over 2-3 AM

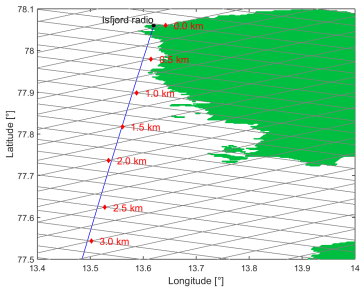

(c) AROME Arctic selected grid points

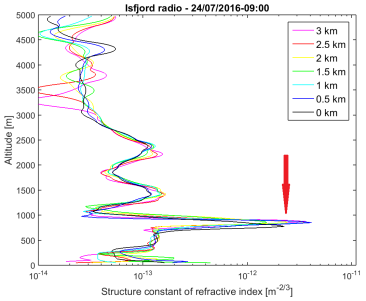

(d) C_n^2 profiles extracted at 9 AM

Figure 7.29 – Scintillation for the 3.2° 19.68 GHz link between Isjord radio and Ka-Sat, and vertical profiles of C_n^2 computed from AROME-Arctic at grid points selected nearest to the slant path for some distances of the slant path vertical projection (0 km, 0.5 km, 1 km, 1.5 km, 2 km, 2.5 km, 2 km, 3 km)

7.4 Concluding remarks

The main observations on the presented applications are summarized as follows:

- in Sec. 7.1, GSO links were simulated for one year and for nine ground stations measuring Alphasat's signal (19.701 GHz, 39.402 GHz). The agreement of the simulated CCDFs with the ITU-R is excellent for the gaseous attenuation. For the clouds, the NWPs underestimate the ITU-R CCDFs' attenuation in value (by $\sim$ half) and in probability to be non-zero.
- in Sec. 7.2, non-GSO links (orbits of METOP satellites) were simulated for one year in Graz, location of an Alphasat station (19.701 GHz, 39.402 GHz) and of a future W-band cubesat experiment (75.0 GHz). The NWP total attenuation CCDFs obtained as a combination of GSO CCDFs are intermediate to those for individual satellites, and they underestimate their ITU-R equivalent at mid-probabilities (most affected by clouds).
- in Sec. 7.3, profiles of C_n^2 were estimated from AROME Arctic 2.5 km NWP data for a scintillation event measured at Isfjord (19.68 GHz, 3.2° in elevation with Ka-Sat). A strong C_n^2 peak is associated with the event.

Chapter 8

Conclusion

In this last chapter, the results presented within the text are first summarised (see Sec. 8.1). Then the position of those results with respect to the literature is stated (see Sec. 8.2). Finally, perspectives are provided for future applications of the described methods and for ways to improve them (see Sec. 8.3).

8.1 Summary of the results

The presentation of the results of this thesis went through the following steps:

1. in Chap. 5, a validation of the attenuation components (gases, clouds, rain) simulated with WRF in Louvain-la-Neuve (19.701 GHz, 26 GHz, 39.402 GHz, 75 GHz), carried out over five years using the NWP model ALARO, weather radar measurements from Wideumont, and the reference CCDFs from the ITU-R. The validation includes GSO links (30° in elevation) and non-GSO links with the orbits of the METOP satellites.

2. in Chap. 6, a validation of the nonrainy attenuation components (gases and clouds) simulated with WRF in Spino d'Adda, carried out over four months using Alphasat propagation beacon data and radiometric data (19.701 GHz, 39.402 GHz). The goal is to compare the performances of WRF to the radiometer in order to complete the excess attenuation extracted from the beacon data and obtain the total attenuation.

3. in Sec. 7.1, an application of the simulator to the nonrainy attenuation for nine European ground stations of the ASALASCA consortium measuring the Alphasat satellite (19.701 GHz, 39.402 GHz). CCDFs of the gases and clouds attenuation are obtained, with the same goal in mind as for Spino, and compared to the ITU-R references. The motivation is the lack of radiometric measurements for the ASALASCA stations.

4. in Sec. 7.2, an application of the simulator to generate non-GSO CCDFs in Graz (19.701 GHz, 39.402 GHz, 75 GHz) for the METOP satellites. The motivation is the situation of Graz as both an Alphasat station and a station for a future W-band cubesat experiment at 75 GHz.

5. in Sec. 7.3, an example of scintillation on a low elevation link in Isjord radio (19.68 GHz, 3.2° in elevation) associated to high turbulence conditions estimated from the AROME Arctic NWP model. The motivation is the very high values of amplitude scintillation, and other possible effects such as multi-paths, that can be encountered at such a low elevation.

From these simulations and experimental set-ups, it was observed that:

1. the GSO attenuation components are modelled with varying degrees of correlations between the NWP models: ~ 0.91 for oxygen, ~ 0.78 for water vapour, ~ 0.11 for the clouds, very low for rain. The GSO CCDFs show similarly a near perfect agreement between WRF, ALARO and the ITU-R for the oxygen, and slightly more deviations or biases for water vapour. The cloud attenuation CCDFs differ remarkably, with ALARO having a larger probability of clouds than WRF, and more in-line with the ITU-R. Both WRF and ALARO underestimate the ITU-R cloud attenuation CCDF by $\sim$ half, though with the Salonen and Mattioli models there is an overestimation by WRF on parts of the curves. For the rain attenuation CCDF, the best agreement with the ITU-R is found using the model with WRF rain rate, and they also both agree well with the CCDF from Wideumont weather radar shown at 19.701 GHz. When looking at the non-GSO CCDFs, the consequence of the divergences in cloud attenuation is particularly notable in the 10 to 0.1 % range of exceedance probabilities. Otherwise the agreement between WRF (rain rate) and the ITU-R is acceptable. Another aspect investigated with the non-GSO CCDFs concerns the differences between two methods to derive them: deriving them from simulated non-GSO time series, or combining GSO CCDFs conditioned to the elevation angles histogram. Even over five years the CCDFs vary between the METOP satellites and with the conditional probability approach. This suggests more sophisticated conditions on the probabilities (e.g. hours of the day for a sun-synchronous orbit) may improve the performances.

2. the correlations and RMSEs on the nonrainy attenuation between WRF (Tiedtke) and the radiometer over four months are 0.88 and 0.11 dB at 19.701 GHz, and 0.59 and 0.26 dB at 39.402 GHz. As the nonrainy attenuation estimate is added to the excess attenuation to obtain the total attenuation, the error on the the nonrainy attenuation is also the one on the total attenuation. These errors are found to be compatible with the estimated accuracy of the radiometric attenuation (< 0.1 dB) and typical accuracy of the excess attenuation ($\sim$ 0.2-0.5 dB).

3. the gaseous CCDFs are still in great agreement between WRF and the ITU-R for multiple stations experiencing different climates. The cloud attenuation CCDFs from WRF also underestimate the ITU-R CCDFs, as observed for Louvain-la-Neuve, roughly by $\sim$ half. The differences in cloud attenuation, and especially probability of cloud attenuation, between the stations suggest climatic discrepancies, and possibly a role of the type of clouds (stratiform or convective).

4. the non-GSO CCDFs of the total attenuation in Graz present the same characteristics as in Louvain-la-Neuve.

5. it is possible to qualitatively associate strong peaks in NWP estimates of the C_n^2 to high values of the scintillation.

8.2 Contributions with respect to the literature

When reviewing the status of NWPs for radio-propagation research in Sec. 1.4, six insufficiently studied aspects were listed. This thesis contributed partly to fill those gaps, or instead did not work enough on them, as such:

1. NWP-based simulations of the attenuation components are given over five years, instead of the periods from six months to one year reported by some of the best results in the literature [36, 39, 53].

2. the resolutions of the NWP models in use vary from 2 km to 4 km horizontally, and from 5 min to 1 h in time. This is on par with the best results reported in that regards, such as in [36], and better than most previously reported results.

3. two approaches to derive the rain attenuation from NWP output were studied (using the NWP volumetric rain content, or its ground rain rate), and two alternatives to derive the cloud attenuation were tested as well (using the NWP volumetric cloud content, or extracting it according to the algorithms of Salonen or Mattioli). Previous results were reported with only one of these options for each effect respectively.

4. the simulation methodology is suitable to generate time series and statistics for both GSO and non-GSO links. Examples of long-term non-GSO CCDFs are provided, and there is also a comparison between CCDFs obtained with non-GSO time series and the more common conditional probabilities approach to combine GSO CCDFs.

5. only very preliminary results on scintillation were reported.

6. true forecasts of the propagation impairments in the near future were not investigated, though the low correlations reported for rain and cloud time series suggest the performances would be poor with only the suggested methods. Also, no direct application of the propagation results to design FMTs were proposed, either based on the time series or CCDFs, though some implications for systems' margins were briefly commented on.

8.3 Perspectives

Considering the current performances of a NWP-based simulator of the propagation impairments as reported in here, and considering other relevant results in the open literature not covered inside this document, here are some avenues that would be worthwhile to explore further in future works:

- a comparison with propagation beacon measurements and/or radiometric measurements for a larger period of time and/or for more distinct geographical areas. Here only four months of concurrent beacon and radiometric data were made available from Spino d'Adda. Besides Spino, the other stations measuring the Alphasat signal are good candidates for extended studies. Louvain-la-Neuve, where measurements started in

March 2017, is of course a good site for a natural extension of this work. Other sites of the ASALASCA consortium, e.g. Chilton/Chilbolton or Aveiro, have beacon measurements with excellent availabilities and are of interest. The Alphasat station in Graz, equipped with a radiometer like Spino, offers a particularly complete dataset. Unpublished comparisons of the NWP nonrainy attenuation correction were actually already conducted over six months in collaboration with Joanneum Research and proved to yield errors of the same magnitude as the ones in Spino. The extension to more diverse climates, notably subtropical climates e.g. in India, Malaysia, Guyana, ... would also be useful.

- a direct assessment of the NWP model output performances, in terms of atmospheric variables or ground parameters and not only the final attenuation values. The goal would be to give more guarantees on the quality of the simulations before their post-processing. This could include comparing two NWP models, e.g. WRF and ALARO, and some examples for the rain rate of 2 m temperature were actually produced by the RMIB. Other options include the global models (e.g. ECMWF), or ancillary data such as radiosoundings, rain gauge or disdrometers measurements, ...

- the inclusion of more complex error metrics to give more insight on the performances of the models. At the level of the time series there are e.g. the systematic and unsystematic root mean square errors [154]. At the level of the CCDFs there are e.g. the Kolmogorov-Smirnov or Cramér-von Mises criterions. For those two latter metrics, it must be noted preliminary tests with the data of Chap. 6 simply reject the hypothesis the measured and simulated distributions could be identical, and this in spite of performances that are acceptable from a practical point of view.

- a more thorough investigation of cloud modelling strategies, possibly methods capable to discriminate between stratiform and convective clouds. The fractional cloud cover is also usually part of a NWP model output and could have applications not foreseen in this text.

- for the clouds, a comparison with satellite radiance data or other measured (or simulated) reference datasets such as those compiled by the International Satellite Cloud Climatology Project (ISCCP) [155].

- a consideration of the solid hydrometeors, in particular the melting species (e.g. in the radar bright band above the freezing level/rain height) which likely affect the attenuation. Of note are also the ice crystals for their contribution to depolarisation, and snow for its impact as it falls on an outdoor antenna.

- the application of the impairments simulated with NWPs to the direct modelling of FMTs, including ACMs and site diversity as in [42].

- the inclusion of ensemble forecasts as suggested by [44, 55].

- the possibility of "nowcasting" of the attenuation, i.e. a short-term forecast (generally up to one or a few hours) based in principle on sophisticated extrapolations of meteorological measurements, and not the full temporal integration of the primitive equations. Nowcasting may not be a great interest for ACMs, as changing the Earth-space link physical layer on the very short-term (seconds) is already possible via feedback loops. However, nowcasting is a prime candidate to exploit site diversity and predict when to best switch gateways. Nowcasting normally implies weather radar systems rather than NWP models, but the method is in turn dependent on the density of the radar network in a particular region and the two approaches could then be complementary.

- the simulation with NWP models of a more varied class of non-GSO links, and the comparison of simulations with non-GSO propagation measurements once more of them become available.

- using a long-term dataset of NWP simulated attenuation time series such as the one produced during this work, the generation of fixed elevation attenuation CCDFs conditioned to the hour of the day, to the month of the year, or the season. CCDFs for every hour would be of particular interest in the case of sun-synchronous orbits. Indeed, as was observed with the simulation of METOP satellites' links with Louvain-la-Neuve or Graz, the concentration of passes at the same moments every day can have an impact on the CCDFs. Then, those CCDFs conditioned to the hour of the day could in principle be used to predict non-GSO CCDFs more accurately. The diurnal and seasonal variation in precipitation is a statistical reality with, for example, maximum precipitations occurring in Belgium in June/July near 3 PM, due to convective storms [156].

- a continuation of the work following the trends of links designed at increasingly higher frequencies. This includes not only higher radio-frequencies, for which results were presented here (W-band, 75 GHz), but also optical frequencies. At optical frequencies, communications are completely halted by the mere presence of clouds [157], and the signal coherence is also heavily affected by turbulence. The characterisation of both clouds and turbulence would benefit from NWPs, though this thesis concluded neither were trivial to model accurately.

Generally, modelling propagation impairments with NWPs ought to remain an attractive prospect thanks to their ability to be applied for any part of the world, and also as the global models such as ECMWF's are in the constant process to be improved i.a. with higher resolutions.

Bibliography

[1] International Telecommunication Union Radiocommunication (ITU-R), "Recommendation ITU-R V.431-8: Nomenclature of the frequency and wavelengh bands used in telecommunications," tech. rep., ITU, Aug. 2015. https://www.itu.int/rec/R-REC-V.431-8-201508-I/en.

[2] D. M. Pozar, *Microwave Engineering*. Wiley, 4 ed., 2012.

[3] G. Gallinaro, A. Vernucci, and C. Moreau, "Protocols and Signalling for Fade Mitigation Techniques (FMT) in DVB-RCS Multi-beam Systems: Final Report," ESTEC 17354/03/NL/ND, ESA, June 2005.

[4] Digital Video Broadcasting (DVB), "DVB Specifications," tech. rep., DVB, Mar. 2020. https://www.dvb.org/specifications.

[5] International Telecommunication Union Radiocommunication (ITU-R), "Recommendation ITU-R P.618-13: Propagation data and prediction methods required for the design of Earth-space telecommunication systems," tech. rep., ITU, Dec. 2017. https://www.itu.int/rec/R-REC-P.618-13-201712-I/en.

[6] L. Ippolito, *Propagation Effects Handbook for Satellite Systems Design, 5th Ed.* Stanford Telecom, 1999.

[7] L. J. Ippolito, "Effect of Precipitation on 15.3- and 31.65-GHz Earth-Space Transmissions With the ATS-V Satellite," *Proc. IEEE*, vol. 59, Feb. 1971.

[8] S. H. Lin, H. J. Bergmann, and M. V. Pursley, "Rain Attenuation on Earth Satellite Paths – Summary of 10-Year Experiments and Studies," *The Bell System Technical Journal*, vol. 59, Feb. 1980.

[9] D. C. Cox and H. W. Arnold, "Results from the 19- and 28-GHz COMSTAR Satellite Propagation Experiments at Crawford Hill," *Proc. IEEE*, vol. 70, May 1982.

[10] T. Ishida, N. Fugono, J. Tabata, M. Ohara, and T. Ishizawa, "Propagation experiment with Japanase satellite ETS-II (KIKU-2)," *Acta Astronautica*, vol. 7, Mar. 1980.

[11] Y. Karasawa and Y. Maekawa, "Ka-Band Earth-Space Propagation Research in Japan," *Proc. IEEE*, vol. 85, June 1997.

[12] F. Carassa, "The SIRIO programme and its propagation and communication experiment," *Alta Frequenza*, vol. XLVII, no. 4, 1978.

[13] P. Sobieski, A. Laloux, and G. Brussaard, "Results of the European Space Agency OTS Propagation Campaign," in *Proc. 14th Eur. Microwave Conf.*, (Liège, BE), 1984.

[14] B. R. Arbesser-Rastburg and G. Brussaard, "Propagation research in Europe using the OLYMPUS satellite," *Proc. IEEE*, vol. 81, June 1993.

[15] C. Riva, "Seasonal and diurnal variations of total attenuation measured with the ITALSAT satellite at Spino d'Adda at 18.7, 39.6 and 49.5 GHz," *Int. J. Satell. Commun. Networking*, vol. 22, July 2004.

[16] S. Ventouras, S. A. Callaghan, and C. L. Wrench, "Long-term statistics of tropospheric attenuation from the Ka/U band ITALSAT satellite experiment in the United Kingdom," *Radio Science*, vol. 41, Apr. 2006.

[17] R. Bauer, "Ka-Band Propagation Measurements: An Opportunity with the Advanced Communications Technology Satellite (ACTS)," *Proc. IEEE*, vol. 85, June 1997.

[18] S. Callaghan, J. Waight, J. Agnew, C. Walden, C. Wrench, and S. Ventouras, "The GBS dataset: measurements of satellite site diversity at 20.7 GHz in the UK," *Geoscience Data Journal*, Mar. 2013.

[19] Y.-H. Chu, S.-P. Shih, and G.-S. Liu, "First measurements of scintillation and attenuation of 19.5 GHz beacon signal for experimental communication payload of ROCSAT-1," in *Space Weather Study Using Multipoint Techniques, Proc. COSPAR Colloquium*, (Wanli, TW), 2000.

[20] C. Amaya, T. Nguyen, A. Rocha, J. M. Riera, A. Bennaroch, Pedro García-del-Pino, J. M. García-Rubia, G. Carrie, and L. Castanet, "Joint Results of 20 GHz Recent Earth-Space Propagation Experiments in Canada and Europe," in *Proc. 5th Eur. Conf. Antennas Propag. (EuCAP)*, (Rome, IT), 2011.

[21] X. Boulanger, B. Gabard, L. Casadebaig, and L. Castanet, "Four Years of Total Attenuation Statistics of Earth-Space Propagation Experiments at Ka-Band in Toulouse," *IEEE Trans. Antennas Propag.*, vol. 63, May 2015.

[22] T. Kostulski, *Ka Band Propagation Experiments on the Australian Low Earth Orbit Microsatellite 'FedSat'*. PhD thesis, University of Technology Sydney, 2008.

[23] C. Amaya and T. Nguyen, "Propagation measurements in Ottawa with the Ka-band beacon of the ANIK F2 satellite," in *14th Int. Symposium on Antenna Technology and Applied Electromagnetics/American Electromagnetics Conf.*, (Ottawa, ON), 2010.

[24] F. Cuervo, M. Schönhuber, C. Capsoni, Lam Hong Yin, Siat Ling Jong, Jafri Bin Din, and A. Martellucci, "Ka-band propagation campaign in Malaysia - first months of operation and site diversity analysis," in *Proc. 10th Eur. Conf. Antennas Propag. (EuCAP)*, (Davos, CH), 2016.

[25] M. Rytir, C. Riva, D. Vanhoenacker-Janvier, and T. Tjelta, "Tropospheric Scintillation Spectra and Transversal Wind Speed for Satellite

Links at Very Low Elevation Angles," in *Proc. 11th Eur. Conf. Antennas Propag. (EuCAP)*, (Paris, FR), 2017.

[26] T. Tjelta, M. Rytir, L. E. Bråten, P. A. Grotthing, M. Cheffena, and J. E. Håkegård, "Results of a Ka Band Campaign for the Characterisation of Propagation Conditions for SatCom Systems at High Latitudes," in *Proc. 11th Eur. Conf. Antennas Propag. (EuCAP)*, (Paris, FR), 2017.

[27] X. Boulanger, B. Benammar, and L. Castanet, "Propagation Experiment at Ka-Band in French Guiana: First Year of Measurements," *IEEE Antennas and Wireless Propagation Letters*, vol. 18, pp. 241–244, Feb. 2019.

[28] T. Rossi, M. D. Sanctis, M. Ruggieri, C. Riva, L. Luini, G. Codispoti, E. Russo, and G. Parca, "Satellite Communication and Propagation Experiments Through the Alphasat Q/V Band Aldo Paraboni Technology Demonstration Payload," *IEEE Aerosp. Electron. Syst. Mag.*, vol. 31, Mar. 2016.

[29] M. K. Mishra, R. Renju, N. Mathew, C. Suresh Raju, M. Sujimol, and K. Shahana, "Rain attenuation of Ka-band signal over a Tropical station," in *Proc. URSI Asia-Pacific Radio Science Conference (AP-RASC)*, (New Delhi, IN), 2019.

[30] J. Flavio, F. Cuervo, M. Schonhuber, M. Schmidt, D. Vanhoenacker-Janvier, A. M. Polegre, and A. Martellucci, "A New Earth-LEO Propagation Campaign at Q and W-band," in *9th Advanced Satellite Multimedia Systems Conf. the 15th Signal Processing for Space Communications Workshop, ASMS/SPSC*, (New Delhi, IN), 2018.

[31] International Telecommunication Union Radiocommunication (ITU-R), "Recommendation ITU-R P.835-6: Reference Standard Atmospheres," tech. rep., ITU, Dec. 2017. `https://www.itu.int/rec/R-REC-P.835-6-201712-I/en`.

[32] D. Hodges, R. Watson, A. Page, and P. Watson, "Generation of attenuation time-series for EHF SATCOM simulation," in *Proc. IEEE Military Communications Conf. (MILCOM)*, (Boston, MA), 2003.

[33] D. D. Hodges, R. J. Watson, and G. Wyman, "An Attenuation Time Series Model for Propagation Forecasting," *IEEE Trans. Antennas Propag.*, vol. 54, June 2006.

[34] D. D. Hodges, R. J. Watson, and G. Wyman, "Initial Comparisons of Forecast Attenuation and Beacon Measurements at 20 and 40 GHz," in *Proc. 1st Eur. Conf. Antennas Propag. (EuCAP)*, (Nice, FR), 2006.

[35] M. Outeiral García, N. Jeannin, L. Féral, and L. Castanet, "Use of WRF Model to Characterize Propagation Effects in the Troposphere," in *Proc. 7th Eur. Conf. Antennas Propag. (EuCAP)*, (Göteborg, SE), 2013.

[36] N. Jeannin, M. Outeiral, L. Castanet, C. Pereira, Danielle-Vanhoenacker-Janvier, C. Riva, C. Capsoni, L. Luini, M. Cossu, and A. Martellucci, "Atmospheric Channel Simulator for the Simulation of Propagation Impairments for Ka Band Data Downlink," in *Proc. 8th Eur. Conf. Antennas Propag. (EuCAP)*, (The Hague, NL), 2014.

[37] N. Jeannin, M. Outeiral-García, L. Castanet, C. Capsoni, L. Luini, C. Riva, D. Vanhoenacker-Janvier, and C. Pereira, "Channel Modelling for Design of Earth Observation Ka-band Data Downlink Systems: TN 4 Simulator Description and Test Document," ESTEC 4000105326/12/NL/LVH, ESA, Sept. 2014.

[38] C. Pereira, D. Vanhoenacker-Janiver, N. Jeannin, L. Castanet, and A. Martellucci, "Simulation of tropospheric scintillation on LEO satellite link based on space-time channel modeling," in *Proc. 8th Eur. Conf. Antennas Propag. (EuCAP)*, (The Hague, NL), 2014.

[39] G. Fayon, L. Féral, L. Castanet, N. Jeannin, and X. Boulanger, "Use of WRF to Generate Site Diversity Statistics in South of France," in *32nd URSI GASS*, (Montréal, CA), 2017.

[40] N. Jeannin and I. Dahman, "Sizing and optimization of high throughput radio-frequency data down link of earth observation satellites," *Int. J. Satell. Commun. Networking*, vol. 34, Mar. 2016.

[41] N. Jeannin, I. Dahman, L. Castanet, V. Pourret, and B. Pouponneau, "Tropospheric propagation forecasts for smart gateways switching algorithms," in *Proc. 8th Advanced Satellite Multimedia Systems Conf. and 14th Signal Processing for Space Communications Workshop (ASM-S/SPSC)*, (Palma de Mallorca, ES), 2016.

[42] N. Jeannin, L. Castanet, I. Dahman, V. Pourret, and B. Pouponneau, "Smart gateways switching control algorithms based on tropospheric propagation forecasts," *Int. J. Satell. Commun. Networking*, vol. 37, Jan. 2019.

[43] I. Dahman, N. Jeannin, P. Arbogast, and B. Bennamar, "Dynamic resource allocation for beam hopping technic based on short range probabilistic weather forecasts," in *Proc. 23rd Ka and Broadband Communications Conf.*, (Trieste, IT), 2017.

[44] I. Dahman, P. Arbogast, N. Jeannin, and B. Benammar, "Rain attenuation prediction model for satellite communications based on the Météo-France ensemble prediction system PEARP," *Natural Hazards and Earth System Sciences*, vol. 18, Dec. 2018.

[45] International Telecommunication Union Radiocommunication (ITU-R), "Recommendation ITU-R P.676-11: Attenuation by atmospheric gases," tech. rep., ITU, Sept. 2016. `https://www.itu.int/rec/R-REC-P.676-11-201609-I/en`.

[46] International Telecommunication Union Radiocommunication (ITU-R), "Recommendation ITU-R P.840-7: Attenuation due to clouds and fog," tech. rep., ITU, Dec. 2017. `https://www.itu.int/rec/R-REC-P.840-7-201712-I/en`.

[47] E. Salonen and S. Uppala, "New prediction method of cloud attenuation," *Electronic Letters*, vol. 27, pp. 1106–1008, Apr. 1991.

[48] J. S. Marshall and W. M. Palmer, "The distribution of raindrops with size," *Journal of Meteorology*, vol. 5, Aug. 1948.

[49] H. C. van de Hulst, *Light scattering by small particles.* Dover Publications, 1981.

[50] M. J. Leitao and P. A. Watson, "Method for prediction of attenuation on earth-space links based on radar measurements of the physical structure of rainfall," *IEE Proc. F - Commun., Radar and Signal Process.*, vol. 133, July 1986.

[51] A. Ishimaru, *Wave propagation and scattering in random media, vol. 2 Multiple Scattering, Turbulence, Rough Surfaces and Remote Sensing.* Academic Press, 1978.

[52] M. M. J. L. van de Kamp, J. K. Tervonen, E. T. Salonen, and J. P. V. Poiares Baptista, "Improved Models for Long-Term Prediction of Tropospheric Scintillation on Slant Paths," *IEEE Trans. Antennas Propag.*, vol. 47, Feb. 1999.

[53] F. Cuervo, F. Las-Heras, M. Schönhuber, J. M. Riera, P. Garcia-del-Pino, D. Pimienta-del-Valle, and A. Martelucci, "Short Term Satellite Channel Characteristics Forecast Using Numerical Weather Prediction Data," in *Proc. 12th Eur. Conf. Antennas Propag. (EuCAP)*, (London, UK), 2018.

[54] K. Grythe, L. E. Bråten, S. S. Rønning, and T. Tjelta, "Predicting near-time satellite signal attenuation at Ka-band using tropospheric weather forecast model," in *Proc. 12th Eur. Conf. Antennas Propag. (EuCAP)*, (London, UK), 2018.

[55] C. Kourogiorgas, A. Z. Papafragkakis, A. D. Panagopoulos, and S. Ventouras, "Long-Term and Short-Term Atmospheric Impairments Forecasting for High Throughput Satellite Communication Systems," in *Proc. 12th Eur. Conf. Antennas Propag. (EuCAP)*, (London, UK), 2018.

[56] A. Marziani, F. Consalvi, G. Fusco, C. Riva, L. Luini, A. Parodi, L. Pulvirenti, M. Lagasio, M. Biscarini, N. Pierdicca, and F. S. Marzano, "Microwave Tropospheric Scintillation and Excess Attenuation Prediction for Satellite to Earth Links Using 3D High-resolution Meteorological Forecast Models: Data Validation and Case Study," in *Proc. 41st PIERS*, (Rome, IT), 2019.

[57] A. Memmo, E. Fionda, T. Paolucci, D. Cimini, R. Ferretti, S. Bonafoni, and P. Ciotti, "Comparison of MM5 integrated water vapor with microwave radiometers, GPS, and radiosonde measurements," *IEEE Trans. Geosci. Remote Sens.*, vol. 43, May 2005.

[58] F. Davarian, S. Shambayati, and S. Slobin, "Deep space Ka-band link management and Mars Reconnaissance Orbiter: long-term weather statistics versus forecasting," *Proc. IEEE*, vol. 92, Dec. 2004.

[59] M. Biscarini, F. S. Marzano, L. Iess, M. Montopoli, K. De Sanctis, S. Di Fabio, L. Bernardini, M. Gregnanin, M. Parisi, M. Montagna, M. Mercolino, and M. Lanucara, "Evaluation of deep space Ka-band data transfer using radiometeorological forecast models," in *Proc. 8th Eur. Conf. Antennas Propag. (EuCAP)*, (The Hague, NL), 2014.

[60] M. Biscarini, F. Marzano, M. Montopoli, L. Iess, K. De Sanctis, S. Di Fabio, M. Montagna, M. Mercolino, and M. Lanucara, "Weather effects mitigation at Ka band by using radiometeorological model forecast in deep space downlinks," in *Proc. 9th Eur. Conf. Antennas Propag. (EuCAP)*, (Lisbon, PT), 2015.

[61] M. Biscarini, F. Marzano, M. Montopoli, L. Iess, K. De Sanctis, S. Di Fabio, M. Montagna, M. Mercolino, and M. Lanucara, "Coupling radio propagation and weather forecast models to maximize Ka-band channel transmission rate for interplanetary missions," in *Proc. USNC-URSI Science Meeting*, (Vancouver, CA), 2015.

[62] M. Biscarini, F. S. Marzano, M. Montopoli, K. De Sanctis, L. Iess, M. Montagna, M. Mercolino, and M. Lanucara, "Optimizing Data Volume Return for Ka-Band Deep Space Links Exploiting Short-Term Radiometeorological Model Forecast," *IEEE Trans. Antennas Propag.*, vol. 64, Jan. 2016.

[63] M. Biscarini, F. Marzano, L. Milani, M. Montopoli, K. De Sanctis, S. Di Fabio, D. Cimini, M. Montagna, M. Mercolino, and M. Lanacura, "Optimizing X and Ka band data volume return for BepiColombo mission using Cebreros and Malargüe data and weather-forecast based methodology," in *Proc. 7th ESA Int. Workshop on Tracking, Telemetry and Command Systems for Space Applications (TTC)*, (Noordwijk, NL), 2016.

[64] M. Biscarini, F. Marzano, and M. Montopoli, "Investigation of millimeter-wave channels for deep-space scientific data transmission using radiopropagation and weather forecast models," in *Proc. 7th ESA Int. Workshop on Tracking, Telemetry and Command Systems for Space Applications (TTC)*, (Noordwijk, NL), 2016.

[65] M. Biscarini, F. Marzano, L. Milani, M. Montopoli, K. De Sanctis, S. Di Fabio, D. Cimini, M. Montagna, M. Mercolino, and M. Lanucara, "Improving weather-forecast based model chain to optimize data-volume transfer for Ka-band deep-space downlinks," in *Proc. 11th Eur. Conf. Antennas Propag. (EuCAP)*, (Paris, FR), 2017.

[66] M. Biscarini, M. Montopoli, L. Milani, K. De Sanctis, S. Di Fabio, K. Magde, G. Brost, and F. Marzano, "Assessing Radiative Transfer Models Trained by Numerical Weather Forecasts Using Sun-Tracking Radiometric Measurements for Satellite Link Characterization Up to W Band," in *Proc. 2nd URSI AT-RASC*, (Gran Canaria, ES), 2018.

[67] M. Biscarini, K. D. Sanctis, S. D. Fabio, M. Montopoli, L. Milani, and F. S. Marzano, "Assessment and Uncertainty Estimation of Weather-Forecast Driven Data Transfer for Space Exploration at Ka- and X-Band," *IEEE Trans. Antennas Propag.*, vol. 67, Feb. 2019.

[68] M. Biscarini, A. Vittimberga, S. D. Fabio, K. D. Sanctis, L. Milani, M. Montagna, and F. S. Marzano, "Modeling and Predicting Down-link Tropospheric Channel above Ku Band for Interplanetary Exploration," in *Proc. 41st PIERS*, (Rome, IT), 2019.

[69] L. Milani, M. Biscarini, S. Di Fabio, K. De Sanctis, M. Montopoli, K. Magde, G. Brost, and F. Marzano, "Validating weather-forecast-driven propagation models at millimeter waves using multisource ground-based radiometric data," in *Proc. 13th Eur. Conf. Antennas Propag. (EuCAP)*, (Krakow, PL), 2019.

[70] International Telecommunication Union Radiocommunication (ITU-R), "Recommendation ITU-R P.453-13: The radio refractive index: its formula and refractivity data," tech. rep., ITU, Dec. 2017. `https://www.itu.int/rec/R-REC-P.453-13-201712-I/en`.

[71] B. R. Bean and E. J. Dutton, *Radio Meteorology*. National Bureau of Standards, 1966.

[72] International Telecommunication Union Radiocommunication (ITU-R), "Recommendation ITU-R P.676-10: Attenuation by atmospheric gases," tech. rep., ITU, Sept. 2013. `https://www.itu.int/rec/R-REC-P.676-10-201309-S/en`.

[73] H. J. Liebe, G. A. Hufford, and M. G. Cotton, "Propagation modelling of moist air and suspended water/ice particles at frequencies below 1000 GHz," in *Proc. AGARD 52nd Spec. Meeting EM Wave Propag. Panel*, (Palma de Maiorca, ES), 1993.

[74] J. Van Vleck and V. Weisskopf, "On the Shape of Collision Broadened Lines," *Review on Modern Physics*, vol. 17, Apr. 1945.

[75] International Telecommunication Union Radiocommunication (ITU-R), "Recommendation ITU-R P.1510-1: Mean surface temperature," tech. rep., ITU, June 2017. `https://www.itu.int/rec/R-REC-P.1510-1-201706-I/en`.

[76] International Telecommunication Union Radiocommunication (ITU-R), "Recommendation ITU-R P.836-6: Water vapour: surface density and total columnar content ," tech. rep., ITU, Dec. 2017. `https://www.itu.int/rec/R-REC-P.836-6-201712-I/en`.

[77] H. J. Liebe, T. Manabe, and G. A. Hufford, "Millimeter-Wave and Attenuation and Delay Rates due to Fog/Cloud Conditions," *IEEE Trans. Antennas Propag.*, vol. 37, Dec. 1989.

[78] P. S. Ray, "Broadband Complex Refractive Indices of Ice and Water ," *Applied Optics*, vol. 11, Aug. 1972.

[79] R. G. Eldridge, "Measurements of cloud drop-size distributions," *Journal of Meterology*, vol. 14, Feb. 1957.

[80] T. Manabe, T. Ihara, and Y. Furuhama, "Inference of raindrop size distribution from attenuaiton and rain rate measurements," *IEEE Trans. Antennas Propag.*, vol. 32, May 1984.

[81] L. Quibus, L. Luini, C. Riva, and D. Vanhoenacker-Janvier, "Use and Accuracy of Numerical Weather Predictions to Support EM Wave Propagation Experiments," *IEEE Trans. Antennas Propag.*, vol. 67, Aug. 2019.

[82] A. Martellucci, J. P. V. Poiares Baptista, and G. Blarzino, "New climatological databases for ice depolarization on satellite radio links," in *Proc. 1st Int. Workshop COST 280 "Propagation Impairment Mitigation for Millimetre Wave Radio Systems"*, (Malvern, UK), 2002.

[83] A. Martellucci, J. P. V. Poiares Baptista, and G. Blarzino in *Proc. URSI 27th General Assembly*, (Maastricht, NL), 2002.

[84] V. Mattioli, P. Basili, S. Bonafoni, P. Ciotti, and E. R. Westwater, "Analysis and improvements of cloud models for propagation studies," *Radio Science*, vol. 44, Mar. 2009.

[85] International Telecommunication Union Radiocommunication (ITU-R), "Recommendation ITU-R P.838-3: Specific attenuation model for rain for use in prediction methods," tech. rep., ITU, Mar. 2005. `https://www.itu.int/rec/R-REC-P.838-3-200503-I/en`.

[86] International Telecommunication Union Radiocommunication (ITU-R), "Recommendation ITU-R P.839-4: Rain height model for prediction methods," tech. rep., ITU, Sept. 2013. `https://www.itu.int/rec/R-REC-P.839-4-201309-I/en`.

[87] International Telecommunication Union Radiocommunication (ITU-R), "Recommendation ITU-R P.837-7: Characteristics of precipitation for propagation modelling," tech. rep., ITU, June 2017. `https://www.itu.int/rec/R-REC-P.837-7-201706-I/en`.

[88] V. I. Tatarskii, *The effects of the turbulent atmosphere on wave propagation.* Israel Program for Scientific Translation, 1971.

[89] A. Ishimaru, *Wave propagation and scattering in random media, vol. 1 Single Scattering and Transport Theory.* Academic Press, 1978.

[90] A. D. Wheelon, *Electromagnetic Scintillation I. Geometric Optics.* Cambridge University Press, 2004.

[91] A. D. Wheelon, *Electromagnetic Scintillation II. Weak Scattering.* Cambridge University Press, 2004.

[92] N. Sengupta, J. M. Warnock, E. E. Gossard, and R. G. Strauch, "Remote Sensing of Meteorological Parameters with the Aid of a Clear-Air Doppler Radar," tech. rep., NOOA Technical Report ERL 431 - WPL, June 1987.

[93] G. d'Auria, F. S. Marzano, and U. Merlo, "Model for estimating the refractive-index structure constant in clear-air intermittent turbulence," *Applied Optics*, vol. 32, May 1993.

[94] F. S. Marzano and G. d'Auria, "Model-Based Prediction of Amplitude Scintillation Variance Due to Clear-Air Tropospheric Turbulence on Earth-Satellite Microwave Links," *IEEE Trans. Antennas Propag.*, vol. 46, Oct. 1998.

[95] H. Vasseur, "Prediction of Tropospheric Scintillation on Satellite Links from Radiosonde Data," *IEEE Trans. Antennas Propag.*, vol. 47, Feb. 1999.

[96] J. Haddon, "Validity of the CCIR amplitude scintillation model for satellite uplink and downlink communication links with reference to small terminal operation at EHF," in *Proc. 26th Eur. Microwave. Conf. (EuMC)*, 1996.

[97] J. Haddon and E. Vilar, "Scattering Induced Microwave Scintillations from Clear Air and Rain on Earth Space Paths and the Influence of Antenna Aperture," *IEEE Trans. Antennas Propag.*, vol. 34, May 1986.

[98] E. Vilar and J. R. Larsen, "Elevation Dependence of Amplitude Scintillations on Low Elevation Earth Space Paths," in *6th Int. Conf. Antennas Propag. (ICAP)*, (Coventry, UK), 1989.

[99] E. Matricciani, M. Mauri, and C. Riva, "Relationship between scintillation and rain attenuation at 19.77 GHz," *Radio Science*, vol. 31, Mar.-Apr. 1996.

[100] L. Luini, C. Riva, C. Capsoni, and A. Martellucci, "Attenuation in Non-rainy Conditions at Millimeter Wavelengths: Assessment of a Procedure," *IEEE Trans. Geosci. Remote Sens.*, vol. 45, July 2007.

[101] L. Luini, C. Riva, R. Nebuloni, M. Mauri, J. Nessel, and A. Fanti, "Calibration and Use of Microwave Radiometers in Multiple-site EM Wave Propagation Experiments," in *Proc. 12th Eur. Conf. Antennas Propag. (EuCAP)*, (London, UK), 2018.

[102] Y. Karasawa and T. Matsudo, "Characteristics of Fading on Low-Elevation Angle Earth-Space Paths with Concurrent Rain Attenuation and Scintillation," *IEEE Trans. Antennas Propag.*, vol. 39, May 1991.

[103] L. Luini and C. Capsoni, "Using NWP Reanalysis Data for Radiometric Calibration in Electromagnetic Wave Propagation Experiments," *IEEE Trans. Antennas Propag.*, vol. 64, Feb. 2016.

[104] F. Barbaliscia, G. Brussaard, A. Hornbostel, J. Lavergnat, C. Mallet, G. Ortgies, F. Murr, A. Martellucci, E. Salonen, and F. Rucker, "Reference book on radiometry and meteorological measurements," in *OPEX Second Workshop of the OLYMPUS Propagation Experimenters*, (Noordwijk, NL), 1994.

[105] A. Martellucci, "Total Water Vapour and Cloud liquid Retrieval coefficients for Radiometric Measurements in Cabauw, The Netherlands," Tech. Rep. TEC-EEP/2007144, ESA, Noordwijk, NL, May 2007.

[106] R. J. Doviak and D. S. Zrnić, *Doppler Radar and Weather Observations 2nd Ed.* Cambridge University Press, 1993.

[107] J. Marshall, W. Hitschfeld, and K. Gunn, "Advances in radar weather," vol. 2 of *Advances in Geophysics*, Elsevier, 1955.

[108] R. Uijlenhoet, "Raindrop size distributions and radar reflectivity–rain rate relationships for radar hydrology," *Hydrology and Earth System Sciences*, vol. 5, Dec. 2001.

[109] D. Atlas and C. Ulbrich, "Path- and area-integrated rainfall measurement by microwave attenuation in the 1-3 cm band," *Journal of Applied Meteorology*, vol. 16, Dec. 1977.

[110] M. Lukach, L. Quibus, D. Vanhoenacker-Janvier, and L. Delobbe, "Rain attenuation statistics at Ka-band estimated from weather radar observations in Belgium," *Int. J. Satell. Commun. Networking*, vol. 36, June 2018.

[111] G. A. Siles, J. M. Riera, and P. García-del-Pino, "An Application of IGS Zenith Tropospheric Delay Data to Propagation Studies: Validation of Radiometric Atmospheric Attenuation," *IEEE Trans. Antennas Propag.*, vol. 64, Jan. 2016.

[112] L. Luini, C. Riva, L. Quibus, D. Vanhoenacker-Janvier, G. Siles, and J. Riera, "Water Vapor Retrieval to Support Electromagnetic Wave Propagation Experiments: Results from Different Techniques," in *Proc. 13th Eur. Conf. Antennas Propag. (EuCAP)*, (Krakow, PL), 2019.

[113] W. C. Skamarock, J. B. Klemp, J. Dudhia, D. O. Gill, D. M. Barker, M. G. Duda, X.-Y. Huang, W. Wang, and J. G. Powers, "A Description of the Advanced Research WRF Version 3," Tech. Rep. NCAR/TN-475+STR, NCAR, Boulder, CO, June 2008.

[114] W. Wang, C. Bruyère, M. Duda, J. Dudhia, D. Gill, M. Kavulich, K. Keene, H.-C. Lin, J. Michalakes, S. Rizvi, X. Zhang, J. Berner, K. Fossell, *et al.*, "ARW Version 3 Modeling System User's Guide," tech. rep., NCAR, Boulder, CO, Jan. 2016.

[115] P. Termonia, C. Fischer, E. Bazile, F. Bouyssel, R. Brozkova, P. Bénard, B. Bochenek, D. Degrauwe, M. Derkova, R. E. Khatib, R. Hamdi,

J. Mašek, P. Pottier, N. Pristov, Y. Seity, P. Smolíková, O. Spaniel, M. Tudor, Y. Wang, C. Wittmann, and A. Joly, "The ALADIN System and its Canonical Model Configurations AROME CY41T1 and ALARO CY40T1," *Geoscience Model Development Discussion*, vol. 11, p. 257–281, Jan. 2018.

[116] R. Randriamampianina, H. Schyberg, and M. Mile, "Observing System Experiments with an Arctic Mesoscale Numerical Weather Prediction Model," *Remote Sensing*, vol. 11, Apr. 2019.

[117] R. Stull, *Practical Meteorology: An Algebra-base Survey of Atmospheric Science*. University of British Columbia, 2017.

[118] R. Laprise, "The Euler Equations of Motion with Hydrostatic Pressure as an Independent Variable," *Monthly Weather Review*, vol. 120, Jan. 1992.

[119] K. V. Ooyama, "A Thermodynamic Foundation for Modeling the Moist Atmosphere," *Journal of the Amtopsheric Sciences*, vol. 47, Nov. 1990.

[120] J. P. Snyder, *Map Projection - A Working Manual*. United States Government Printing Office, 1987.

[121] NCAR, "WRF Model Physics Options and References," Mar. 2020. `https://www2.mmm.ucar.edu/wrf/users/phys_references.html`.

[122] CNRM, "ALADIN operational physics documentation (2005)," Mar. 2020. `http://www.umr-cnrm.fr/gmapdoc/spip.php?article12`.

[123] ECMWF, "IFS Documentation," Mar. 2020. `https://www.ecmwf.int/en/publications/ifs-documentation`.

[124] S. Hong and J. J. Lim, "The WRF Single-Moment 6-Class Microphysics Scheme (WSM6)," *Journal of the Korean Meteorological Society*, vol. 42, Mar. 2006.

[125] K. S. Lim and S. Hong, "Development of an effective double–moment cloud microphysics scheme with prognostic cloud condensation nuclei (CCN) for weather and climate models," *Journal of the Korean Meteorological Society*, vol. 138, May 2010.

[126] M. Tiedtke, "A Comprehensive Mass Flux Scheme for Cumulus Parameterization in Large-Scale Models," *Monthly Weather Review*, vol. 117, Aug. 1989.

[127] G. Grell and S. Freitas, "A scale and aerosol aware stochastic convectice parameterization for for weather and air quality modeling," *Atmospheric Chemistry and Physics*, vol. 14, May 2014.

[128] National Imagery and Mapping Agency (NIMA), "Department of Defense World Geodetic System 1984: Its Definition and Relationships with Local Geodetic Systems 3rd Ed.," Tech. Rep. TR8350.2, NIMA, Jan. 2000. `https://earth-info.nga.mil/GandG/publications/tr8350.2/wgs84fin.pdf`.

[129] N. K. Pavlis, S. A. Holmes, S. C. Kenyon, and J. K. Factor, "The development and evaluation of the Earth Gravitational Model 2008 (EGM2008)," *Journal of Geophysical Research*, vol. 117, Apr. 2012.

[130] N. Pavlis, "EGM2008 - WGS 84 Version," June 2019. https://earth-info.nga.mil/GandG/wgs84/gravitymod/egm2008/egm08_wgs84.html.

[131] D. A. Vallado, P. Crawford, R. Hujsak, and T. Kelso, "Revisiting Spacetrack Report #3: Rev 2," in *AIAA/AAS Astrodynamics Specialist Conference*, (Keystone, CO), Aug. 2006. https://celestrak.com/publications/AIAA/2006-6753/AIAA-2006-6753-Rev2.pdf.

[132] F. R. Hoots and R. L. Roehrich, "Spacetrack Report no. 3: Models for Propagation of NORAD Element Sets," tech. rep., NORAD, Dec. 1980. https://www.celestrak.com/NORAD/documentation/spacetrk.pdf.

[133] B. Rhodes, "sgp4 1.4," Jan. 2015. https://pypi.org/project/sgp4/.

[134] T. Kelso, "NORAD Two-Line Element Sets Current Data," Feb. 2018. https://celestrak.com/NORAD/elements.txt.

[135] International Telecommunication Union Radiocommunication (ITU-R), "Working Party 3M Fascicle on testing variables used for the selection of prediction methods," Tech. Rep. 3M/FAS/1-E Revision 1, ITU, July 2016. https://www.itu.int/oth/R0A04000007/en.

[136] International Telecommunication Union Radiocommunication (ITU-R), "SG 3 Databanks - Formatted Tables," June 2019. https://www.itu.int/en/ITU-R/study-groups/rsg3/Pages/dtbank-form-tables.aspx.

[137] A. Berne, M. ten Heggeler, R. Uijlenhoet, L. Delobbe, P. Dierickx, and M. de Wit, "A preliminary investigation of radar rainfall estimation in the Ardennes region and a first hydrological application for the Ourthe catchment," *Natural Hazards and Earth System Science*, vol. 5, Mar. 2005.

[138] R. Hamdi, H. Van de Vyver, and P. Termonia, "New cloud and microphysics parameterisation for use in high-resolution dynamical downscaling: Application for summer extreme temperature over Belgium," *International Journal of Climatology*, vol. 32, Nov. 2012.

[139] Meteomanz, "SYNOP/BUFR observations. Data by hours," Mar. 2020. http://www.meteomanz.com/sy1?ty=hp&l=1&cou=6260&ind=16080&d1=01&m1=01&y1=2015&h1=00Z&d2=31&m2=01&y2=2015&h2=23Z.

[140] J. Berckmans, R. Van Malderen, R. Pacione, and R. Hamdi, "Validating the water vapour content from a reanalysis product and regional climate model over Europe based on GNSS observations," Nov. 2018. https://www.atmos-chem-phys-discuss.net/acp-2018-1097/acp-2018-1097.pdf.

[141] N. Jeannin, X. Boulanger, L. Féral, L. Castanet, and F. Lacoste, "Inter-annual variability, risk and confidence intervals associated with propagation statistics. Part I: theory of estimation," *Int. J. Satell. Commun. Networking*, vol. 32, Sept. 2014.

[142] X. Boulanger, N. Jeannin, L. Féral, L. Castanet, F. Lacoste, and F. Carvalho, "Inter-annual variability, risk and confidence intervals associated with propagaiton statistics. Part II: parameterization and applications," *Int. J. Satell. Commun. Networking*, vol. 32, Sept. 2014.

[143] F. Teschl, R. Teschl, and H. Paulitsch, "Path Length in Rain Media and Effective Path Length Derived from Weather Radar Measurements," in *Proc. 11th Eur. Conf. Antennas Propag. (EuCAP)*, (Paris, FR), 2017.

[144] L. Quibus, L. Luini, C. Riva, and D. Vanhoenacker-Janvier, "Numerical Weather Prediction Models for the Estimate of Clear-Sky Attenuation Level in Alphasat Beacon Measurement," in *Proc. 12th Eur. Conf. Antennas Propag. (EuCAP)*, (London, UK), 2018.

[145] Radiometer Physics GmbH, "Humidity And Temperature PROfilers," Dec. 2018. `https://www.radiometer-physics.de/products/microwave-remote-sensing-instruments/radiometers/humidity-and-temperature-profilers/#tabs-container-1`.

[146] K.-H. Min, S. Choo, D. Lee, and G. Lee, "Evaluation of WRF Cloud Microphysics Schemes Using Radar Observations," *Weather and Forecasting*, vol. 30, Dec. 2015.

[147] S. Ventouras, R. Reeves, F. Perez-Fontan, F. Machado, V. Pastoriza, A. Rocha, S. Mota, F. Jorge, A. D. Panagopoulos, A. Z. Papagragkakis, C. I. Kourogiorgas, O. Fiser, V. Pek, P. Pesice, M. Grabner, A. Vilhar, A. Kelmendi, A. Hrovat, D. Vahoenacker-Janvier, A. Graziani, L. Quibus, and G. Gousetis, "Large Scale Assessment of Ka/Q Band Atmospheric Channel Across Europe with ALPHASAT TDP5: The Augmented Network," in *Proc. 11th Eur. Conf. Antennas Propag. (EuCAP)*, (Paris, FR), 2017.

[148] S. Ventouras, A. Martellucci, R. Reeves, E. Rumi, F. Perez-Fontan, F. Machado, V. Pastoriza, A. Rocha, S. Mota, F. Jorge, A. Panagopoulos, A. Papafragkakis, C. Kourogiorgas, O. Fiser, V. Pek, P. Pesice, M. Grabner, A. Vilhar, A. Kelmendi, A. Hrovat, D. Vanhoenacker-Janvier, L. Quibus, G. Goussetis, A. Costouri, and J. Nessel, "Assessment of spatial and temporal properties of Ka/Q band earth-space radio channel across Europe using ALPHASAT Aldo Paraboni payload," *Int. J. Satell. Commun. Networking*, vol. 37, Sept. 2019.

[149] M. Razavian, L. Quibus, and D. Vanhoenacker-Janvier, "Using Numerical Weather Predictions to Compare the LEO Attenuation Statistics Computed from Fixed-Elevation Statistics and from LEO time series," in *Proc. 25th Ka and Broadband Communications Conf.*, (Sorrento, IT), 2019.

[150] F. Cuervo, A. Martellucci, J. R. Castro, M. Schmidt, and M. Schönhuber, "The Alphasat Aldo Paraboni scientific and communication experiments at Ka and Q/V bands in Austria," *Int. J. Satell. Commun. Networking*, vol. 37, Sept. 2019.

[151] D. Vanhoenacker-Janvier, L. Quibus, M. Rytir, and T. Tjelta, "Measurement and modelling of tropospheric scintillation in Ka/Q band," in *Proc. 11th Eur. Conf. Antennas Propag. (EuCAP)*, (Paris, FR), 2017.

[152] C. de Villenfagne de Vogelsanck, "Analyse et modélisation de la scintillation troposphérique sur les liaisons terre-satellite à très faible angle d'élévation," Master's thesis, UCLouvain, 2016.

[153] J. Kervyn de Meerendre, "The scintillation phenomenon at low elevation angles in earth-space communications," Master's thesis, UCLouvain, 2017.

[154] C. J. Willmott, "Some Comments on the Evaluation of Model Performance," *Bulletin of the American Meteorological Society*, Nov. 1982.

[155] ISCCP, "International Satellite Cloud Climatology Project: Project Description, Participants and Status," Mar. 2020. `https://isccp.giss.nasa.gov/describe/`.

[156] E. Goudenhoofdt and L. Delobbe, "Statistical Characteristics of Convective Storms in Belgium Derived from Volumetric Weather Radar Observations," *Journal of Applied Meteorology and Climatology*, Apr. 2013.

[157] N. K. Lyras, C. I. Kourogiorgas, and A. D. Panagopoulos, "Cloud Free Line of Sight Prediction Modeling for Optical Satellite Communication Networks," *IEEE Communications Letters*, vol. 21, July 2017.